1994

AN INVESTIGATION OF SEISMIC ATTENUATION IN MARINE SEDIMENTS

RODERICK DAVID EDDIES

PHD

AN INVESTIGATION OF SEISMIC ATTENUATION IN MARINE SEDIMENTS

EDDIES, RODERICK DAVID

Award date:
1994

Awarding institution:
University of Plymouth

AN INVESTIGATION OF SEISMIC ATTENUATION IN MARINE SEDIMENTS

by

RODERICK DAVID EDDIES

A thesis submitted to the University of Plymouth
in partial fulfilment for the degree of

DOCTOR OF PHILOSOPHY

Department of Geological Sciences
Faculty of Science

June 1994

ABSTRACT

AN INVESTIGATION OF SEISMIC ATTENUATION IN MARINE SEDIMENTS

RODERICK DAVID EDDIES

There have been relatively few investigations into the attenuation properties of unconsolidated sediments using marine surface seismic data.

Several methods of measuring attenuation were assessed for reliability in a noise-free case and with the addition of noise using a set of synthetically absorbed and dispersed wavelets. Wavelet modelling proved to be superior to the other techniques, followed by spectrum modelling and the spectral ratios method. Complex trace analysis using the analytical signal proved to be unreliable for non-sinusoidal wavelets, whilst the risetime method was found to be very susceptible to noise for practical purposes.

Numerical modelling was carried out to assess the spectral effects of layering on a propagating pulse. The thin layer / peg-leg phenomenon has varying filtering effects on the propagating pulse. In particular, layers which are less than the "tuning thickness" of the propagating pulse have a low-pass effect.

The quality factor, Q, was measured in two case studies. In the first, the mean Q was determined from wavelet and spectrum modelling and found to be 60 for fine sands and 47 for coarse sands in the 1 kHz to 3 kHz frequency band. In the second, Q was determined as 59 for poorly sorted sandy diamicts in the 100 Hz to 240 Hz frequency band. The close fit between synthesised spectra and wavelets and observed data showed that a constant-Q mechanism would account for the spectral changes between the seabed and the deeper target reflection events in the two case studies. The spectra of the target reflection events in both case studies were lacking in low frequencies which is likely to be due to low-pass filtering from composite reflection events due to thin bed layering. For practical purposes, the determination of Q from a mean normalised seismic trace yielded the same result as measuring a mean Q from individual traces.

In a third case study, the seabed multiple was compared to the seabed reflection using wavelet and spectrum modelling. A lack of low frequencies in the seabed multiple showed that the seabed can act as a low-pass filter to an incident pulse. As the numerical methods rely on the seabed as having a white reflection and transmission response, the low-pass effect will result in erroneous estimates of the quality factor, Q.

CONTENTS

Chapter 4: A Single Layer Dispersive Model To Assess the Effective Reliability of Techniques to Estimate Q.

Chapter 5: Block 49/10 Case Study

Chapter 6: Bruce and Atlantic Frontiers Case Studies

Chapter 7: Discussion and Summary

Appendices

Enclosures

Enclosure 4a Floppy disk containing essential elements of project FORTRAN software (ASCII Listing):

Hilbert.For	Complex Trace Analysis Program
Risetime.For	Risetime Measurement Program
Match.For	Matching Technique Program
Specmod.For	Spectrum Modelling Program
Specrat.For	Spectral Ratios Program
Wavemod.For	Wavelet Modelling Program

Enclosure 5a Seismic Line 261, 49/10a-B

Enclosure 6a Relative Amplitude Stack Line UHR-304 Block 9/9.
Enclosure 6b Relative Amplitude Stack Line UHR-307 Block 9/9.
Enclosure 6c Relative Amplitude Stack Line UHR-308 Block 9/9.
Enclosure 6d Relative Amplitude Stack Line UHR-309 Block 9/9.
Enclosure 6e Relative Amplitude Stack Line UHR-320 Block 9/9.

FIGURES and TABLES

Figures

Tables

Acknowledgements

I would like to thank Phil Walker of Shell, Andy Hill of BP and Ian Grieves of Geoteam for their generous provision of the bulk of the data used within this study.

I am very grateful for the discussions I have had with my persevering supervisors, Dr. John Reynolds and Professor Don Tarling of the University of Plymouth. Special thanks go to Dr. Robert Whittington from my old college, the University College of Wales, Aberystwyth, who gave his time very freely and diligently as a key supervisor.

I would finally like to express my gratitude to my friends who have never ceased to ask when I would submit this work.

Author's Declaration

At no time during the registration for the degree of Doctor of Philosophy has the author been registered for any other University Award.

This study was financed with the aid of a research assistantship from the National Advisory Board.

Signed.....

Date..June 7th 1994.

Chapter 1: Introduction and Review of Seismic Attenuation

1.1 Introduction

The exploitation of the Earth's crust for oil and gas hydrocarbons has led to significant advances in field, analytical and experimental techniques in reflection seismology. Most hydrocarbon exploration has taken place within sedimentary basins, zones of the Earth's crust where great thicknesses of sediments have accumulated. 'Deep' seismic exploration generally involves the use of seismic waves generated by various sources of a frequency of less than 100 Hertz. Subsequent to their generation at or near the Earth's surface, these seismic waves are reflected back to the surface from layers within the crust, where they are recorded digitally for five to six seconds onto magnetic media for post-acquisition processing and subsequent interpretation. 'Shallow' seismic surveys are used for the investigation of the near subsurface with seismic sources ranging from single airguns, with frequencies up to about 700 Hertz to Pingers with frequencies up to about 10 kHz. Digital recording of sub-500 Hertz shallow seismic data at a 0.5 ms or 1 ms sampling interval is commonplace for investigations of shallow gas accumulations which present a serious hazard for drilling operations. However, much shallow seismic data is recorded in an analogue format on paper rolls, especially for investigations into the geotechnical properties of the uppermost, unconsolidated sediments. Such investigations are concerned with the anchoring sites for semi -submersible drilling rigs, the footings for jack-up drilling rigs, and subseabed conditions for outfall pipes, harbour developments and other marine structures. The use of acoustic techniques to assess seabed sediment properties may be found in Buchan *et al.* (1972), and Taylor Smith (1974).

The qualitative interpretation of analogue seismic data is based broadly upon the character of the seismic events, sometimes in relation to previous investigations, and the experience of the interpreter. In relation to the quantity of analogue data that is acquired, (for example, more than 90 line-kilometres from a typical rig-site survey),

very little quantitative analysis has been carried out on this high-frequency, and thus high resolution analogue data. The great majority of high-resolution analogue surveys utilise an electrical or electro-mechanical source, coupled with a single receiver, a series of pressure sensitive piezo-electric devices, collectively known as a hydrophone . The seismic data, typically reflected energy from the uppermost 50 metres, or less, of unlithified sediments are amplified and bandpass filtered to produce an interpretable seismic section. This is typical of single-channel acquisition. 'Deep' marine seismic surveys use many groups of receivers and arrays of sources, and multi-channel and multi-fold acquisition is the standard method. From the variation of the arrival times with source-receiver offset (move-out) for a particular reflector, an estimate of the velocity structure of the subsurface can be obtained from multi -channel acquisition. This acquisition method also allows for a significant increase in the signal-to-noise ratio of data as each part of the subsurface is sampled several times. Single-channel data, however, display no move-out, thus seismic velocity is not a parameter that can be measured in any way from the data without reference to nearby borehole information. However, in common with multi-channel data, single-channel data exhibit a general loss of reflected energy with two-way traveltime (termed 'attenuation' for this work), with a greater proportion of high frequency loss with increasing travel time, the causes of which may be both elastic and anelastic.

This thesis is concerned with an investigation into the effects of frequency-selective attenuation of high frequency seismic energy within unconsolidated sandy sediments. This chapter introduces, outlines and reviews attenuation mechanisms within unlithified sediments from the literature. Chapter Two considers the contributions of inelastic and elastic losses for seismic waves. In Chapter Three, the various methods for measuring frequency-selective attenuation are reviewed; Chapter Four assesses these methods in the noise-free case and in the presence of noise. A case study of Quaternary sediments undertaken with data from the North Sea is outlined in Chapter Five. Two case studies from the Bruce area of the North Sea and from the North-West Atlantic Approaches are described in Chapter Six. In Chapter Seven the results and a discussion

of the project is presented along with recommendations for future work.

1.2 Basic Definitions - Attenuation and Absorption

This chapter reviews the theory and mechanisms of both frequency - dependent and frequency-independent attenuation within unlithified sediments. The most important characteritics of plane elastic waves can be found in several geophysical texts including Sheriff and Geldhart (1982) and Waters (1978). However, this chapter principally reviews propagation of acoustic waves through porous, granular, elastic media rather than through solid elastic media, therefore the theory developed by Maurice Biot (1941, 1956a, 1956b, 1962a, 1962b) will be used as a theoretical basis for the review discussion, rather than a dissection of the elastic wave equation.

For the current work, the term "attenuation" will refer to the measurable amplitude losses or energy losses from elastic seismic waves without any reference as to the cause or mechanism of the energy or amplitude loss. The term "absorption" is used for the specific case of attenuation where the elastic seismic energy is gradually absorbed by the medium and converted to heat. The discrimination of the absorption element of seismic attenuation is of key interest in the study of the propagation of seismic energy through unconsolidated sediments.

1.3 Expressions For Attenuation

The amplitude of a plane-wave sinusoidal pulse undergoes an exponential decay as it travels through a medium given by:

$$A(x) = A(o).e^{-\alpha x} \quad \ldots\ldots\ldots 1(1)$$

where $A(o)$ is the initial amplitude, $A(x)$ is the amplitude after a distance x and α is the attenuation coefficient (e.g. Klimentos and McCann 1990)

Various other terms are used to express the amount of energy loss from a vibrational type of motion:

d is the "logarithmic decrement" which is the decrease in amplitude per cycle of an oscillation (e.g. Born 1941)

Q is the quality factor, (or $1/Q$ is the specific dissipation function) defined as 2π/(fraction of energy lost per cycle) (e.g. Knopoff 1964).

Q and d may be related by the formula $Q = \pi/d$

Yet another related term is ***n***, the exponent of frequency in the equation:

$$\alpha = kf^{n} \quad \ldots\ldots\ldots 1(2)$$

where α is the absorption coefficient, sometimes referred to as the attenuation coefficient, in db/unit distance, k is a constant and f is frequency in kHz (e.g. Hamilton 1972)

1.4 In-Situ and Laboratory Measurement of Absorption

The work of several authors summarised the conclusions of many investigations into the absorption characteristics of lithified rocks, including Knopoff (1964), White (1965), Bradley and Fort (1966), Kjartansson (1979), Johnston and Toksöz (1980) and Toksöz and Johnston (1981). The techniques that have been previously used to measure absorption within lithified material, for example the rise time method of Gladwin and Stacey, (1974) were also used for investigating unlithified sediments, for example in Badri and Mooney (1987). Several papers summarised much experimental work into seismic absorption within

unlithified sediments in the last fifty years including Hamilton (1972,1980,1987), Hampton and Anderson (1974), Hampton (1985) and Kibblewhite (1989).

Hamilton (1956,1963,1970) conducted a series of in -situ measurements in the sea floor off San Diego at frequencies of 3.5 ,7 ,14, 25 and 100 kHz respectively and at depths of less than 1 m. The data presented appeared to show a loose dependence of absorption on the first power of frequency for the fine, medium and coarse sands. Using data from a number of authors, Hamilton (1972) reported a relationship of $n = 1$ for the exponent of frequency (eqn. 1(2)) with α expressed in db/m, and f in kHz, that is, absorption varying as the first power of frequency. More specifically, Over a frequency range of 3.5 kHz to 1500 kHz, 25 values of the exponent of frequency, n, fell between 0.94 and 1.26 (with 23 values falling between 0.94 and 1.11). However, no single data set used covered more than two orders of magnitude in frequency. The work of Hamilton, (the 1972 paper in particular), showing that there appears to be a first-power dependence of absorption on frequency , has been a major contribution to the belief that absorption within sediments takes place at grain-grain contacts, that is, a frictional sliding process. The remaining variable, k, was shown to vary with either grain size or porosity, shown in Figures 1.1 and 1.2. In general terms, the bulk of the data indicated that the higher absorption rates were to be found in the coarser material (sands and silts) whilst the finer clays exhibited the lower absorption rates. The data collated by Hamilton (1972) included that of McCann and McCann (1969), from land and beach sediments using a frequency of 30 kHz. By comparing in-situ acoustic measurements to variations in absorption predicted by Biot's theory (Biot, 1956a,b) they concluded that for "real" sediments (in this case poorly sorted sands at 2m depth of burial) the dominant loss mechanism was solid friction between the particles (being a linear absorption mechanism). For a very well sorted sediment, the viscous mechanism may be more important, being due to the fluid mobility predicted by Biot theory. This viscous mechanism was the key factor in Stoll's proposal (Stoll, 1989) for a non-linear absorption mechanism in coarser sediments. McCann and McCann (1969) also proposed that for clays and silts (of up to 6 ϕ mean grain diameter), viscous loss between the non-clay fraction (with inactive particle surfaces) and the clay-water fraction was responsible for the

Figure 1.1

Mean grain size versus k. Data from surveys off San Diego: diamonds-(1966-70); triangles-(1956); inverted triangles-(1962); circles-(Shumway, 1960); open symbols-data in averages; X-literature value from Table 4a (Hamilton, 1972).
(after Hamilton, 1972).

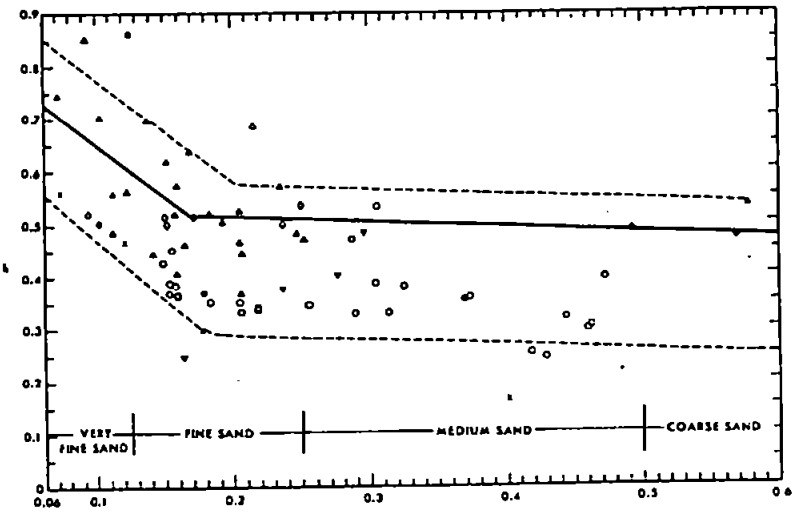

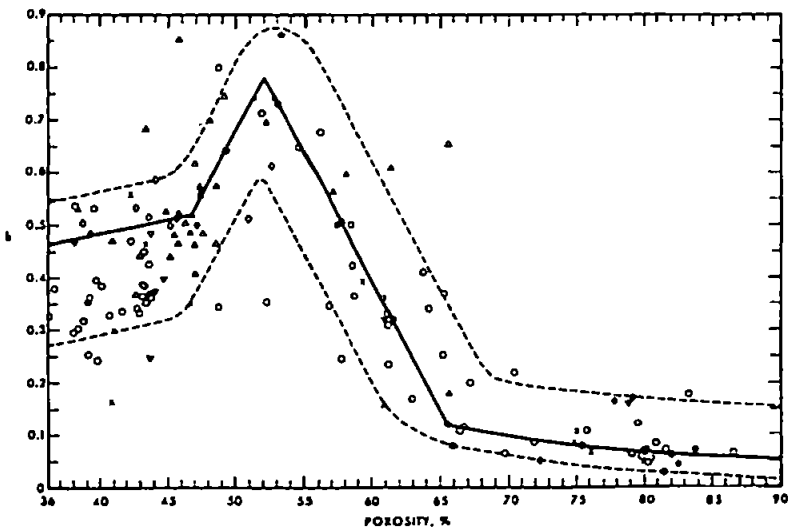

Figure 1.2

Porosity n, percent, versus k. Data from surveys off San Diego: diamonds-(1966-70); triangles-(1956); inverted triangles-(1962); circles-(Shumway, 1960); open symbols-data in averages; X-literature value from Table 4a (Hamilton, 1972).
(after Hamilton, 1972).

absorption observed. The absorption figures that were computed were in agreement with the 30 kHz measurments of Shumway (1960), and the 368 kHz measurements of D. McCann (1968). The non-clay fraction may be seen as a solid and the clay-water lattice may be considered a lossless fluid having negligible bulk and shear moduli. However, for marine clays with no non-surface-active particles, viscous losses became very small. This was due to the clay lattice and the fluid displaying a similar acoustic velocity, with viscous losses being a function of velocity differential (C. McCann 1969).

C. McCann (1969) extended the work of Urick (1947,1948) on compressional wave attenuation in clay suspensions. Urick showed that there was a linear variation of absorption coefficient in clay suspensions up to a concentration of about 10%. C. McCann extended the theory to concentrations up to 40% by considering the electrical forces between the particles, and thus a linear dependence of absorption with frequency would be expected for very high porosity clays, where each particle moves with the surrounding fluid with very small viscous effects. The low absorption values observed in marine clays (Shumway, 1960) appeared to support these results. When the concentration of particles having non-active surfaces became such that a clay lattice structure could not be formed, solid friction mechanism was dominant over the viscous mechanism.

McLeroy and DeLoach (1968) used frequencies from 15 kHz to 1500 kHz in beach sands and silty clays (remixed and settled under laboratory conditions). They found a value of 1 for n, the exponent of frequency, with k varying between 0.222 for silty clays and 0.050 for a quartz sand. Wood and Weston (1964) used frequencies from 4 kHz to 72 kHz in a tidal mud flat in Emsworth harbour, southern England, although the mechanical properties were not described. This was probably the first attempt at measuring seismic absorption in unconsolidated sediments *in-situ*, at a depth of about 0.5 m (Figure 1.3 after Wood and Weston (1964)). They found a linear dependence of absorption on frequency from 4 to 50 kHz, with an absorption coefficient of 0.02 of the frequency in kHz. The quality factor,Q was found to be 280 for tidal muds, although no statistical parameters were given on this figure. Their findings were compared to those of Shumway (1960), who used a resonant bar technique (described in Shumway, 1956) at frequencies

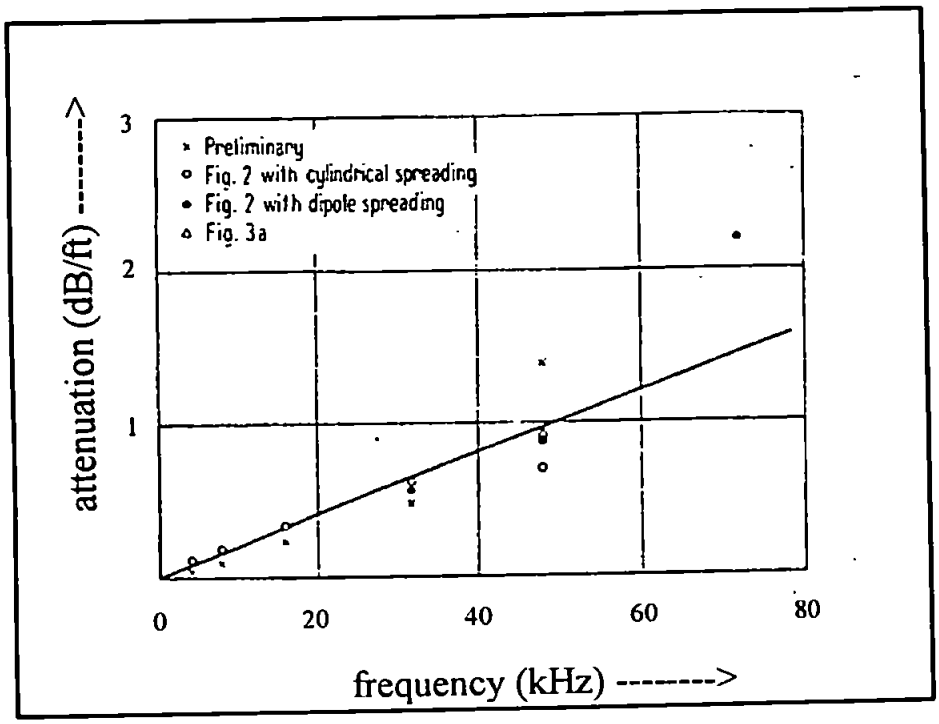

Figure 1.3

Experimental values for absorption in Elmsworth mud.
(after Wood and Weston, 1964)

between 20 kHz and 37 kHz in the laboratory. From some 65 samples, the data yielded an average value of n = 1.79, with a standard deviation of 0.98 . The findings of Shumway (1960) were criticised on two points by Hamilton (1972). Firstly, there were examples in the data of measured absorption decreasing with increasing frequency. Secondly, the exponent n varied from 0.6 to 3.4 in similar sediment types. These results were not in accord with any theoretical work or any experimental findings. Shumway (1960) suggested that as natural sediments displayed a variety of pore sizes and particle sizes, their absorption characteristics would lie between the square-root and squared dependency suggested by Biot (1956a,b). One of the few data sets obtained using a seismic reflection technique was from Bennet (1967), who used frequencies between 40 Hz and 900 Hz and found a linear relationship between absorption and frequency and an absorption coefficient of 0.066 with the frequency expressed in kHz . The technique used was not reported in detail, but involved comparing the seabed reflection to a buried reflector over a wedge of sediment of varying thickness, with the resultant absorption measured as a function of sediment thickness. Cole (1965) used bottom-loss curves from the Gulf of Alaska to extend the linear absorption-frequency relationship to the 100 Hz to 900 Hz band. However , the method used to produce this result could not yield absolute absorption estimates because of the lack of geometrical knowledge of the transmission path between source and receiver. Ulonska (1968) reported *in-situ* absorption coefficients of 54 dB/m and 26.2 dB/m in clay and clayey silt at 250 kHz from Baltic Sea sediments at a depth of about 2m. Schirmer (1970) used a frequency of 1 kHz at a depth of about 2 m in Baltic Sea sediments to report an absorption coefficient of 0.2 dB/m. Tullos and Reid (1969) used a vertical seismic profile (VSP) technique to measure absorption in Gulf of Mexico sediments with frequencies between 50 and 400 Hz, from 2 m to 34m depth. They reported a k value of 0.093 in clayey sands, assuming $n = 1$.

Badri and Mooney (1987) used a land seismic reflection technique to acquire data in the 45 Hz to 750 Hz band. Several methods of Q estimation were used for data from soft, wet clays with thin sand lenses, yielding a wide range of Q-values, which appeared to be largely dependent on the mathematical treatment of the data (see Chapter 2).

Edrington and Calloway (1984) measured absorption in gassy marine sediments (gassy soft to very soft clays) in the Mississippi delta area *in-situ* with frequencies from 400 Hz to 1 kHz yielding a value of k of about 1.4 dB/kHz-m. This figure was an order of magnitude greater than typical values for k for non gassy sediments (*c.f.* Hamilton, 1972). It was also assumed that absorption was proportional to frequency, as the authors have assumed frictional losses as being the dominant mechanism.

Jannsen *et al.* (1985) used and evaluated four mathematical methods to estimate Q using single-channel, vertically-incident marine reflection data from the Baltic Sea. A 1000 joule sparker source with a quoted frequency range of 150 Hz to 450 Hz was used and the resulting data digitised at 5 kHz. A value of Q was computed for several layers, but with little geological information of the sub-surface. A figure of Q = 15 was given for muddy sands close to the seabed. A 25% accuracy was quoted for their results, with a comment that all methods to determine Q failed given a noise level above 20% in the field data (which would deform the shape and spectrum of the wavelet), with only one particular method giving consistent results above 10% .

In a more recent review, Hamilton (1987) reaffirmed his view that absorption varies as the first power of frequency. However, Kibblewhite (1989) examined some more recent low-frequency data sets and concluded that there was a deviation from the linear relationship at low frequencies. The data from Hamilton (1987) was included, as well as more recent contributions from Webb and Cox (1986) and Zhou *et al.* (1987). Absorption appeared to become non-linear at frequencies of less than 100 Hz for sands (although no reliable data exists below 10 Hz) and between 1000 Hz and 10000 Hz for silts. This generalised interpretation is shown in Figure 1.4 (after Kibblewhite, 1989). Kibblewhite (1989) describes these physical characteristics as being compatible with the Biot-Stoll formulation for the attenuation of acoustic waves in porous media, which is discussed in the following section. No attempt was made by Kibblewhite to formulate a theory for attenuation in noncohesive sediments, and within the review, no mention was made of the work of McCann and McCann (1985) who did formulate a theory for the attenuation of compressional waves in noncohesive sediments.

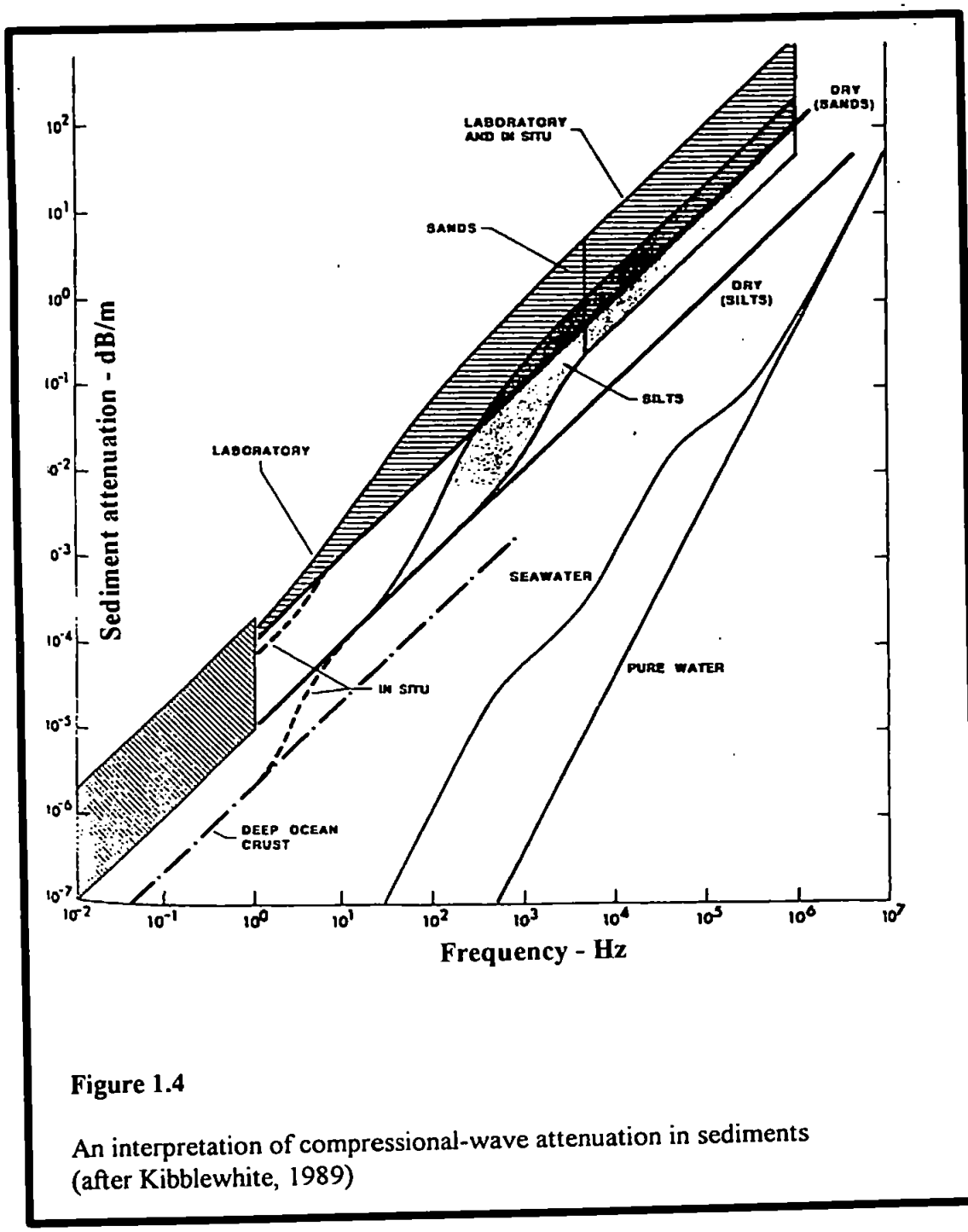

Figure 1.4

An interpretation of compressional-wave attenuation in sediments (after Kibblewhite, 1989)

1.5 Biot Theory

Biot (1941, 1956a, 1956b, 1962a, 1962b) developed a comprehensive theory for the response of a skeletal frame containing compressible fluid. His theory predicts that three types of body wave (i.e. with the absence of boundaries) may exist in a fluid saturated porous medium. Two of these were compressional waves, subdivided into the 'first kind ' and 'second kind '. The wave of the first kind was one in which there is little phase difference between the movement of the solid and fluid components. The wave of the second kind was one where an appreciable phase difference occurs between the two components, and was characterised by large intrinsic damping (Biot 1965b). The other is a shear or rotational wave. The first kind of wave and the shear wave were analogous to the 'P' and 'S' body waves that travel through elastic solids; the former implies a change in volume of a piece of material that the wave propagates through, without a change in shape, whilst the latter implies a change in shape without a corresponding change in volume . Fluids have no shear strength and thus cannot support shear waves.

The detailed mathematical content of the Biot theory is outside the scope of this work. However it is necessary to outline the important elements of the theory and to examine the relevance of the theory to the current work. In essence, Biot derived a set of equations which describe the motion of an element of volume attached to a skeletal frame and for the motion of pore fluids moving into or out of this element of volume . This theory is, therefore, relevant to any investigation of the acoustical properties of saturated unconsolidated sediments. The mathematical details of the theory have been summarised by Stoll (1989), from which the following has been taken:

Consider one-dimensional wave motion in the x-direction; the stress-equation of wave motion for the volume attached to the frame is:

$$\nabla^2(He - C\zeta) = \frac{\partial^2}{\partial t^2}(\rho e - \rho_f \zeta) \quad \text{.....1(3)}$$

The second equation which describes the motion of the fluid relative to the frame is:

$$\nabla^2(Ce - M\zeta) = \frac{\partial^2}{\partial t^2}(\rho_f e - m\zeta) - \frac{\eta}{\kappa}\frac{\delta\zeta}{\delta t} \quad \text{.....1(4)}$$

where:

ρ is the bulk density of the medium

ζ is the increment of fluid content

H, **C**, **M**, are Biot's coefficients (functions of the bulk moduli of the porous frame, pore fluid and the solid material of the frame)

ρ_f is the density of the pore fluid

e is the volumetric strain ($e_x + e_y + e_z$ in a cartesian system)

m is an apparent mass ($m > \rho_f/ß$) as not all of the fluid moves in the direction of the macroscopic pressure gradient (due to a tortuous porosity)

ß is the porosity

k is the coefficient of permeability

η is the viscosity of the pore fluid

By solving this pair of differential equations, a relationship was obtained between absorption and frequency for a saturated medium with a linear elastic frame under Poiseuille flow (constant ratio of fluid flow to pressure gradient, or where there is no difference in phase between the velocity and the friction force). Stoll (1989) described certain inadequacies to this model; Up to a threshold frequency, absorption would increase with increasing frequency. With constant flow resistance, absorption would then become constant with increasing frequency, due to Poiseuille flow . Absorption would be proportional to the square of the frequency (Biot 1956a) ,or $n = 2$ in eqn. 1(2). Poiseuille flow only occurs at the lowest frequencies therefore the frequency dependence of viscous resistance to fluid flow must be accounted for (that is, the viscosity coefficient of the fluid becomes a variable parameter, rather than a constant , Biot (1956b)). Most natural

materials display non-elastic properties to varying degrees (for example frictional losses between sand grains), which must be taken into consideration. Local fluid motion between and near the intergranular contacts can also lead to energy loss which must also be incorporated into any behavioural model. Biot (1956b) accounted for the viscous flow effects by deriving a complex correction factor, valid for wavelengths which are large relative to the pore size, which for natural sediments allows for frequencies up to a few MHz . This correction factor would make absorption to be proportional to the square root of frequency. Stoll (1977) redefined several of Biot's operators as being linear viscoelastic rather than elastic, to account for the inelasticity of the skeletal frame, and local viscous damping. Essentially, the shear modulus and bulk modulus of the skeletal frame were considered as viscoelastic variables, whilst the bulk moduli of the skeletal elements and the fluid were considered as elastic constants. For coarser, more permeable materials, viscous losses are the dominant cause of absorption, with large amounts of fluid motion relative to the frame, and differing acoustic velocities of the sediment particles and the surrounding fluid. For dry, coarse material, Mindlin (1949) showed that the dominant mechanism of energy loss was frictional loss due to intergranular slippage confined to a small area of contact. This form of loss was essentially frequency-independent and was referred to as 'solid-friction' in much of the literature (Born ,1941; McCann and McCann, 1969). It was also the same loss reported in much of the literature concerning seismic absorption in lithified rocks, such as in Attewell and Ramana (1966), Hunter et al (1961), Knopoff and MacDonald (1958), , White (1966) and Wyllie et al (1962). However, McCann and McCann (1985), stated that the solid-friction mechanism was amplitude-dependent, implied no velocity dispersion and necessitated that energy was transferred from one frequency to another, implying the superposition theorem did not hold.

When the coarse material was saturated, viscous losses became the dominant source of absorption at frequencies of only a few Hz (Stoll, 1989). Local viscous damping was considered to be negligible (from "squeeze film motion", Biot (1962b)). However, for finer materials, with much lower permeability, there was less fluid motion relative to the frame, and thus losses from the skeletal frame predominated, including a)

frictional losses b) relaxation of intergranular bonds and c) local frequency dependent viscous losses due to squeeze film motion. The latter effect became larger with smaller particle size and shorter distance between particle surfaces. Two very different responses for finer and coarser materials have been proposed. In particular the response of water saturated sands was predicted to be non-linear at all but the lowest of frequencies (Stoll, 1977,1989). This work was significantly different to the published findings of many other workers in that absorption was proposed to vary other than with the first power of frequency (Hamilton, 1972, 1987; McCann and McCann, 1969). In essence, the work of both Biot and Stoll predicts that absorption within sediments will have a non-linear relationship with frequency given that viscous losses provide the primary damping mechanism. Intrinsic absorption will vary as the square of frequency at low frequencies ($\alpha = k.f^2$), as a linear function of frequency for intermediate frequencies ($\alpha = k.f^1$) and as the square root of frequency at high frequencies ($\alpha = k.f^{0.5}$). The linear section is predicted to extend to a decade of frequency values. McCann and McCann (1985) showed that the variation of absorption with frequency can be explained by a viscous dissipation mechanism, and that the absorption is predictable given an estimation of the pore-size distribution. Their work involved a modification of Biot's theory to incorporate a distribution of pore sizes in the frequency range of 10 kHz to 2.25 MHz. The model they proposed was a sediment with porosity consisting of a distribution of cylindical pores of varying radii (a). All the pores of a given radius form a segment of sediment with the same porosity (ϕ) as the sediment as a whole. With each pore radius having a fractional porosity V_a, the length of each segment is set to V_a/ϕ. As a compressional wave traverses each segment in turn, it finds no change in elastic moduli or density as ϕ remains constant from segment to segment, and the viscous forces causing attenuation through each segment can be summed, and with the traveltime, an attenuation estimate of the sediment can be made. For a glass-bead sediment they found n, the exponent of frequency to be 0.96 ±0.07 (at 0.535, 1.02 and 2.4 MHz) and for a beach sand they found n to be 1.02 ±0.13 (at frequencies between 7.5 and 51 kHz). Both data sets indicated a linear absorption mechanism which could be explained using a theory based upon a viscous dissipation

mechanism, without invoking solid friction losses.

1.6 Non-Absorption Mechanisms For Seismic Attenuation

As well as the effects of absorption, many other factors must be considered that affect the recorded amplitude of an acoustic pulse as it propagates through sediments (Figure 1.5 (after Sheriff, 1975)). These factors include raypath divergence, reflection and transmission at interfaces, including the effects of thin layers and cyclic sedimentary sequences and scattering losses. Other factors such as instrumental response and source characteristics are involved, but more as scaling factors, assuming a broad band response across the frequency band of interest.

1.6.1 Raypath Divergence

Given a constant velocity earth and a point source, the amplitude (pressure amplitude) of a seismic wave would be inversely proportional to the distance travelled by that wave, (Newmann, 1973) and for all but the near field and far from the source, the wavefront will be spherical. With the complex velocity structure of the earth, the waves would be affected by refraction and thus raypath curvature will occur. In most cases, velocity increases with depth, and thus geometrical spreading would attenuate amplitude more quickly than in the constant velocity ideal. However, the effect is well understood and can be corrected if necessary. Within the literature, however, the assumption of a plane wave is often made. This is because at a certain distance from the source, the raypaths hardly diverge (commonly referred to as "the far field" , where the $1/r^2$ terms in solutions to the wave equation become negligible, (Sheriff and Geldhart,1982)). If this was the case then the amplitude loss due to spreading was considered negligible between two points of plane wave propagation.

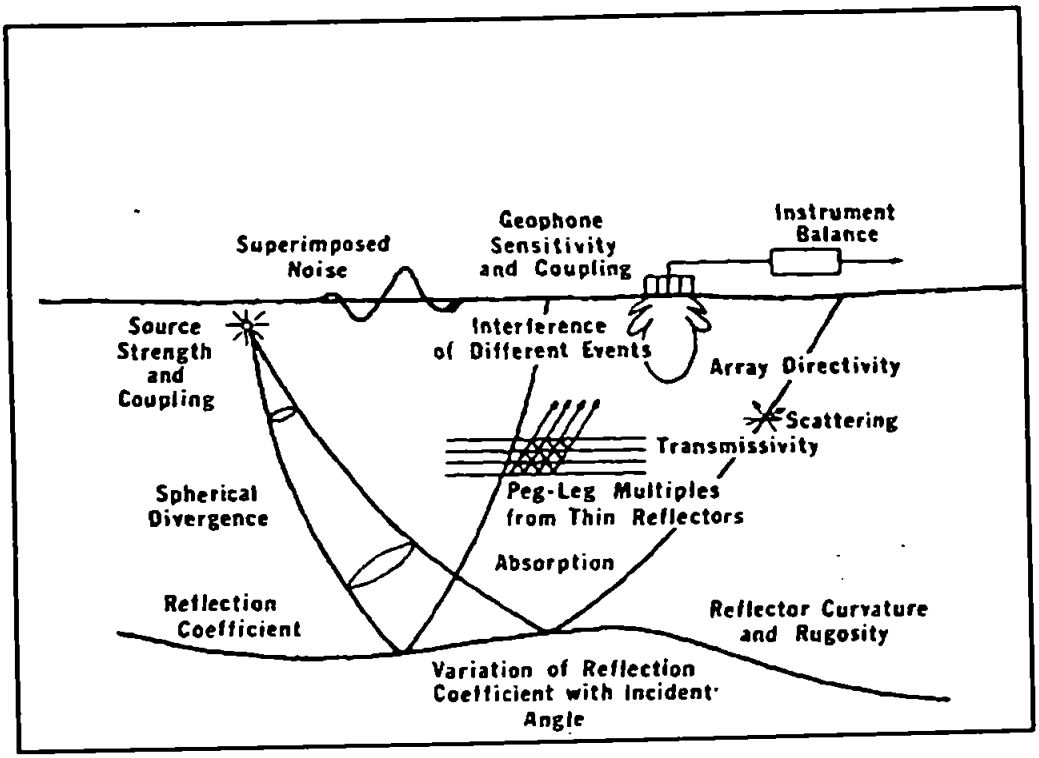

Figure 1.5
Factors affecting the Recorded Amplitude of a Reflected Pulse
(after Sheriff, 1975)

1.6.2 Reflection and Transmission at Interfaces

At an interface between two layers of differing elastic properties, a propagating wave will have part of its energy reflected back into the upper medium, and part transmitted into the lower medium. Normal incidence of the wave upon the interface is assumed, and thus mode conversion is not considered. This energy partition is summarised by the reflection coefficient, **R**, which is the ratio of reflected and incident amplitude (Zoeppritz, 1919). The transmission coefficient, T is defined as 1 - R. In terms of wave amplitude, the partition may be expressed as:

$$R_{12} = \left(\frac{Z_2 - Z_1}{Z_2 + Z_1}\right)^2 \quad \ldots\ldots 1(5)$$

$$T_{12} = \frac{4Z_1Z_2}{(Z_2 + Z_1)^2} \quad \ldots\ldots 1(6)$$

where $\mathbf{Z_1}$ and $\mathbf{Z_2}$ are the acoustic impedances of the layers above and below the interface, and R_{12} T_{12} are the proportions of the incident amplitude that are reflected and transmitted respectively. The derivation of the reflection coefficients using wave theory and ray theory can be found in Ziolkowski and Fokkema (1986).

For interfaces between "thick", "welded", elastic layers, the reflection and transmission process can be treated as being independent of frequency. "Thick " in this instance refers to a layer which has none of the frequency-dependent reflection characteristics of a thin bed (see below). "Welded" in this instance refers to two layers which are connected by a continuity of pressure and displacement. Stoll (1977), and Stoll and Kan (1981) looked at the reflection coefficients of marine sediments within the framework of Biot's theory. Stoll and Kan (1981), showed that even with normal incidence there is a difference between the elastic ideal and sediments which lose energy in the skeletal framework and the intervening fluid. This was computed for a simple model of water over sand, with a porosity of 47%. For the 10 Hz to 10 kHz band, Stoll and Kan

(1981) proposed that the interface would act as a non-white filter to a seismic pulse. Their model interface would preferentially reflect lower frequencies below a certain angle of incidence but preferentially reflect higher frequencies above a certain angle of incidence. This had the obvious consequences for any investigation into absorption which assumes a white response from any reflector or sequence of reflectors, in that spectral changes in reflected pulse character would not be solely attributable to absorption effects. A case was also considered, again within the framework of Biot's theory, of a mud of relatively low permeability overlying a sand of several magnitudes higher permeability. Biot's theory proposed that waves of the first kind and second kind were generated at the interface between the layers. As stated in section 1.4, waves of the second kind would have very high absorption characteristics, as the frame and the fluid would be moving largely out of phase. This generation at the interface, and subsequent frequency-dependent absorption would again have resulted in the preferential reflection of lower frequencies (below a few hundred Hz) because of the energy lost to second kind wave generation and subsequent rapid absorption above this frequency. For a single interface, this loss mechanism would have little effect, but in the case of a sequence of sand and muds, with cyclic layering (i.e. with many lossy interfaces) , a preferential removal of high frequencies would occur (Stoll, 1977).

O'Doherty and Anstey (1971) indicated that there was a possibility of large transmission losses in the case where there was cyclic layering of thin layers with contrasting acoustic impedances. Widess (1973) stated that the reflection response is at a maximum when the thickness a layer is a quarter of the wavelength of the dominant frequency, conversely, the transmission response is at a mimumum at the same frequency. Given a pulse propagating through a cyclic sequence, with a few percent of energy reflected at each interface, very little energy would be available after many interfaces. However, the work of Anstey (1960), Berzon (1967) and others has shown that the peg-leg multiples generated within the thin layers actually preserved the amplitude of the downgoing pulse, albeit at the lower frequencies and with a short time delay (Figure 1.6). For many of these thin layers, O'Doherty and Anstey (1971) concluded that it would make

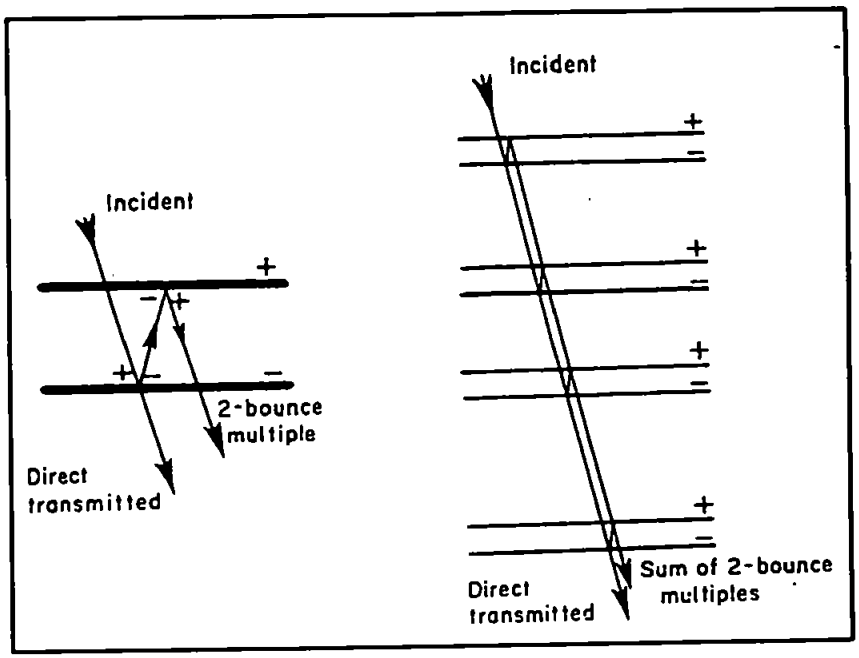

Figure 1.6

The basic thin plate defined between interfaces having reflection coefficients of opposite sign, and the cumulative effect of the multiple reflections from four such thin plates. (after O'Doherty and Anstey, 1971)

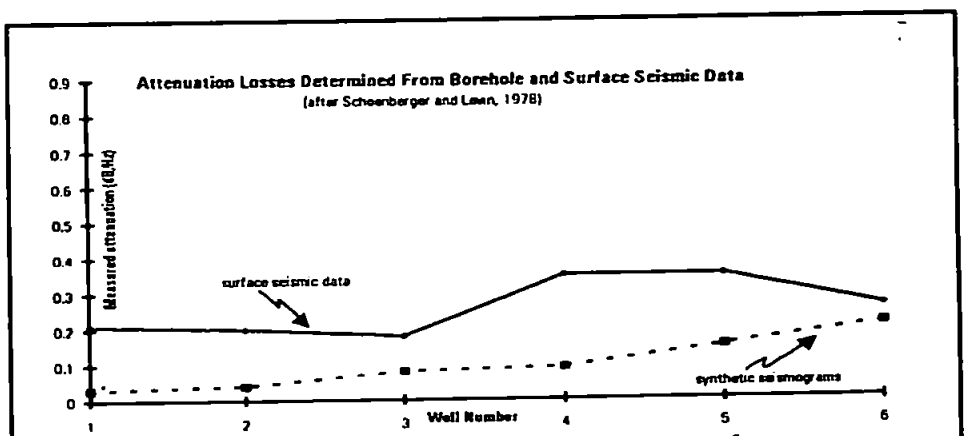

Table 1. Fraction of total attenuation due to intrabed multiples.

Well	α_1 Intrabeds	α_2 Surface data	$\frac{\alpha_1}{\alpha_2} \times 100$ percent
	Measured attenuation (dB/Hz)		
I	.03	.21	14
II	.04	.20	20
III	.08	.18	44
IV	.09	.35	25
V	.15	.35	43
VI	.21	.26	80

Figure 1.7

Comparison of Attenuation determined from Synthetic Seismograms and Attenuation determined from Surface Seismic Data (after Schoenberger and Levin, 1978)

no difference if the primary downgoing pulse did not exist, as the useful seismic information was carried by the short-delay (from thin layers) multiple reflections. They did not, however, indicate the required number of multiples that would facilitate this effect. One of the necessary products of this mechanism was a progressive loss of amplitude and a progressive broadening of the downward propagating pulse which are, of course, two of the characteristics of absorption. A comparison of the spectral effects of the two mechanisms was not given. The high-frequency cut effect of cyclic layering appeared to be of a constant dB/wavelength, and of a magnitude that might have exceeded the losses due to absorption. The effects of cyclic layering, therefore, cannot be overlooked when spectral characteristics of propagated pulses are investigated.

Schöenberger and Levin (1974) confirmed the findings of O'Doherty and Anstey (1971) by using real wells and generating synthetic seismograms. They concluded that transmission losses tended to lower the amplitude uniformly at all frequencies, whilst short-delay multiples preferentially lowered the amplitudes at the higher end of the frequency spectrum. The latter effect occurred because the short-delay multiples had the same polarity as the primary pulse. The spectral changes of the seismic pulse due to multiple short-delay reflections was compared to that of absorption. Using a spectral ratio method the synthetic seismograms (0 Hz to 240 Hz) were compared to seismic reflection data traversing the two wells at a shallow and deeper depth interval. The attenuation due to intrabed multiples was found to be 0.056 dB/wavelength for Well A and 0.061 dB/wavelength for Well B. The "total" attenuation between the two intervals was calculated using seismic reflection data from the same interval, yielding values of 0.019 and 0.014 dB/wavelength respectively. The conclusion they made was that by a simple subtraction, the intrinsic absorption was about 50% to about 66% responsible for the attenuation observed (assuming a linear dependence of loss on frequency, irrespective of the loss mechanism). Schöenberger and Levin (1978) followed their earlier work by using the same technique on a further 31 wells from all over the world. Figure 1.7 (after Schöenberger and Levin 1978) shows the attenuation determined from synthetic seismograms computed from six wells compared to the attenuation determined from six

seismic lines passing through those wells using the spectral ratio method. Assuming that the seismic data contained the effects of both of the loss mechanisms, the effects of short-delay multiples accounted for between 14 % and 80 % of the amplitude loss measured from the seismic data.

Spencer *et al.* (1977) investigated the attenuation effect of layering along with attempting to determine the threshold at which the attenuation due to layering became significant. They proposed a process of 1-D scattering i.e. a decrease in the coherence of the energy, without any net losses from the system. The model was termed non-interactive, as only the short delay multiples generated within the layer effected the transmitted primary pulse. For their scattering model (Figure 1.8), the two-way transmission coefficient $Q_i(f)$ for a layer **i** embedded in an infinite homogenous medium was given by:

$$Q_i(f) = \frac{(1-R_i^2)^2}{(1+R_i^2)^2 - 4R_i^2.\cos^2 2\pi f\Delta_i} \quad \text{.....1(7)}$$

In equation 1(7), R_i is the reflection coefficient at the interfaces of the layer and the infinite medium, and Δ_i is the one way traveltime across the layer. For any particular pulse, there will be a maximum of attenuation when the layer thickness equals 1/4 of the wavelength of the pulse (with a positive reflection coefficient at the top and a negative at the bottom) with decreasing attenuation below and above this node (Figure 1.8). With thicker layers, this major node would be shifted towards lower frequencies. With a smaller reflection coefficient, the nodal effect became less pronounced. From DC to the nodal frequency, the attenuation was proportional to the square of frequency, this band of course being that outwith which the layer thickness was less than 1/4 of the wavelength, and therefore, nonresolvable. Using a slightly different nomenclature to that of Spencer *et al.*, an attenuation coefficient ,α , for stratigraphic attenuation, was proposed in the form:

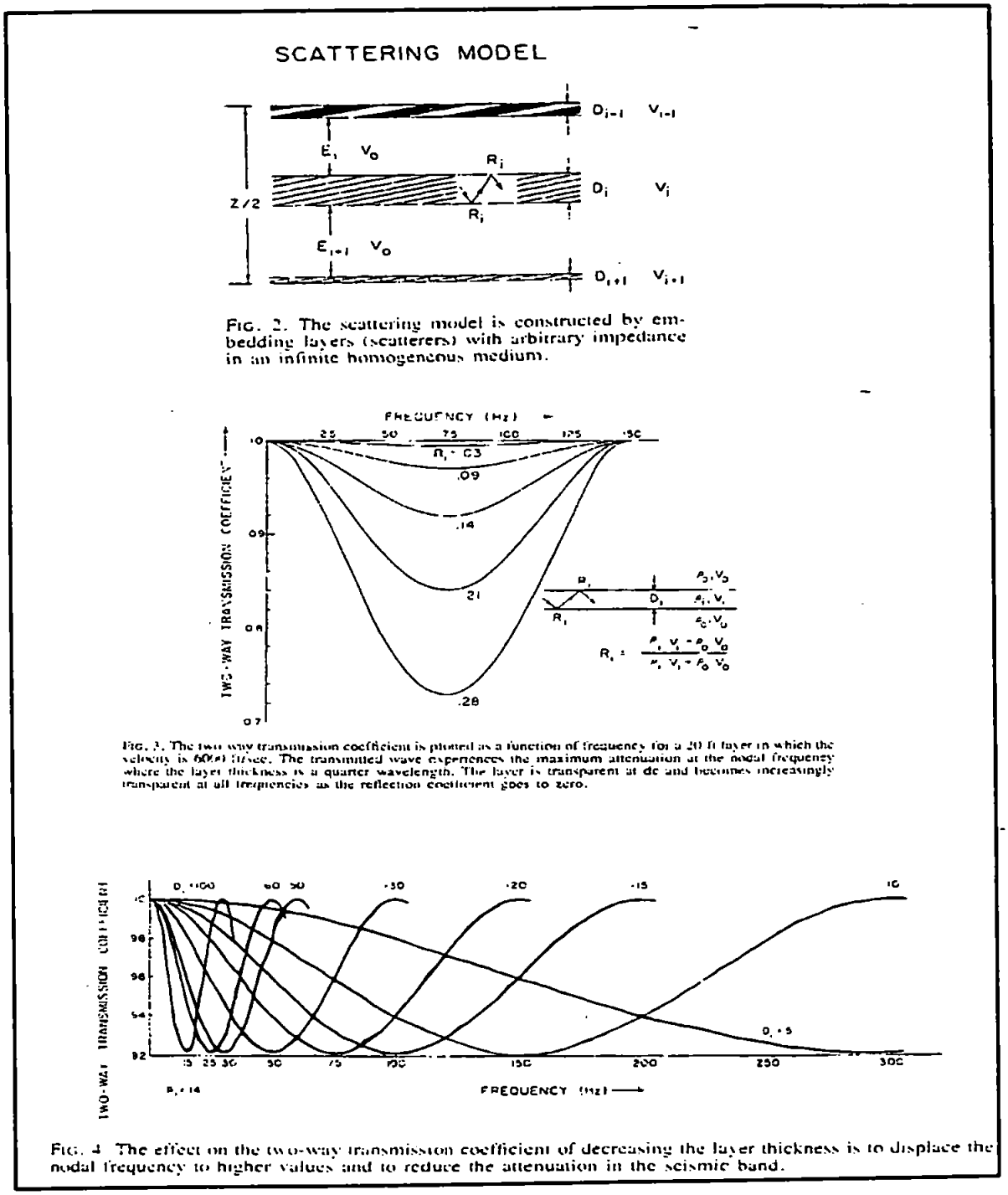

FIG. 2. The scattering model is constructed by embedding layers (scatterers) with arbitrary impedance in an infinite homogeneous medium.

FIG. 3. The two-way transmission coefficient is plotted as a function of frequency for a 20 ft layer in which the velocity is 6000 ft/sec. The transmitted wave experiences the maximum attenuation at the nodal frequency where the layer thickness is a quarter wavelength. The layer is transparent at dc and becomes increasingly transparent at all frequencies as the reflection coefficient goes to zero.

FIG. 4. The effect on the two-way transmission coefficient of decreasing the layer thickness is to displace the nodal frequency to higher values and to reduce the attenuation in the seismic band.

Figure 1.8

One-Dimensional, Non-Interactive Scattering Model
(after Spencer et al., 1977)

$$\alpha = kf^2 \quad \text{.....1(8)}$$

where:

$$k = \frac{(8\pi^2\phi)}{D}.(\sum_{i=1}^{M} P_i R_i^2 \Delta_i^2) \quad \text{.....1(9)}$$

and:

ϕ is the fraction of the zone in which the scattering layers are embedded that the layers occupy

D is the mean layer thickness

P_i is the fraction of scatterers of the ith type

M is the number of different types of scatterers (type being a function of R and Δ)

For frequencies of up to 100 Hz, and with reflection coefficients of $R < 0.08$ which they proposed was likely in sand-shale sequences, the stratigraphic component was likely to be negligible.

The problem of linear, elastic frequency-dependent attenuation was further investigated by Ziolkowski and Fokkema (1986). They proposed that "The seismic reflection data must exhibit a progressive attenuation of high-frequency energy with time, whether irreversible effects are present or not. ". They pointed out (as previously shown by Treitel and Robinson (1966)) that with the simple case of normal incidence and elastic plane layers, the frequency response of the sequence cannot be white unless there was a perfect reflector at the base of the sequence. Only this perfect reflector would have ensured all the energy that went into the system came out, albeit with frequency-dependent phase delays (the "all pass theorem" of Robinson and Treitel, (1966)). Each layer was elastic and cannot create energy or convert it. The investigation into the plane layer response was taken further to look at the "thin layer" problem.

Using wave theory, Ziolkowski and Fokkema (1986) derived alternative expressions for the transmission (T) and reflection coefficients (R):

$$R = \frac{(1 - e^{\frac{2j\omega d}{v_2}}).R_p}{1 - (R_p^2.e^{\frac{2j\omega d}{v_2}})} \quad \text{.....1(10)}$$

$$T = \frac{(1 - R_p^2).e^{j\omega d(\frac{1}{v_2} - \frac{1}{v_1})}}{1 - (R_p^2.e^{\frac{2j\omega d}{v_2}})} \quad \text{.....1(11)}$$

The exponential component can be expressed:

$$e^{\frac{2j\omega d}{v_2}} = \cos(\frac{2\omega d}{v_2}) + j\sin(\frac{2\omega d}{v_2}) \quad \text{.....1(12)}$$

Consider the case of:

$$\frac{2\omega d}{v_2} << \pi \quad \text{.....1(13)}$$

Then equation (1(12)) can be expressed as

$$e^{\frac{2j\omega d}{v_2}} = 1 + \frac{2j\omega d}{v_2} \quad \text{.....1(14)}$$

This corresponded to the case where the dominant wavelength was less than one quarter of the thickness of the layer.

Putting 1(12) into 1(9), the layer response is:

$$R(\omega) = \frac{-j\omega R_p . 2\dfrac{d}{v_2}}{1 - R_p^2 - jR_p^2 . 2\omega\dfrac{d}{v_2}} \quad \ldots\ldots\ldots 1(15)$$

The imaginary part of the denominator of the RHS of eqn. 13 for realistic values of R ($R_p < 0.4$) is negligible therefore:

$$R(\omega) \approx \frac{-j\omega R_p . 2d}{v_2(1 - R_p^2)} \quad \ldots\ldots\ldots 1(16)$$

This was the thin layer reflection response to a normally incident plane wave (Ziolkowski and Fokkema 1986). This was used in Figure 1.9 (Koefoed and de Voogd, 1980) where the reflection response was plotted as a function of reflection coefficient and layer thickness. The amplitude of the thin bed reflection response increased with increasing impedance contrast above and below the bed and the thickness of the bed. More alarmingly, the reflection response of a thin bed was also a function of frequency (the factor $j\omega$ in (1(14)). For a given bed thickness and reflection coefficient, equation 1(14) predicted that the lower frequency components would be preferentially transmitted, with a linear decrease in the amplitude of the reflection response. The reflected wave, therefore, would be proportionally richer in high frequencies than the incident wave, whilst the transmitted wave will be proportionally richer in low frequency energy relative to the incident wave (caused directly by the short-delay multiples). Thus the thin bed would behave as a high-pass filter (in terms of the reflection response). The case of a sequence of thin beds was then considered. The transmission response of a sequence of n thin layers was expressed as:

$$|T(\omega)|^n = \frac{\left|1 - R_p^2\right|^n}{\left|1 - R_p^2 . e^{\frac{2j\omega d}{v_2}}\right|^n} \quad \ldots\ldots\ldots 1(17)$$

which was the effect of the transmitted wave passing through a low pass filter n times.The filtering effect was squared as the wave would have had to pass through the sequence twice, once down, once up. The conclusion derived from this analysis was that any sequence containing thin layers (relative to the frequencies contained within the wavelet) would have a reflection response (in a seismic section) containing the higher frequencies at earlier times and the lower frequencies at later times. This effect, of course, may be difficult to distinguish from the effects of absorption. Attention should also be paid to the characteristics of the low-frequency end of the spectra of reflected events. A necessary effect of the low-pass transmission response was that the very lowest frequencies may be lacking in the reflected pulses relative to the spectrum of the incident wave, which according to Ziolkowski and Fokkema (1986) required more research. This work indicated that before any analysis of absorption losses could take place, the effects of linear frequency-dependent elastic effects had to be accounted for.

1.6.3 Scattering Losses

Rayleigh Scattering is a process that only occurs when wavelengths are much shorter that the average grain size of the material. Busby and Richardson (1957) proposed that with such short wavelengths, attenuation occurs with $n = 4$ in eqn. 1(2).

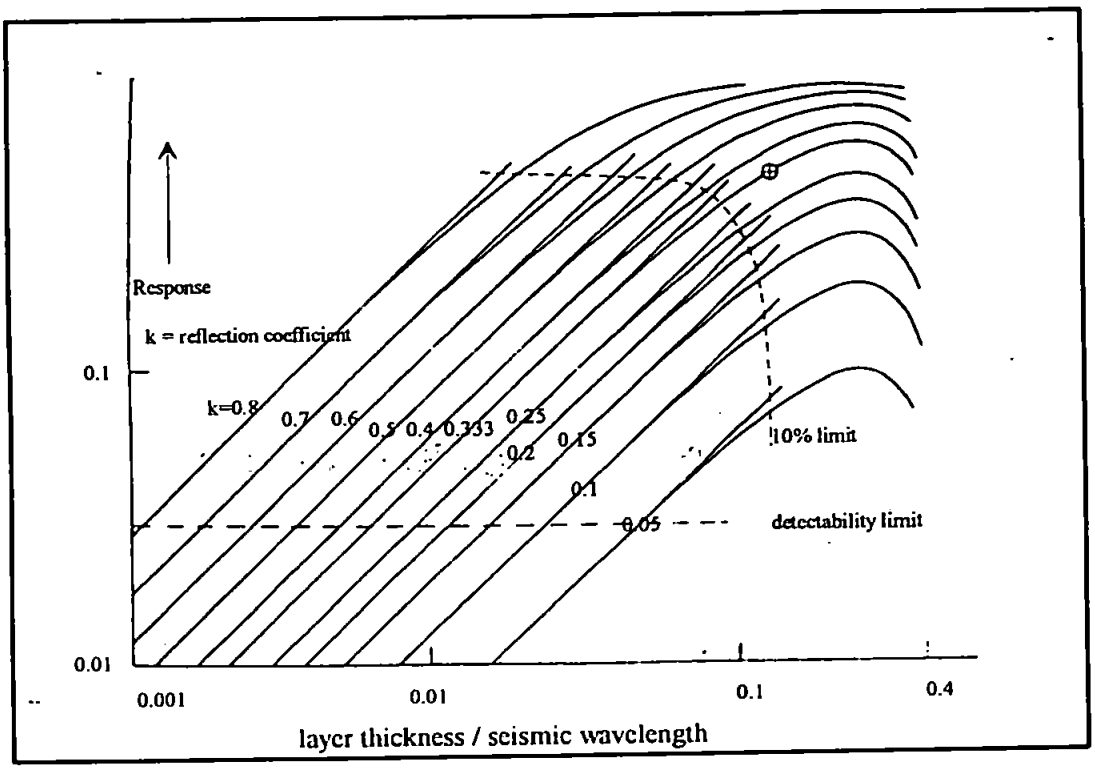

Figure 1.9

Reflection response for a sinusoidal wave of an interbedded layer as a function of layer thickness and reflection coefficient. (after Koefoed and de Voogd, 1980)

Chapter 2: Elastic and Inelastic Considerations

2.1 Introduction

Before any investigation of amplitude losses in real materials can be carried out, it would be useful to determine the losses in considering simple earth models. In this way the potential contributions of absorption or layering effects can be asessed. A homogenous absorbing earth is considered along with the effects of dispersion. A simple single- and multi-layered non-absorbing earth model is considered in both the time-and frequency-domain.

2.2 Isotropic Absorbing Earth

To estimate the scale of losses that may be ascribed to absorption, several curves have been derived for differing values of the Q, the seismic quality factor, and Δt, the two-way traveltime in ms. In order to relate the modelling to the case study in chapter 5, the frequency range chosen was 500 Hz to 2.4 kHz, whilst Δt ranged from 10 to 25 ms. The curves are a graphic representation of the equation;

$$A(t) = A(o).e^{\frac{-\pi f \Delta t}{Q}} \quad \text{.....2(1)}$$

where $A(t)$ is the amplitude of a plane wave after t seconds of propagation

$A(o)$ is the amplitude at time t=0

f is the frequency in Hertz

Δt is time in seconds

Q is the seismic quality factor

Equation 2(1) may be expressed (e.g. Tonn 1991) as:

$$A(t) = A(o).e^{-\alpha x} \quad \ldots\ldots\ldots 2(2)$$

where α is the absorption coefficient and x is the distance travelled.

Values of Δt were chosen for t =10, 15, 20 and 25 ms. Values of Q were chosen for Q = 30,50,60,75 and 100. The latter values were chosen as they covered the range of Q-values most quoted from the literature for unconsolidated sediments (Hamilton, 1972). The exponential loss of amplitude with increasing travel time is shown in Figures 2.1a to 2.1d A perfect reflector with a reflection coefficient of 1.0 is assumed at time of t/2.

For a value of Q = 50, about 50% of the amplitude of a plane wave at 1 kHz will be lost to absorption after only 10 ms. The same effect can be achieved by increasing Δt to 20 ms and increasing Q to 100, as is obvious from the equation above. For what may be described as a more 'lossy' sediment, with Q = 30, about 90% of the amplitude will be lost for frequencies over 1.5 kHz, and with propagation times over 15 ms. This 90% threshold applies to frequencies above 900 Hz with propagation times in excess of 25 ms. To relate these curves to a more realistic near surface model, an interval velocity of 1.7 metres per second may be assumed. A certain type of seismic source (the surface-towed Uniboom), has a frequency range centred on about 1.5 kHz, which will be assumed as the dominant or central source frequency. For such a source, assuming no losses in the water column, no geometric spreading, and no losses at the seabed, the following one-way depths would be achievable before 90% of the amplitude of the propagating wave would be absorbed for various values of Q.

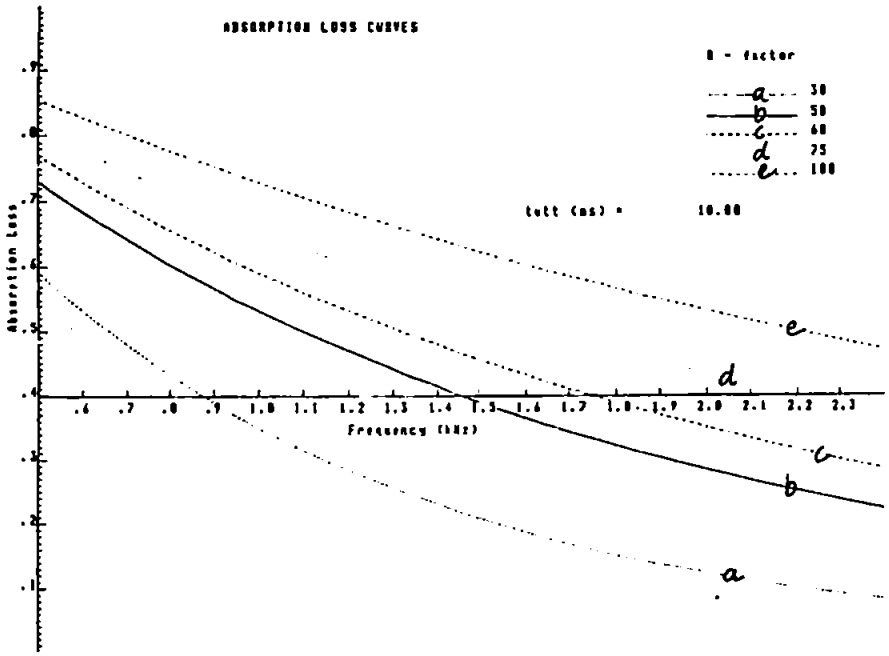

Figure 2.1a
Amplitude Loss Curves for Q = 30 to 100
One-way transmission of 10 ms

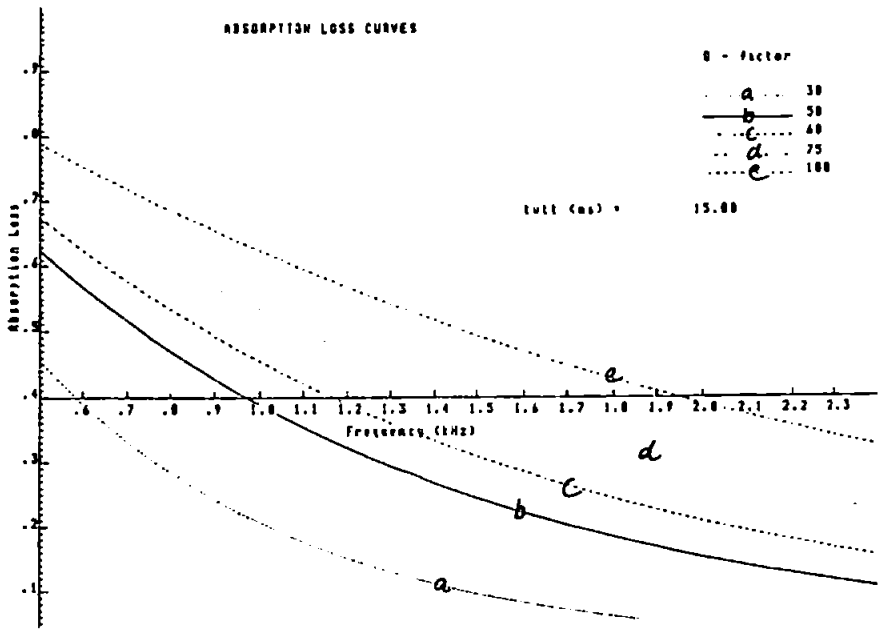

Figure 2.1b
Amplitude Loss Curves for Q = 30 to 100
One-way transmission of 15 ms

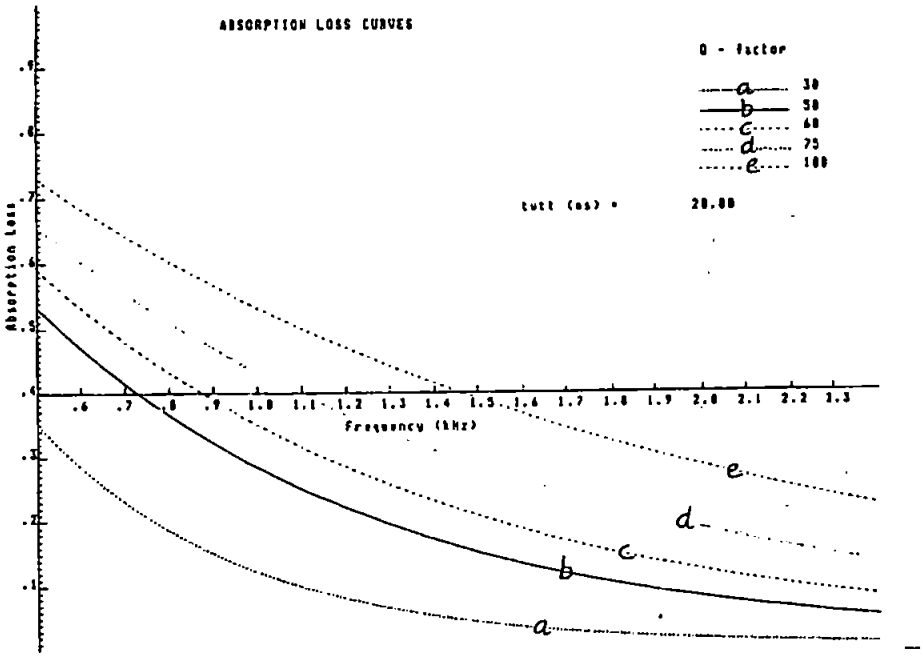

Figure 2.1c
Amplitude Loss Curves for Q = 30 to 100
One-way transmission of 20 ms

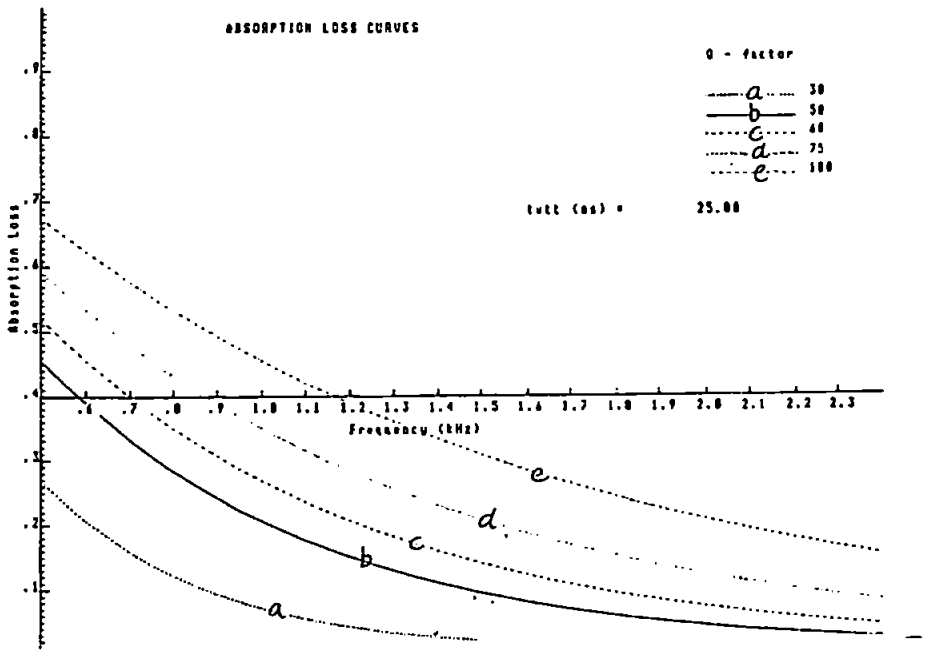

Figure 2.1d
Amplitude Loss Curves for Q = 30 to 100
One-way transmission of 25 ms

Table 2.1 Depth at which a sinusoidal wave is reduced to 10% of its initial amplitude for varying Q.

Depth (m)	Q
8.3	20
12.5	30
16.6	40
20.8	50
25.0	60
29.1	70
33.2	80
37.5	90
41.5	100
83.0	200

(assuming $v = 1700$ ms^{-1})

For unconsolidated sediments, most Q values from the literature fall below $Q = 100$ (Hamilton 1972), giving a penetration limit of between 8 and 40 metres for a 1.5 kHz source, down to only 10% of its original signal level, in the absence of any other form of loss. If reflection at the seabed is considered, a reflection coefficient (R_c) of about 0.3 will result in a 30% loss of the amplitude to the water column at this depth, both on the downward and the upward path. A 30% loss in amplitude is equivalent to a 9% loss in energy reflected. The curves and the table indicate that sources whose dominant frequencies are in the 1 kHz to several kHz range are likely to suffer high amplitude losses in homogenous near-surface sediments within the top 40 metres or so. The effectiveness of the source to penetrate the near subsurface will be limited by the intrinsic Q of the medium, and indirectly limited by the signal to noise levels that are achievable with the seismic equipment available. Devices such as Pingers, with dominant frequencies in the 3-10 kHz range, have very limited potential in investigating the absorption characteristics of the deeper sub-surface. For a surface unit of $Q = 60$, a pulse of 10 kHz frequency would be reduced to 10% of its original amplitude in 4.4 ms of one-way travel, or just under 4 metres of two-way travel assuming $v = 1700$ ms^{-1} , again ignoring losses at the seabed.

Consider an extension of the simple model whereby the seabed is assumed to have a reflection coefficient of 0.3 and a strong single reflector with a reflection coefficient of 0.25 occurs at 15 ms (twtt) below the seabed reflector. If we assume that a plane wave of unit amplitude occurs at t = 0, then at the seabed the wave will be transmitted with amplitude 0.7 . After 7.5 ms, assuming Q = 60, and f = 1500 Hz, absorption will have reduced the amplitude to 0.39; after reflection at 7.5 ms, the amplitude will be 0.13; more absorption for 7.5 ms will further reduce the amplitude to 0.072, which will be transmitted through the seabed with an amplitude of 0.058 at t = 15 ms (twtt). In summary, the original plane wave is reduced to less than 6% of its original amplitude given the simple model outlined above. It should be noted that reflectors with R_c = 0.3 and R_c = 0.25 will transmit 91% and 93.75% of the normally incident energy. If absorption lowers the amplitude of a plane wave by 30% , then 50% of the energy has been irreversibly lost.

As well as providing a filtering mechanism for amplitudes at various frequencies, absorption may also change the phase properties of the propagating pulse (Futterman, 1962). Angeleri and Loinger, (1984), found that with high absorption rates (low-Q) there was appreciable phase distortion, which was less apparent with lower absorption. This effect manifested itself in two ways. Firstly there was a change in the waveshape as certain frequencies lagged by as much as 1 radian (with Q = 30, a bandwidth of 0 - 78.125 Hz and 1170 m of wave propagation). Secondly, there was a time delay suffered by the pulse, with a greater time delay for higher absorption. This was the case of the energy of the pulse not travelling at the group velocity (Brillouin, 1960). The effects of absorption on phase characteristics are not considered in the current work . However, further work is warranted on the phase effects of low-Q layers which may occur close to the sediment-water interface. For Q = 30, Angeleri and Loinger, (1984) found appreciable phase distortion (c. 0.8 radians lag) of frequencies around 30 Hz over a depth interval of just over 800 m, or about .5 secs one-way traveltime . This represented about 15 cycles of propagation at that frequency. If we now draw an analogy to this situation (with a scale change) to a seismic investigation of the near sub-surface, 15 cycles of two-way propagation at a frequency of 1500 Hz would occur in only 5 ms twtt, or at an interval

velocity of 1600 ms^{-1}, within 8 metres of the seabed. As far as the author is aware, no detailed investigation of phase distortion due to low-Q layers has been carried out near the sub-surface using frequencies around those used in shallow seismic investigations. Causality dictates that dispersion of the separate frequency components of a pulse must occur with absorption (Futterman 1962). That is, the frequency components have differing velocities of propagation. The form of the transform function of the Futterman operator , H , was given by Badri and Mooney (1987) and is slightly modified as:

$$H(R,\omega) = (R1/R2).e^{\frac{-\omega\Delta t}{2Q}}.e^{j\omega\Delta t.\frac{Ln(\frac{\omega}{\omega'})-2}{Q}} \quad \ldots\ldots\ldots 2(3)$$

where *R1/R2* is a term accounting for geometrical spreading and ω' is the angular Nyquist frequency.

The first exponential term described the frequency selective amplitude loss. The traveltime (Δt) was based on a velocity v_o , which was that of the lowest resolvable frequency of the signal. The second exponential term contains the phase delay $j\omega\Delta t$. This term was simply a time shift equal to the distance travelled divided by v_o.

The term

$$\frac{Ln(\omega/\omega')-2}{Q} \quad \ldots\ldots\ldots 2(4)$$

described the dispersive effect. The value of this term would vary from a minimum for the lowest frequency components to a maximum at the Nyquist frequency, and would obviously be lower for low absorption rates (high-Q). Higher frequencies, therefore, would have shorter arrival times than lower frequencies. A causal pulse (Futterman,1962) ,

therefore, would have a higher frequency earlier portion, and a lower frequency rear end.

Without dispersion the attenuated pulse is symmetrical about its arrival time, which is simply distance/group velocity. With dispersion the pulse has a sharper front end, with a shorter arrival time , if taken from the peak amplitude. Despite dispersion necessitating a dependence of absorption on frequency, Q has been considered to be largely frequency-independent (*e.g.* Badri and Mooney, 1987; Hamilton, 1972). For dry materials, Q was experimentally found to be independent of frequency (e.g. Nur and Winkler, 1980; Toksoz and Johnston, 1981), but for fluid-saturated materials there is doubt about such a linear relationship (Stoll 1977). Keller (1989) proposed a model based partly on Biot theory (see Chapter 1) and constant-Q, where the attenuation was proportional to a functional power of frequency in order to preserve causality. Keller considered fully saturated fine- and coarse-grained material in the model, comparing them to previously published empirical data from real materials of this type. Depending on grain size, and having set other model parameters (such as the bulk moduli mass densities of the fluid and grains, permeability, porosity etc.) the model predicted a highly non-linear attenuation response with respect to frequency for sands. In other words, although Q itself may be independent of frequency (the frame response) , the total response of fluid-saturated granular media would be highly frequency-dependent, especially for coarser materials.

2.3 Single and Multi- Plane Layer Within Homogenous Medium

As shown in the review Chapter 1, the effects of layering on the spectral characteristics of the transmitted pulse cannot be ignored. The following equation (Ziolkowski and Fokkema, 1986) describes the spectral transmission response T(ω) of one or more plane layers.

$$|T(\omega)|^n = \frac{\left|1 - R_c^2\right|^n}{\left|1 - R_c^2 . e^{\frac{2j\omega d}{v_2}}\right|^n} \quad \ldots\ldots\ldots 2(5)$$

where n is the number of layers

R_c is the reflection coefficient at the bounding interfaces of the layer

j is the imaginary number $\sqrt{-1}$

d is the thickness of the layer

v is the layer velocity

ω is the angular frequency ($=2\pi f$, with f in Hz)

The R_c term has a constant sign, because the upper and lower interfaces to the layer have opposite signs relative to the direction of the downward propagating pulse. Accordingly, any internal multiple leaving the layer through the lower interface will have the same sign as the direct wave. It must be stressed that this response is only applicable to the amplitude spectrum of the propagating pulse. The complex exponential term:

$$e^{\frac{2j\omega d}{v}} \quad \ldots\ldots\ldots 2(6)$$

has a modulus of one, and therefore has no effect on the amplitude spectrum. However, this term has a important effect in the time-domain. The product of equation 2.6 and the complex Fourier spectrum at a particular value of ω does not affect the modulus of the complex spectrum at that frequency, that is, its amplitude. However, the phase spectrum is affected, in that the component of the wave of frequency ω will be phase shifted in the time domain by an amount t, the two-way travel time of the wave through the layer.

A computer program was written to calculate the transmission response for a single

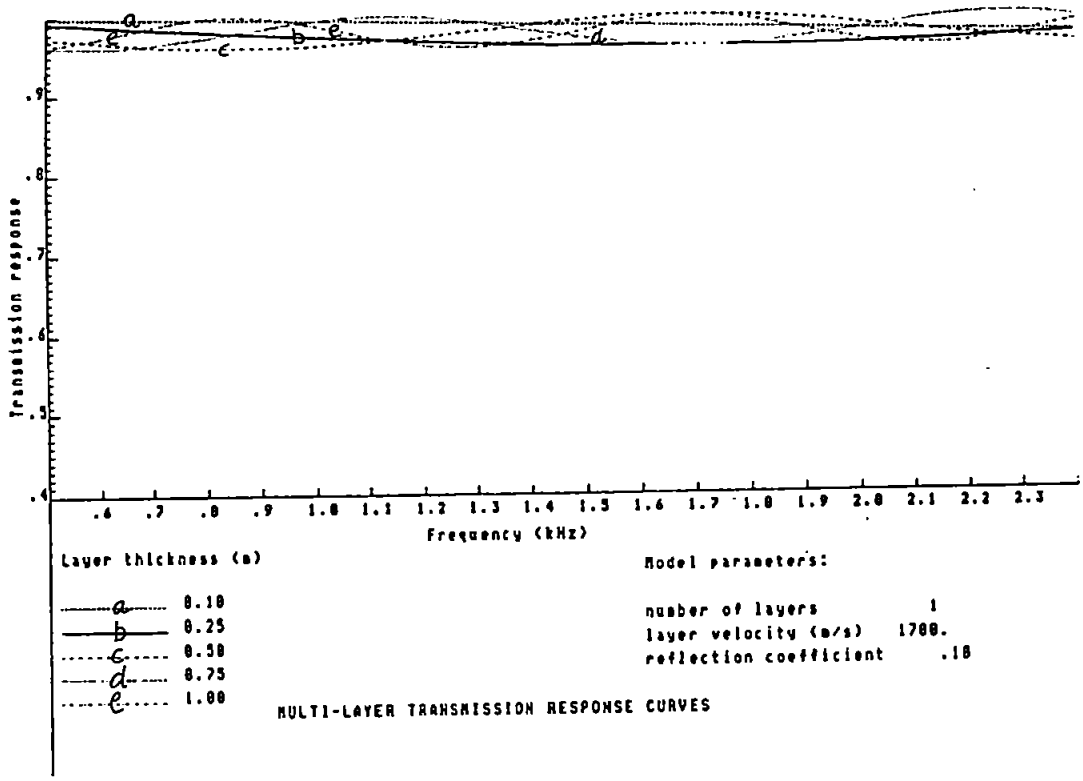

Figure 2.2a
Transmission Response For Single Layer as a function of Layer Thickness
Reflection Coefficient = 0.10

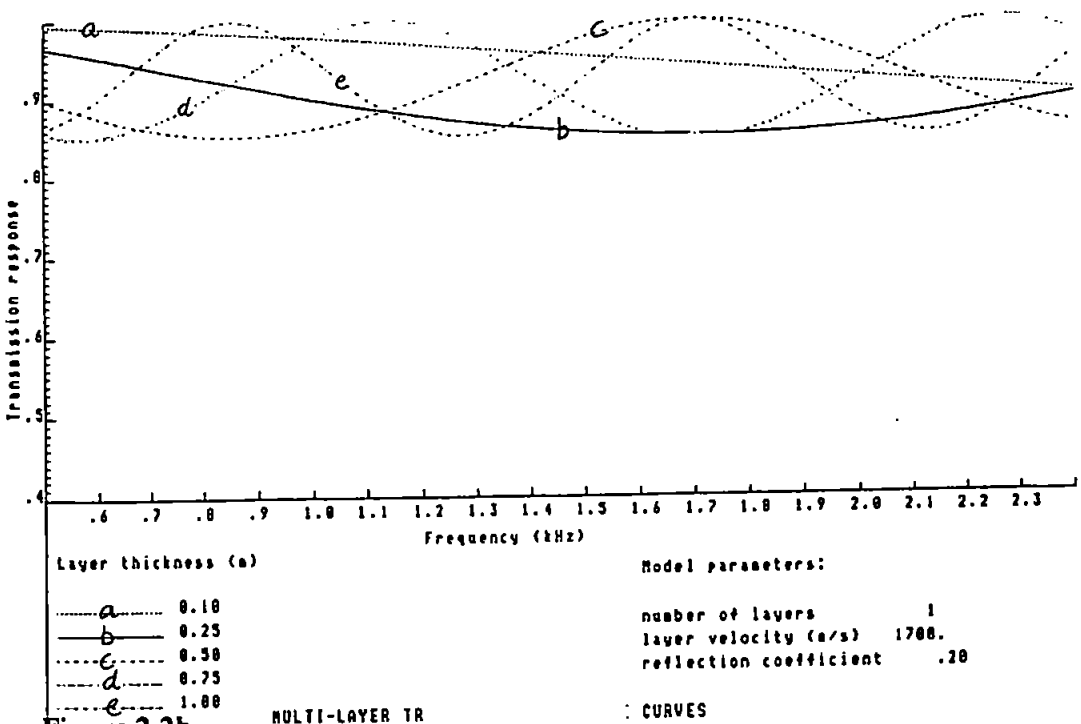

Figure 2.2b
Transmission Response For Single Layer as a function of Layer Thickness
Reflection Coefficient = 0.15

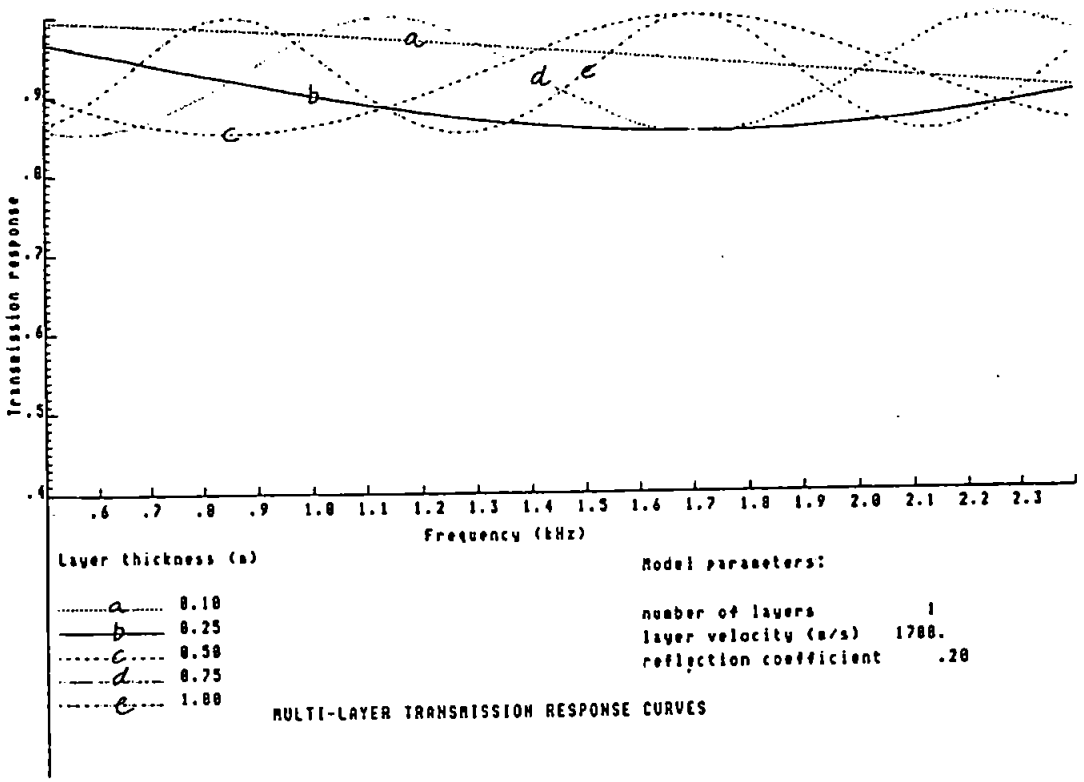

Figure 2.2c
Transmission Response For Single Layer as a function of Layer Thickness
Reflection Coefficient = 0.20

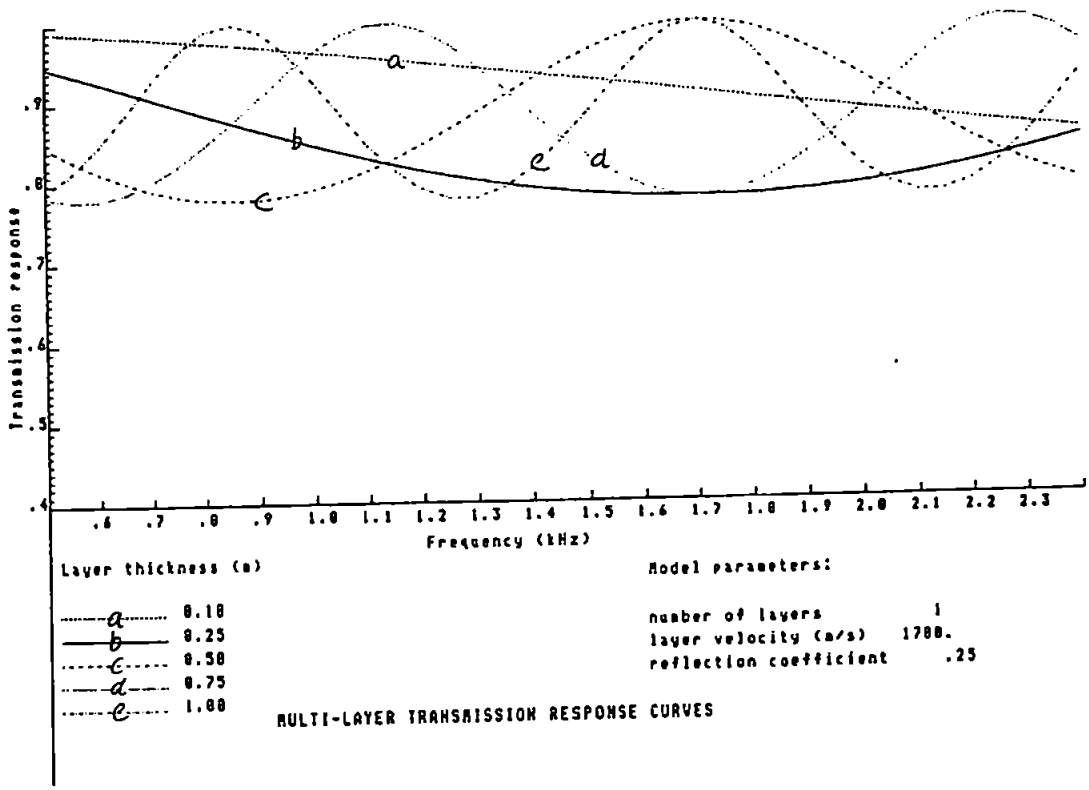

Figure 2.2d
Transmission Response For Single Layer as a function of Layer Thickness
Reflection Coefficient = 0.25

layer. The frequency band under consideration extended from 500 Hz to 2.4 kHz. Layer thickness was varied from 1 m to 0.1 m, with reflection coefficients of 0.1 up to 0.25. The upper limit for R_c was chosen from velocities and densities from Hamilton (1972), approximating to clay over sand. The interval velocity was held constant at 1700 ms^{-1}. Figures 2.2a to 2.2d show the effects of varying layer thickness and reflection coefficient for a one-layer model. Several features of the curves obtained are worthy of note. Firstly, for any layer thickness, and any reflection coefficient, there will be nodes and antinodes in the transmission response. The location of these features on the frequency axis is a function of the thickness of the layer and the wavelength of the disturbance through the layer. For example, it is well known that acoustic 'tuning' occurs when two reflectors of opposite sign are separated by a distance equivalent to a quarter of a wavelength (Widess, 1973). Mathematically, this situation occurs when $\lambda = 4d$. A look at Figure 2.2d shows a node, or a minima of transmission response at 1.7 kHz for a layer 0.25 m thick. Given $v = 1700$ ms^{-1}, $\lambda = 1\ m = 4 \times 0.25$, the thickness of the layer. A maxima for the reflection response, or 'tuning' will therefore occur at this frequency. Below this frequency, the transmission response can be considered to be increasingly low-pass, as pointed out by Ziolkowski and Fokkema (1986). Clearly, there is also an increasingly low-pass response above this frequency, up to an antinode or maxima in the transmission response, where the layer becomes transparent to that particular frequency. The position of the first node at $\lambda = 4d$ dictates the frequency band within which there will be a monotonic decrease in the transmission response. Given a constant velocity, the width of this band will increase with decreasing layer thickness, for example the width is 1700 Hz for $d = 0.25$ m, but only 850 Hz for $d = 0.50$ m (Figure 2.2d). Figures 2.2a to 2.2d also show that whatever the layer thickness, there is a lower limit to the antinodes of the transmission response at $(1-R_c^2)/(1+R_c^2)$. The reflection coefficient, therefore, limits the amplitude of the transmission response curves. Figures 2.2a to 2.2d show the effect of increasing R_c from 0.10, 0.15, 0.20 to 0.25 on the transmission response. Broadly, the greater the reflection coefficient, the more pronounced is the low-pass transmission effect. The effects of different velocity values were not modelled. Increasing the velocity for a given layer thickness would move

the position of the first node to a higher frequency, and *vice versa* for decreasing the velocity. The case for $\lambda < 4d$ is considered a 'thin-bed' case, in that seismic resolution is often described as being practicable when two reflectors are separated by a minimum of a quarter of the seismic wavelength (Sherrif and Geldhart, 1982 ,p.119). In effect, the above case describes the effects of features that are beyond the seismic resolution limit, preferential reflection of the higher frequencies from irresolvable layers, leading to a low-pass transmission response. If two reflectors are separated by more than a quarter of the dominant seismic wavelength, then providing the reflection coefficients are large enough for the signal not to be masked by noise, multiples and other unwanted events, two distinct events may be recognised on the seismic section.

The low-pass transmission response curves are periodic. Figure 2.2d shows that given a layer thickness of 0.75 m, the primary node occurs at 567 Hz, with a similar node at 1700 Hz (567×3). These curves indicate that although two separate events may be distinguishable in the time domain, they may present processing problems in the frequency domain. Techniques that use mathematical methods to look at spectral character from one event on a seismic section relative to another must at some stage take samples of the data in windows of a finite length prior to Fourier transformation. The curves indicate that if a window contains two events, whatever their separation, then the transmission response, and correspondingly the reflection response of the events will not have flat amplitude spectra. If this is the case, any technique that relies upon aspects of spectral shape, such as peak frequency location or spectral slope will be prone to fluctuations in spectral character because of interference between the two events. To ensure that a later event does not influence the spectral character of an earlier event, the two events should be separated by at least 1 wavelength, in order that *1*) there is no constructive or destructive interference and *2*) that it is possible to isolate and sample the earlier event.

The multilayer case is now considered. Equation 2(5) is now used to calculate the transmission response for a sequence of *n* layers. The wave is modelled as passing through the sequence once, being reflected by a single, isolated reflector (which has a flat frequency response), and passing through the sequence once more, thus squaring the one-

way transmission response. Figures 2.2e to 2.2m (Appendix A) graphically illustrate the effects of multilayering on the transmission response. It is clear that by increasing the number of layers, the amplitude of the low-pass effect becomes increasingly pronounced; the positions of the nodes and antinodes are not affected. With the combined effects of increasing the number of layers and increasing the size of the reflection coefficient, the effect becomes quite dramatic. Consider a situation in which there are 10 thin layers (each 0.1 m thick), with $v = 1700\ ms^{-1}$, with $R_c = 0.25$. A plane wave with a frequency of 1.5 kHz would lose 55% of its amplitude on its two-way passage through such a sequence, at 2.0 kHz, over 70% would be lost. Such a model is geologically plausible; a sequence of interbedded clays and sands could have R_c values alternating between $-0.2 \leq R_c \leq 0.2$.

2.4 The Transmission Response of the Single and Multilayered Model in the Time Domain

In order to clarify the effects of layering on the propagating seismic pulse, a computer program was written to model the effects of frequency-selective transmission and reflection. The inputs to the model are detailed below;

wave - a digitised wavelet to represent the seismic pulse
d - the thickness of the layers
v - the layer velocity
n - the number of layers
Rc - the reflection coefficient at the layer boundaries

The Fast Fourier Transform of the wavelet is first computed. The product of these complex values and the transmission response (eq. 2.(7))

$$T = \frac{(1-R_p^2).e^{j\omega d(\frac{1}{v_2})}}{1-(R_p^2.e^{\frac{2j\omega d}{v_2}})} \quad \ldots\ldots\ldots 2(7)$$

is then used to form a new complex array which undergoes an inverse Fast Fourier transform back to the time domain and a calculation of the amplitude spectrum .

A single-layer case is initially considered, where a spike of unit amplitude is incident on a single layer, and is transmitted through the layer twice, to emulate a downward and upward path. Various parameters are considered; layer velocity is fixed at 1600 ms^{-1} , and the reflection coefficient is fixed at 0.2. Frequencies up to 10 kHz were considered, although it should be noted that a spike has a flat amplitude spectrum at all frequencies. The thickness of the layer was varied from 0.08 m ,0.16 m , 0.24 m , 0.32 m to 0.40 m (Figures 2.3a to 2.3e). Increasing the thickness of the layer will increase the complexity of the spectrum of the output waveform. With d = 0.08, there is a node at 5 kHz, where λ = 0.32 m = 4d, the tuning frequency. Below 5 kHz there is a monotonic low-pass transmission effect. With increasing d , the number of nodes increases, as does the time gap between the direct pulse and the first peg-leg multiple. Using the spike input waveform, it is clear that the complexity of the output spectrum occurs because the peg-leg multiples are considered to be part of the output waveform when the inverse Fast Fourier transform is performed. *The low-pass transmission effect, and peg-leg multiples are therefore inextricably linked.* If the multiples were omitted from the output waveform, the transmitted pulse would have a flat spectrum, the response of the layer would therefore be white. Figure 2.3f shows that decreasing the reflection coefficient to 0.1 flattens the spectrum of the output waveform as the size of the peg-leg multiple is reduced.

Figures 2.3g to 2.3i illustrate the effects of increasing the number of layers from 5 to 20 layers. Clearly the effect in the frequency domain is to amplify the low-pass transmission, whilst the effect on the output waveform is to build the amplitude of the peg-leg multiples, increasing the complexity of the waveform. In Figure 2.3i the peg-leg amplitude has become greater than that of the primary spike. It should be noted that

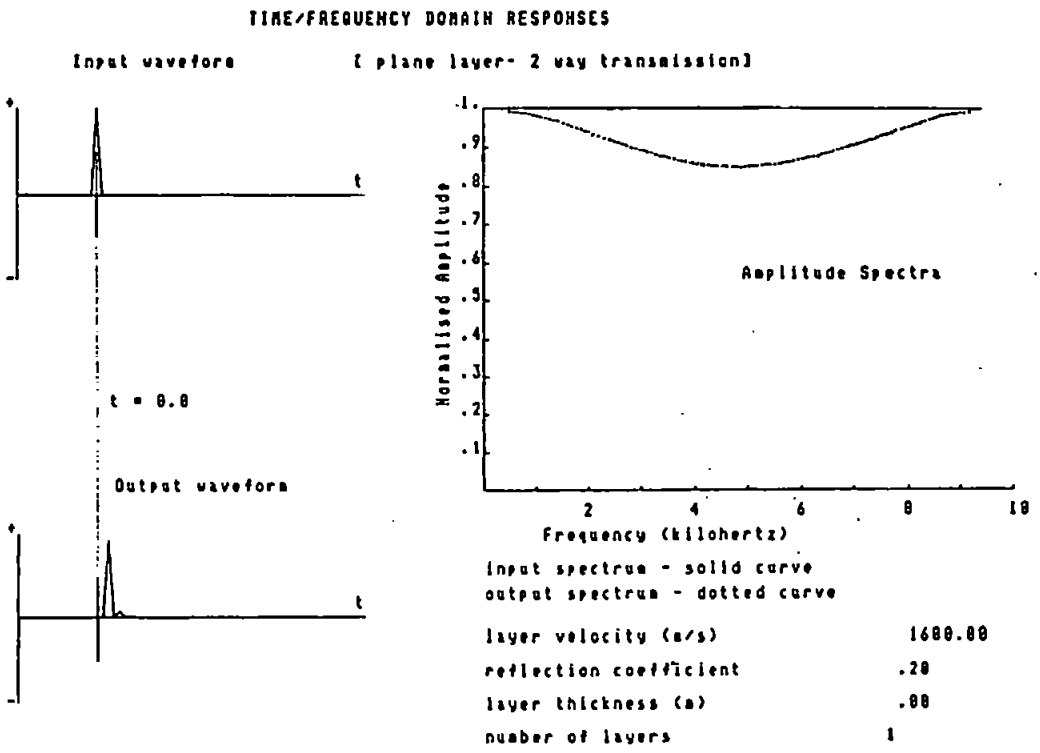

Figure 2.3a
Time and Frequency Domain Responses of a Single 0.08 m Layer using an Impulsive Input Waveform

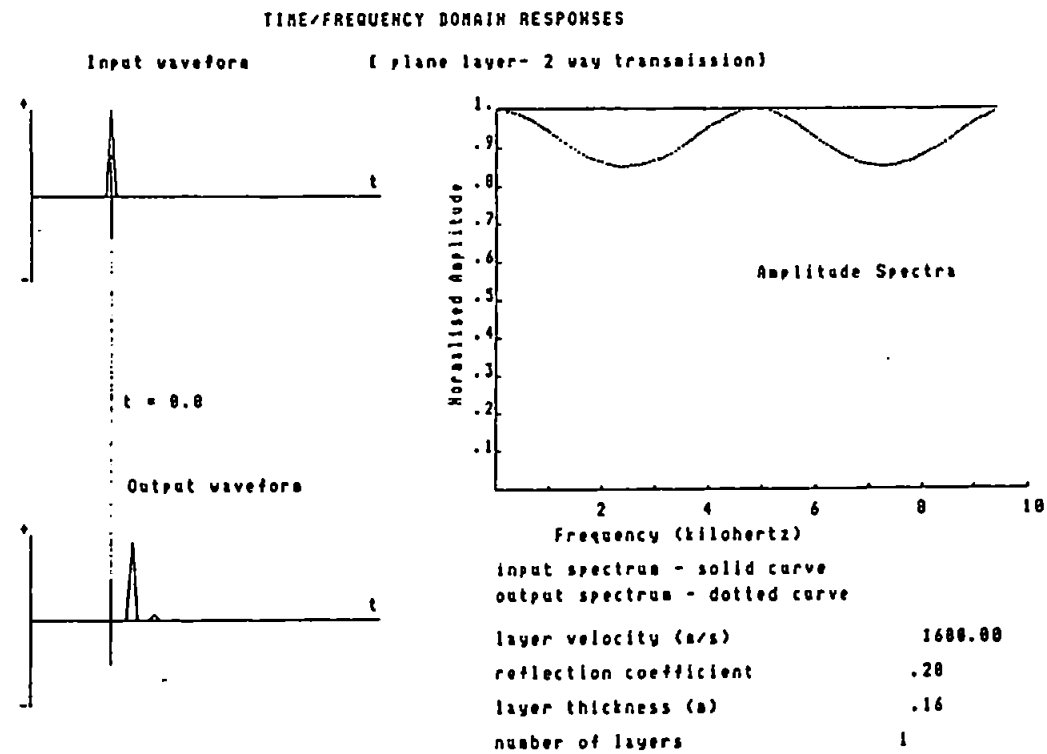

Figure 2.3b
Time and Frequency Domain Responses of a Single 0.16 m Layer using an Impulsive Input Waveform

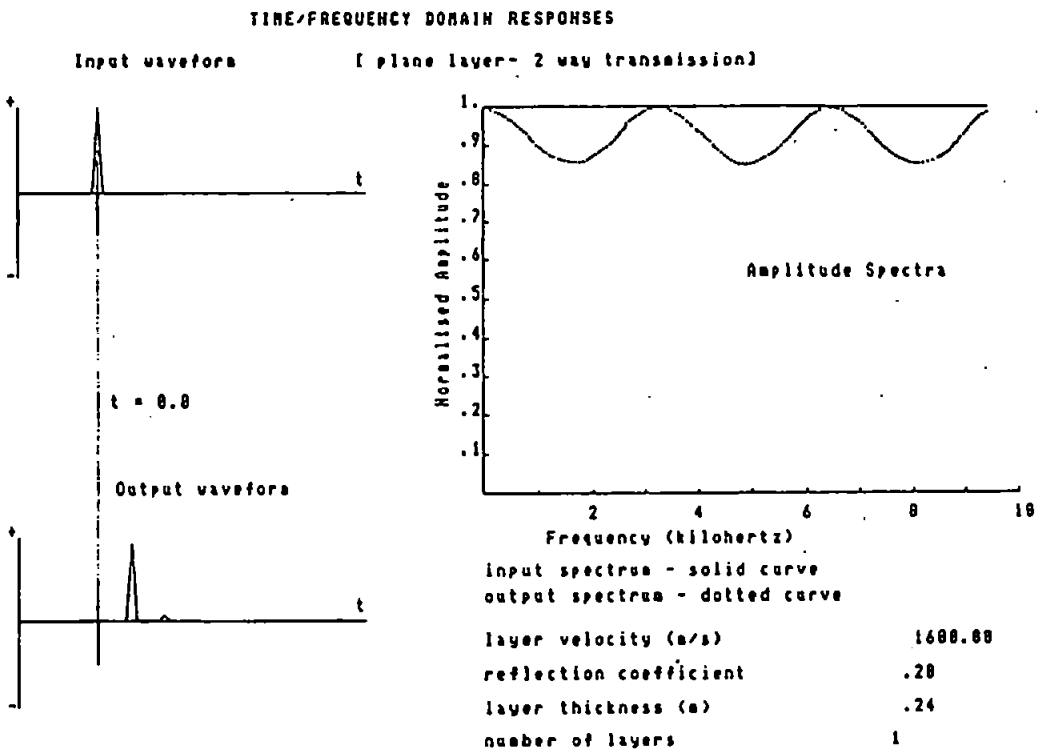

Figure 2.3c
Time and Frequency Domain Responses of a Single 0.24 m Layer using an Impulsive Input Waveform

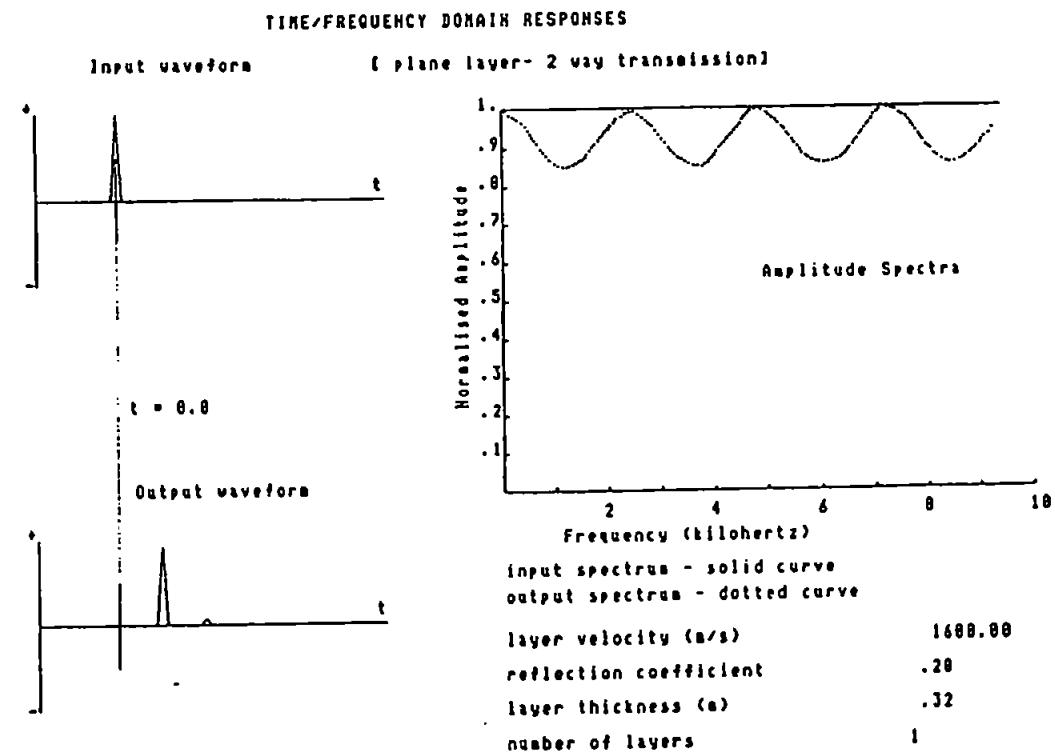

Figure 2.3d
Time and Frequency Domain Responses of a Single 0.32 m Layer using an Impulsive Input Waveform

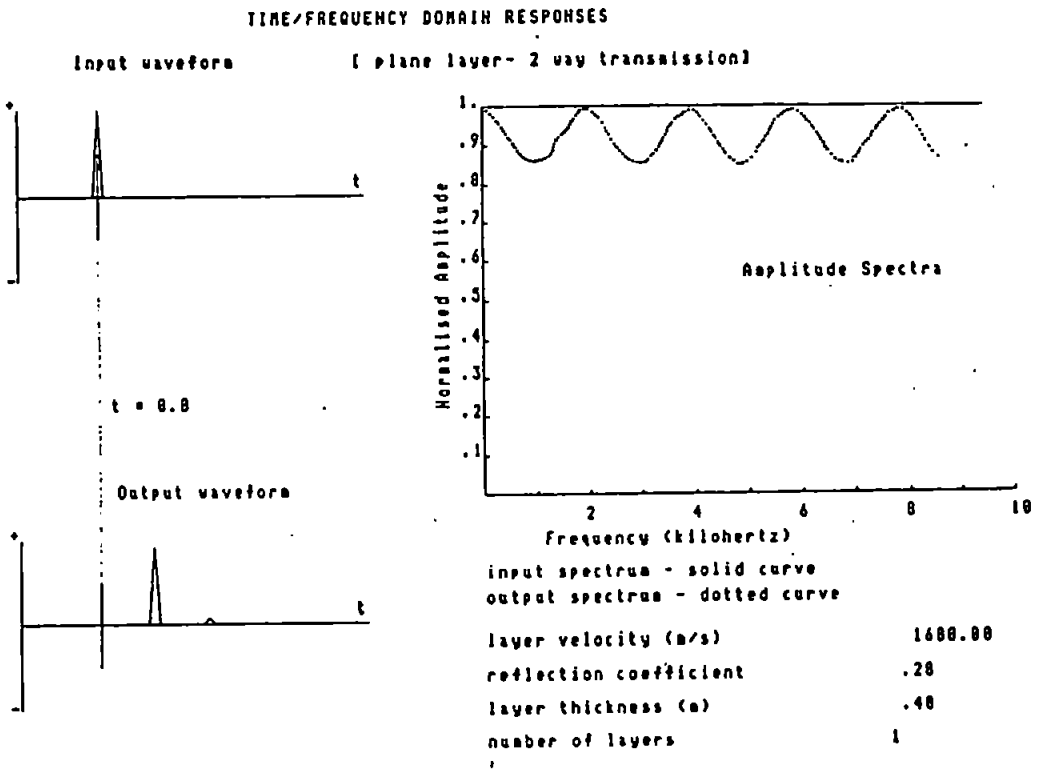

Figure 2.3e
Time and Frequency Domain Responses of a Single 0.40 m Layer using an Impulsive Input Waveform

modelling using a spike as an input waveform has a distinct disadvantage. The values of d and v must be such that their quotient is a multiple of the sampling interval of the input waveform for one way transmission. For example, if we consider the spectrum of the input waveform over the 0 kHz to 10 kHz band (10 kHz being the Nyquist frequency), then our assumed sampling frequency is 20 kHz, that is a sampling interval of 0.0005 seconds, equivalent to one time unit. At v = 1600 ms^{-1} , values for d of 0.08, 0.16, 0.24 , 0.32 etc. will lead to phase delays of 1, 2, 3, 4 ,5 etc. time units. A failure to multiply the complex term $j\omega$ by a value other than a multiple of the sampling interval will result in a correct representation of the output waveform in the frequency domain, but when the inverse transform is performed, a ripple effect will occur away from the direct spike which is a product of the mathematical treatment of the data rather than an elastic effect,(as illustrated in Figure 2.3j) . For two-way transmission the values of d may be halved. This effectively puts the lower limit of layer thickness that can be modelled at a value whereby the transit time through the layer is equivalent to half of the sampling interval of the data, as shown in Figure 2.3k. This is, of course, also the quarter wavelength threshold.

In this highly simplified model, it would be easy to distinguish an isolated reflector from an a thin bed reflection. However in the real world seismic sources are of a finite bandwidth, and therefore cannot exhibit such an impulsive shape in the time-domain. Accordingly a similar procedure to that above was carried out on an input waveform with a peak frequency of 2 kHz. Figures 2.4a to 2.4d show the effects of varying the layer thickness on the output waveform. Clearly the positions of the nodes of the transmission response dictate the modifications to the input spectrum. The peg-leg contributions to the output waveform are seen as a short, low-amplitude tail at the end of the output waveform, otherwise little modification to the original waveform occurs after two-way transmission through a single layer. Again it should be emphasised that the spectral modification only occurs because the treatment of the data does not allow the separation of the primary or direct wave from the peg-leg multiples. Figures 2.4e to 2.4g show the effects of transmission through 5, 10 and 20 layers. With a greater number of layers, the spectral effects of the nodes in the transmission response are increasingly more apparent, as is the

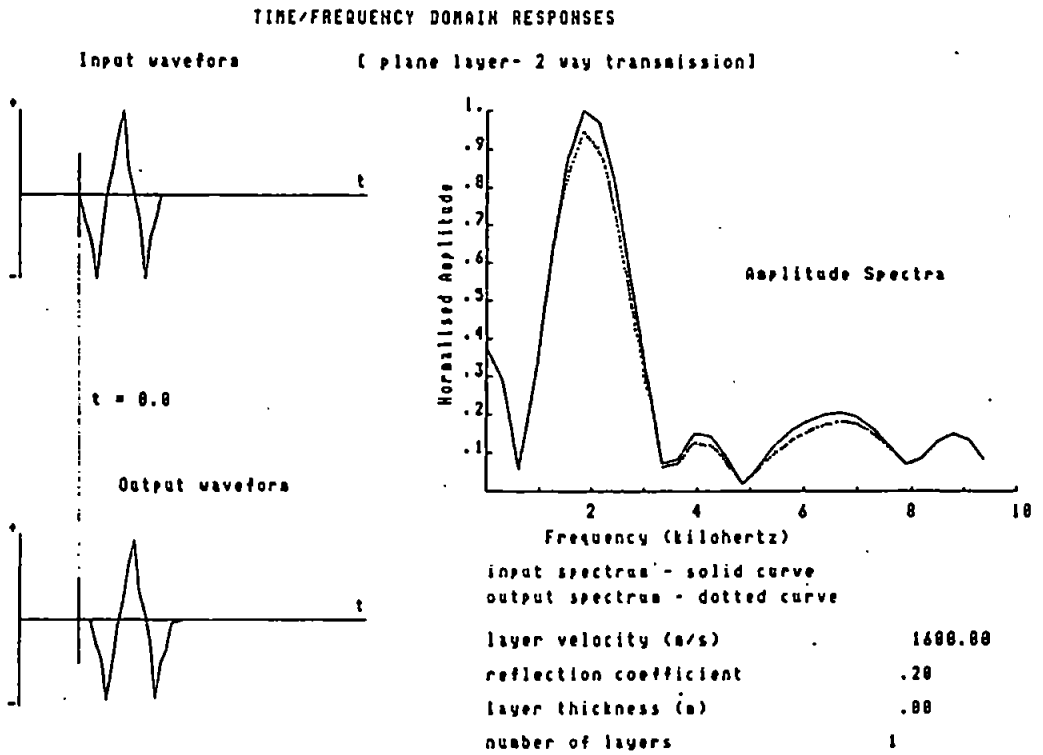

Figure 2.4a
Two-Way Transmission Response of a Single 0.08 m Layer to a 2 kHz Wavelet (Rc = .20)

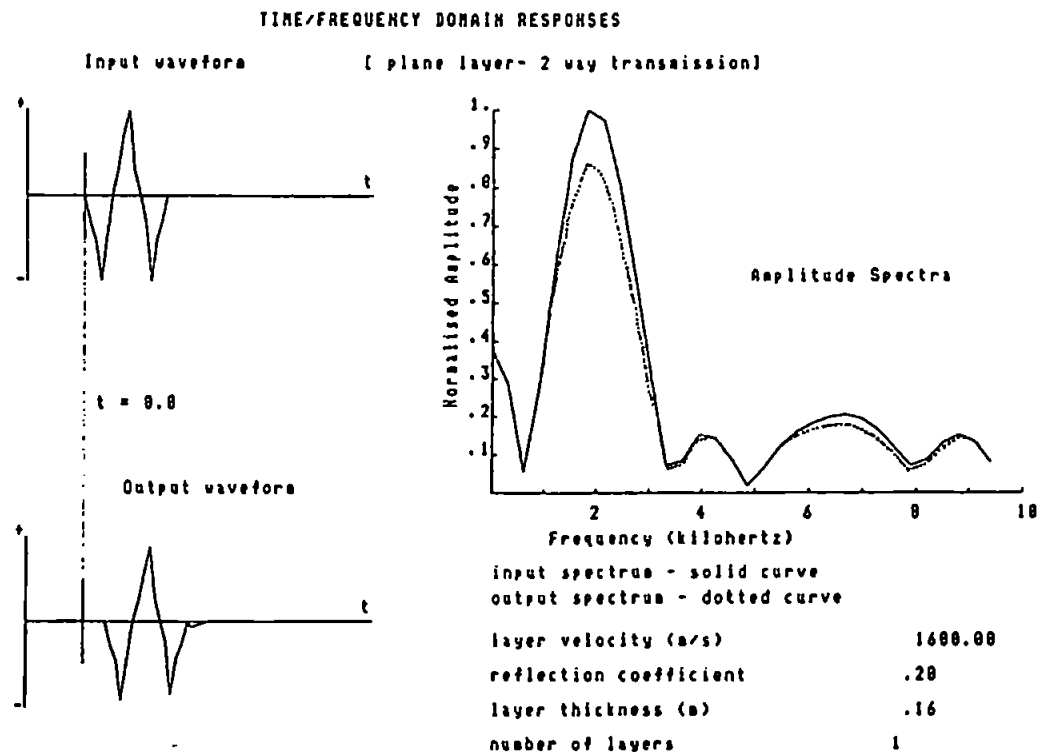

Figure 2.4b
Two-Way Transmission Response of a Single 0.16 m Layer to a 2 kHz Wavelet (Rc = .20)

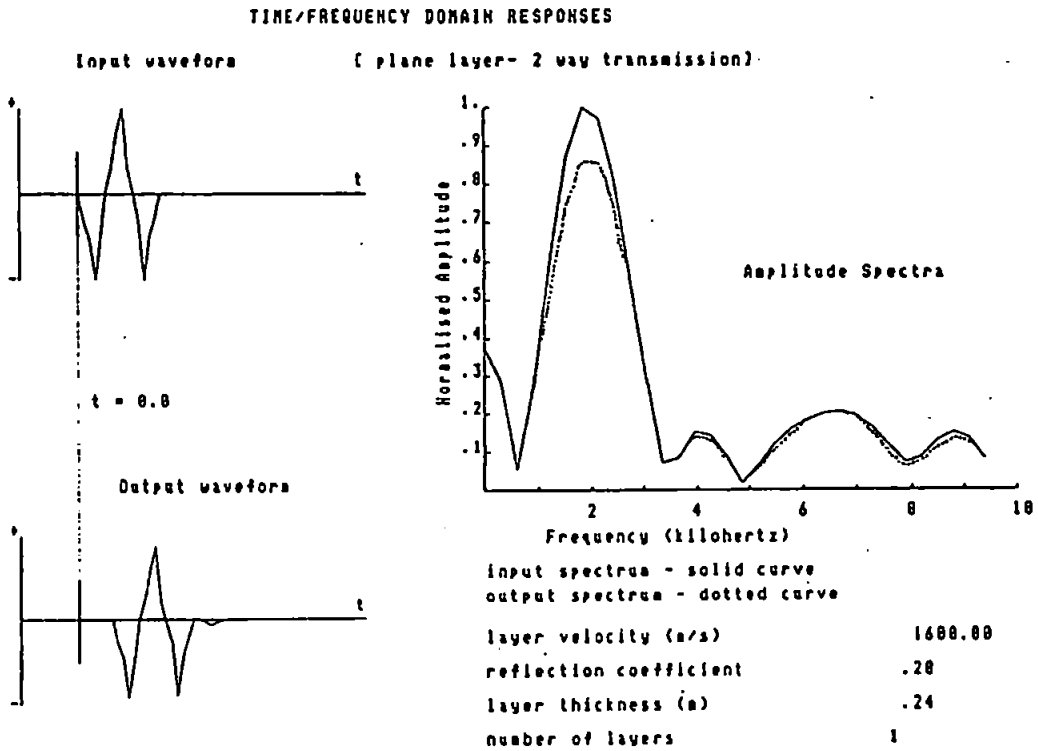

Figure 2.4c
Two-Way Transmission Response of a Single 0.24 m Layer to a 2 kHz Wavelet (Rc = .20)

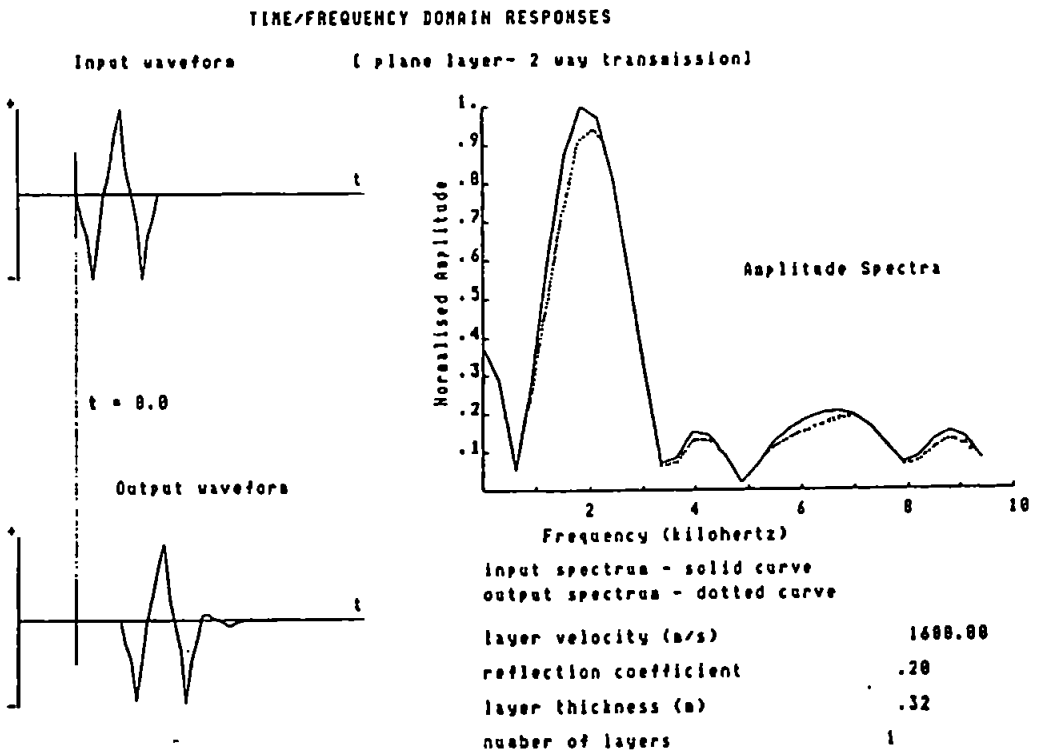

Figure 2.4d
Two-Way Transmission Response of a Single 0.32 m Layer to a 2 kHz Wavelet (Rc = .20)

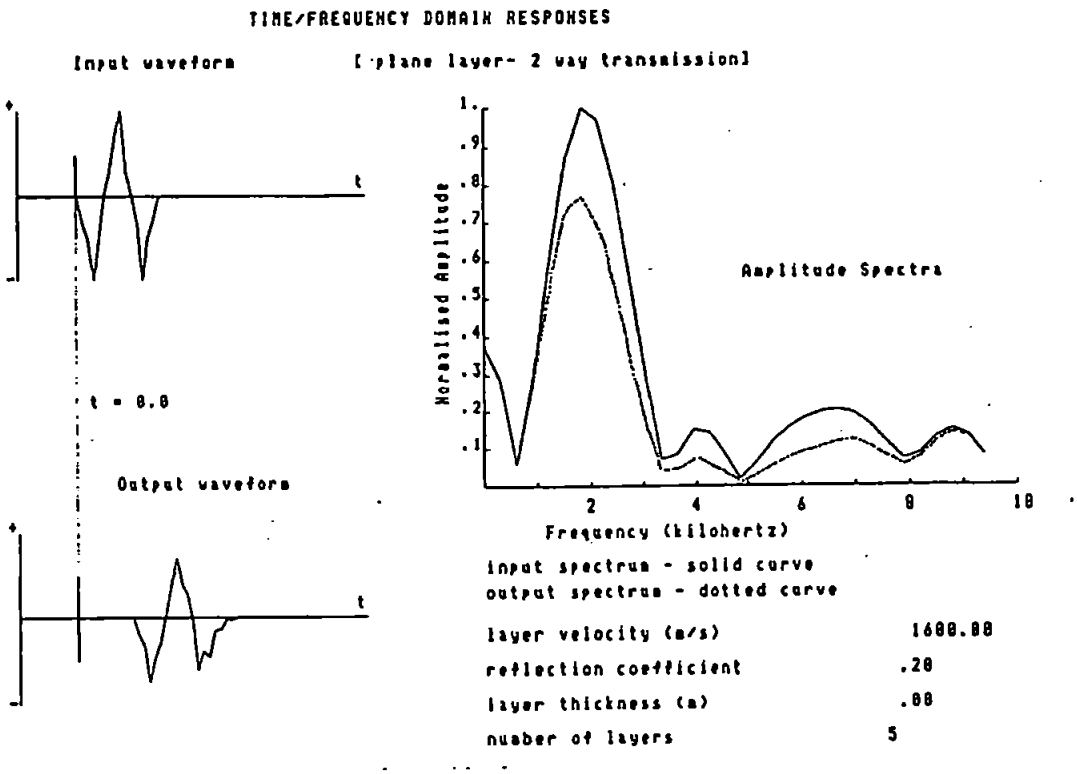

Figure 2.4e
Two-Way Transmission Response of 5 0.08 m Layers
to a 2 kHz Wavelet (Rc = .20)

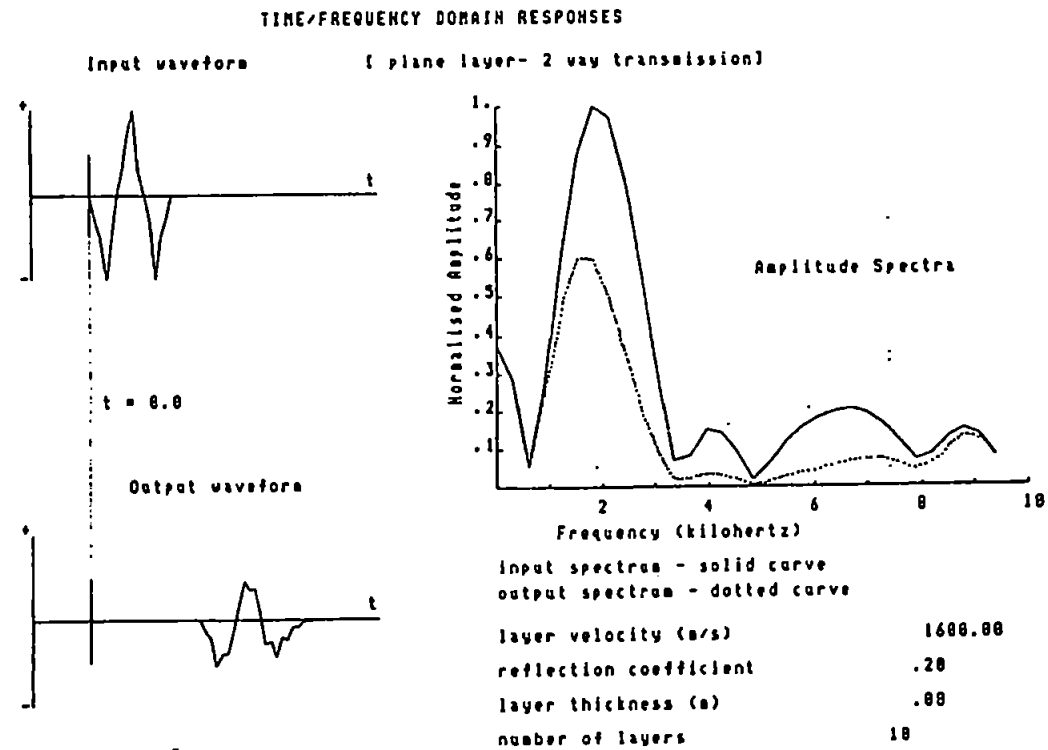

Figure 2.4f
Two-Way Transmission Response of 10 0.08 m Layers
to a 2 kHz Wavelet (Rc = .20)

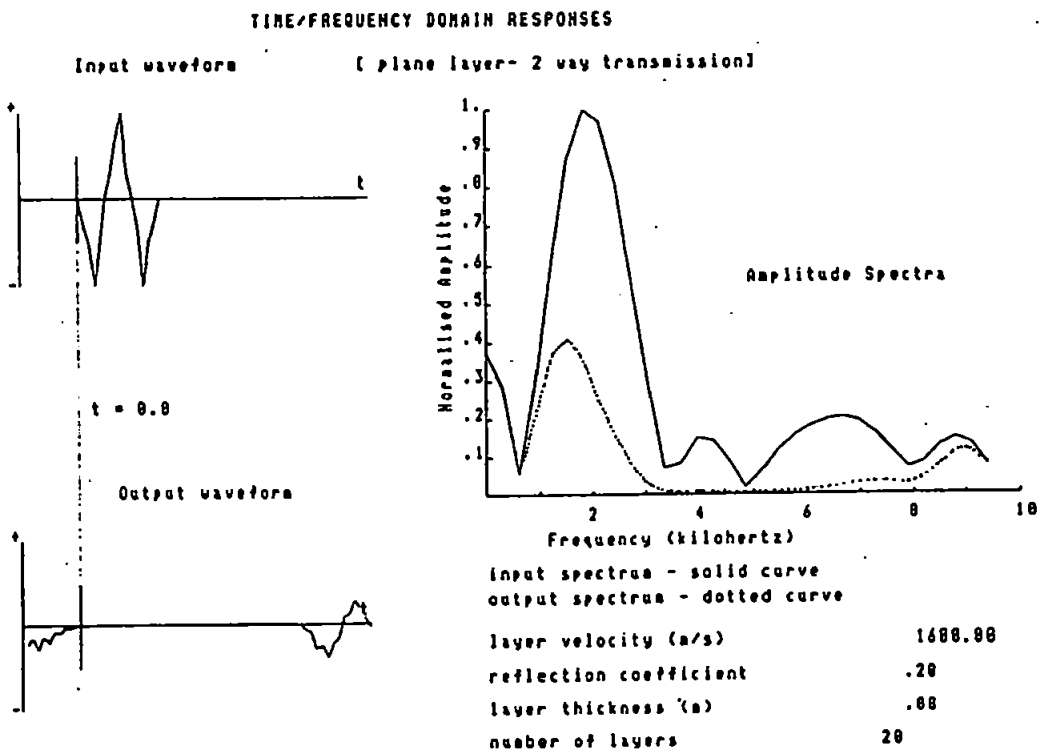

Figure 2.4g
Two-Way Transmission Response of 20 0.08 m Layers
to a 2 kHz Wavelet (Rc = .20)

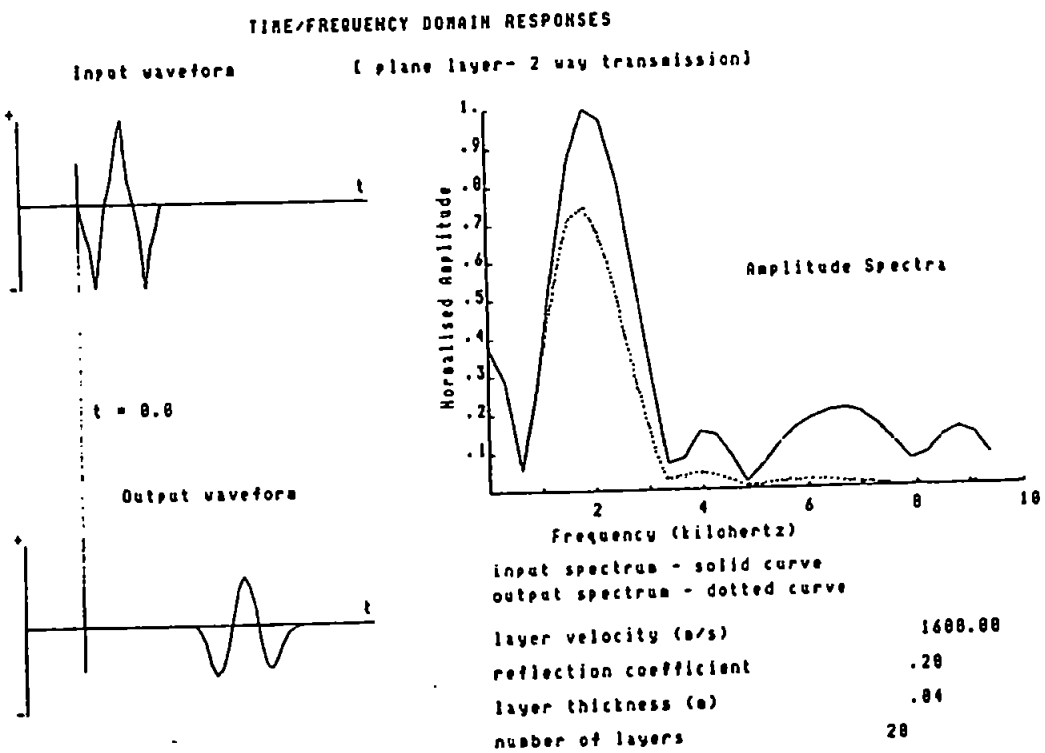

Figure 2.4h
Two-Way Transmission Response of 20 0.04 m Layers
to a 2 kHz Wavelet (Rc = .20)

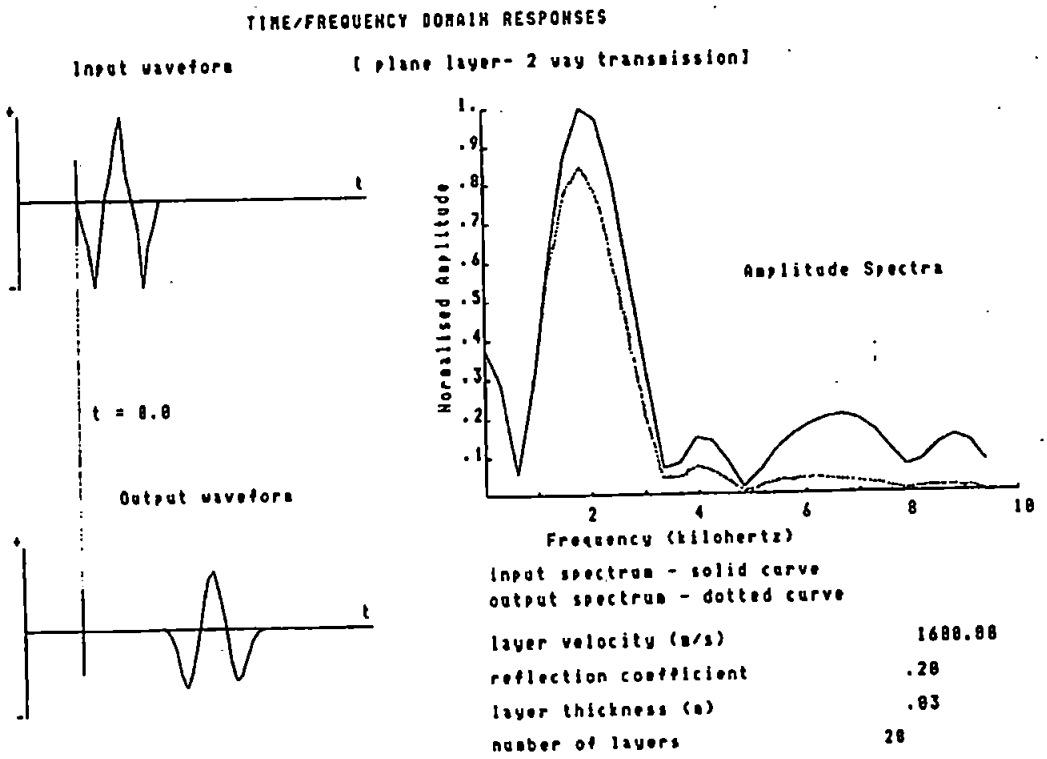

Figure 2.4i
Two-Way Transmission Response of 20 0.03 m Layers
to a 2 kHz Wavelet (Rc = .20)

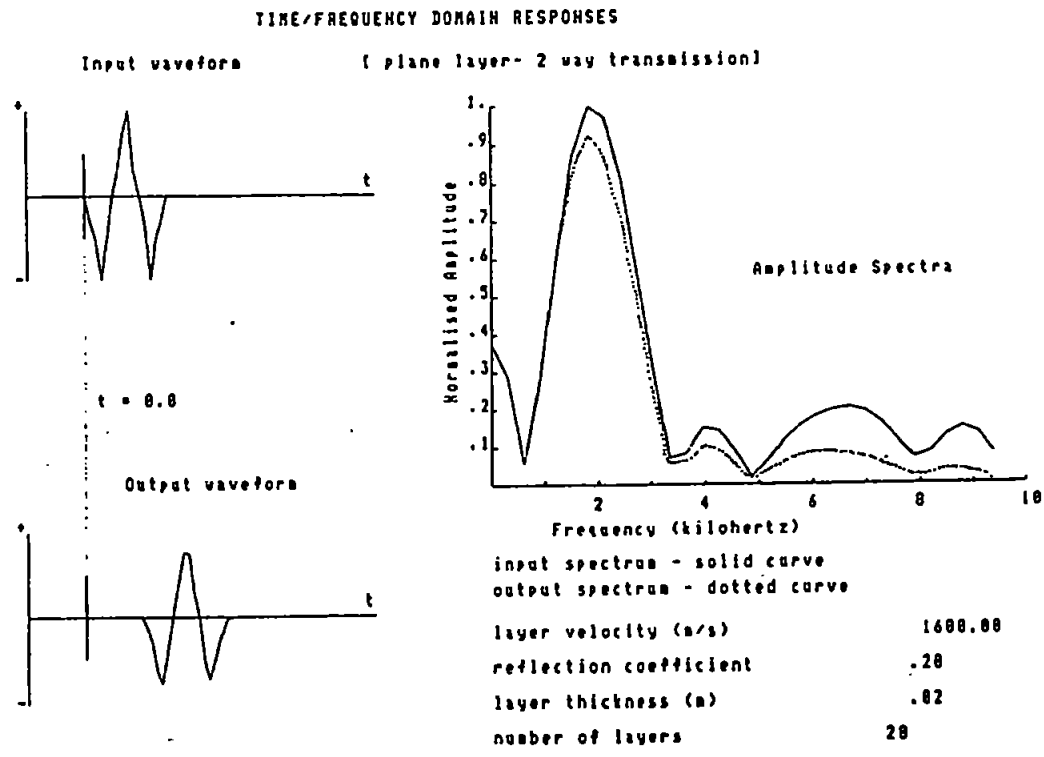

Figure 2.4j
Two-Way Transmission Response of 20 0.02 m Layer
to a 2 kHz Wavelet (Rc = .20)

modification to the waveform in the time-domain. Figure 2.4f shows that after a two-way transmission through 10 layers the pulse still retains its basic shape, even though there is much spectral modification. If the layer thickness is reduced to 0.04 m, the spectrum of the input waveform is subject to a low-pass filtering effect across the whole of the bandwidth. This produces a smooth output waveform shown in Figure 2.4h (*c.f.* Figure 2.3k) . Further reduction of the layer thickness causes a decrease in the low-pass effect, as seen in figs. 2.4i and 2.4j. A close look at the output waveforms in these Figures shows small amplitudes building prior to the beginning of the pulse, this again is acausal, occurring before time-zero, a product of the inverse Fourier transform.

2.5 Summary

The discussion outlined above indicates that for given values of the number of layers, their thickness and velocity, and the reflection coefficient, frequency-selective attenuation will occur within a layered earth. Whether or not the values that have been used in the simple models above are in any way representative in terms of the real earth is a question that will be addressed later on in the current work. However, several preliminary conclusions may be drawn from the modelling outlined above. Great care must be taken with mathematical modelling of the data. If a Fast Fourier transform is to be used to obtain real, time-domain data from a complex spectrum, then consideration of the sampling interval of the input waveform should be undertaken to avoid spurious amplitudes when returning back to the time domain. This is graphically obvious when using a spike as the input waveform. The low-pass transmission effect and the contribution of peg-leg multiples to the direct wave amplitude are intimately linked. This occurs because the peg-leg amplitudes are within the time window that is described as the downward propagating pulse. When the complex spectrum of this pulse is calculated , part of the spectrum will have lower amplitudes relative to the input spectrum. If the peg-leg multiples could be separated from the direct wave no such process would occur. In general, increasing the value of the reflection coefficient will amplify the low-pass effect of the layer(s), as will

increasing the number of layers. Increasing the layer thickness will increase the number of nodes of the transmission response within the spectral limits, and will thus increase the complexity of the propagating pulse. Decreasing the layer thickness will reduce the low-pass effect if the shortest wavelength component of the pulse (at the Nyquist frequency) is greater than four times the layer thickness. If the tuning frequency (at $\lambda = 4d$) is near the upper limit of the bandwidth of the input waveform, then the whole spectrum will be subject to a low-pass response, which will result in a smooth output waveform. The contribution of the peg-leg amplitudes will accordingly be very difficult to detect in the time-domain. Conversely, if the tuning frequency is less than the Nyquist frequency of the input waveform, modifications to the shape of the input waveform will be detectable in the output waveform as irregular subcycles, in the absence of noise. It is likely, therefore, that thin layers whose thickness is less than a quarter of the seismic wavelength at the upper frequency limit of the incident pulse bandwidth (whether it be at the Nyquist frequency or at the upper limit of the effective bandwidth) will be the most problematic in any investigation into the spectral character of seismic reflections. It is clear, that in the absence of geological control, the discrimination of the effects of peg-leg multiples present a formidable problem to any investigation into seismic attenuation.

Chapter 3: Measurement of Attenuation

3.1 Introduction

This chapter examines the methods that can be used to measure attenuation through unconsolidated media using marine seismic reflection data. There have been some published works comparing the methods available, including Jannsen *et al.* (1985), Badri and Mooney (1987) and Tonn (1991) - the latter primarily concerned with Q measurements from VSP data. Several methods will be reviewed, some of which are widely accepted, such as (i) the risetime method (Gladwin and Stacey, 1974), (ii) the spectral ratios method (Båth, 1974), (iii) wavelet modelling (Jannsen *et al.*, 1985) and (iv) spectrum modelling (Jannsen *et al.*, 1985). The methods can be broadly divided into those that are carried out in the frequency domain and those that use the time domain.

3.2 Fourier Methods (Frequency Domain Methods)

Fourier transforms, their variants and uses, are detailed in several texts including Champeney (1973), Båth (1974), Elliot and Rao (1982) and Press *et al.* (1986). In terms of seismic data processing, one of the most common uses of the Fourier transform is to estimate the amplitude or power spectra of seismic waveforms, as well as other processes such as the application of filters in the frequency-domain, waveshaping and deconvolution. This project is concerned primarily with changes in the spectral characteristics of seismic waveforms that have been propagated through the near sub-surface, so the estimation of the amplitude spectrum is of great importance.

A seismic trace can be considered as the result of discretely sampling of a continuous function. If the sampling frequency is defined as Δt, the Nyquist Frequency

(F_{nyq}) is defined as $1/(2\ \Delta t)$. If the undigitised seismic trace (i.e. the continuous function) contains frequencies above the Nyquist frequency, aliassing will occur, whereby frequencies above the Nyquist frequency become folded back around F_{nyq}, and will effectively contaminate lower frequencies below F_{nyq}. In order that a continuous function is truly represented in a digital form, the sampling rate should be at least twice that of the highest expected frequency.

The Fast Fourier Transform (FFT) is commonly used as a method to estimate the amplitude spectrum of a finite-length signal, such as a seismic waveform, although other methods of spectral analysis do exist such as methods using maximum entropy (Childers, 1978).

3.2.1 Spectral Ratios Method

For a given window of N time samples, the FFT consists of N complex numbers, which contain amplitude and phase information at discrete frequencies between $-F_{nyq}$ and $+F_{nyq}$. That is, the spectral information is essentially contained in one side of the FFT. By taking the modulus of each of the complex numbers, the signal amplitude at (N/2 + 1) frequencies may be obtained. (The spectral ratios technique has variants which are discussed by Båth, 1974; the following is concerned with the frequency-ratio variant). The phase information can be found by taking arctangent (imaginary / real component) at each value of ω of the FFT. The mathematical basis of the spectral ratios technique of attenuation measurement is based upon calculation of the amplitude spectrum. The spectral ratios technique involves comparison of a reference wavelet from an earlier arrival time with that of a wavelet recorded at a later arrival time. The amplitude spectrum of the later wavelet, in an inelastic medium would be relatively more deficient in the higher frequencies due to absorption. The effects of dispersion, geometrical spreading, reflection and transmission losses and scattering are not considered at this stage. In the noise-free case, the seismic quality factor, Q, can be calculated from the slope of the logarithmic ratios of the amplitudes of the reference and later events by the formula:

$$Q = \frac{2\pi}{1 - e^{(\frac{4\pi m}{T})}} \quad \ldots\ldots\ldots 3(1)$$

where:

m is the slope of the ratio function of the spectra

T is the two way traveltime between the events

As the signal-to-noise ratio is a function of frequency because of the band-limited nature of the seismic data, Q can be estimated from only the portion of the spectrum where a good signal to noise ratio occurs. Clearly this is a technique which lends itself to a least-squares statistical approach. By comparing the spectra of two wavelets in the far field, the effects of source variation can be minimised; for instance, a spectral notch, due to 'ghosting' from the sea surface, would be a character of the primary downgoing wavelet at earlier and at later arrival times. More than one notch may be present due to the differing depths of both source and receiver. As only spectral slope is used in this technique, geometrical spreading effects are not a consideration.

The time-samples used as the input are subject to windowing prior to application of the FFT. When the FFT is performed on discrete data, the amplitude spectrum is calculated at certain values of ω, and not as a continuous function of ω. This causes the spectral estimate at any particular value of ω_n to contain power from frequency components that lie between the discrete values of ω_{n-1} and ω as well as ω and ω_{n+1}, as discussed by Press *et al.*, (1986). If the data are not windowed in any way this is equivalent to using a rectangular window. The Fourier Transform of the rectangular window has a non-neglible high frequency component due to the rapid fall-off at the edges of the window. The rectangular window has the narrowest central concentration of spectral power for a given ω, but also has large sidelobes of spectral leakeage away from ω. Most windowing techniques aim to reduce the amplitude of the sidelobes albeit at the expense of widening the central concentration of spectral power around ω. Such windows include the triangular (Parzen), Hanning, Hamming and Welch variants (Press *et al.*, 1986).

All of these windows have the symmetrical characteristic of starting from zero, rising to a peak and falling back to zero. Press *et al.* (1986) found no effective difference between the various windows (except rectangular) and recommended the Parzen or Welch windows. However, Pujol and Smithson (1991) emphasised the importance of the window type and length, pointing out that the frequency-dependence of Q may be biassed by the method of data windowing. Sams and Goldberg (1990) suggested that the use of only those frequencies near the peak frequency would improve Q estimates using the spectral ratio method. Tonn (1991) suggested that Jannsen *et al.*, (1985) reported that a rectangular window was the most suitable type. This was somewhat misleading as Jannsen *et al.*,(1985) do not use any windowing because the 54-point input data has already been padded with zeros for a 1024-point FFT. This process makes the resultant spectrum smoother than using a 64-point FFT, for example, and was seen to make any windowing of the input data unnecessary.

In order to assess the potential effects of windowing upon the input data, an arbitrary seismic trace taken from the case study in Chapter 5 was analysed using the spectral ratio method. The trace has a sample interval of 0.05 ms. Forty samples were taken for reflection events 1 and 2 respectively. These samples were padded with zeros to form 512-point samples which were subsequently multiplied by various window functions, of the Parzen, Hanning, Welch and rectangular type. The forms of the window types are found in Press *et al.*, (1986):

Parzen Window

$$W(j) = 1 - \left| \frac{j - 1/2(N-1)}{1/2(N+1)} \right|$$

Hanning Window

$$W(j) = 1/2[1 - \cos(\frac{2\pi j}{N-1})]$$

Welch Window

$$W(j) = 1 - (\frac{j - 1/2(N-1)}{1/2(N+1)})^2$$

where N is the length of the window. The resulting amplitude spectra where compared and a Q estimate obtained for a bandwidth of 0 Hz to 4 kHz. Applying the rectangular, Hanning and Welch windows has an identical effect in terms of the final Q estimate of 63. Only the Parzen window shows a slight variation in a Q estimate of 65. For the bandwidth that is of interest in the current work, using a 512-point sample length leads to a smoothing of the amplitude spectra that effectively masks the effects of applying any particular type of window. However, if the length of the sample were reduced (e.g. to 64 points) the effects of the windows would be more dramatic as the slopes of the window, from the peak at N/2 samples would be steeper for smaller values of N. For this study, therefore, a rectangular window was used, which is equivalent to no windowing at all.

The spectral ratios technique relies on fitting a straight line through a series of scattered data points. One of the most common ways of achieving this is through a linear least-squares approach. This approach has the disadvantage of being sensitive to outlying points. For example, a reference spectrum (such as from the seabed) has a severe spectral notch (for example from one of the sea-surface ghosts) at a certain frequency, f, with amplitudes around f above background noise levels. At a later time, given an absorbing earth, frequency-selective attenuation will have taken place. Using the spectral ratios technique, a straight line can be fitted through the natural logarithmn of the ratios of the amplitudes of the reference spectrum and the spectrum of a later reflected event (against frequency). If a notch occurs in the middle of the bandwidth of interest in the reference spectrum, it will occupy the same position in the attenuated spectrum. However, the notch frequency amplitudes cannot be attenuated below the noise levels and thus the spectral ratio will be too high and will cause a spike in the distribution. If a least-squares line is fitted to the data, the spike will reduce the gradient of the best fit line, and will

overestimate the value of Q. The deeper the initial notch in the reference spectrum, the greater this effect will be, if all other parameters remaining constant. Slight variation in the source and/or receiver depth will cause small variations in the notch frequency which will lead to scattered spectral ratios.

Under such circumstances, a more robust technique is required. A computer routine was given by Press *et al.*, (1986) which fitted a line of the form y = mx + c by the criterion of minimum (least) absolute deviations rather than minimising χ^2. The technique uses the median, rather than the mean, to fit a straight line, being the value which minimises the sum of the absolute deviations (Press *et al.* 1986). The function to be minimised is:

$$\sum_{i=1}^{i=N} |y_i - \alpha - mx_i| \quad \ldots\ldots\ldots 3(2)$$

where α = the median of $\{y_i - mx_i\}$. The routine calculates an initial least-squares estimate of the parameters m and c, and the standard deviation (σ_1) is calculated from χ^2 . The median is found by bracketing and bisection using a starting point for the bracketing at σ_3 . If this method is used to fit a straight line in the case of the spectral notch, a lower value of Q, more representative of most of the data points, will be estimated using the spectral ratios technique. The routine also calculates a statistical goodness of fit, *i.e.* the mean absolute deviation of the x and y points in y from the fitted line. It must be noted that this approach gives an idea as to the goodness of fit of the straight line through the data, independent of how the data were derived. A method for examining the validity of the spectral estimates, or the errors involved will be discussed later in this section.

Jannsen *et al.*, (1985), reported a 15% upper limit for the spectral ratio technique to give acceptable results (permissible error of 25% in the Q estimate) in the presence of noise. Tonn (1991) found the spectral ratio technique to be reliable in the noise-free case for VSP investigation, but unsatisfactory in noisy cases. The spectral ratio technique also assumes that the reflection coefficients and phase velocity (no dispersive effects) are

independent of frequency (Båth, 1974). The technique also has the advantage of not requiring any input of the geometrical spreading factor, as this is incorporated as part of the intercept c in the straight-line model. The standard deviation of the mean of a particular sample of data (Y) of length n is known as the standard error, *SE*, (Clarke and Cooke, 1992), defined as:

$$SE(Y) = \frac{\sigma}{\sqrt{n}} \quad \text{.....3(3)}$$

where σ is the standard deviation

For spectral estimates of a raw power (or amplitude) spectrum, the standard error is identified (Raikes and White, 1984) as:

$$\frac{SE(R)}{R} = \sqrt{\frac{1}{n}} \quad \text{.....3(4)}$$

where n is a spectral smoothing factor, and R is the power or amplitude estimate. White (1992) gave the variance of the estimated amplitude ratios as:

$$\text{var}\left(Ln\left|\frac{A_2(f)}{A_1(f)}\right|\right) = \frac{1}{2bt} \quad \text{.....3(5)}$$

where b is the width of the frequency bin of the spectral estimate (see below) and t is the duration of the data segment (see below). The standard error (SE) of the spectral ratios is the square root of their variance:

$$SE = \sqrt{\frac{1}{2bt}} \quad \text{.....3(6)}$$

The spectral estimates are independent providing they are spaced at least b, the analysis bandwidth, apart (White,1992).

The spectral smoothing factor , n, reduces the variance (and standard deviation) of each spectral estimate. White (1980) described n as a measure of the spectral averaging used in the analysis of the data, equivalent to the product of the length of the data segment (t) that undergoes a transformation and the width (b) of each frequency 'bin' at which a spectral estimate is given. For example, if a seismic trace is digitised at 20 kHz, and a window 512 samples in length is selected for spectral analysis, the duration of the window is 512x0.00005 = 0.0256 seconds. The raw power spectrum has a power estimate at 512/2 frequencies plus a 0 Hz component. This would yield a spectral estimate at every 39.0625 Hz up to 39.0625x256 = 10 kHz, the Nyquist frequency. Each estimate contains spectral power from ±39.0625/2 Hz away from the frequency of that particular estimate. The frequency 'bin' therefore, has a width of 39.0625 Hz. This is equivalent to no spectral smoothing, as:

$$n = bT = .0256\text{x}39.0625 = 1.0$$

An increase in the width of the frequency bins increases the smoothing factor, which will yield smaller standard errors in the spectral estimate. This process also reduces the spectral resolution of the power spectrum.

If any regression analysis is to be performed on the data to obtain a Q estimate, there will be a conflict between spectral resolution and the stability of each spectral estimate, especially if the data under analysis have a limited bandwidth with only a few spectral estimates at the raw power spectrum stage. By grouping estimates of power at n discrete frequencies, the standard error is reduced by a factor $n^{0.5}$. If no smoothing takes place, the standard deviation of each spectral estimate is therefore 100 % of its value.

Assuming a Gaussian distribution, confidence limits may be determined from the χ^2 distribution. Firstly the lower and upper % points of χ^2 are found from tables of the χ^2

distribution . With a spectral smoothing factor of n, there are $2n$ degrees of freedom. For example if a 95% confidence interval is required, and n = 8, there are 16 degrees of freedom. The χ^2 distribution yields a 2.5% point of 6.91 and a 97.5% point of 28.85. As the expectation value is 16, the upper confidence limit is 10 log (6.91/16) dB = +3.65 dB, whilst the lower limit is 10 log (28.85/16) dB = -2.56 dB. Expressed in terms of the amplitudes, the upper limit is 1.52 times the value of the spectral estimate, whereas the lower limit is 0.74 times the value. For a 90% confidence interval, the χ^2 distribution table should be consulted for the 5% and 95% points. Because the spectral ratios technique compares two independent data sets from different windows, the resulting power or amplitude spectra are independent χ^2 variates (Raikes and White 1984). Fisher's F distribution can be used with these variates to provide a confidence interval for the ratio of the spectra from the two windows; the ratio of the spectra will follow the F-distribution . With ($2n$,$2n$) degrees of freedom, the 5% and 95% points of F (for a 90% confidence interval) can be found from a tabulated F distribution (those values which would by chance be exceeded with a probability of 5% if both samples were actually drawn from Gaussian distributions with the same variance). In the above example, the upper limit is +10 log(2.33) = +3.67 dB, whilst the lower limit is -10 log(2.33) = -3.67 dB from the spectral estimate (power); expressed in amplitudes the limits are 1.53 times the estimated value and 0.66 times the estimated value.

For a spectrum of 0 to 10 kHz, with a spectral estimate based on 16 bins of 625 Hz width each, n is 16, so there are 32 degrees of freedom for the F-distribution of the linear spectral amplitude ratio i.e. an upper 95% limit of 1.24 times the linear ratio and a lower limit of 0.81 times the ratio. The 5% and 95% confidence linits will be presented on a log-scale along with the spectral amplitude ratio.

3.2.2 Spectrum Modelling

After having performed a FFT on the input data, instead of using an approach which fits a straight line to the relationship between the earlier and later events, as in the above case, there is an alternative strategy known as spectrum modelling (Jannsen *et al.*, 1985). The

reference spectrum is, in essence, synthetically attenuated using Q as a a variable to try to achieve a match to the amplitude spectrum of the later event. The fit between the model spectrum and that of the later event does not have to be evaluated using least-squares or least absolute deviations, but by methods such as using the L_1-norm or L_2-norm criteria. The L_1-norm involves minimising the sum of the absolute difference between the amplitudes of the two spectra (Claerbout, 1976). The L_2-norm minimises the sum of the squares of the difference between the amplitudes of the two spectra (Claerbout, 1976). Clearly the latter weights larger amplitudes preferentially, which would attach more importance to the dominant frequencies. The reference amplitude spectrum can be envisaged as a source amplitude multiplied by:

$$e^{\frac{-\pi f \Delta t}{Q}} \times G \times R \quad \text{.....3(7)}$$

where G is a geometrical spreading factor and R is a factor to account for reflection losses to model the absorption albeit in a non-dispersive manner. However, the effects of geometrical spreading can be one order of magnitude larger than that of absorption and must be accurately accounted for (Pujol and Smithson, 1991). The amplitude decay will be proportional to the two-way travel time provided the pulse has travelled through a constant velocity medium. Unfortunately the marine environment will have at least a two-layer velocity structure considering just one sediment layer. The geometrical spreading factor can be approximated to the ratio of the distances travelled by the reference and the later events. If spherical spreading and a constant velocity structure is assumed, then this factor can be approximated to the ratios of the arrival times of the two events. Errors in this procedure will arise from the assumed velocity structure and errors in the arrival times of the events. Thus it is probable that VSP data will provide a better estimate of G than single-channel marine reflection data. Tonn (1991) found that this technique was the most reliable one for VSP work if true amplitude recordings were not available. Given true amplitudes, it was found to be the second most reliable method after a time-domain technique involving complex trace analysis. The method has a disadvantage that the phase

information within the complex spectra is not used. A method must also be found to account for the ill-constrained geometrical and reflection factors if an absolute comparison to the observed spectrum is to be made.

In the following equation

$$Ln\frac{A_2(\omega)}{A_1(\omega)} = Ln|(G)| + Ln|R_2(1-R_1^2)/R_1| - 2\alpha[(x_2 - x_1)] \quad \text{.....3(8)}$$

where:

$$-2\alpha[(x_2 - x_1)] = \frac{\pi f \Delta t}{Q} \quad \text{.....3(9)}$$

R_1 ,R_2 are the reflection coefficients at distance x_1, x_2

A_1, A_2 are the amplitudes at x_1, x_2

α is the absorption coefficient

G is the geometrical spreading term

the left term is the spectral ratio, whilst the far right term accounts for absorption. The central terms form a frequency-independent constant. Providing there are no drastic lateral velocity changes or marked lateral reflectivity changes across the area of study, an approximation to the sum of these frequency-independent constants can be obtained using the spectral ratio technique.

The case for the absorption of low frequencies has already been discussed. As ω approaches zero, the far right term approaches zero. At low frequencies, the intercept of the best-fit line on the y-axis will therefore approach the value of the sum of the geometrical and reflection terms. One possible approach is to examine many spectral ratios plots over the area of study and to average the values of the intercept to find a representative value. This value (c) can then be substituted for the G and R terms:

$$A_2(\omega) = A_1(\omega).e^{\left[c-\frac{\pi f \Delta t}{Q}\right]} \quad \ldots\ldots\ldots 3(10)$$

where c = Ln (G) + Ln (R) = Ln $G.R$. A knowledge of the arrival times and an estimation of the likely reflection coefficients may indicate the validity of the substitution. Spectrum modelling could then take place, by varying the arrival time and Q for an optimum model using L_1 and L_2 norm criteria. Consider the situation for Q = 60, with an event having an arrival time 15 ms after a reference event (with an arrival time of 30 ms) at a frequency of 1 kHz. The geometric factor will be Ln (30ms/45ms) = -0.4 . With a seabed reflection coefficient (R_C) of 0.3 and a deeper R_C of 0.2, Ln ($G.R$) = -0.9. The absorption term is (-π×1000×0.015/60) = -0.79. The total amplitude loss is therefore:

$$e^{(-0.9+(-0.79))} = 0.18 \quad \ldots\ldots\ldots 3(11)$$

= a 72% loss in amplitude.

This indicates that the combined reflection and geometric term is of the same order of magnitude as the frequency-dependent term. Therefore, without a reasonably accurate estimation of this term, the results of absolute spectrum modelling may be erroneous. A simpler approach is to obtain the optimal fit to the observed spectrum without inputs for G or R as these may be considered frequency-independent terms. By varying Q an optimal fit may be obtained which matches the observed spectrum except for a gain factor. It should not be assumed, that the observed amplitude losses are proportional to frequency (Stoll, 1977; Keller, 1989). An 'effective' Q can be calculated for the individual frequency components if necessary.

3.2.3 Wavelet Modelling

Wavelet modelling (Jannsen *et al.*, 1985) provides an extension to the spectrum modelling technique. Instead of using only the amplitude spectrum, the phase characteristics (dispersion) are also considered. A reference wavelet is transformed to the frequency-domain using an FFT. The absorption and dispersive effects are then applied prior to an

inverse FFT to the time domain. The calculated wavelet can then be compared with the observed wavelet for goodness of fit. The amplitude spectrum ($A_2(\omega)$) for a wavelet reflected from a single layer beneath the seabed (used as the reference reflector) is calculated by:

$$A_2(\omega) = A_1(\omega).G_{x_2}.R_2.e^{j\omega\Delta t.\frac{V_0}{V_{(\omega)}}}.e^{\frac{\omega\Delta t.Ln(1-(\frac{2\pi}{Q}))}{4\pi}} \quad \text{.....3(12)}$$

where G and R account for the geometrical spreading between the seabed and the reflector, $A_1(\omega)$ is the complex spectrum of the seabed reflector, and Δt is the interval two-way traveltime for the layer .

The second exponential term contains the absorption relation (equivalent to the exponential term in eq. 3(7), while the first (complex) exponential term is a frequency-dependent phase shift to account for dispersive effects, with a modulus of one, and therefore not affecting the amplitude spectrum.

Jannsen et al., (1985) used the dispersion relation (see Chapter 2) of Futterman (1962):

$$\frac{V_0}{V_{(\omega)}} = 1-[\frac{1}{\pi Q}.Ln(\frac{\omega}{\omega_{(0)}})] \quad \text{.....3(13)}$$

where V_O is the reference (slowest) phase velocity at ω_O, and $V(\omega)$ is the phase velocity at frequency ω.

To obtain a Q estimate, Jannsen *et al.*,(1985) also proposed that both Δt and Q could be varied in order to obtain a close fit to the observed wavelet in the time-domain. The calculated wavelet was then compared to the observed wavelet by minimising the sum of the amplitudes of the absolute difference between the calculated and observed wavelets

over the time period of the pulse. From this minima, an optimum Q was obtained. The correct arrival time was found between the minimum of the covariance function (between the seismic trace and the reference wavelet) and a quarter of a wavelength before.('quarter of a wavelength' presumably referring to the dominant wavelength). Using a synthetic data set with increasing levels of noise, they found that, in the case of no noise, the wavelet modelling technique was superior to the spectrum modelling and spectral ratios techniques in that it provided the correct Q estimate (±25%) with less than 1.5 wavelengths separation between two events. The spectral methods required at least three dominant wavelengths of separation. With the addition of 15% noise (expressed as the ratio of the noise variance to the signal variance), all methods failed to achieve the arbitary 25% accuracy except for the wavelet modelling method, providing there was a minimum separation of 2 wavelengths.

The wavelet modelling technique was applied to a marine reflection data set from a 1 kJ sparker source and Q estimates obtained. The Q estimates were derived after having created synthetic traces based on equation 3(12). As has been shown, this equation contains two unknown terms in addition to Q, namely the geometric and reflection terms. No mention of the input of these parameters to the synthetic traces was mentioned. It must therefore, be assumed that constant values were used for these terms. Thus this technique does not attempt to find a match to the observed wavelet, but rather an optimum fit considering Q and Δt as input parameters. As the comparison between the wavelets occurs in the time-domain, this is strictly a time-domain technique but the technique is heavily reliant on Fourier analysis. The comparison of fit may be compared in both the L_1 and L_2 norms. For VSP data, Tonn (1989) found the technique to be superior to other techniques in the specific case of thin layers (*c.f.* Jannsen *et al.*, 1985), but generally inferior to certain time-domain techniques and spectral modelling. To see how much difference the inclusion of phase information makes to the simpler spectral modelling, the dispersion relation of Futterman (1962) may be examined (eq. 3(13)).

Considering a seismic trace digitised at 20 kHz, then this will nominally contain frequencies up to 10 kHz, assuming no aliassing. If a spectral estimate of any window of the data is required, assuming a 512-point FFT, then the amplitude spectrum is defined at

(512/2 + 1) frequencies, the lowest non-zero frequency being (10000/256) Hz = 39.0625 Hz. This frequency can be taken as ω_O in eqn. 3.12. Futterman (1962) defines this value as a non-zero low-frequency cutoff. The phase velocity $V(\omega)$ increases with increasing frequency. These effects can be considered for $\omega = \omega_O$, $\omega = 128\omega_O$, and $\omega = 256\omega_O$, which are equivalent to 39Hz, 5 kHz and 10 kHz.

If $Q = 100$ and $Q = 50$, the velocity ratio $V_O/V(\omega)$ is given in Table 3.1 :

Table 3.1

Variation of the velocity ratio $V_O/V(\omega)$ as a function of ω for Q = 50 and 100

ω	**$V_0/V(\omega)$ {$Q = 100$}**	**$V_0/V(\omega)$ {$Q = 50$}**
ω_O	1	1
$128\omega_O$	0.9845555	0.9691110
$256\omega_O$	0.9823491	0.9646983

Dispersive effects will increase with greater absorption (lower Q), but for reasonably realistic Q values that have been measured in natural materials (e.g. Hamilton, 1972), the increase in phase velocity with frequency will be very small, even approaching the Nyquist frequency. The logarithmic dependence of the phase velocity on frequency derived by Futterman is probably the reason why dispersion is not usually observed in the field. The first exponential term in eq. 3(12) shows that for decreasing values of $V_O/V(\omega)$ there will be a shorter time delay through a medium for increasing frequencies. This is graphically shown in Figure 3 of Futterman (1962). Thus although the wavelet modelling technique may use more of the information content in a wavelet than the spectrum modelling technique, the logarithmic dependence of the phase velocity change on frequency, coupled with realistic Q values for near-surface earth materials, will make the contribution of the phase changes due to dispersion very small in terms of the calculated wavelet relative to the reference wavelet. Its inclusion in wavelet modelling gives the method more physical correctness in that a method that does not consider dispersion is

acausal, but may not necessarily arrive at better Q estimates. One possible practical advantage of spectrum modelling over wavelet modelling is that an inverse FFT is not required prior to wavelet comparison. As with wavelet modelling, both Q and Δt may be used as input parameters to the calculated wavelet.

3.2.4 Matching Technique

Raikes and White (1984) used the matching technique to determine either the complex operator or the complex transfer function that transforms an earlier recorded pulse into a later recorded pulse and *vice versa*. This technique yields estimates of both the amplitude and phase response of the attenuation operator, as well as providing a statistical measure of the response at each frequency. It also indicates and minimises local interference as well as noise effects. The transfer function, H_{12}, and its inverse, H_{21}, (where $_{12}$ indicates the prediction of the later pulse from the earlier pulse and $_{21}$ indicates the prediction of the earlier pulse from the later pulse), are initially calculated as the complex spectra of prediction filters h_{12} and h_{21} . The difference between the squares of the moduli of the spectra indicate the effects of noise and interference on the amplitude spectrum. Once calculated, the transfer functions can be compared to see at which frequency the spectra start to diverge. Below this frequency, a best-fit line is obtained for the natural logarithm of the ratios of the power spectra vs. frequency. Q is calculated from the slope of the best fit line.

In more detail, the transfer function H_{12} can be approximated by the ratio of the complex crosspower spectrum, $\Phi_{1,2}$ (between the reference and the later wavelet) and the power spectrum, $\Phi_{1,1}$ of the reference wavelet (White 1980):

$$H_{1,2}(f) = \frac{\Phi_{1,2}(f)}{\Phi_{1,1}(f)} \quad \text{.....3(14)}$$

The crosspower spectrum of two wavelets is the Fourier transform of their cross-correlation (Sengbush, 1983). The complex crosspower spectrum can then be derived by multiplying the complex conjugate of the FFT of the first wavelet by the FFT of the second wavelet. The complex conjugate can then be formed by changing the sign of the imaginary component of the complex spectrum.

The power spectrum of the first wavelet may be obtained by squaring the modulus of the FFT of that wavelet although this is, strictly speaking, the energy spectrum of a finite-length wavelet (without any normalisation per unit time for power estimation). The transfer function may be calculated in the same manner. The power transfer functions can then calculated as the moduli squared of the transfer functions. Their geometric mean is then determined from the power spectral ratios, the natural logs. of which are plotted against angular frequency for a Q estimate as:

$$Ln(\text{power ratios}) = Ln(\text{constant frequency effects}) - \frac{\omega \Delta t}{Q} \quad \text{.....3(15)}$$

with a slope (m) of:

$$m = -(\frac{\Delta t}{Q}) \quad \text{.....3(16)}$$

When compared to the slope (m') of the spectral ratios plot,

$$m' = \frac{\Delta t}{4\pi} . Ln(1 - \frac{2\pi}{Q}) \quad \text{.....4(17)}$$

there is little but a difference of a factor of 2 between the two estimates. This is because the slope of the plot from the matching technique is from a log-power plot rather than a log-amplitude plot. The fact that this technique can yield the phase response of the

attenuation operator is not necessarily a great advantage, in that the dispersion may be negligible for realistic Q in near-surface sediments. For multi-channel surface seismic and VSP data, the matching technique could yield statistics on the quality of the spectral estimates (White, 1973,1980,1992). For single-channel seismic data, the technique could be used to obtain the amplitude response of the attenuation operator as well as the spectral ratios. The coherence function is based upon signal-to-noise (S/N) ratio estimation in the bandwidth of interest between two reflected events. This function cannot be determined using single channel data, but in order to consider the S/N ratio within absorption determination, a measure of S/N can be obtained in consideration of certain spectral features. Figure 3.1 shows two amplitude spectra, one determined from a seabed reflection, the other from an event some 13 metres below the seabed. The seabed event has a peak frequency of about 2.0 kHz and contains considerable energy up to about 7 kHz, above which there is a flatter 'tail'. The deeper event has a peak frequency of about 1.8 kHz, and has energy up to almost 4 kHz, above which there is a flat 'tail' out to the upper limits of the frequency spectrum. An estimate of the noise levels can be obtained by determining the mean amplitudes of the non-signal parts of the spectra, and dividing the amplitudes of respective spectra at each frequency by the mean noise amplitude. An indication of the joint S/N measure (S_{12}) between the two spectra can be given by: (SN_{12}) = $(1/(1+SN_1))\times(1/(1+SN_2))$, where SN_1 and SN_2 are the S/N ratio estimates at each frequency for the two spectra (White, 1973). Although this procedure gives only a broad indication of spectral quality in terms of S/N ratios, most previous works using single channel data have omitted this consideration (e.g. Jannsen *et al.*, 1985). Clearly, the lower limit of the noise 'tail' of the deeper event will define the uppermost practical limit for absorption estimation with techniques that use spectral ratios.

3.3 Time-Domain Methods

There are several methods that come under the term 'time-domain'. Three sub-types can be identified; the amplitude-decay method, the risetime method (Gladwin and Stacey, 1974)

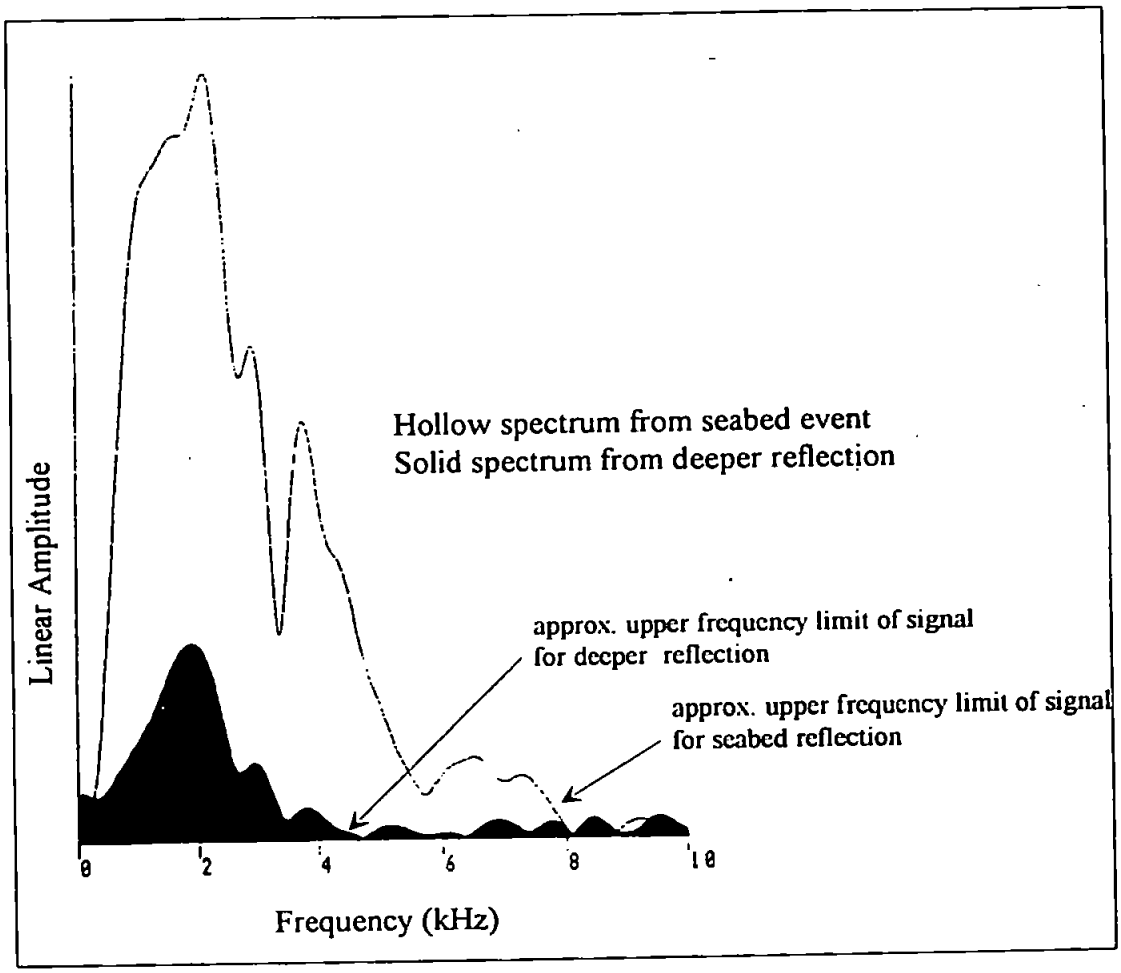

Figure 3.1
Amplitude Spectra of Seabed and Deeper Reflection Event showing high-frequency noise tails (from 49/10 case study)

and methods based upon complex trace analysis (Taner *et al.*, 1979). As Tonn (1989) found the amplitude-decay method to be very unreliable as an estimator of Q, even in the noise-free case; only the latter two types will be considered.

3.3.1 Risetime Method

Gladwin and Stacey (1974) carried out ultrasonic measurements on acoustic pulses that had propagated through massive rocks to derive an empirical formula that related the risetime (τ) of a pulse to the time of propagation of a pulse, t. The theoretical background was given in Kjartansson (1979). The pulse risetime was the time interval between the intersections of the steepest rise of a pulse onset with the zero amplitude level and peak pulse amplitude . Their empirical relation was:

$$\tau = \tau_0 + c\int Q^{-1} dt \quad \text{.....3(18)}$$

or for a particular Q estimate:

$$Q = \frac{c\Delta t}{\tau - \tau_0} \quad \text{.....3(19)}$$

where τ_0 is the risetime of the source (often the seabed) and c is a constant (see below). Tonn (1991) gave an erroneous form of the risetime as:

$$\tau = \tau_0 + cQ\Delta t \quad \text{.....3(20)}$$

In general, the higher the absorption of the media, the more a pulse will broaden and lower in amplitude. Gladwin and Stacey (1974) observed a $\tau \propto Q^{-1}$ and $\tau \propto t$ relationship, in disagreement with the results of Ricker (1953) who found a $\tau \propto t^{0.5}$

relationship.

The risetime technique has the advantage over other methods, such as the spectral ratios technique, of only using the leading part of a pulse i.e. a very short part of the record, as well as not requiring any geometrical spreading considerations. This former feature makes it less prone to the effects of interfering events which cause serious problems with the both the spectral ratios and matching techniques. The technique also has its problems. Firstly the value of c is only constant for $Q > 20$ (Kjartannson, 1979), *i.e.* that risetime had a linear relation with traveltime for $Q > 20$ although for unconsolidated sands and muds where Q is generally above 25 (Hamilton, 1972) this may not be a problem. Gladwin and Stacey (1974) found the value of c to be 0.53 ± 0.04 and possibly $c = 0.5$ precisely. Jannsen *et al.*(1985) found a value of $c = 0.33$ by adjusting eq. 3(18) to their particular data set. This can only be carried out if data are available from different arrival times. The constant, c, may be a function of the receiver (Jongmans, 1990a), but the main problem is noise. Jannsen *et al* (1985), using synthetic data, found the technique gave >25% errors in the estimates of Q with a noise level of only 5%. The method can also be seen to be partially dependent on the sampling frequency of the data in that the slope of the deflection, and its maximum, may not be well defined at low sampling rates. Using shallow land reflection data Jongmans (1991) found that near field effects (including the onset of surface waves) control the pulse shape at short distances from the source (within 1.2 wavelengths) rather than attenuation effects . The risetime (or pulse-broadening) method was found to be adequately reliable for distances greater than about 1.2 wavelengths from the source.

3.3.2 Complex Trace Analysis

Taner *et al.*, (1979) introduced complex trace analysis as an interpretational aid by examining the interplay and spatial variations of certain quantities that can be determined by the analysis. They saw the seismic trace as a projection into the real plane of a complex trace (i.e. treating the trace as an analytical signal). From this complex trace, quantities such as envelope amplitude (or reflection strength), instantaneous frequency and

instantaneous phase could be determined (known as seismic attributes).

The real seismic trace $f(t)$ can be expressed as an amplitude $A(t)$ and a phase $\gamma(t)$, both of which are functions of time:

$$f(t) = A(t).\cos\gamma(t) \quad \text{.....3(21)}$$

The quadrature trace, $f^q(t)$, is 90° out of phase with the real trace:

$$f^q(t) = A(t).\sin\gamma(t) \quad \text{.....3(22)}$$

The complex trace $F(t)$ is represented by:

$$F(t) = f(t) + jf^q(t) \quad \text{.....3(23)}$$

and as $\cos(x) + j\sin(x) = e^{jx}$ .....3(24)

the complex trace can be represented by the amplitude and phase as:

$$F(t) = A(t).e^{j\gamma} \quad \text{.....3(25)}$$

The envelope amplitude $A(t)$ can be calculated as the modulus of the complex trace:

$$A(t) = [f(t)^2 + f^q(t)^2]^{\frac{1}{2}} = |F(t)| \quad \text{.....3(26)}$$

The instantaneous phase $\gamma(t)$, is formed from the arctangent of the ratio of the qaudrature and real traces:

$$\gamma(t) = \arctan\frac{f^q(t)}{f(t)} \quad \text{.....3(27)}$$

The instantaneous frequency ω^i is defined as the rate of change of phase with respect to time:

$$\omega^i = \frac{d}{dt}\arctan[\frac{f^q(t)}{f(t)} \quad \text{.....3(28)}$$

The computational procedure for the instantaneous frequency will be discussed in the following chapter.

Engelhard *et al.* (1986) related $A(t)$ and ω^i to Q in the expression:

$$Q = \frac{\omega^i(T)\Delta t}{2\Delta L n(\frac{a(T)}{G})} \quad \text{.....3(29)}$$

where G accounts for geometrical spreading, $a(T)$ is the maximum of the envelope amplitude and Δt is the travel time. The relationship between the internal time T and travel time difference, Δt is shown in Figure 3.2 (after Tonn 1989).

Three ways of using this method were given by Tonn (1991) for VSP data. The first is to use only the maxima of the envelope amplitudes. The second uses every sample of the reflections that are being analysed to average the quality factors in order to yield an average Q estimate. The third way uses the same relation as a linear relation. Q can be calculated from a plot of envelope amplitude vs. average instantaneous frequency, which will have a slope of $\Delta t/Q$. Unfortunately, the presence of dispersion necessitates correct synchronisation between the two reflections. The latter two approaches may be problematic as they rely on being able to compare, for example, the $a(T)$ and $\omega^i(T)$ at T/2

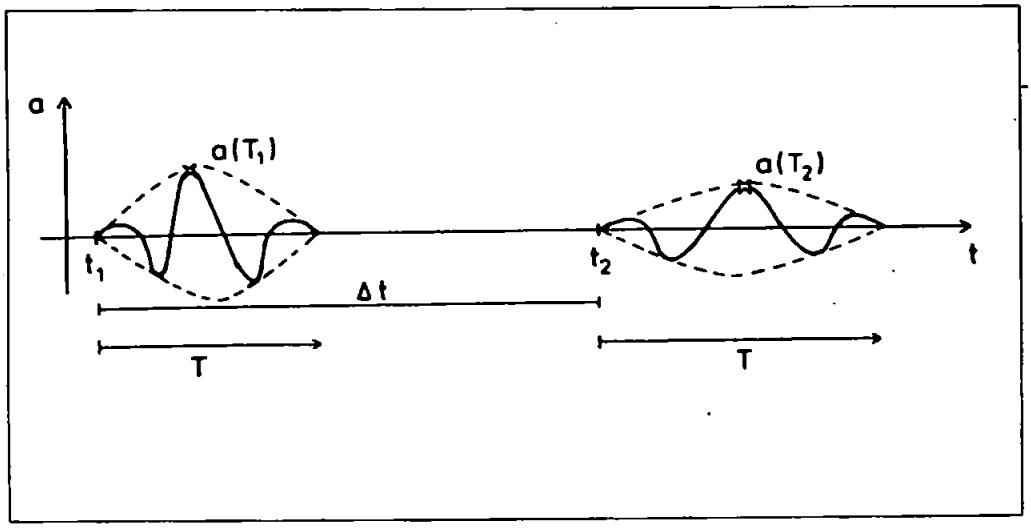

Figure 3.2
Diagram to illustrate the relationships between internal time T and the travel time difference between two events (after Tonn, 1989).

internal time for the reference event to the $a(T)$ and $\omega^i(T)$ at T/2 internal time for the later event. The first method attempts to overcome this by using only the maximum of $a(T)$ for both events as these should be at the same internal time for both events. The degree of phase distortion, due to absorption, and its relation to Q was investigated by Angeleri and Loinger (1984) and was discussed in Chapter 2. They showed the distortion of a synthetic zero-phase wavelet would lead to a shift of the central peak (nominally at T/2 internal time) after propagation through an absorbing earth model. The use of the maxima does require an estimate of the geometric factor (G) in the analysis. In the analysis of a VSP data set, Tonn (1991) found the maximum of the envelope to be generally superior to all other techniques currently available for Q estimation.

Computationally, the complex trace is easily determined using the Fast Fourier Transform (FFT). Firstly the (real) seismic trace is transformed to the frequency domain. Secondly the amplitudes for $\omega < 0$ are set to zero, and are doubled for $\omega > 0$. An inverse transform is then performed to form a complex trace. Alternatively the quadrature trace (90° out of phase with the real trace) can be determined using the Hilbert transform (Taner *et al.* 1979) in the time domain (in truncated form), which can then be combined with the real trace to form the complex trace.

3.4 Summary

The methods outlined in the discussion above yield an estimate of the quality factor, Q, made up of the contributions of intrinsic absorption and stratigraphic effects. Several methods have been used in absorption studies of marine seismic reflection data - specifically the risetime, spectral ratios, spectrum modelling and wavelet modelling techniques, the latter three being heavily dependent on Fourier techniques. Two further methods, the matching technique and complex trace analysis, are VSP methods and are not commonly used in marine seismic reflection studies. This chapter has shown for the

relevant techniques, the type of data windowing function is not important for practical purposes . As marine seismic data will have spectral notches due to variation in the geometry of the source and receiver set-up, fitting a best-fit line to spectral regression data is can be carried out using the median for minimising absolute deviations rather than the mean. Some form of spectral smoothing should be carried out in order to reduce the uncertainty of raw spectral estimates from the Fourier transform. In doing so, confidence limits may be established for the methods involving spectral ratios. The modelling methods attempt to parameterise the problem into two parameters, absorption and transit time, with the addition of dispersion in the case of wavelet modelling. With single-channel data, multiple coherence analysis can not be used to define noise levels within the observed spectra, but an estimation procedure has been proposed assuming that the noise is white and has a constant variance across the spectrum. This project investigates the absorption properties of the very near subsurface, down to depths of generally less than 80 m beneath the seabed. It is thus concerned with much smaller scales than most of the previous studies using marine reflection data (*c.f.* Jannsen *et al.*, 1985; Raikes and White, 1984). As the propagation paths are very short, the frequency range of interest is also much higher than that for 'deep' seismic investigations, being several hundred Hz to a few kHz rather than the 10 Hz to 60 Hz band used for deeper investigations (Raikes and White, 1984). The following chapter numerically evaluates the techniques that have been discussed above in the noise-free case and with the addition of random noise.

Chapter 4: A Single-Layer Dispersive Model to Assess the Effective Reliability of Techniques to Estimate Q

4.1 Introduction

Before any measurement of amplitude loss or spectral broadening of a seismic wave can be carried out, it is necessary to evaluate the reliability of the techniques that are to be used. A synthetic data set has been created to assess the reliability of techniques described in the previous chapter . A reference wavelet is synthetically absorbed through a single medium of constant velocity and finite thickness. Initially, the techniques are assessed in a noise-free case. The next stage is to introduce random noise into the system. Within real seismic data there will be correlatable and random noise. The simple model assumes no correlatable noise; random noise with increasing variance (relative to the variance of the wavelet signal) is introduced to examine the deterioration of the reliability of the derived estimates for the quality factor, Q.

4.2 Synthetic seismic trace construction

In order to evaluate the various numerical techniques, synthetic traces have been created based on equation 3(12). Initially, the Fourier Transform (512-point) of the impulse (or delta function) is calculated. As the impulse and its processed form are real (rather than complex) in the time domain, only the positive frequencies are required for processing (Press *et al.*, 1986). The complex spectrum is then scaled by the exponential term for absorption, and shifted by the exponential term for dispersion. The former is a function of frequency, travel-time and the quality factor, whilst the latter depends upon frequency, travel-time and the phase velocity. The resultant waveform is synthesised from the Fourier

components by an inverse Fast Fourier Transform (512-point).

The effects of varying Q and the travel time upon the input impulse are illustrated in Figures 4.1a-4.1c. The initial input impulse has an amplitude of 1000 (arbitary units) at t = 0.0 ms and a flat (white) frequency spectrum extending up to 10 kHz. The synthesised waveforms are computed at 10, 15, 20 and 25 ms of propagation. Four effects are visible. (i) The waveform broadens and is (ii) reduced in peak amplitude with increasing time. (iii) The initial slope or rise also becomes less steep with increasing time.(iv) Clearly the time difference between the initial disturbance (at the front of the wavelet) and the arrival time (distance divided by the phase velocity at the lowest resolvable frequency) also increases with increasing propagation time (*c.f.* 10 ms and 25 ms wavelets).

By increasing the quality factor (reducing the rate of intrinsic absorption) the decay of peak amplitude is reduced, less broadening takes place, and the initial slope remains steeper. Kjartannson (1979) derived scaling relationships for pulse propagation and showed that, for a given Q, the width or risetime of the pulse is exactly proportional to travel time. Futterman (1972) proposed a dispersion relation whereby the phase velocity is a function of Q; this is seen when comparing the wavelet at 25 ms for quality factors of 50, 75 and 100. An increase of absorption will lead to a greater time difference between the initial disturbance and the arrival time calculated for the phase velocity at the lowest frequency. If the dispersion relation is characteristic of real sediments, possible small errors could theoretically arise when measuring absorption, as all methods require a knowledge of the arrival time of a wavelet relative to some reference. However, even for very low Q sediments (*c.* Q = 30 for sands, Hamilton, 1972), combined with high frequencies (*e.g.* 3.5 kHz), and assuming a low-frequency cutoff of 39 Hz, the difference between the phase velocity at 1 kHz and 3.5 kHz is about 1.3 % .

4.3 Software Development

All of the software used within the scope of this project was written in Microsoft Fortran (v. 5.0) using an Intel 80486 (32-bit architecture microchip) - based personal computer. In

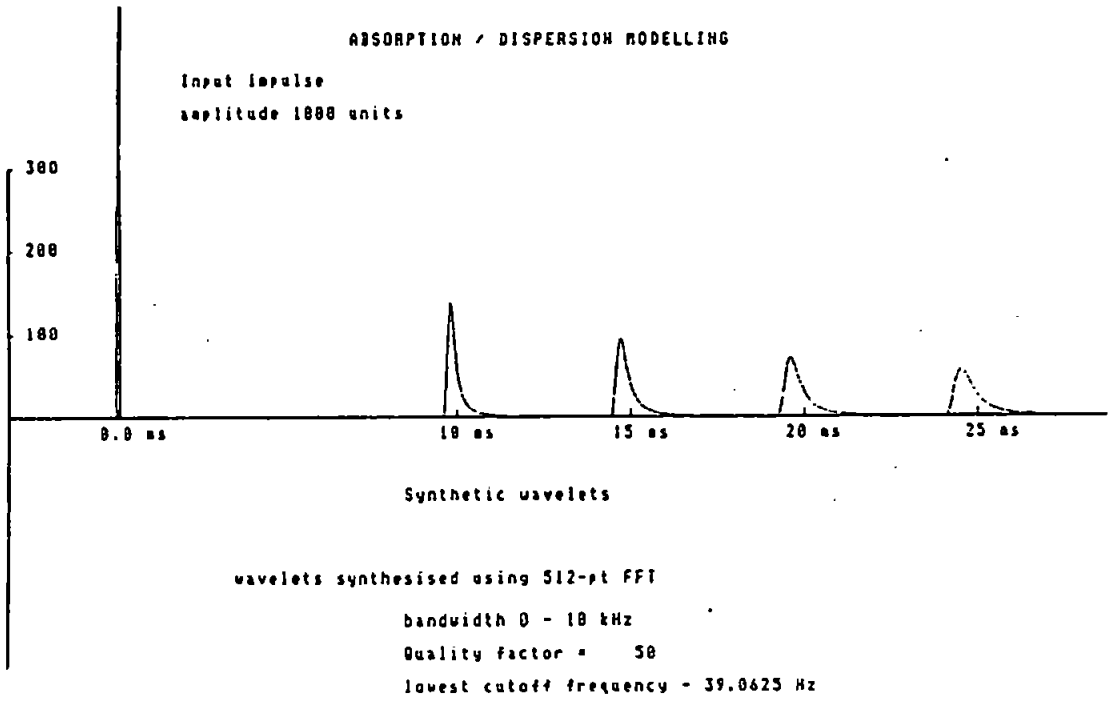

Figure 4.1a
Synthetic Absorbed and Dispersed Wavelets for $Q = 50$

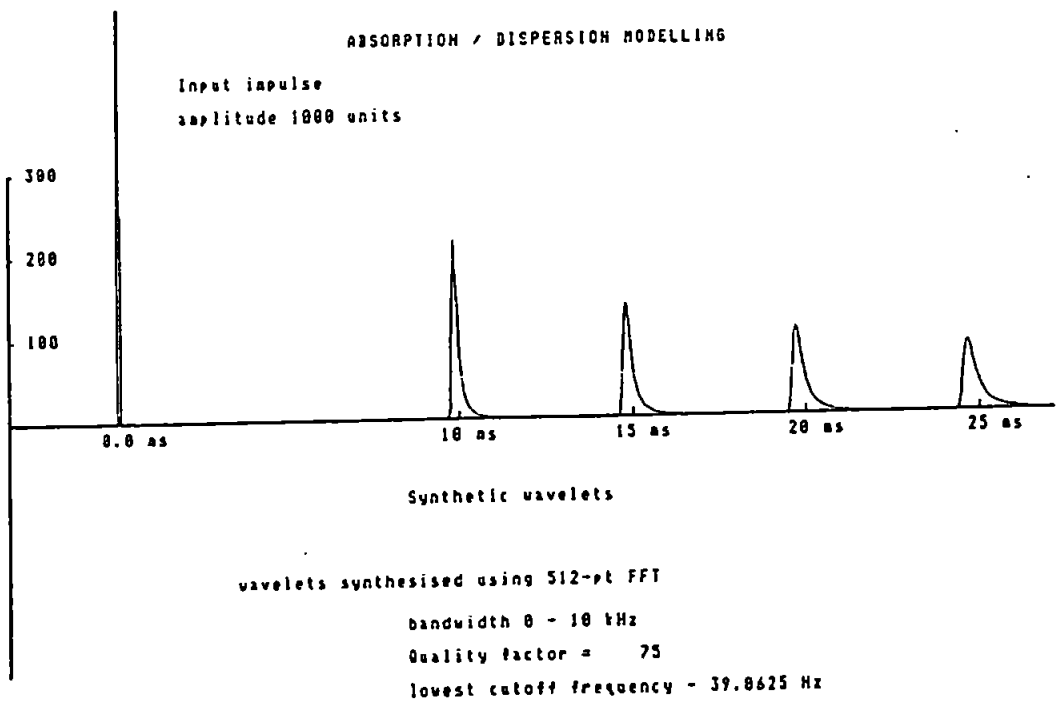

Figure 4.1b
Synthetic Absorbed and Dispersed Wavelets for $Q = 75$

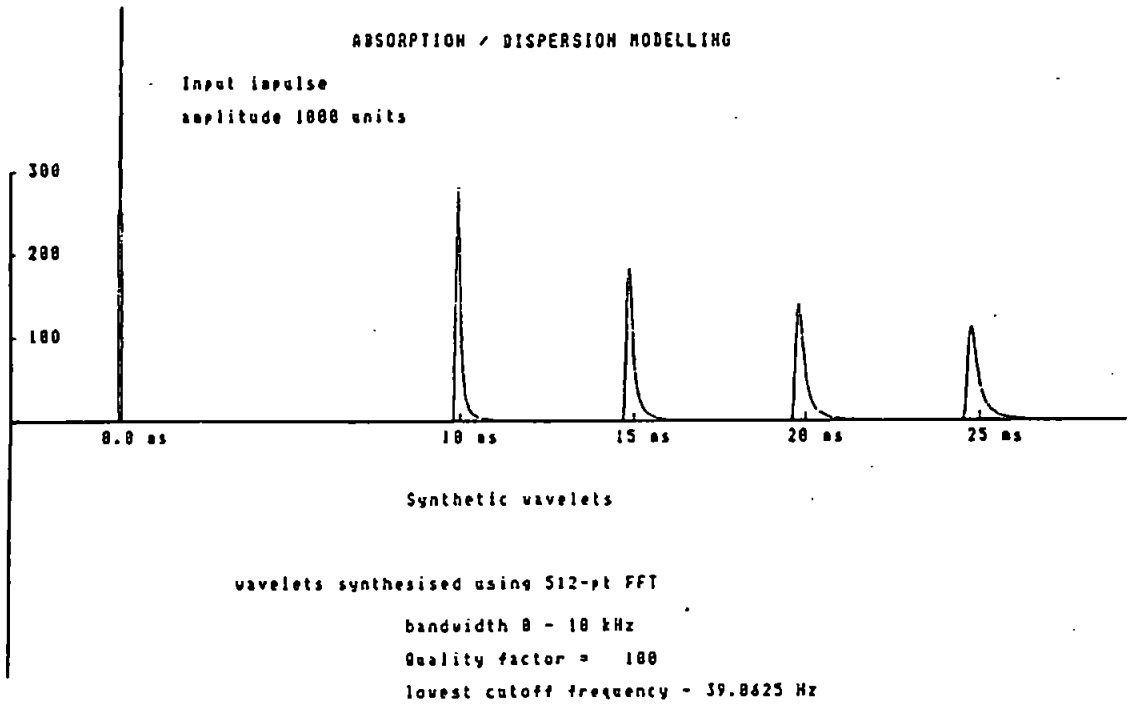

Figure 4.1c
Synthetic Absorbed and Dispersed Wavelets for $Q = 100$

addition, the interactive graphics computer programs contain elements of the Graphics Kernel System (GKS) standard (supplied by Graphics Software Systems). The latter provides subroutines to allow the creation and manipulation of graphic images embodied within a Fortran main program. In order to have sufficient resolution for graphics work, a Video Graphics Adaptor (VGA) standard colour monitor was used with a resolution of 1024 by 768 pixels. Both the Fortran implementation and the GKS graphics were run under the Microsoft MS-DOS (v. 6.0) operating system. The following sections describe and test the programs that were written to implement the numerical techniques discussed in the previous chapter.

4.3.1 Spectral Ratios Program

The mathematical basis for the spectral ratios technique was discussed in section 3.2.1. The program uses a graphically represented single seismic trace as the primary input data. By using a screen mouse, the user is prompted to select two windows of data from the trace (the seabed event plus a deeper reflector). Once selected, the windows (nominally 40 samples in length) are embedded within a 512-point array, prior to input into a Fast Fourier Transform subroutine. The amplitude spectra are then computed and plotted. The user then selects the natural logarithm plot of the spectral ratios vs. frequency. A frequency band within which Q is required is then chosen. Once selected, a straight line will be fitted to the data based on the criterion of minimising the absolute deviations (see 3.2.1.). A summary screen is output at the end of the program which contains the original seismic trace with the selected windows, the plotted amplitude spectra, the spectral ratios plot, the measured Q, time between events and mean absolute deviation values (m.a.d.) . In addition, the user is supplied with confidence limits for the spectral ratios, as well as the peak frequencies for both spectra. To assess the software in the case of no noise, three synthetic wavelets were used as the input for the program, illustrated in Figures 4.2a to 4.2c. The first shows a relatively low-absorption, low-dispersion example, with a theoretical wavelet derived with Q = 100 and Δt = 10 ms. The program derived a Q-estimate of Q = 97.9, from a Δt of 9.80, with m.a.d. = 0.00 (to 2 dec. places). An

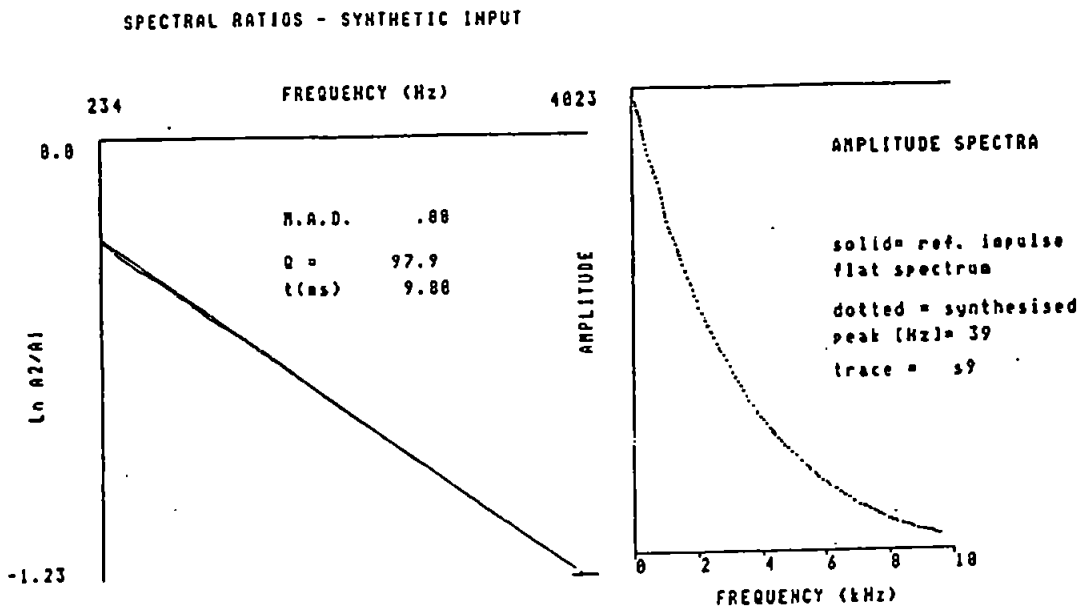

Figure 4.2a
Measurement of Q by spectral ratios method, synthetic noise-free wavelet ($Q = 100$, t = 10 ms).

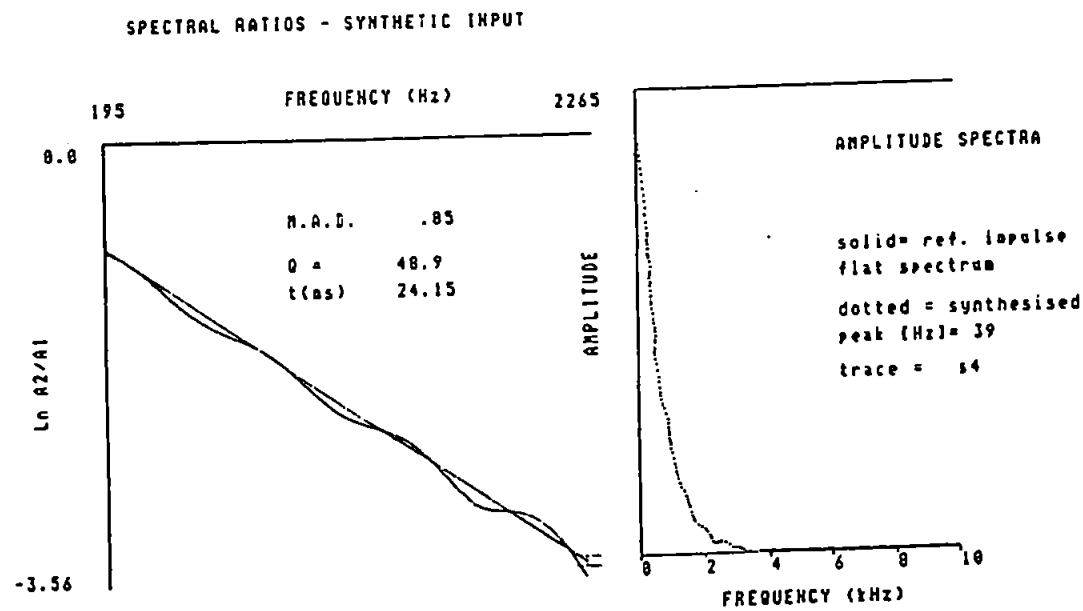

Figure 4.2c
Measurement of Q by spectral ratios method, synthetic noise-free wavelet ($Q = 50$ t = 25 ms).

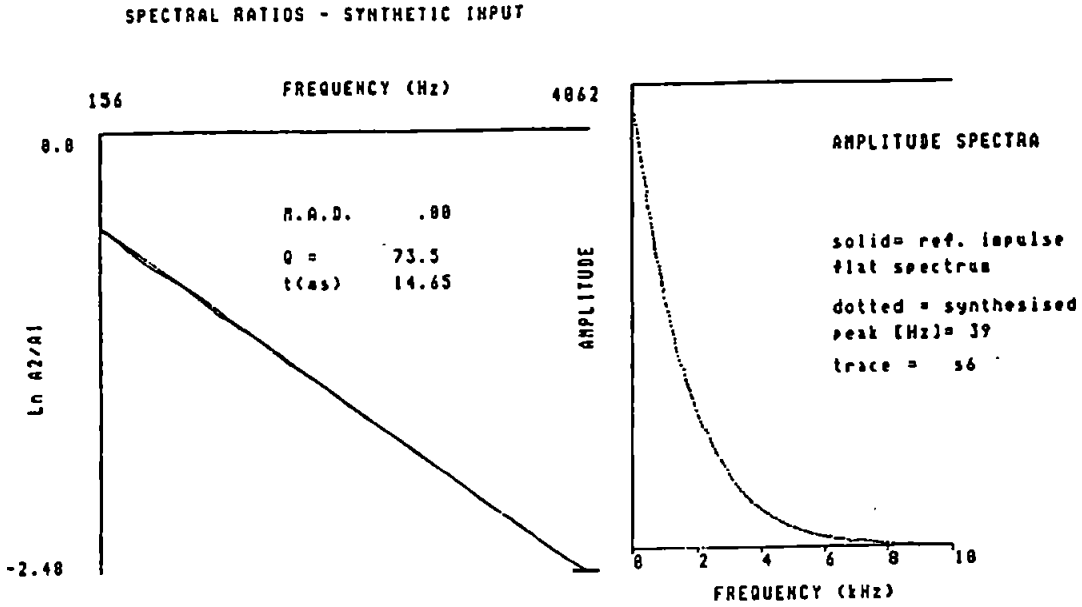

Figure 4.2*b*
Measurement of Q by spectral ratios method, synthetic noise-free wavelet ($Q = 75$, t = 15 ms).

intermediate absorption/dispersion wavelet (Q = 75, Δt = 15 ms) was then used as input. The program derived a Q-estimate of Q = 73.5 from a Δt of 14.65. Finally, a high absorption/dispersion wavelet (Q = 50, Δt = 25 ms) was used. For this example, a Q estimate of 48.9 was derived, from a Δt of 24.15 ms. The figures show that the software underestimates the true value of Q by about 2%. This is because the Δt estimate used in the calculation is taken from the time difference between the initial onsets of energy at the beginnings of the two events. This will always be less than the 'true' Δt because of the increasing phase velocity with frequency. A correction factor could be applied, for example, by multiplying the initial estimate of Δt by the factor $V(\omega)/V(o)$ (see eq. 3.(14)), at some frequency at which there is a certain amplitude within the spectrum. For example, in Figure 4.2c, the value of $V(\omega)/V(o)$ at 2 kHz is 1.0263, given a Q of 48.9, which yield a corrected Q of 50.19 (true Q = 50). For Figure 4.2a, a correction based upon $V(\omega)/V(o)$ at 8 kHz yields a corrected Q of 99.62 by the same method (true Q = 100). Yet another technique would be to use the time difference between peak amplitudes of the two events, or use some form of correlation function such as the covariance (Jannsen *et al.* 1985) or autocorrelation. However, as the changes between the estimates for Q are small, no correction factors were incorporated into the program. It is of note that any technique, without *a priori* knowledge of the true value of Δt, will overestimate the level of absorption (underestimate Q) if the reference event is impulsive and Δt has not been estimated more accurately by using, for example, wavelet modelling.

4.3.2. Risetime Method Program

The mathematical basis for the program was discussed in section 3.3.1. . The user is presented with a single trace on the monitor, and using a screen mouse, selects two events for processing. The time interval between the events is calculated by the autocorrelation of the trace. For computational speed and to accommodate long lags for deeper reflections, the trace was inserted into a 2048-point array prior to use of the Fast Fourier Transform. To calculate τ and τ_0 (see 3.3.1.) the initial slope of each event was searched for the

maximum amplitude difference between two successive samples. The peak amplitude divided by this value and multiplied by the sample interval gave τ for each event, in milliseconds. In the case of an impulsive input, τ_0 was taken to be zero. The software was tested on the same synthetic data as used in section 4.3.1. The results for theoretical wavelets generated with a quality factors of 50, 75 and 100 are summarised in table 4.1 below:

Table 4.1
Risetime measurement and Q determination from risetime method using synthetic wavelets

τ	Δt (est.)	Δt (true)	Q (est.)	Q (true)
0.10570	9.85	10.00	46.59	50.00
0.15498	14.75	15.00	47.58	50.00
0.19920	19.65	20.00	49.32	50.00
0.24683	24.55	25.00	49.72	50.00
0.08834	9.90	10.00	56.02	75.00
0.10423	14.85	15.00	71.23	75.00
0.13815	19.75	20.00	71.47	75.00
0.17367	24.70	25.00	71.11	75.00
0.08884	9.95	10.00	55.99	100.00
0.08259	14.90	15.00	90.20	100.00
0.10378	19.85	20.00	95.63	100.00
0.12702	24.75	25.00	97.41	100.00

Clearly, under certain circumstances, there are substantial differences between the estimated and the underlying true values of the quality factor. Table 4.1 illustrates the effects of two factors. The first is the error in the estimation of the arrival time of the second event. For short Δt, the theoretical wavelets are sharp, the autocorrelation function will, therefore, yield a reasonably accurate Δt estimate. For long Δt, the dispersion effect shortens the time to the peak amplitude, Δt will be underestimated, and so, therefore will Q. The second factor is error within the synthetic wavelet amplitudes. With short Δt (*e.g.*

10 ms), the value of τ will approach the sample interval (for example τ = 0.08834 ms for Q = 75, Δt = 10 ms, with a sample interval of 0.05 ms). As the wavelets were constructed using a finite-length discrete Fourier Transform (not the more accurate continuous Fourier integrals), there will be errors in the constructed wavelets, due to a limited number of discrete frequency components. For the very sharpest of pulses, the discrete inverse transform may not be able to exactly reproduce the absorbing and dispersive effects that can be exactly expressed in a continuous or integral form with only three or four time samples containing the major amplitudes. Spectral leakage in the frequency domain will cause amplitude errors in the time domain, which will entail that a) the peak amplitude will be in error, and b) the maximum gradient of the initial rise will be in error. This can be seen to be analogous with under-sampling of the data, in the sense that the maximum gradient of the initial rise will always be smaller with fewer time samples to make up the initial rise.

For Q = 50, the risetime method measured the correct Q to within 10% for a given Δt. The errors in t for longer Δt are more than offset by the better estimation of τ due to the broader, and therefore better sampled initial rise. This is seen in the convergence of the Q estimates towards the true value of Q = 50 (49.72 at 25 ms).

For Q = 75, the initial estimate for Q at Δt = 10 ms is 56.02, due to the second effect. However, with the broadening of the wavelet at Δt =15 ms and 20 ms, the estimates improve dramatically to Q = 71.23 and Q = 71.47 respectively. However, by 25 ms the dispersion effects cause an underestimation of Δt to reduce the Q estimate to 71.11.

For Q = 100, the initial estimate is again too low by a considerable degree (Q = 55.99). The synthetic wavelet has a calculated τ of 0.08884 ms, which is longer than τ calculated for the wavelet at 15 ms, when it should actually be shorter. As with the above case, this is due to poor reproduction of dispersion and absorption effects by the use of discrete functions. For Δt = 20 ms and 25 ms, the Q estimates are close to the real value of 100 because the Δt calculated by autocorrelation are accurate, and the wavelets are sufficiently broad enough to not suffer from the second effect, yielding estimates of Q = 95.63 and Q = 97.41 respectively.

The risetime method, therefore, will be successful only if there are sufficient

samples to be able to define a maximum gradient of the initial rise (for both wavelets, with the exceptional being an impulsive reference wavelet) and if a combination of high absorption (low Q) and long travel time (high dispersion) do not cause large errors in the estimation of Δt. This is of course assuming a noise free case.

4.3.3 Wavelet Modelling Program

Wavelet modelling attempts to model both of the effects of absorption and dispersion. The software was again tested on the noise-free synthetic data set used in the previous examples. The user is presented with a single seismic trace on the screen; the software has already calculated an initial arrival time estimate for the later event from a 2048-point autocorrelation, using a Fast Fourier Transform. The user is prompted for a minimum theoretical Q to start at, and the number of steps, or increments in Q to take, each increment being an increase of 1. The program will generate M times N theoretical wavelets, where M is the number of increments of Q, and N is the number of increments of Δt. In this case N was the value of Δt calculated from the autocorrelation, minus 0.5 ms, and then incremented twenty times in steps equivalent to the sampling interval of the data, 0.05 ms, *i.e.* N = 20. The user is prompted to pick the upper time limit to the reference pulse using a mouse; this is then embodied within a 512-point FFT prior to the application of the effects of absorption and dispersion. The resultant complex spectrum is subject to a 512-point inverse FFT back to the time domain. This procedure is repeated (MxN)-1 times. After every resultant theoretical wavelet, the amplitudes of the theoretical wavelet and the actual input wavelet are compared (by the L_2-norm) over the interval of the wavelet, which was nominally set at 60 time samples. For any given value of Q, the minumum of this function was stored. At the end of the processing sequence, the minimum of these minima for the range of possible Q values was calculated and presented as the optimum Q estimate. A similar process was used to obtain the optimum Δt. These two values were then used to construct the optimum-fit wavelet, which is presented on the screen along with the estimates of Q, Δt, and the original input trace. For the noise-free synthetic data set (which includes the effects of dispersion), the results of using the wavelet

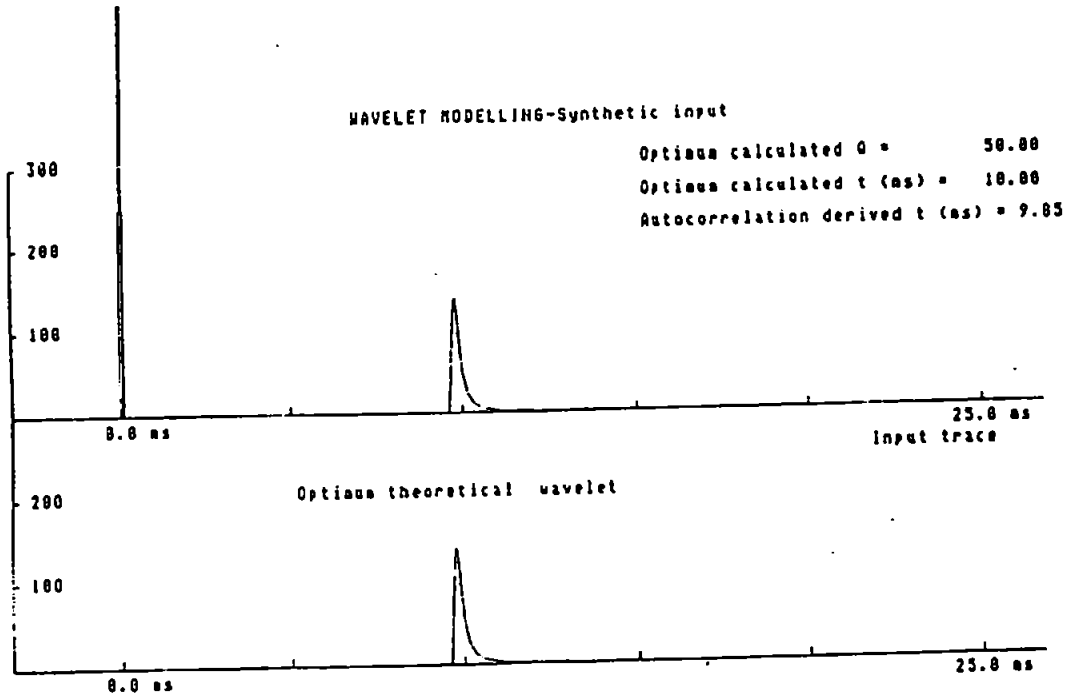

Figure 4.3a
Results of Wavelet Modelling of Synthetic Wavelets
Using $Q = 50$, t = 10 ms, noise free.

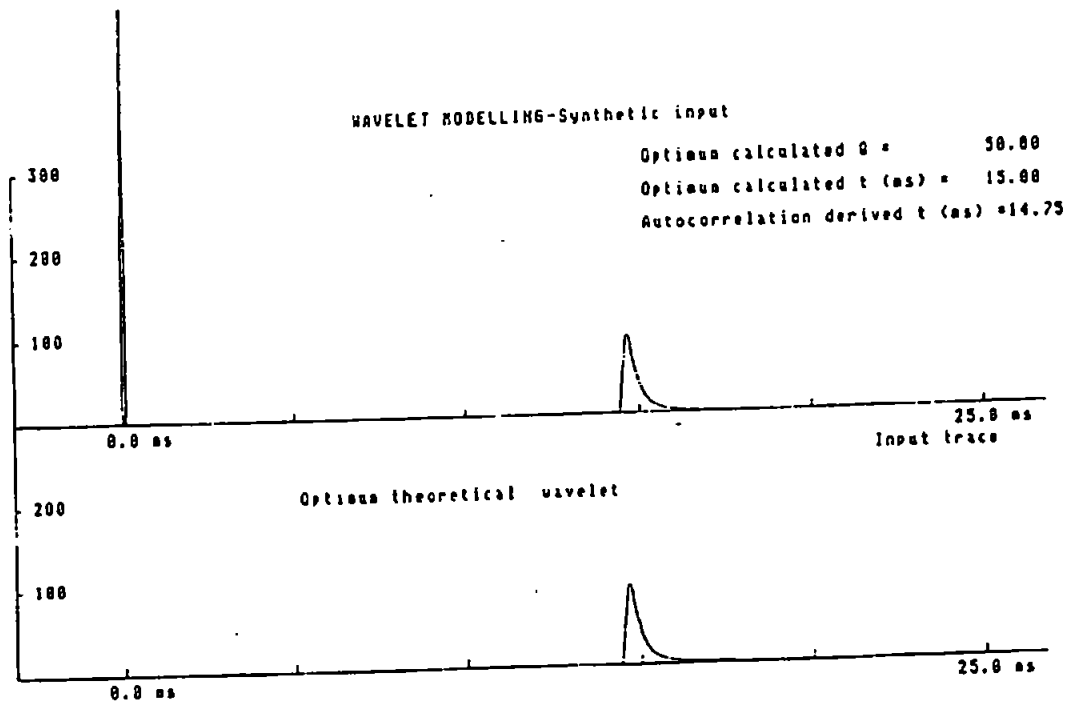

Figure 4.3b
Results of Wavelet Modelling of Synthetic Wavelets
Using Q = 50 , t = 15 ms, noise free

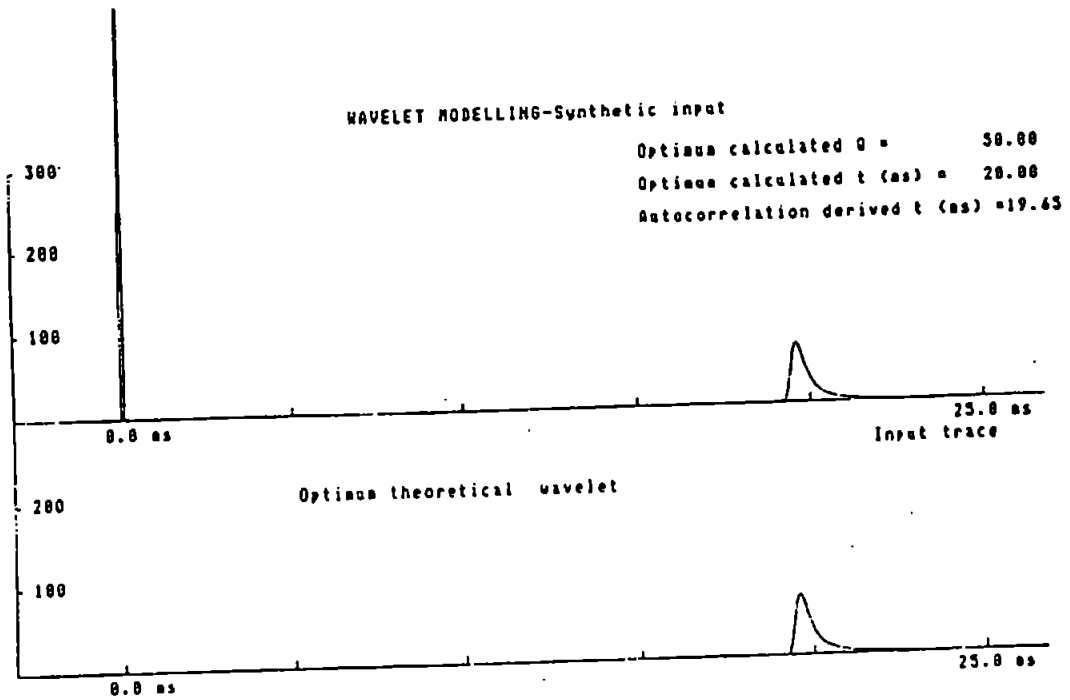

Figure 4.3c
Results of Wavelet Modelling of Synthetic Wavelets
Using Q = 50 , t = 20 ms, noise free

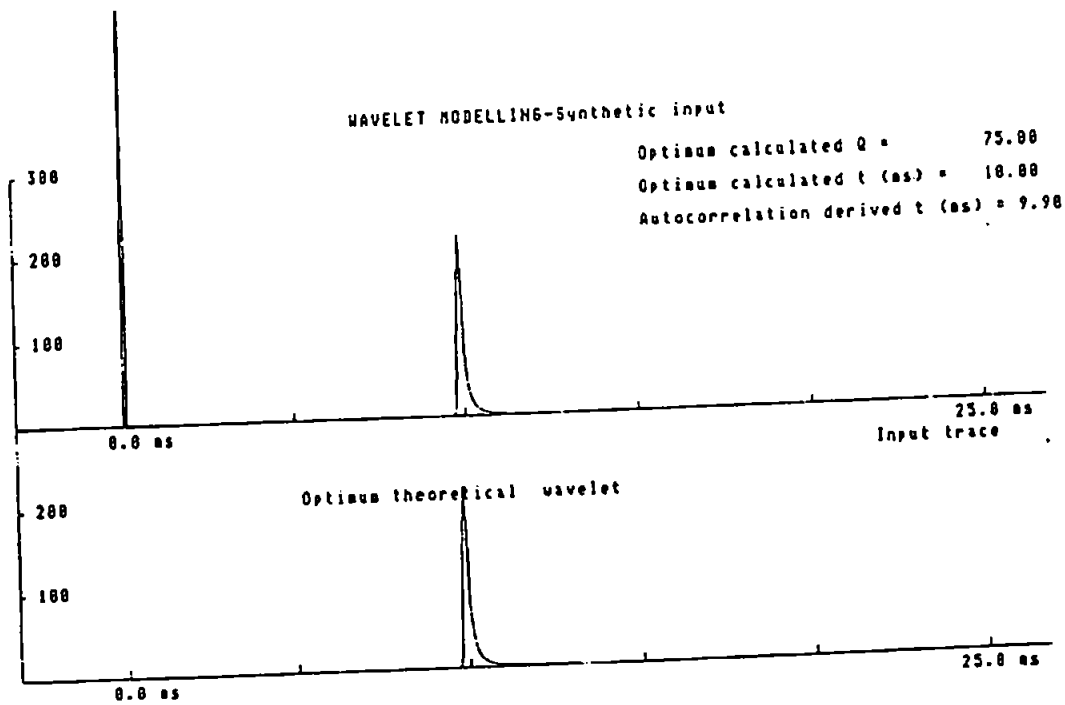

Figure 4.3d
Results of Wavelet Modelling of Synthetic Wavelets
Using Q = 75 , t = 10 ms, noise free

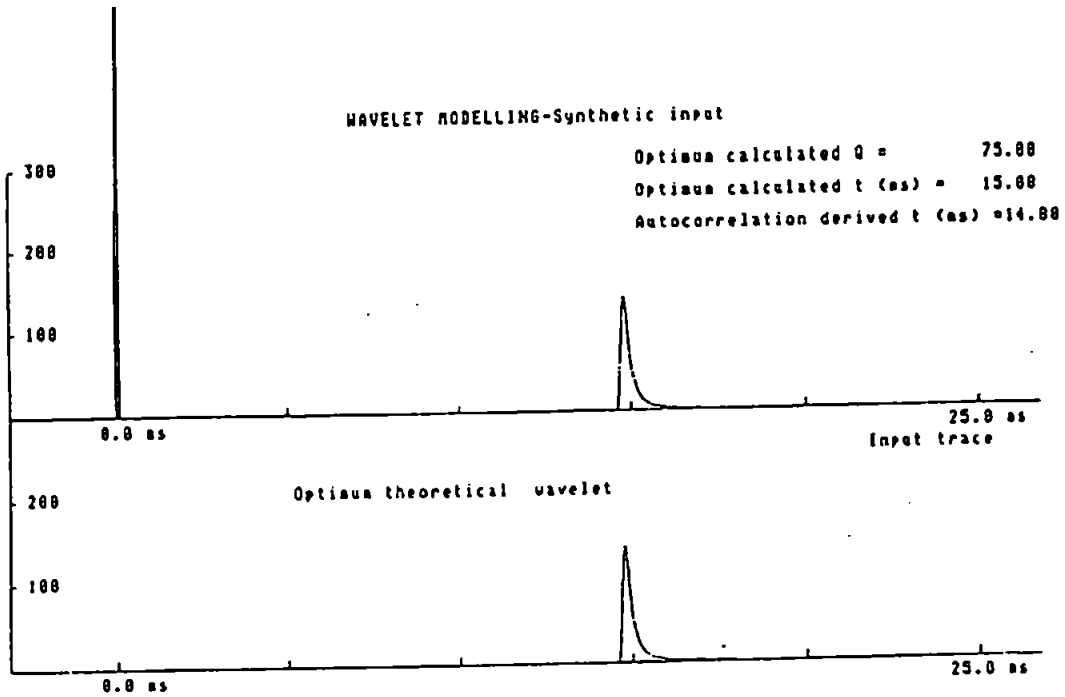

Figure 4.3e
Results of Wavelet Modelling of Synthetic Wavelets
Using Q = 75 , t = 15 ms, noise free

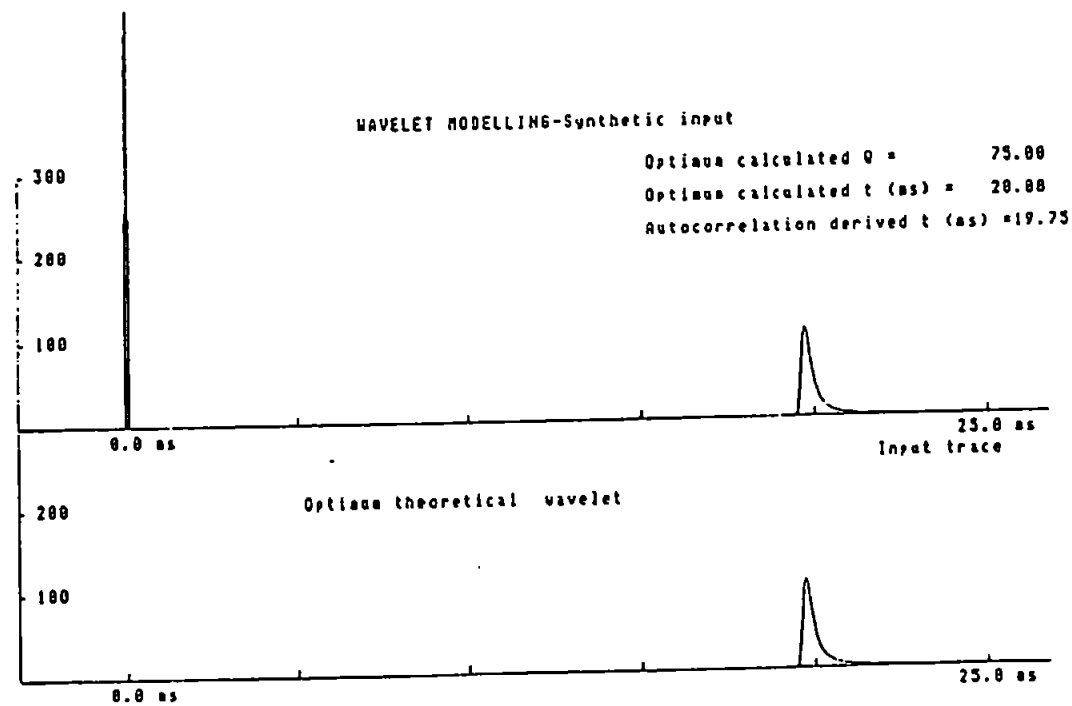

Figure 4.3f
Results of Wavelet Modelling of Synthetic Wavelets
Using Q = 75 , t = 20 ms, noise free

modelling software should be, and were, virtually error-free. The program was tested for Q = 50 and Q = 75 over Δt ranging from 10 ms to 20 ms. Figures 4.3a to 4.3f show the optimum Q and Δt estimates, along with the optimum theoretical wavelets. The derived wavelets are indentical to the theoretical wavelets in every case.

4.3.4 Spectrum Modelling Program

As was explained in the previous chapter, spectrum modelling is a by-product of wavelet modelling, without the phase information. The aim of the method is to fit a theoretical amplitude spectrum to an observed spectrum using known values of angular frequency, Q and Δt. Before any consideration of software, a potentially serious problem arises out of the use of discrete Fourier Transforms. Consider the following case. A reflection event, being part of a seismic trace, is windowed; the window being 64 time samples in length. A Fast Fourier Transform is then applied to yield the complex spectrum. If an inverse FFT is now applied to the complex spectrum and the result normalised by an algorithmn-dependent factor, (in this current work this factor is $1/n$, where n is the number of non-zero discrete frequencies within the complex spectrum), then the result will be equal to the original data set. However, in the study of the spectral characteristics of seismic events, it is commonplace to put a finite-length window of data into a much longer window. This is done for two reasons. Firstly, the effects of terminating large amplitudes at either end of a short window leads to spurious amplitudes at certain frequencies in the frequency domain subsequent to transformation. This is because the Fourier Transform of the rectangular window function has quite high amplitudes at high frequencies, caused by the abrupt terminations of the function. By the embodiment of the short selected window into a much longer, zero-amplitude window, these effects are minimised. The second reason for using a longer window is to achieve a greater degree of spectral resolution. For a real time series (no imaginary component), of length N, the FFT will yield a complex spectrum consisting of N/2 discrete non-zero frequencies. Obviously, the longer N is, the greater will be the spectral resolution (not considering the robustness of each spectral estimate). This is

particularly important when using bandwidth-limited sources; for spectral methods, as many estimates as possible within the effective bandwidth are desirable. The following describes the practical problems of this procedure. Consider the case of the embodiment of the short window within the longer window. If an FFT is performed on the data of length N, the complex spectrum of the data will be the result. As before, if we now apply the inverse FFT, the original N data will be obtained. However, if after the initial transformation, an operation is performed on the complex spectrum, (for example multiplication by the exponential absorption term), and the inverse transform is applied, the result will be close to what might be predicted from a continuous form of the process. Whereas the original long window will have had zero amplitudes before and after the embedded short window, the resultant data set will have non-zero amplitudes 'noise' in these places, even given the fact that the process itself may extend the length of the data in the short window in some way. The cause of the 'noise' can again be found in the use of discrete transforms; although the process is applied at discrete frequencies, the initial amplitudes at those frequencies are only representative of a band of frequencies.This is the situation that occurs when forming the type of synthetic data set which encompasses absorption and dispersion effects on a discrete-frequency complex spectrum. For example in Figure 4.1a, each of the theoretical wavelets is represented by only 60 time samples of the result of a 512-point inverse FFT. The other 452 time samples will be small, but non-zero. If we now use the synthetic data set and form a 60-point window of one of the wavelets, pad it with zeros to a 512-point transform, and obtain the complex spectrum and then the amplitude spectrum, it cannot yield the 'true' spectrum which reflects the process that formed the wavelet. Spectrum modelling is a method which will clearly suffer from this subtle effect. The spectrum modelling program was originally designed along the lines of the previous program, in that an initial guess at the arrival time Δt of the second wavelet is obtained via autocorrelation (FFT method), and synthetic spectra are then calculated from different values of Q and Δt, based on the real reference spectrum. The best fit of the theoretical to the observed spectrum yields an estimate of optimal Q and optimal Δt. The spectrum modelling software estimated Q and Δt to within a few percent of the true values,

but not exactly, due to an erroneous estimation of the true spectrum. In order to refine the technique, a better method of obtaining Δt should first be used. In this case a more robust Δt estimate is available from the wavelet modelling technique. If the spectrum modelling software has *a priori* knowledge of Δt, then the program will select the correct optimum Q from the synthetic data set. The synthetic spectra used to form the tables were compared using the lower 64 frequencies of a 256-frequency complex spectrum. The working version of the software presents the user with a single seismic trace. The user interactively picks two reflection events. The amplitude spectra of both events are computed, with the earlier reflection acting as a reference spectrum for the generation of synthetic spectra. The user picks a minimum value and a maximum value for Q, and is prompted for a value for Δt which in this case will be obtained from wavelet modelling. An optimum fit spectrum is computed and plotted with the real spectrum and the spectrum of the reference wavelet (which will usually be the seabed), along with the optimal estimated value for Q. In addition, the function which acts as the comparison between actual and computed synthetic spectra (the delta function) is also plotted. Figures 4.4a to 4.4d show the results of using the spectrum modelling software on the synthetic data set discussed earlier in the chapter. Four representative cases were tested; 1)Q = 75, Δt=10; 2)Q = 75, Δt = 15; 3)Q = 50, Δt = 10; 4)Q=50, Δt = 25. The true values for Q were obtained in all the cases.

In summary, in the noise-free case, the spectrum modelling technique appears inferior to the wavelet modelling technique in two respects. Firstly it does not provide a consistent and independent method of estimating the true Δt. Secondly, it suffers from windowing effects more than the wavelet modelling technique, in that exactly the same window length (60 time samples) was used a) to compare real and theoretical waveforms in wavelet modelling and b) to generate the real and synthetic spectra in spectrum modelling. However, in the case of a pre-known Δt the spectrum modelling software yields the correct Q in all noise-free synthetic cases.

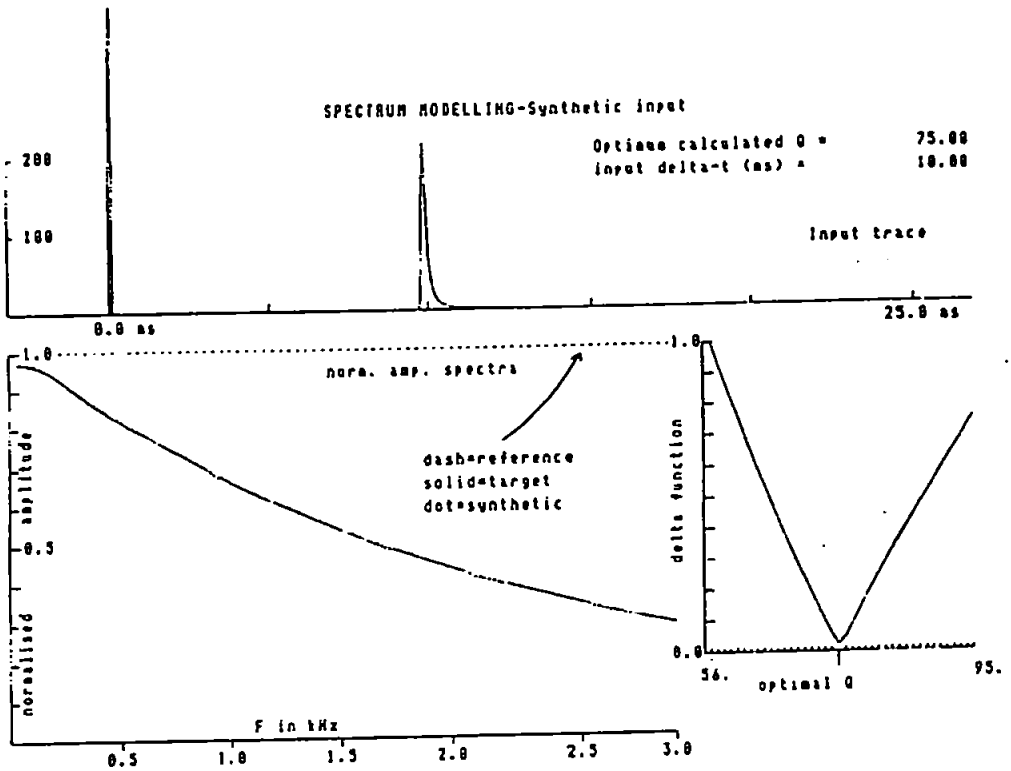

Figure 4.4a
Measurement of Q by spectrum modelling method, synthetic noise-free wavelet (Q = 75, t = 10 ms)

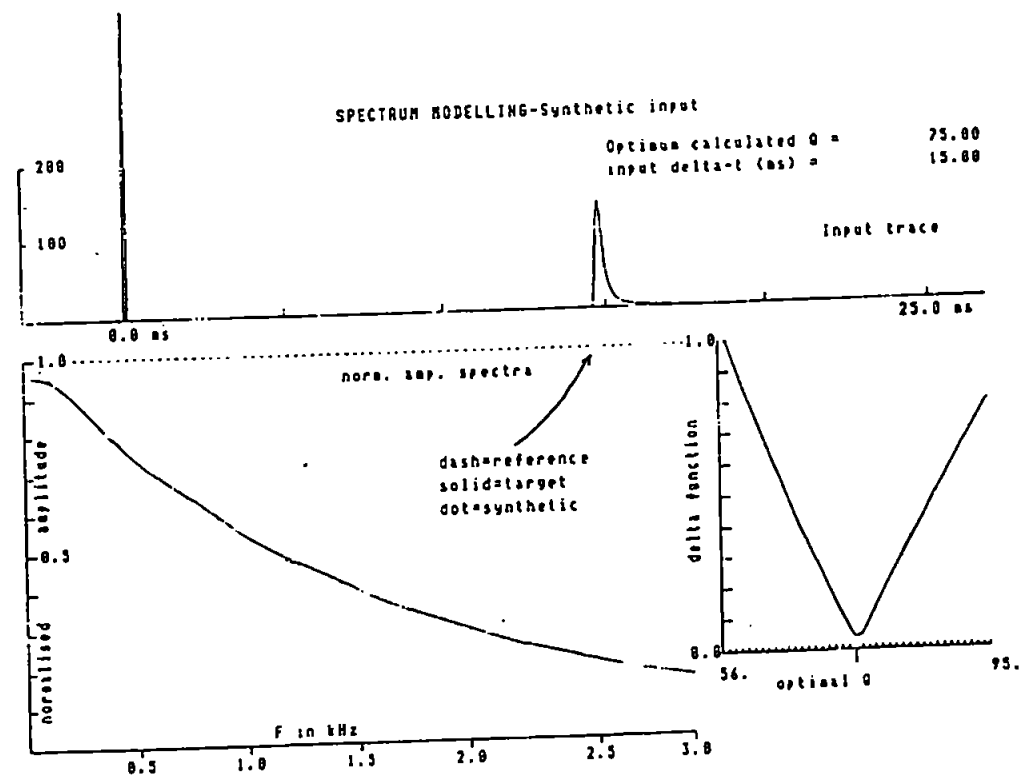

Figure 4.4b
Measurement of Q by spectrum modelling method, synthetic noise-free wavelet (Q = 75, t = 15 ms)

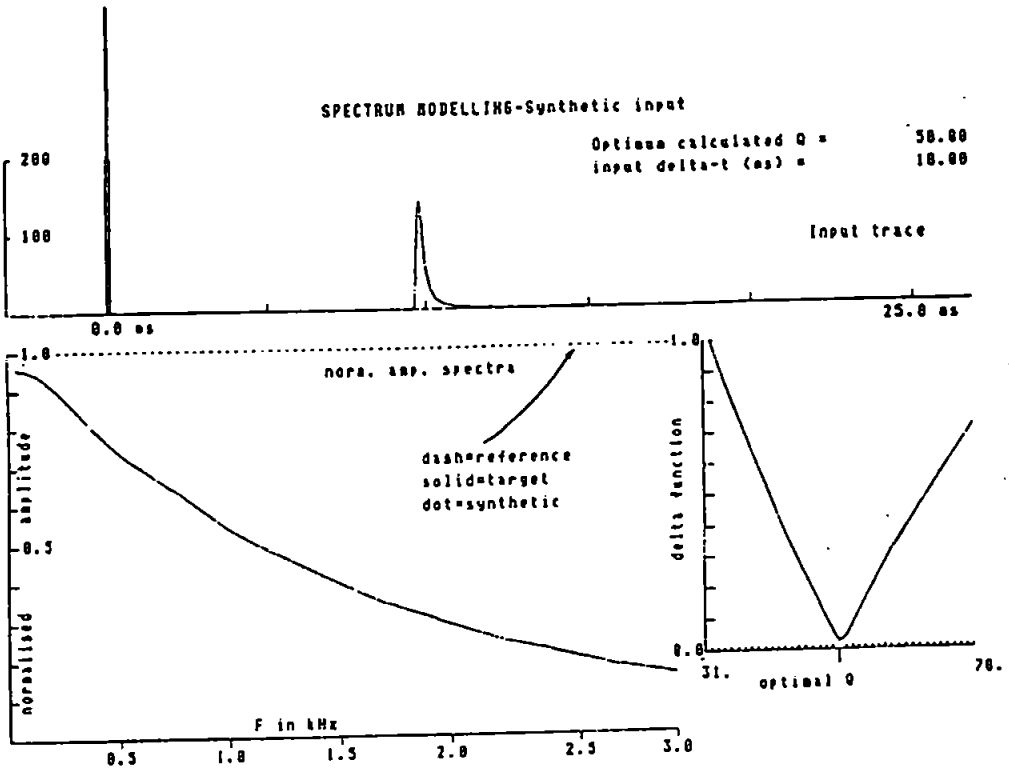

Figure 4.4c
Measurement of Q by spectrum modelling method, synthetic noise-free wavelet (Q = 50, t = 10 ms)

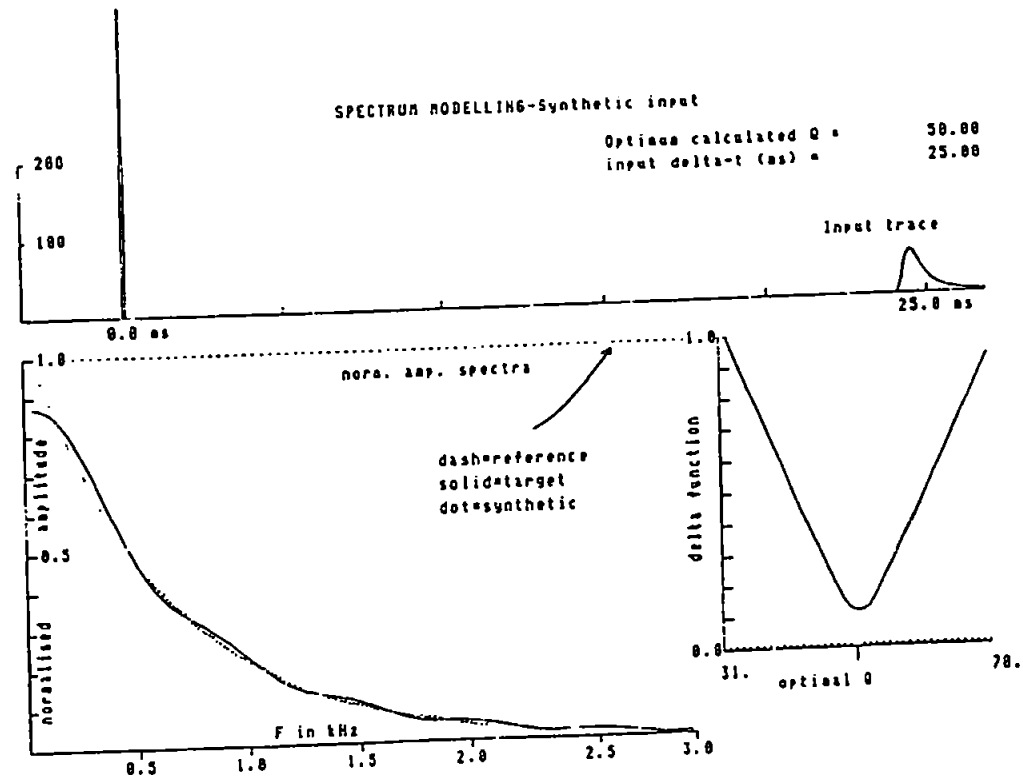

Figure 4.4d
Measurement of Q by spectrum modelling method, synthetic noise-free wavelet (Q = 50, t = 25 ms)

4.3.5 Complex trace analysis program

The definitions of instantaneous frequency, instantaneous phase, amplitude envelope, complex and quadrature trace were presented in the previous chapter. The first computational procedure is to calculate the complex trace from the real trace (the latter being the seismic trace). The input traces were the noise-free synthetic traces used to assess the other numerical techniques throughout this chapter. Two possible methods are available to calculate the complex trace. Firstly, a time-domain approach may be taken, whereby the quadrature trace (the imaginary component of the complex trace) may be calculated as a convolution using a time domain operator via the Hilbert Transform (see Taner *et al.*, 1979). An equivalent, and computationally more efficient method is to carry out the procedure in the frequency domain. Providing the input trace is real and not complex, the Fast Fourier Transform may be used to generate the complex spectrum of the input trace; by doubling the real and imaginary values of this spectrum, the amplitude spectrum is doubled whilst the phase at each frequency component remains unchanged. An inverse FFT , after normalisation, will yield the real and the quadrature trace at each time sample as the real and imaginary components of the resultant complex time function (complex trace). The latter method was used in this instance. The second step is to obtain the amplitude envelope at each time sample by calculating the modulus of the complex trace. The third step is to obtain the instantaneous phase at each time sample by calculating the arctangent of the real component divided by the imaginary component of the complex trace. (The real time function is equivalent to the product of the cosine of the phase and the amplitude envelope, the quadrature similarly using the sine of the phase). The intrinsic function 'ATAN' (in Fortran 77) calculates the arctangent of the quotient of two arguments (in this case the real and quadrature traces) and yields an answer (principle value) in the range $-\pi$ to $+\pi$ (in radians). Clearly this presents a problem. The instantaneous frequency is defined as the rate of change of the phase with respect to time. Under this definition, the phase must be continuous and not contain jumps once phase values values exceed π in any direction. For the synthetic data set the phase calculation is simplified because the theoretical time-domain waveforms start from near-zero amplitude at early times, build to a

peak amplitude and end at near-zero amplitudes at later times. Accordingly, during the interval of non-zero amplitudes, the absolute value of the phase will not exceed π and will, therefore, be continuous. The instantaneous frequency must now be calculated as the first derivative of the instantaneous phase with respect to time. There are esssentially two methods for calculating the first derivative of the phase. Firstly the derivative can be expressed in terms of the real and quadrature traces and their first derivatives, which follows from the definition of the phase from the previous chapter:

$$\gamma(t) = \frac{f(t).\frac{df^*(t)}{dt} - f^*(t).\frac{df(t)}{dt}}{f^2(t) + f^{*2}(t)} \quad \ldots\ldots\ldots 4(1)$$

where $\gamma(t)$ is the phase in radians, $f(t)$ is the real trace and $f^*(t)$ is the imaginary trace. This is the approach adopted by Taner *et al.* (1979). However it has the disadvantage of requiring that two derivatives must be calculated in order to derive one. An alternative method is to calculate the first derivative of the phase directly. Again, there are alternate ways to evaluate the derivative of a time function whose form cannot be expressed analytically. The first is to transform the data to the frequency domain via an FFT, to multiply the complex spectrum by $j\omega$ (the derivative theorem), and then to use an inverse FFT to obtain the first derivative of the function. The use of this method is complicated by the effects of using different lengths of transform and end-effects, as it is a convolution, albeit carried out in the frequency domain. For this project an alternative and more robust method to find the first derivative of the phase is achieved using polynomials . In detail, five time samples from the phase function are windowed, with the central sample being at the value of (t) at which the instantaneous frequency is required. The five samples are then used to fit a 4^{th} order polynomial (P^4) through the data, where:

$$P^4 = a + c_1x + c_2x^2 + c_3x^3 + c_4x^4 \quad \ldots\ldots\ldots 4(2)$$

Once the polynomial is calculated, the coefficients c_n can be used to calculate the value of the polynomial at a required *(t)*, along with the first derivative, *dP(t)/dt*. This method is elegant in that it requires only a few data points and leads to very small errors between the computed polynomial and the actual value of the instantaneous phase at any given *(t)*. This method is particularly useful in the instance of only using relatively short sections of the seismic trace with a few time samples. It would, however, be unwieldy when used with a complete trace, or series of traces, where the number of phase jumps at the limit of the principle value of the phase would be considerable. This would be the case when the seismic attributes might be used over the whole of a seismic section for qualitative or semi-quantative interpretation. In dealing with short wavelets with few zero-crossings, the method is both efficient and accurate.

To illustrate the accuracy of the instantaneous frequency measurement, the instantaneous phase and the polynomial representation of the phase is given below from part of the theoretical wavelet generated by using $Q = 50$, and $\Delta t = 15$ ms:

computed polynomial from eq. 4(2):

$$P(t) = \{1.611395 - 0.3003238t + 0.00185766t^2 - 0.004333512t^3 + 0.0007919919t^4\}$$

$t = (1,2,3,4,5)$

Table 4.2
Comparison of calculated polynomial and instantaneous phase for theoretical wavelet ($Q = 50$, $\Delta t = 15$ ms)

time	**calculated phase** (radians)	**polynomial value** (radians)
14.55	1.309387	1.309387
14.60	0.9961814	0.9961813
14.65	0.6742887	0.6742887
14.70	0.3652272	0.3652272
14.75	0.1095232	0.1095232

computed dP(t)/dt = -0.3206475 radians/time sample (t=14.65)

As can be seen, a fourth order polynomial, fits the phase data down to a minimum of five decimal places, which is of sufficient accuracy for this type of work. The software thus runs through the following steps:

1. Calculation of the complex trace using the FFT to emulate a Hilbert Transform.

2. Calculation of the amplitude envelope of the complex trace.

3. Calculation of the instantaneous phase of the complex trace.

4. Unwrapping of the phase in order that it is continuous beyond $\pm\pi$.

5. Selection of time sample at which instantaneous frequency is required.

6. Calculation of fourth-order polynomial around the selected time sample, and computation of the angular instantaneous frequency in radians/time sample.

The values obtained from the above procedure can then be used by the 'maximum method' to calculate Q using seismic attributes (Engelhard *et al.* 1986). The quality factor ,Q, may be calculated as:

$$Q = \frac{-\omega^{i}(T)\Delta t}{2\Delta Ln(\frac{A(T)}{G})} \cdot \frac{1}{dt} \quad \ldots\ldots\ldots 4(3)$$

where: ω^{i} is the angular instantaneous frequency, Δt is the time difference between maxima of the analytical envelope for the two events, $\Delta Ln(x)$ is the difference between amplitudes of amplitude envelope maxima, G is the geometric factor and dt is the sample interval (in secs.) of the data

For the synthetic data set, plane waves are assumed, therefore the geometric factor

will be unity. To fully assess the reliability of this method in the noise-free case, Q was estimated initially for an absorbed input sinusoid and secondly for the 12 synthetic traces that have been used to assess other methods. In the first case, a series of theoretical absorbed and dispsersed sinusoidal wavelets were generated.

Figure 4.5a shows an input sinusoid at t = 0.0 ms, along with the quadrature trace, amplitude envelope and instantaneous phase (with $\pm\pi$ limits shown). The quadrature trace is 90 degrees out of phase with the real trace, but is plotted in the real plane for convenience. Using the procedure outlined above, the maximum of the envelope was calculated as 120.022 amplitude units, whilst the instantaneous frequency at that point is 2239.7 Hz (using a arbitary sampling rate of 20 kHz). Figure 4.5b shows the same sinusoidal wavelet after a theoretical (plane-wave) progagation time of 20 ms, through a medium with a quality factor of Q = 75. The maximum of the amplitude envelope is now reduced to 25.097 amplitude units whilst the instantaneous frequency has dropped to 1505.6 Hz. Using a propagation time of 19.9 ms between the maxima of the envelope, the estimated quality factor using this method was calculated as Q = 74.81, an error of less than 0.25 % . Figures 4.5c and 4.5d illustrate the use of the method using the same input sinusoid and propagation time, but with quality factors of Q = 50 and Q = 100 respectively. Again, the results are close enough (Q = 49.74, Q = 99.56) to suggest that for a sinusoidal input wavelet, the maximum method using complex trace analysis will yield an accurate estimate of the quality factor Q. By definition, the sinusoidal input has a narrow bandwidth; in a discrete complex Fourier spectrum, the spectrum would only contain amplitudes at a single frequency, assuming the wavelet has a zero mean amplitude. The effect of 'dispersing' this single frequency is to force a time shift on the wavelet, whilst leaving the shape of most of the wavelet intact for the first half-cycle. In other words the effects of dispersion on the maximum method are not tested by using a sinusoidal input pulse of a very narrow bandwidth.

The method was then applied to the synthetic wavelets used throughout this chapter. In this case, each of the wavelets is the result of an input impulse at t = 0.0 ms theoretically propagated using various Δt and Q. The bandwidth of each wavelet, therefore

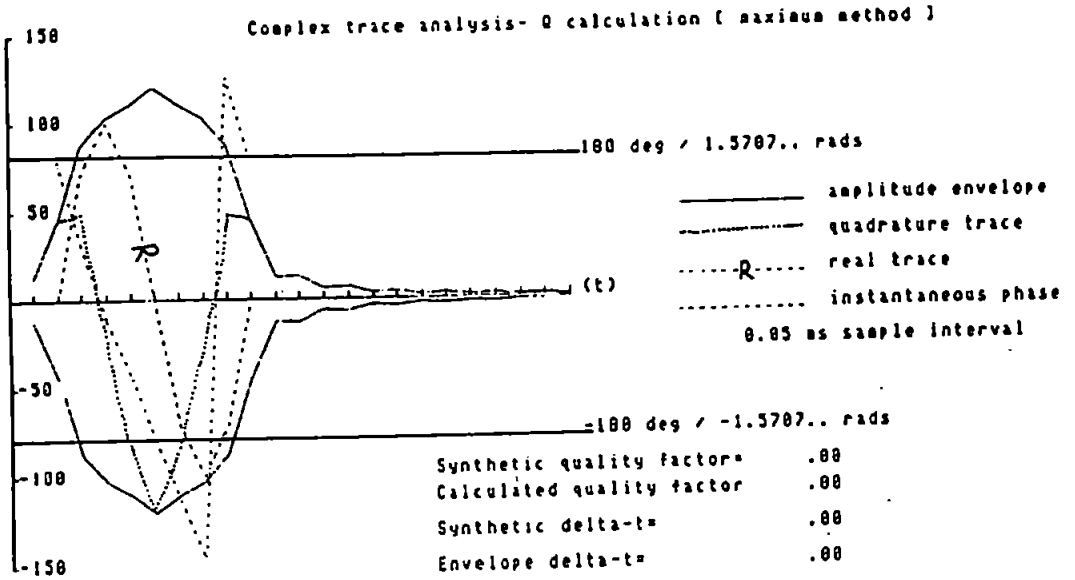

Figure 4.5a
Complex Trace Analysis of a Sinusoidal Wavelet

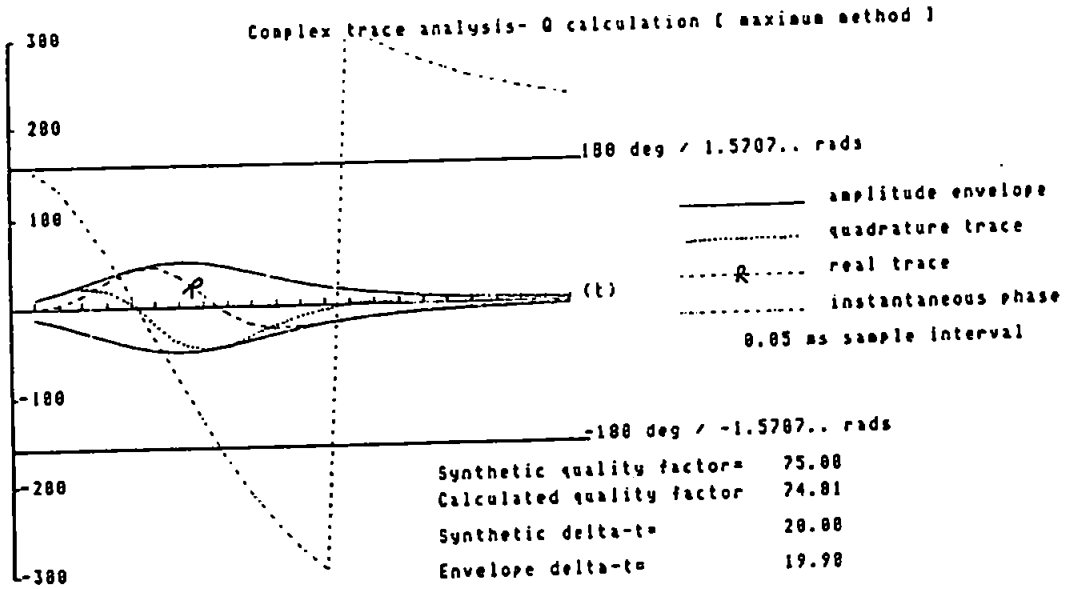

Figure 4.5b
Measurement of Q by complex trace analysis, synthetic noise-free sinusoidal wavelet (Q = 75, t = 20 ms)

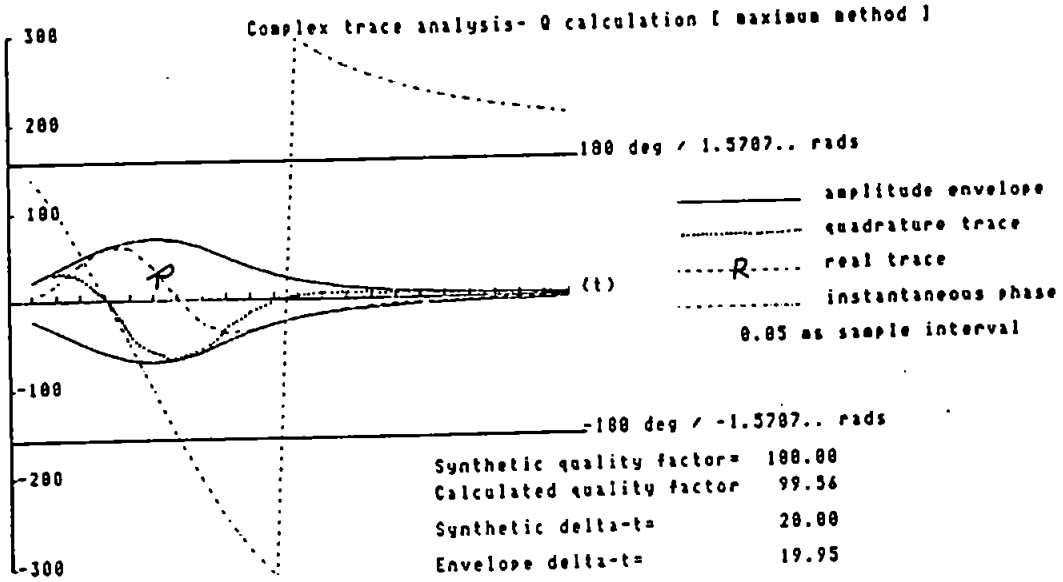

Figure 4.5c
Measurement of Q by complex trace analysis, synthetic noise-free sinusoidal wavelet (Q = 100 t = 20 ms)

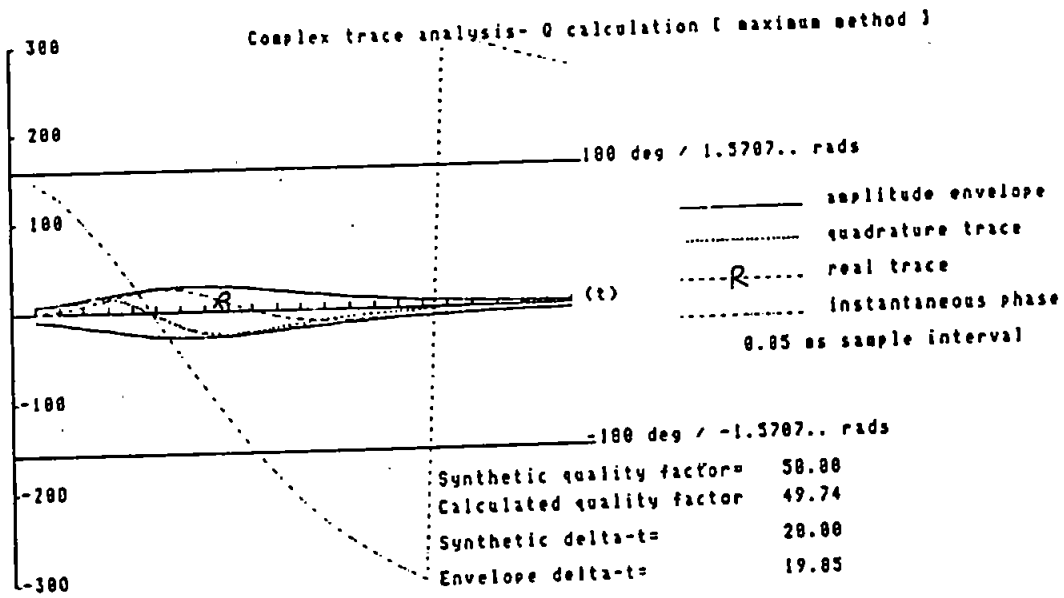

Figure 4.5d
Measurement of Q by complex trace analysis, synthetic noise-free sinusoidal wavelet (Q = 50, t = 20 ms)

decreases with increasing Δt, but increases with increasing Q. The results of these analyses are illustrated in Figures 4.6a to 4.6l For each value of true Q, the estimated Q increases with increasing propagation time. For each value of Δt, the estimated Q tends to be more accurate with a higher true Q value. The results are summarised in Tables 4.3 and 4.4 below:

Table 4.3
Estimated quality factor (in italics) from complex trace analysis using synthetic wavelets (Q = 50, 75, 100, Δt = 10, 15, 20, 25 ms)

		True Δt			
		10	**15**	**20**	**25**
	50	*52.32*	*60.55*	*68.52*	*76.73*
True Q	**75**	*71.34*	*78.87*	*87.33*	*94.26*
	100	*93.09*	*103.06*	*105.59*	*114.62*

Table 4.4
Errors (%) in estimated quality factor (in italics) from complex trace analysis using synthetic wavelets (Q = 50, 75, 100, Δt = 10, 15, 20, 25 ms)

		True Δt			
		10	**15**	**20**	**25**
	50	*4.46*	*21.10*	*37.04*	*53.46*
True Q	**75**	*4.88*	*5.16*	*16.44*	*25.68*
	100	*6.91*	*3.06*	*5.59*	*14.62*

Clearly at low Q values, very large errors appear in the estimate. At higher Q values the estimates are still overestimating the true Q, but by a lesser degree. Thus there is a contrast in the reliability of the method between its application to narrow bandwidth wavelets and its application to broader bandwidth wavelets. However, it is unlikely that it is the bandwidth which is the cause of the error in the latter case, as the error (Table 4.4) generally decreases with lower absorption, or higher Q, where wavelets will retain a wider

bandwidth than with lower Q. Instead, the above results indicate that it is the effects of dispersion expressed in the absorbed and dispersed time-domain wavelet that leads to errors in what is essentially a time-domain technique. The synthetic wavelets generated at 10ms, 15 ms and 20ms for Q = 50 ,75 and 100 will all have the same amplitude spectrum, but will have different phase spectra, as the complex exponential term (including the Futterman operator) that describes the dispersion effect (see previous chapter) is partly a function of Q and partly a function of Δt. The combined effects of absorption and dispersion, given an impulsive input function, produce a causal wavelet that does not yield accurate Q estimates when analysed using the maximum method of Q estimation using complex trace analysis. This is in stark contrast to the success of the method in analysing an artificial wavelet generated from an absorbed and dispersed sinusoidal input. If it is assumed that the type of dispersion relation that is described by the Futterman operator is characteristic of the dispersion of real seismic waves, then the maximum method must be considered to be inappropriate for use in the measurement of absorption in real sediments whose Q will lie somewhere in the range of Q = 30 to Q = 150, (Hamilton,1972). A possible remedy to the problem outlined above may be found by using a sine transform coverting the waveform to sine waves only, rather than a Fourier Transform which uses both sines and cosines. These sine wave elements could then be analysed individually using the maximum method of complex trace analysis. This development is outside the scope of the current project.

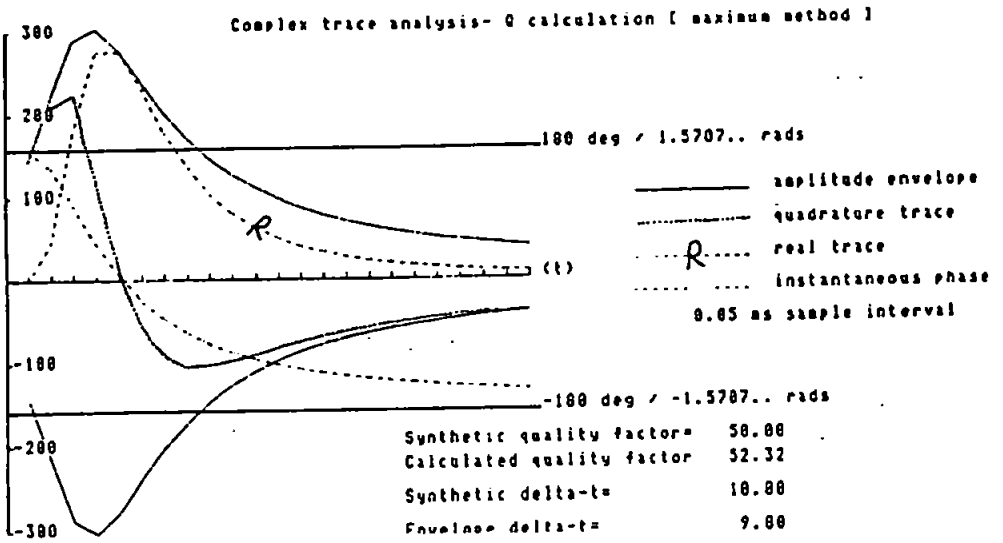

Figure 4.6a
Quality Factor Calculation from Complex Trace Analysis
Using Synthetic Wavelet (Q = 50, t = 10 ms)

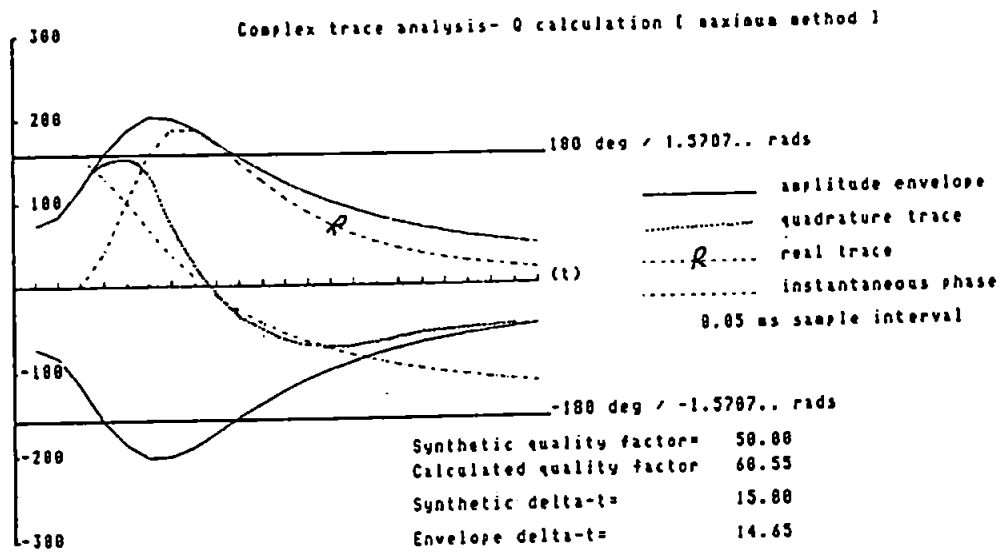

Figure 4.6b
Quality Factor Calculation from Complex Trace Analysis
Using Synthetic Wavelet (Q = 50, t = 15 ms)

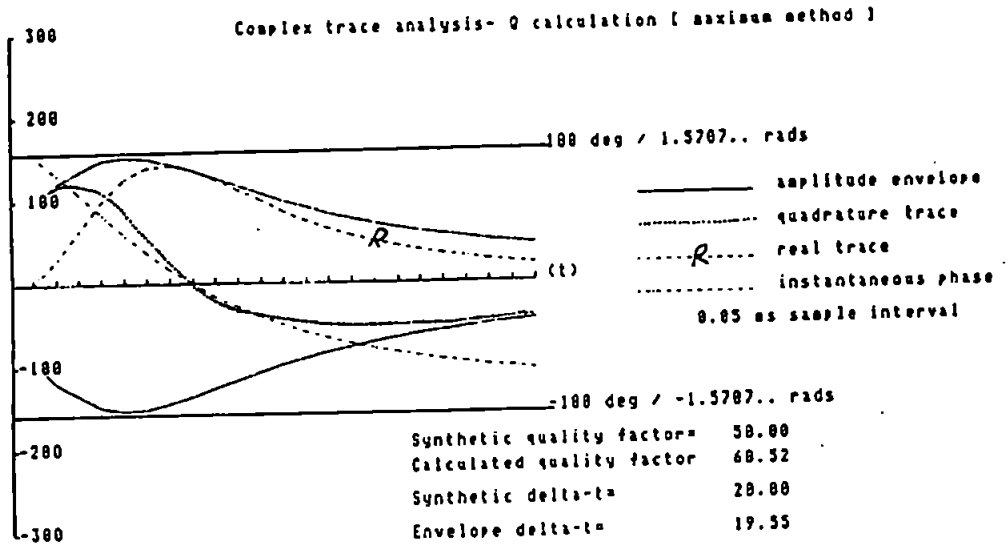

Figure 4.6c
Quality Factor Calculation from Complex Trace Analysis
Using Synthetic Wavelet (Q = 50, t = 20 ms)

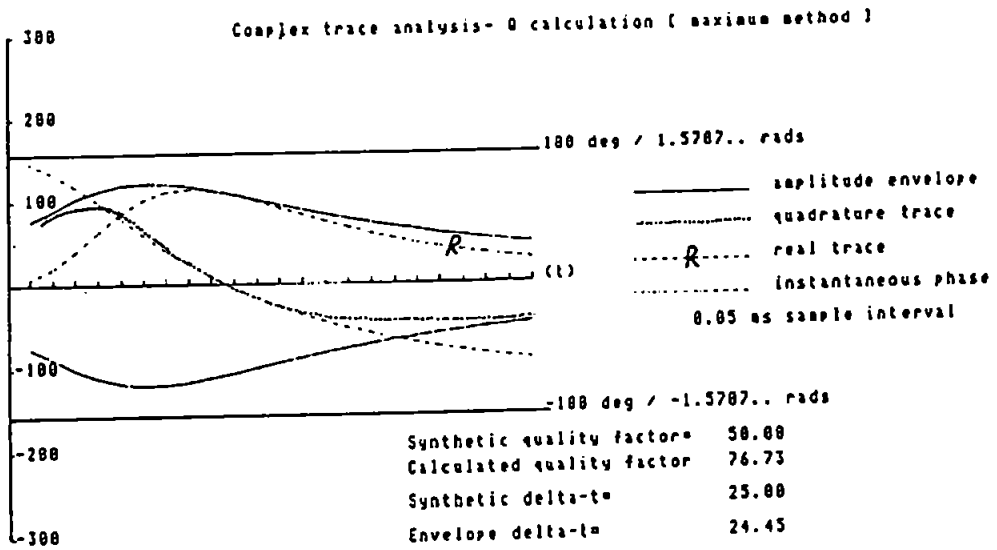

Figure 4.6d
Quality Factor Calculation from Complex Trace Analysis
Using Synthetic Wavelet (Q = 50, t = 25 ms)

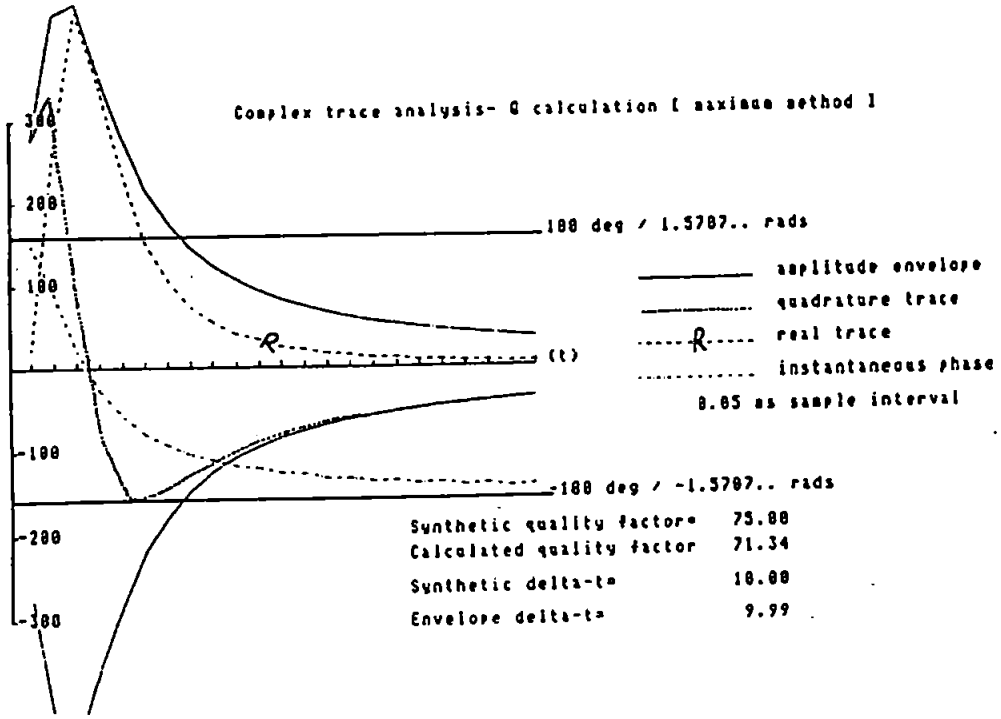

Figure 4.6e
Quality Factor Calculation from Complex Trace Analysis
Using Synthetic Wavelet (Q = 75, t = 10 ms)

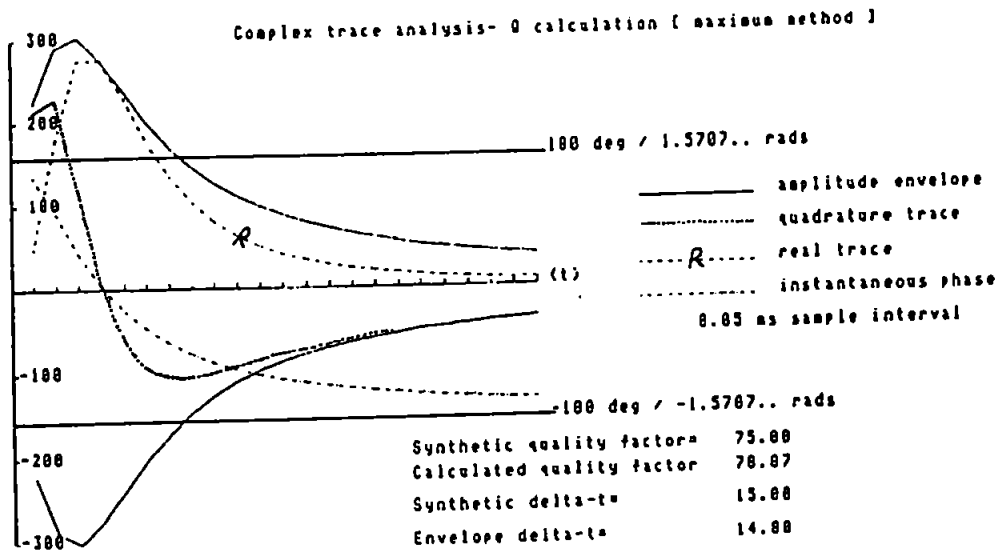

Figure 4.6f
Quality Factor Calculation from Complex Trace Analysis
Using Synthetic Wavelet (Q = 75, t = 15 ms)

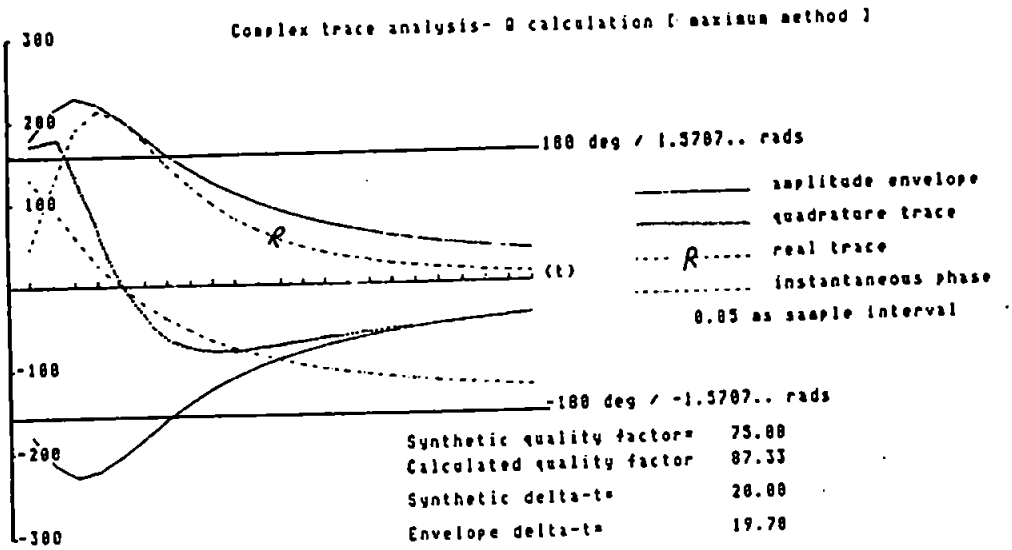

Figure 4.6g
Quality Factor Calculation from Complex Trace Analysis
Using Synthetic Wavelet (Q = 75, t = 20 ms)

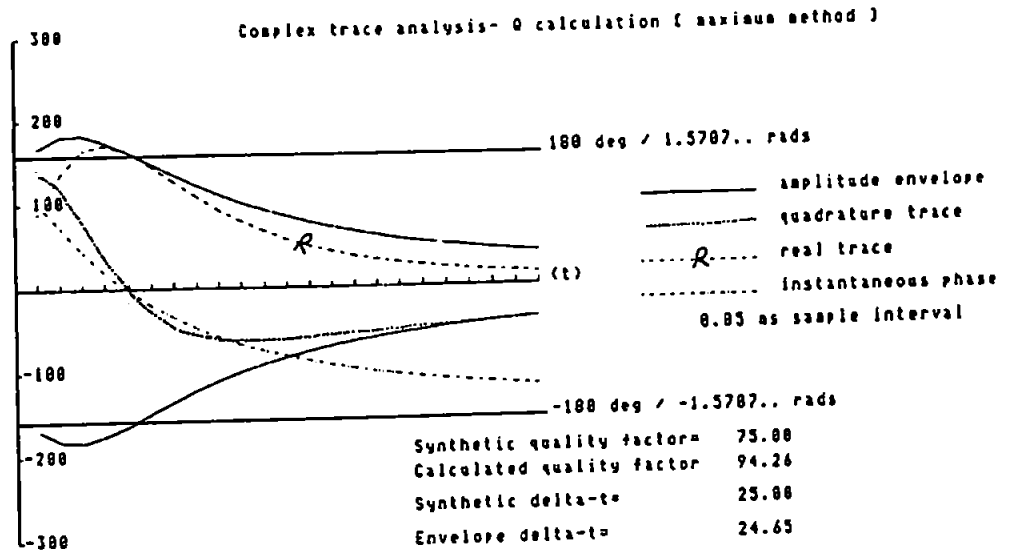

Figure 4.6h
Quality Factor Calculation from Complex Trace Analysis
Using Synthetic Wavelet (Q = 75, t = 25 ms)

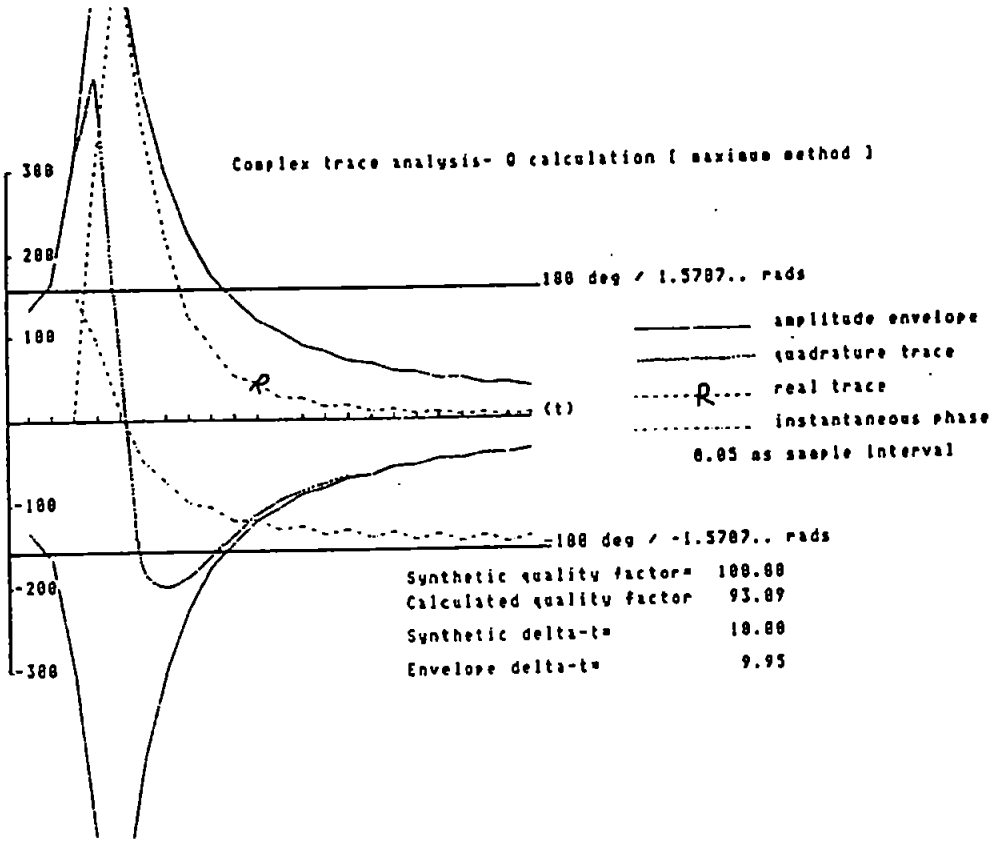

Figure 4.6i
Quality Factor Calculation from Complex Trace Analysis
Using Synthetic Wavelet (Q = 100, t = 10 ms)

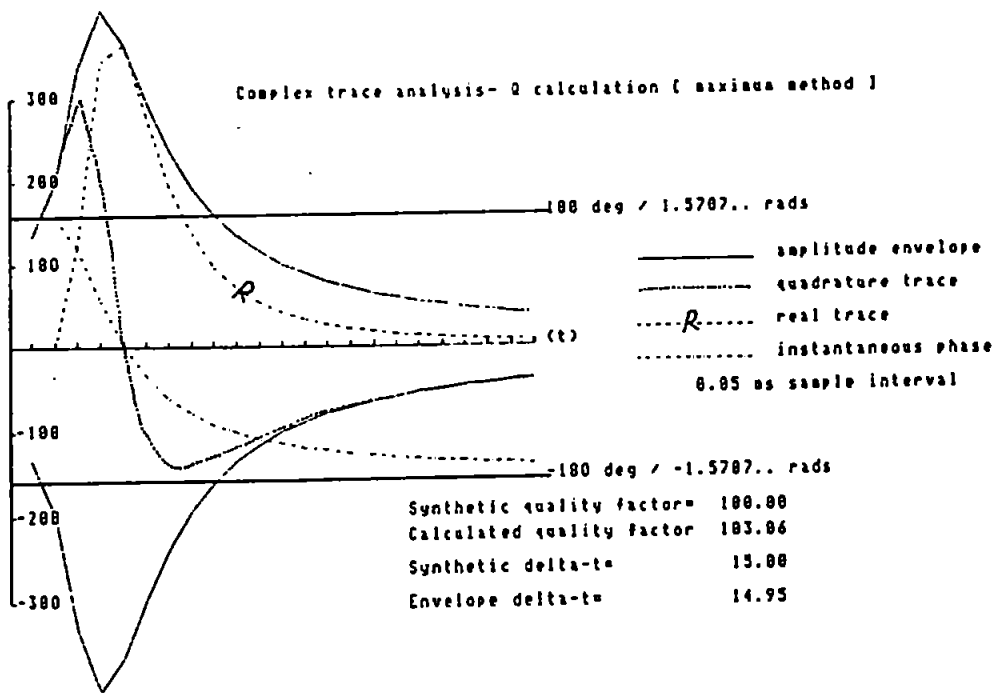

Figure 4.6j
Quality Factor Calculation from Complex Trace Analysis
Using Synthetic Wavelet (Q = 100, t = 15 ms)

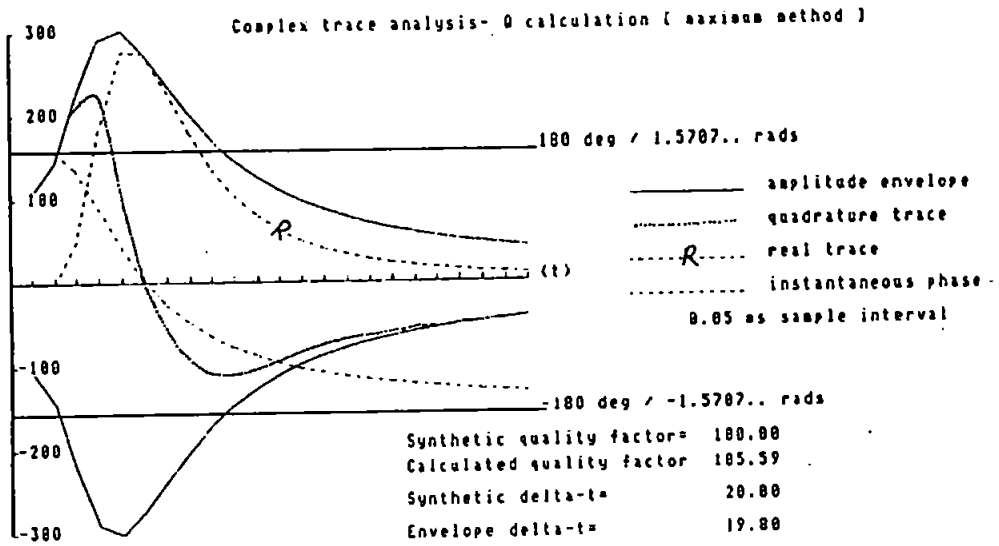

Figure 4.6k
Quality Factor Calculation from Complex Trace Analysis
Using Synthetic Wavelet (Q = 100, t = 20 ms)

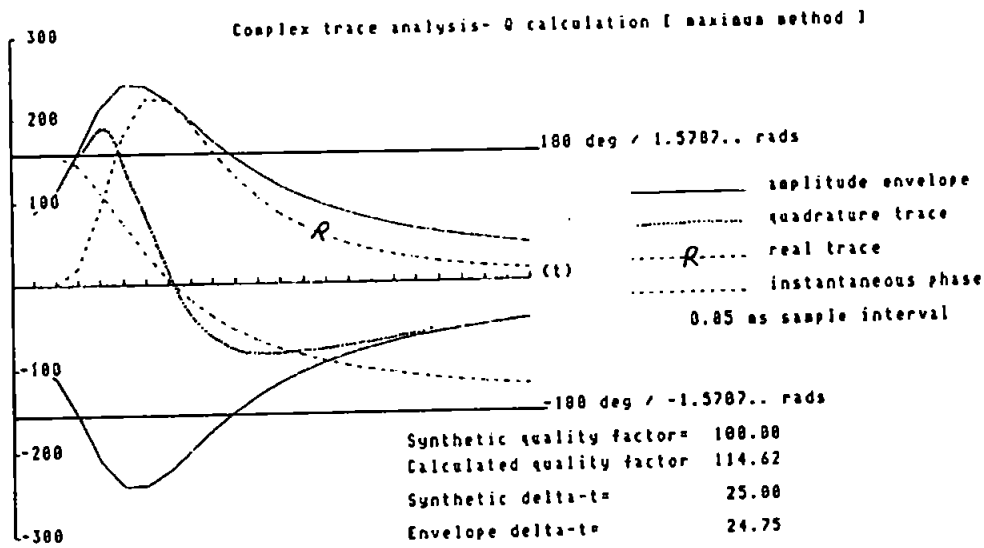

Figure 4.6l
Quality Factor Calculation from Complex Trace Analysis
Using Synthetic Wavelet (Q = 100, t = 25 ms)

4.3.6 Matching Technique Program

The mathematical details of the matching technique were described in the previous chapter. Two wavelets, one shallower, one deeper are used to calculate complex transfer functions. These are the frequency-domain expressions of the prediction filters which predict the deeper wavelet from the shallower wavelet and *vice versa*. The power spectral ratios and prediction filters are calculated from the transfer functions and the spectral coherence respectively. The interactive software deals with input on a trace by trace basis. Initially, a single trace is displayed from which the user isolates reflection events using a screen mouse. These events are embodied within two 512-point arrays prior to application of a Fast Fourier Transform. Using complex conjugates, the crosspower spectra of the two events are computed; subsequent division by the respective power spectra yields the complex transfer functions (H) for the prediction of deeper from shallower ($H_{12}(\omega)$), and shallower from deeper ($H_{12}^{-2}(\omega)$). At this stage the program uses an inverse 512-point FFT on the H_{12} function to calculate the time-domain attenuation operator $h_{12}(t)$, the prediction filter for the deeper wavelet from the shallower wavelet. As with the other techniques, the matching technique software is initially tested on the synthetic data set. As the wavelets within the data set were generated from an impulsive input, the form of the time-domain attenuation operator computed by the technique should yield the shape of the absorbed and dispersed wavelets (in essence the shape of the Futterman attenuation operator). The power spectral ratios may be calculated from the natural logarithmn of the geometric mean of the moduli of the complex transfer functions. The user is presented with three graphs on the summary screen, A) the moduli (amplitude spectra) of the complex transfer functions plotted against frequency in kHz, B) the time-domain attenuation operator and C) the power spectral ratios (vs frequency in kHz). The user may then interactively select a frequency band for estimation of Q based upon the behaviour of the transfer functions and the linearity of the power spectral ratios in the noise-free case. Q is calculated from the arrival time and the slope of the selected frequency band. As with the other methods, the matching technique is dependent upon a reasonably accurate arrival time for the later pulse; the optimal estimate for this is determined from wavelet modelling.

Examples of the output from the program are given in Figures 4.7a to 4.7c. The method successfully reproduces the theoretical wavelets in the form of the attenuation operator $h_{12}(t)$, as well as accurate estimations of the quality factor, Q. However, a closer look at the method when used in this way reveals that it will not yield more accurate absorption estimates than the spectral ratio method. Tonn (1991 ,Fig.13) applied the matching technique in the same manner to VSP data. The following procedure was adopted. Firstly the complex crosspower spectrum between two signals, (1,2) was calculated as $\Phi_{12}(\omega)$ along with the crosspower spectrum $\Phi_{21}(\omega)$. Subsequent division of the first signal by the power spectrum of signal 1, $\Phi_{11}(\omega)$ (the Fourier transform of the autocorrelation of signal 1 [Wiener-Khintchine theorem (Wiener 1930; Khintchine 1934)]) and of the second signal by the power spectrum of signal 2 $\Phi_{22}(\omega)$ yields the complex transfer functions $H_{12}(\omega)$ and $H_{21}(\omega)$.

If the moduli of these transfer functions are calculated, they will be seen to be the inverse of each other; a simple numerical example will illustrate:

1. At a certain value of ω, the complex value of the FFT for signal 1 is,for example (15,9). At the same ω, the FFT of signal 2 has a value of, for example, (7,2).

2. The following may be calculated:

$\Phi_{12} = (15,-9)*(7,2) = (87,93)$

$\Phi_{21} = (15,9)*(7,-2) = (123,33)$

$\Phi_{11} = (15,9)^2 = 306$

$\Phi_{22} = (7,2)^2 = 53$

H_{12}=(0.284311,0.303922)

H_{21} =(2.320755,0.622642)

$|H_{12}| = 0.416762$ ...

$|H_{21}| = 2.402828 \ldots$

3. Therefore $|H_{12}| = |(H_{21})^{-1}|$.

The matching technique, used in the manner by Tonn (1991), for two pulses at an earlier and a later time will yield transfer functions that are the inverse of each other. Although this technique will yield the form of the attenuation operator, it will not be able to improve on the Q estimate by providing statistical figures based upon the ordinary coherence function (White 1973). White (1973) defines the problem of estimating the signal spectrum as one of determining the signal-to-noise ratio of the signal (as a function of frequency).

The power spectrum $\Phi_{jj}(\omega)$ of a wavelet may be represented as the sum of signal $S_j(\omega)$ and noise $N_j(\omega)$ contributions:

$$\Phi_{jj}(\omega) = S_j(\omega) + N_j(\omega) \quad \ldots\ldots\ldots 4(4)$$

or,

$$\Phi_{jj}(\omega) = S_j(\omega)[1 + \frac{1}{\rho_j(\omega)}] \quad \ldots\ldots\ldots 4(5)$$

where

$$\rho_j(\omega) = \frac{S_j(\omega)}{N_j(\omega)} \quad \ldots\ldots\ldots 4(6)$$

is the signal to noise ratio at each angular frequency. If the signal to noise ratios can be estimated at each frequency for two wavelets then the estimate of spectral coherence $SN_{12}(\omega)$ between the two spectra can be written as:

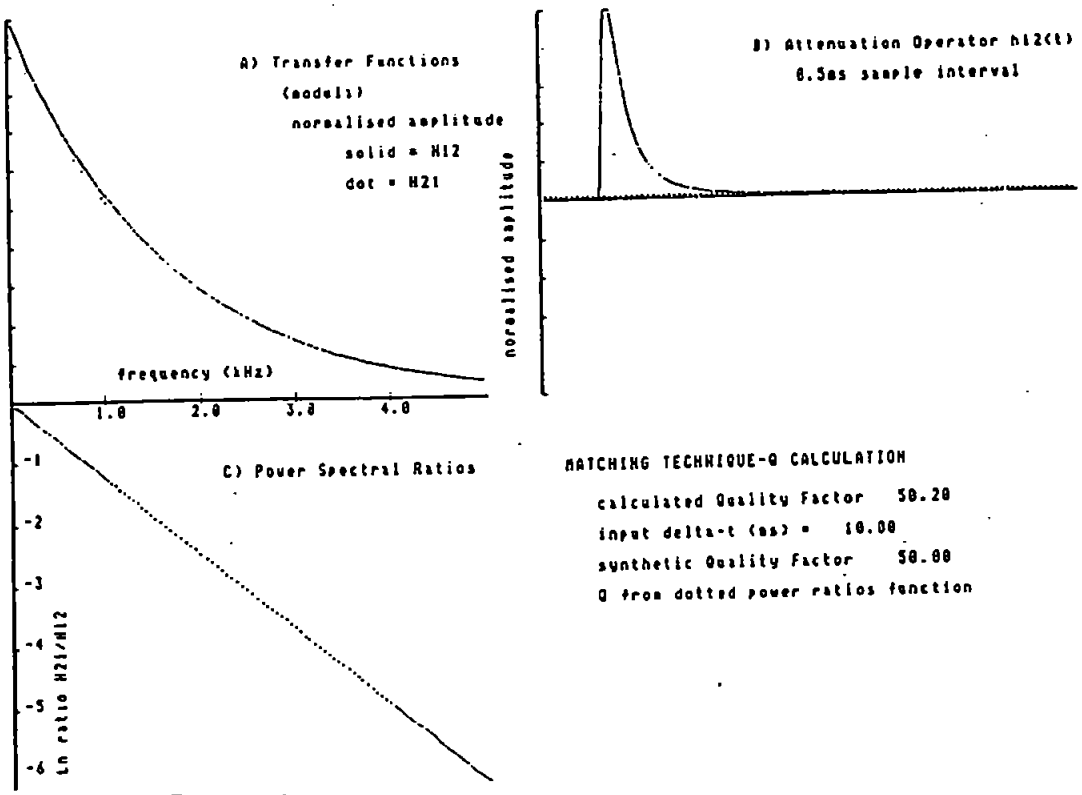

Figure 4.7a
Quality Factor Calculation from Matching Technique
Using Synthetic Wavelet (Q = 50, t = 10)

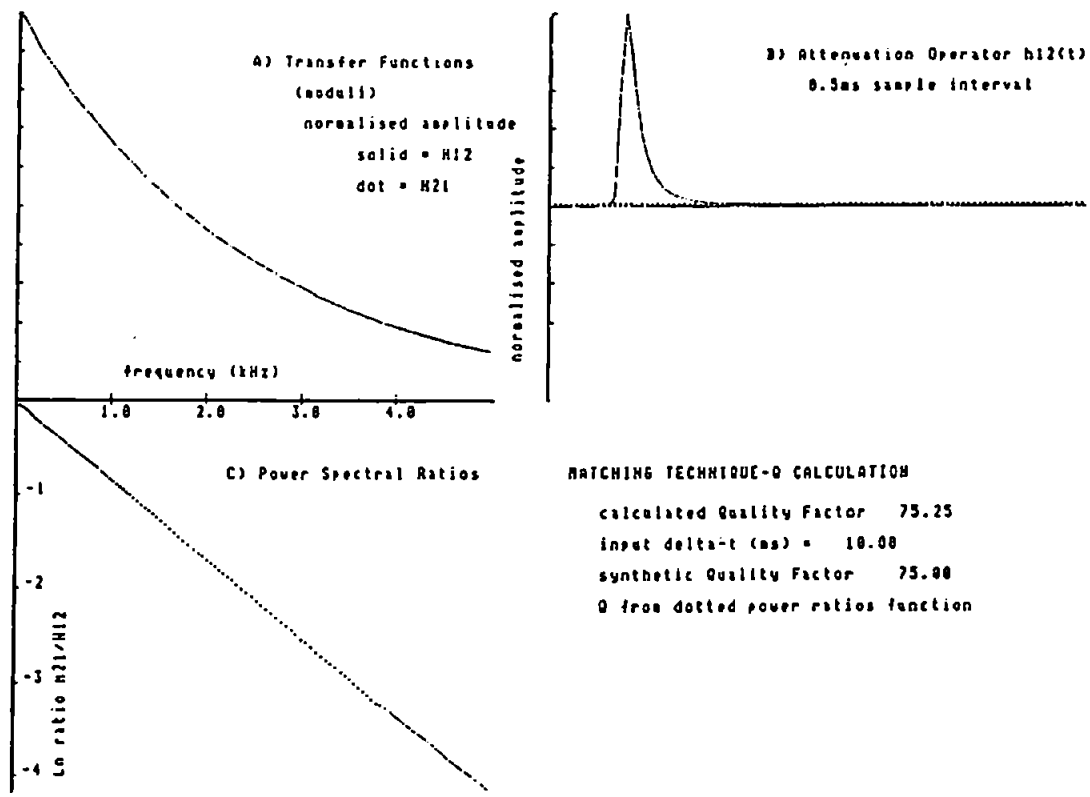

Figure 4.7b
Quality Factor Calculation from Matching Technique
Using Synthetic Wavelet (Q = 75, t = 10)

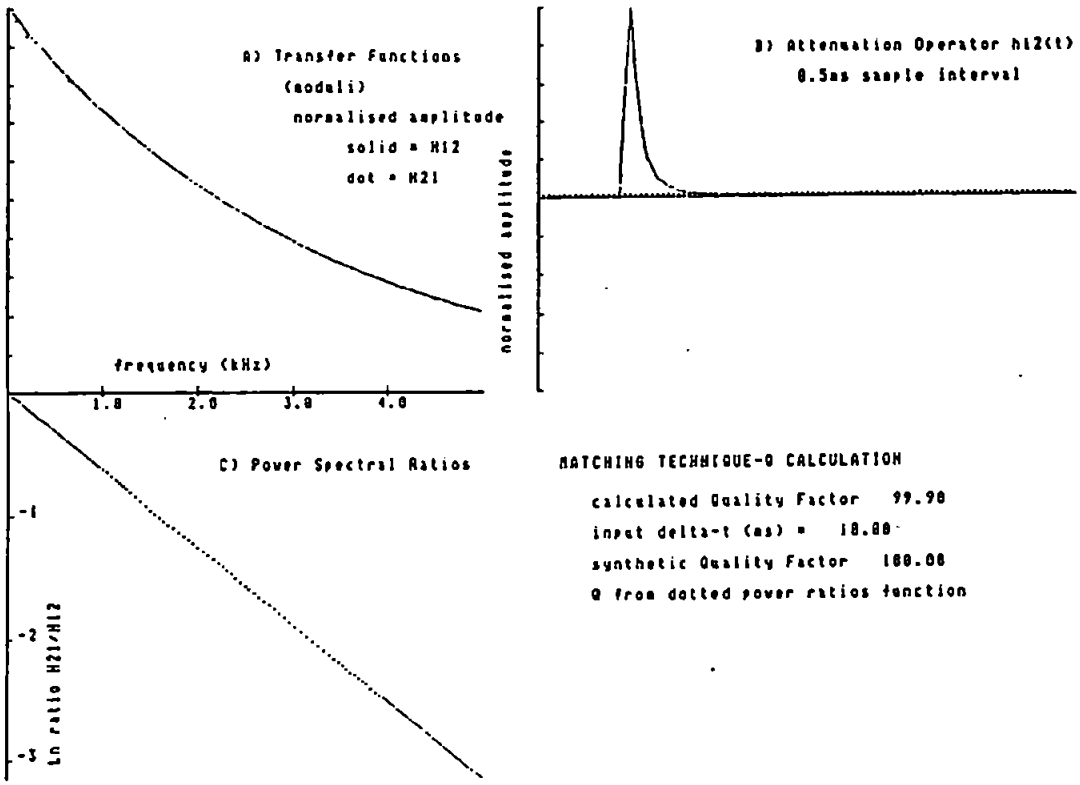

Figure 4.7c
Quality Factor Calculation from Matching Technique
Using Synthetic Wavelet (Q = 100, t = 10)

$$SN_{12}(\omega) = \left(\frac{\rho_1(\omega)}{1+\rho_1(\omega)}\right).\left(\frac{\rho_2(\omega)}{1+\rho_2(\omega)}\right) \quad \text{.....4(7)}$$

where ρ_1 and ρ_2 are the signal to noise ratios of the two wavelets (Foster and Guinzy, 1967; White,1973).

This project is concerned with the analysis of band-limited, finite-length wavelets embodied within much longer seismic traces. The undesirable amplitudes within the trace may arise from many sources. One possible way to estimate noise contributions is to undertake a noise analysis by looking at the spectral characteristics of the reflected event spectra above the frequencies which,(by eye), can be seen as zones of coherent signal. This inelegant but practical method of noise assessment is more generally expressed in Press *et al.* (1986, pp. 417-419), where a power spectra peak was discriminated from a noisy tail by eye as an initial procedure for optimal (Wiener) filter design (*e.g.* Figure 3.1). The signal to noise ratios may then be used to calculate the spectral coherence estimate, and thus the optimal bandwidth for absorption measurement from the spectral ratios.

4.4 Method Reliability In The Presence Of Noise

The effects of noise upon the reliability of the methods for Q-estimation will be addressed in this following section. The first problem to be considered is the quantifying of the amount of noise relative to the signal. This project uses the same procedure as Jannsen *et al.* (1985), in that the noise level is expressed in terms of the variance of the noise relative to the variance of the signal over the time period of the wavelet duration. A sequence of 600 random numbers was generated using a program based upon the RAN3 random number generating function given in Press *et al.* (1986, p.199). The 30 ms noise trace constructed from these numbers is shown in Figure 4.8a; the values are scaled to obtain a required variance, and shifted to ensure a zero mean. The noise trace is divided into ten 3 ms sectors (60 time samples assuming a sampling frequency of 20 kHz). In order to assess the above methods in the presence of noise, the noise trace, on a sector by sector basis, was added to synthetic data set over the duration of the synthetic wavelets and over a 3 ms period from the input impulse. For any given noise-free theoretical trace, the input impulse may be contaminated by any one of the ten sectors, whilst the absorbed wavelet may be contaminated by any of the other nine. In this way, 90 possible sector combinations are available for a given trace analysis, although this was reduced to 15 to avoid excessive processing time. The reason for following this procedure is that although the statistical characteristics of the noise trace may be stationary over the period of the complete trace, short time windows may not obey this stationarity, *i.e* have varying statistical properties on a sector by sector basis, which could very well occur within actual seismic data.

One example of this is the variance. A long 'random' sequence might be generated with a certain variance, but short windows of the sequence will have different variances. If signal to noise estimations are based on variance, then they too will not be constant across the whole trace. The use of many sectors to contaminate both the reference and the target events will yield a more comprehensive analysis of the reliability of the methods in the presence of noise. Figure 4.8b shows the addition of sectors 5 and 6 of the noise trace to the reference and target wavelets respectively (using a synthetic trace generated from $Q =$

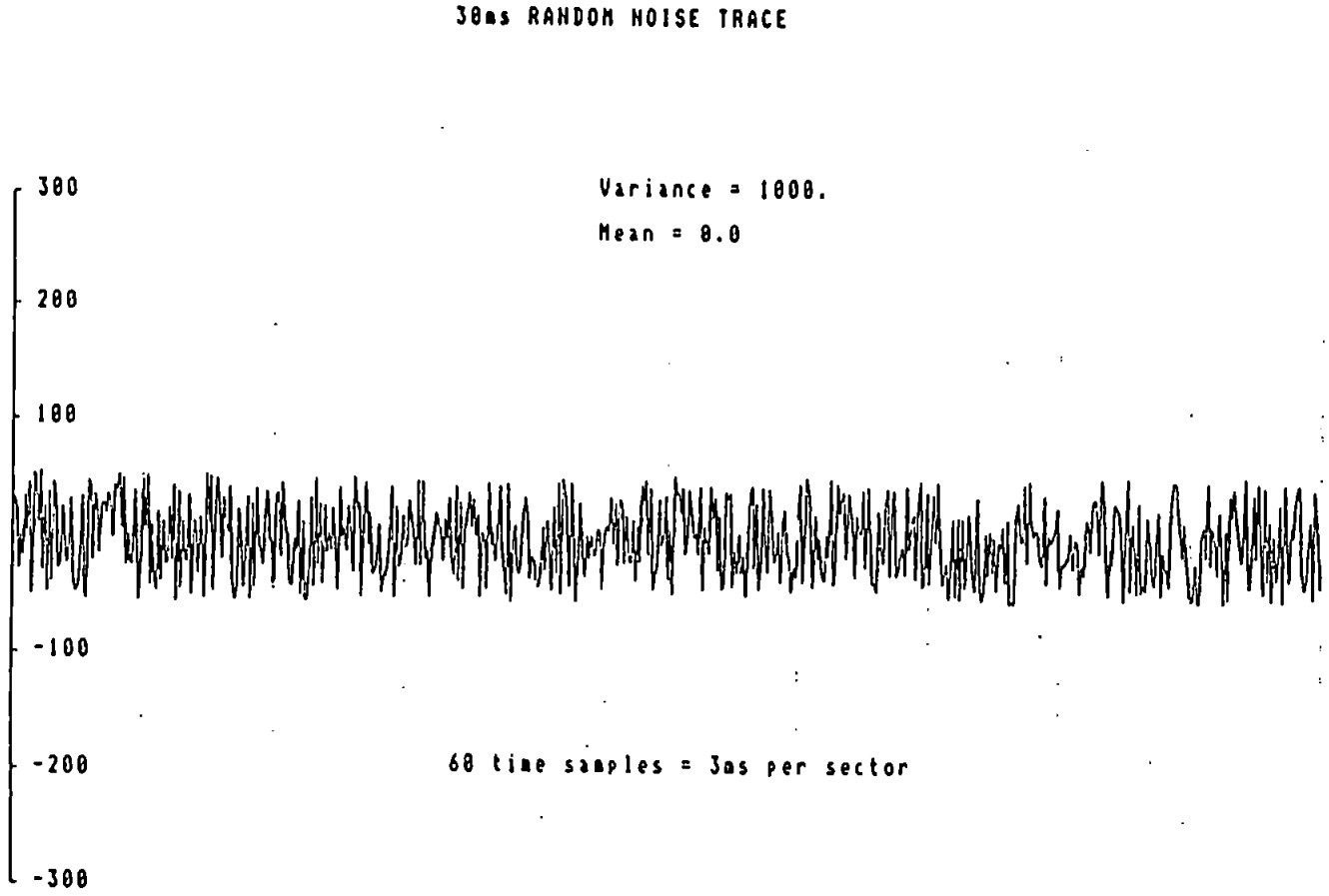

Figure 4.8a
30 ms Noise Trace to Assess Reliability of Numerical Techniques
as a Function of Added Random Noise

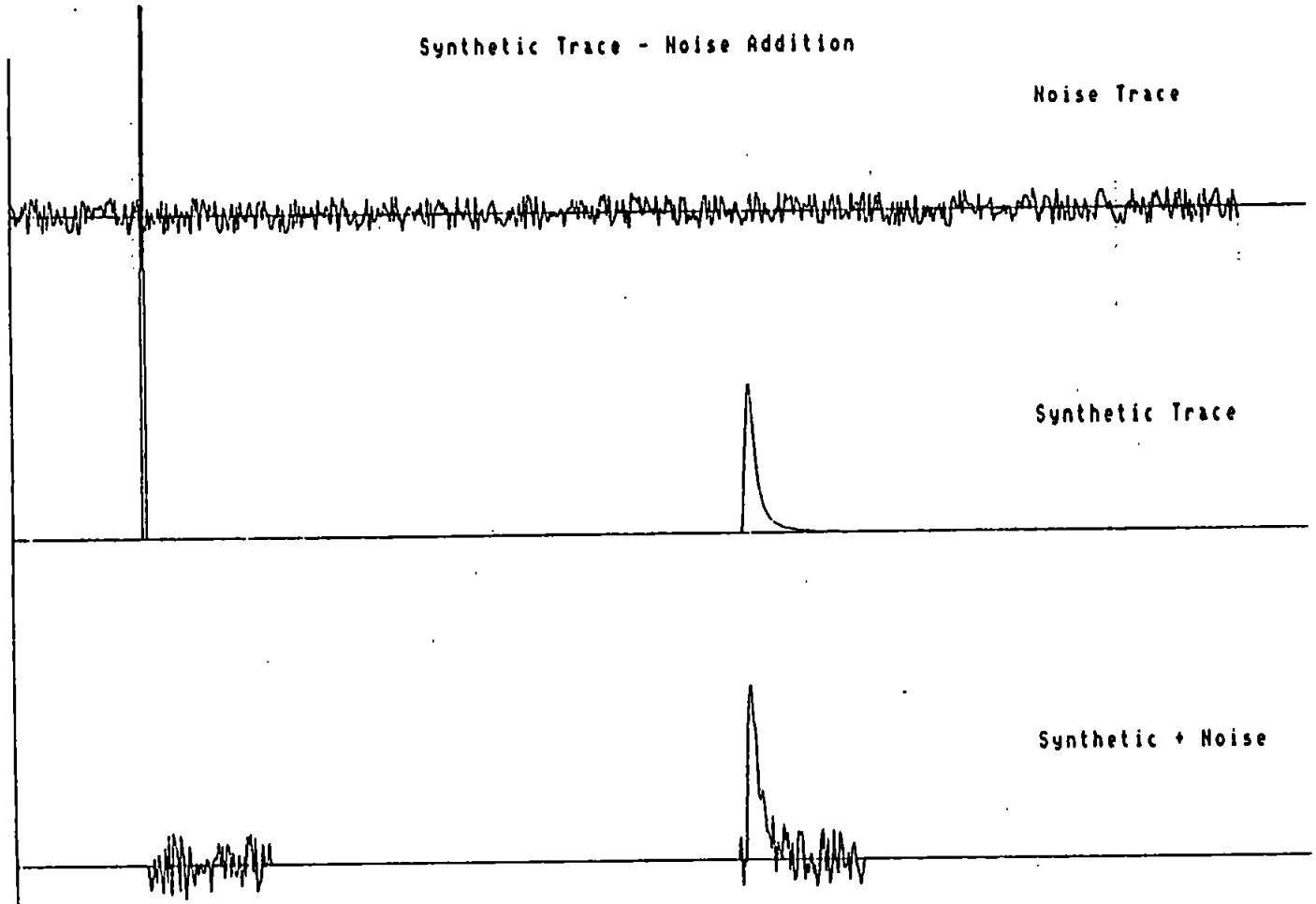

Figure 4.8b
Addition of sectors 5 and 6 of the 30 ms Noise Trace to the Synthetic Wavelet
(from $Q = 75$, t = 15 ms)

75, t = 15 ms). The variance of the noise is adjusted to be a fixed percentage of the variance of the absorbed wavelet prior to the addition to the noise-free trace, in this case 30% . For clarity the input impulse (of amplitude 1000 units) is not shown in the final trace. This procedure was carried out for noise levels from 5% to 30 % of the signal level of the absorbed wavelets, in 5% increments, for Q = 50, Q = 75 and Q = 100, and a t of 15 ms. For each wavelet, the absolute mean error from the true Q value was calculated at each level of noise addition. The results are summarised in Figure 4.8c; absolute errors above 20% were not plotted. At a noise level of 5%, all the methods could estimate the true Q to within ±10%. Above 10% the risetime method yielded large errors, which gave an approximate the upper noise ceiling for this method for a Q of 50 and above. Jannsen *et al.* (1985) give a value of about 5% for this limit. With noise levels of over 20% only the wavelet modelling method yielded errors less than 20% for Q = 75. At 30% none of the methods could yield an estimate with an error of less than 20% for Q = 75 and Q = 100. In general, the spectral ratio, matching and spectrum modelling methods yielded similar results. All three could yield estimates to within ±20% for Q = 100, providing the noise levels were 20% or lower. In general, an increase in Q for a given noise level will lead to larger errors in the Q estimates for any of the techniques. Although computationally slow, the wavelet modelling technique appeared to be the most robust method in the presence of noise at all three Q values. The interpretation of the plotted data warrants a certain amount of caution; the plot should only be seen as being broadly comparitive between the methods.This is because each of the methods is open to a certain degree of human intervention in the derivation of the final estimate. Each of the methods is dependent upon a reasonably accurate estimate of Δt. The optimal source of this value is from wavelet modelling, although a reasonable estimate may be provided by trace autocorrelation. The Δt values for the spectrum modelling and matching techniques were provided by wavelet modelling. Another method might be to use initial amplitude onsets, which will underestimate the true Q:-this was the case with the spectral ratio method, another would be the autocorrelation, which was used by the risetime method. The spectral methods are problematic in that Q may be calculated from only a very short section of the ratios curve,

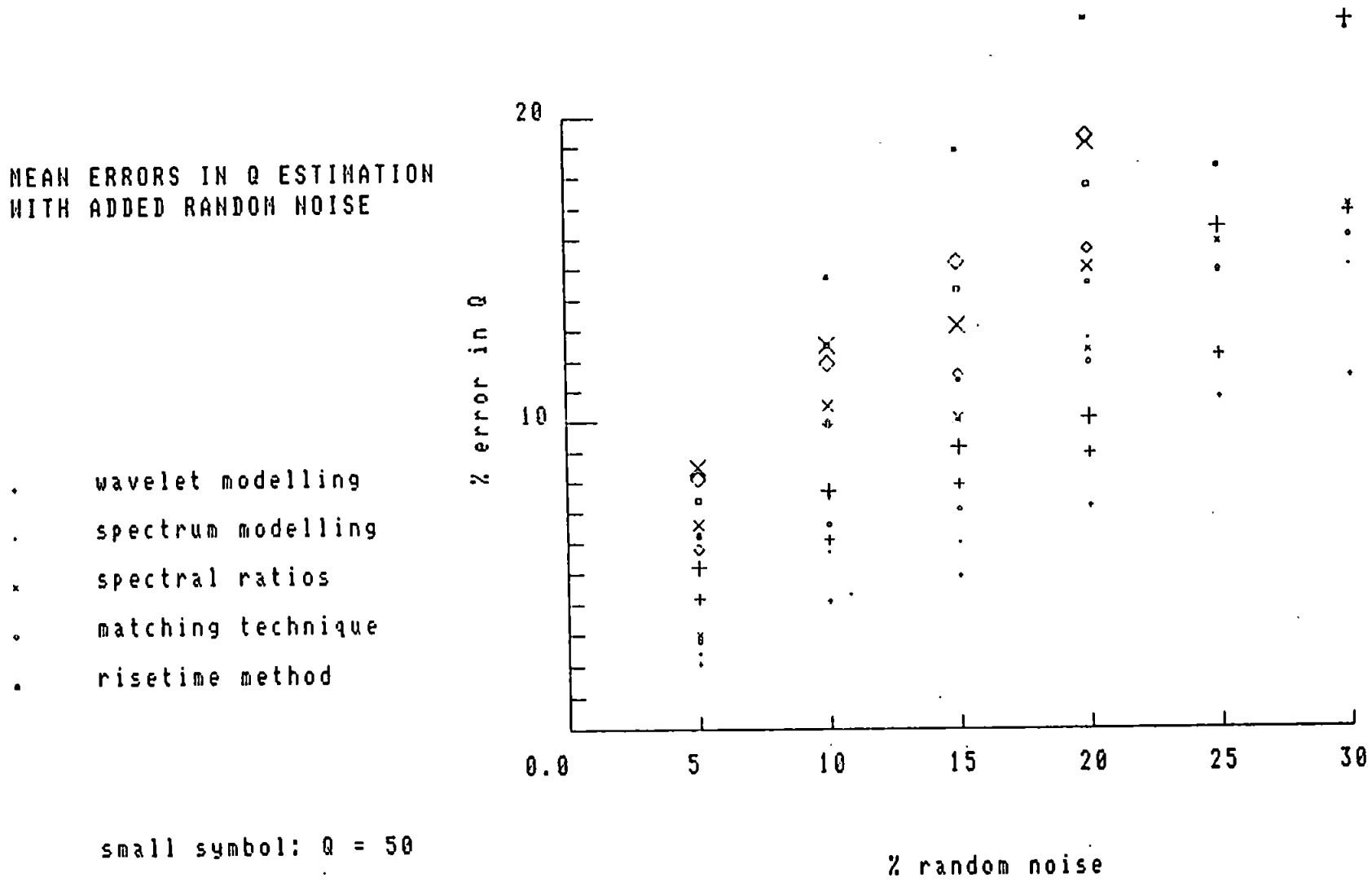

Figure 4.8c
Mean Errors (%) in Estimation of Quality Factor, Q, as a function

from only a few spectral components. The spectrum modelling and wavelet modelling techniques will yield different Q values depending upon the bandwidth (or for wavelet modelling the time interval) over which the modelling takes place, and for noisy traces, whether the calculation is conducted in the L_1 or L_2 modes, the latter being preferable as it favours larger amplitudes, and therefore larger signal to noise levels. In terms of the significance of the plotted data to practical applications, the risetime method may be too sensitive to noise (and suffer from an inadequate sampling rate) for marine seismic work, although its use has been shown for short propagation paths and low-Q terrestrial sediments (Jongmans, 1990a).

In the current application of the software, the spectral ratios, and matching techniques do not yield significantly different results. Spectral modelling does appear to give smaller errors for a given noise level than these methods. For the practical applications of this project, the matching technique (in this variant form) will be used to calculate the spectral ratios. The spectral coherence determined from signal-to-noise power ratios will indicate the optimal band over which to calculate absorption for the spectral ratios and spectrum modelling methods. The preferred technique is wavelet modelling (which although compututationally slow), encompasses both absorption and dispersive effects. It appears to be a reasonably robust estimator of Q in the presence of noise for Q values that are not unrealistic for unconsolidated sediments, for transit times of up to 25ms (about 22 m of sediment thickness), and for an initial seabed spectrum of up to 10 kHz.

4.5 Summary

The application of several time domain and frequency-domain methods to estimate the quality factor, Q, have been considered. A synthetic data has been created that encompasses both of the effects of absorption and dispersion for high Q and low Q sediments, (Q = 50 ,75 ,100) and for t values of 10 ms to 25 ms (depths of 8.5 m to 22 m in sediments with a velocity of 1700 ms^{-1}). With the likely quality factors of soft sediments, coupled with the short propagation paths and the likely frequency bands involved in shallow marine seismic experiments, it is questionable whether dispersion can be considered an important modelling parameter.

All of the methods yield reasonably accurate Q estimations in the noise free case, with the exception of the method based upon complex trace analysis. This method will not be applied in the case studies described in chapters 5 and 6, as the modelling using the synthetic data set shows it has serious reliability drawbacks with absorbed and dispersed broadband wavelets. With the spectral methods, several problems have to be considered before arriving at a Q estimate, including the length of windowed data, length of Fourier transform, the bandwidth over which Q is to be measured and signal-to-noise ratios over the width of the spectrum.

The matching technique yields the form of the prediction filter that converts an earlier pulse into a later pulse. In the case of the synthetic data set, the calculated prediction filter resembled the form of the Futterman attenuation operator. With real data, the determination of the prediction filter may be able to reveal either the simplicity or the complexity of the process that changes the spectral characteristics of a pulse between the top and bottom of a seismic unit.

The risetime method is practically applicable only in the noise free case, and is not considered for use within the case studies, despite the fact that the method only uses a small portion of the waveform. It has particular problems when tau, the rise time of the pulse, approaches the sample interval, and the initial slope is under-represented by discrete samples in the time-domain.

In the case of random noise added to the synthetic data, wavelet modelling appears to be the most robust Q estimator (in the L_2-norm), followed by spectrum modelling and the two spectral ratios methods. Statistical analysis yielding confidence intervals of the spectral estimates may be applied in the latter two methods. The next stage of the project will use wavelet and spectrum modelling, and the matching technique (to calculate the spectral ratios) on shallow marine seismic data from three surveys carried out in conjunction with investigations of the near-seabed geology.

Chapter 5: Block 49/10 Case Study

5.1 Introduction

The Block 49/10 case study uses data from Quadrant 49, Block 10 of the southern North Sea. The survey area lies to the north-east of the Indefatigable and Viking gas fields, on the eastern limit of the United Kingdom designated section of the Southern North Sea (Figure 5.1). The data were acquired by Britsurvey Ltd. on behalf of Shell (U.K.) Ltd. in 1988. The purpose of the seismic survey was to acquire shallow penetration data in order to assess the surface and sub-surface geological conditions prior to potential drilling operations. The seismic data would assist in the evaluation of seabed topography, lithology and formation types within the Quaternary and uppermost Tertiary sequence, and in the determination of the potential hazard of shallow gas accumulations. For the seismic data used in this case study, the depth of investigation is restricted to lie within the Quaternary.

5.2 Survey Details

A total of 33 seismic lines were run with an average spacing of about 70 m, each approximately 1 km in length, forming a 1 km by 1 km grid over a proposed drilling location (the lines running N-S and E-W). The primary positional control was provided by the 'Syledis' positioning system, giving a positional accuracy of about 5 m. The source pulse was provided by an E.G & G. Model 230 "Uniboom" Boomer, a surface-towed, electro-mechanical device whose power input was set to 200 joules from an E.G.&G. Model 234 Energy Source delivering a pulse centred on about 1.5 kHz. An E.G. & G. Model 265 single channel hydrophone was used to receive the reflected data. Both source and receiver were towed 26 metres to 33 metres behind the boat, from 2 to 3 metres apart. The source was fired every 375 ms whilst the sweep was set to 125 ms (the time window

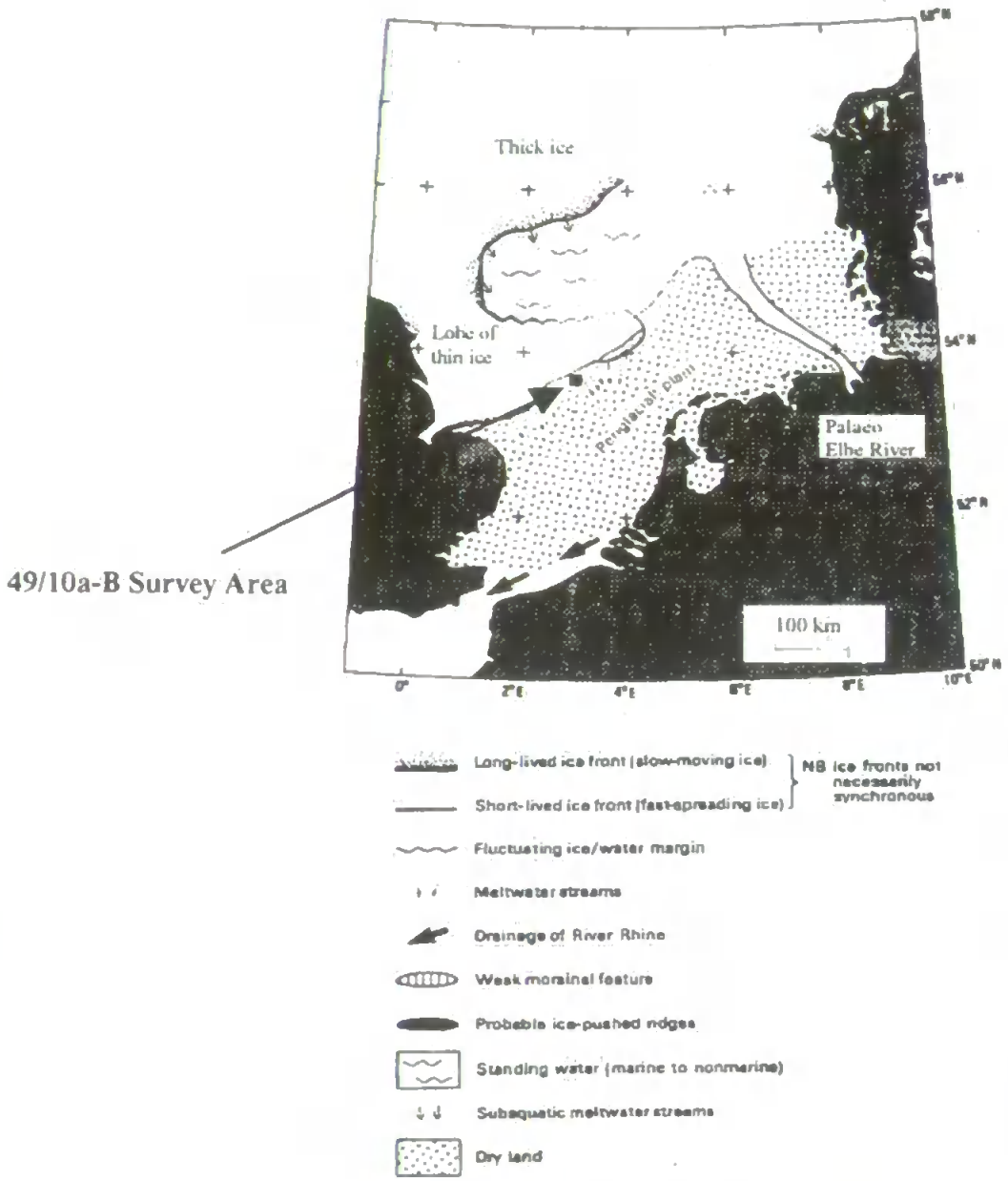

Figure 110 Generalised palaeogeography of the southern North Sea at the Weichselian ice maximum. Based on Eisma et al. (1979), BGS/RGD mapping, and Nilsson (1983).

Figure 5.1 Location of 49/10a-B survey area and generalised palaeogeography. (after Cameron et *al.*, 1992).

for which data were recorded following the firing of the source). The speed of the survey boat, coupled with the firing rate, produced a shot interval of about 40 cm. The incoming signals were recorded on analogue tape recording equipment and simultaneously reproduced as analogue seismic sections on continuous paper rolls. In order to produce paper sections with optimal visual detail, analogue filtering was applied to the data. For the beginning of the sweep, the pass band was set to 600 Hz - 4 kHz, which was linearly opened out to 7 kHz for the end of the sweep. In addition a TVG (time-variant gain) was applied in order to amplify the weaker signals from deeper reflectors at the end of the sweep. The analogue signals were recorded on a Racal Store-7 tape recorder, including one track for the recording of the firing pulse at t = 0.0 ms. Only a 10 kHz low-pass analogue filter was applied to the data prior to being written to tape.

5.3 Post-Acquisition Processing

The aim of post-acquisition processing was to extract information from the analogue tapes and to present the it in a digital format for numerical analysis. The data were recorded on 0.5" master tape. This information was copied on to 0.25" tape for a working copy. Given such a large data set it was necessary to select certain parts of the data set prior to analogue to digital conversion. This was achieved by initially selecting parts of the data set from the paper records. The output spectrum of the Uniboom source has a potential bandwidth extending from a few hundred Hz to about 10 kHz (E.G.&G. Bulletin 2-100A). In order to preserve the spectral content of the data, a sampling rate of 20 kHz was selected for digitising the analogue data. The data were played back on a Racal Store-4 tape recorder linked to a 80386-based computer which contained an internal analogue-to-digital conversion card. The digitisation process was software-controlled from the keyboard. The digital data were written to the hard-disk of the computer in binary format as the digital representation of a voltage (± 0.5 volts) and from there copied to floppy-disk with traces written in a continuous number stream. The trace-by-trace format provided the

input for the software prior to numerical analysis.

5.4 Bathymetry and Geology of the survey area

5.4.1 Introduction

The bathymetric chart for the survey area, drawn up from echo-sounder data, shows a general slope of the seabed down towards the north and the east. The water depth ranges from 35.4 metres in the south-west to 40.8 metres in the north-east, corrected to lowest astronomical tide (LAT).

The deeper geology of the survey area includes a basinal sequence of sediments from Carboniferous to Tertiary in age which is at least 4000 metres thick (Cameron *et al.*, 1992). It is at the UK-Netherlands median line just to the east of the survey area where Upper Cretaceous to Quaternary sediments attain their greatest thickness in the southern North Sea.

The Quaternary geology of the southern North Sea is summarised on the 1:250 000 scale, Quaternary Geology series of maps published by the British Geological Survey which result from seismic and seabed sampling surveys between 1979 and 1984. The details of the Quaternary sequence have been based on the interpretation of shallow-seismic data which have been calibrated using BGS shallow borehole data and released commercial well data. The 49/10a-B survey area is covered by the 'Indefatigable' Sheet 53°N-02°E (1986), and is supplemented by the United Kingdom Offshore Regional Report 'The geology of the southern North Sea', (Cameron et al., 1992).

5.4.2 Quaternary Geology

The early Pleistocene geology of the region is largely a result of deltaic systems which migrated in a north-westward direction from continental Europe. The products and effects of glacial erosion and deposition dominate the later Pleistocene history up until about 10000 years ago when the marine, strongly tidal environment of the Holocene was

FORMATION	DEPOSITIONAL ENVIRONMENT	CHRONOSTRATIGRAPHY	THIS PROJECT
(superficial)	marine	HOLOCENE	UNITS A and B
Boulders Bank	glacial (till)	UPPER WEICHSELIAN	not present
TWENTE	periglacial : aeolian	UPPER WEICHSELIAN	UNITS C1 AND C2
EEM	marine	EEMIAN	UNITS D and lower
SWARTE BANK	subglacial : glacilacustrine to glacimarine	ELSTERIAN	
YARMOUTH RDS.	non-marine (fluvial) to intertidal	LOWER- MIDDLE PLEISTOCENE	

Table 5.1 Holocene and Quaternary Formations of the 49/10a-B survey area.

established. The Indefatigable sheet indicates a thickness for the Quaternary sequence of about 250 metres for the survey area, of which all but the top few metres are of Pleistocene age. As a guide to the depth of interest for the case study, the base of the seismic sections is at 125 ms TWTT. At an average velocity of 1500 ms^{-1} for water and 1700 ms^{-1} sediment, the base of the sections represent reflections from a depth of about 100 metres, or about 65 metres of sediment thickness. The Indefatigable sheet indicates that the oldest sediments that are likely to be found at about 100 metres below current sea level are those of the Yarmouth Roads Formation (Table 5.1), of late Lower Pleistocene age (Waalian to Elsterian). The detailed Quaternary geology of the survey area will be examined with a seismo-stratigraphic analysis of the available data from the 49/10 site survey.

5.4.3 49/10 Survey: Seismo-Stratigraphic Interpretation

A flat (in the west) to gently undulating (in the east), laterally continuous, strong event (termed the 'Red Event' for this work) at 51 ms TWTT (in the west) to 54 ms TWTT (in the east) bounds the seabed and several distinct seismic units. To the western end of Line 261 (Enc. 5a) , a triangular shaped unit (termed unit C_1), with a strong, easterly-dipping upper boundary appears to rest directly on the Red Event (Figure 5.2). Unit C_1 appears to pinch out at its eastern limit against the Red Event, and is characterised by strong, parallel to sub-parallel, steeply dipping (apparently south-westwards) internal reflectors. Line 261 shows a maximum time-thickness of 11 ms TWTT for the unit. Immediately to the east, a wedge-shaped unit (termed unit B) thinning to the east is bound by the seabed and the Red Event. It is characterised by moderately strong, easterly-dipping parallel to sub-parallel reflectors (Figure 5.3). Gravity cores taken at the time of the seismic survey show Unit B to be composed predominantly of coarse sands. No further geotechnical information is available. Eastwards, unit B thins and the internal structure becomes more complex, being made up by wedge-shaped packets of reflectors, each packet having a slightly different reflector dip relative to adjacent packets. At its eastern limit the internal structure is one of laterally continuous, sub-horizontal events. On line 261 unit B appears to wedge out

against a triangular-shaped unit (termed unit C_2) which rests directly on the Red Event (Figure 5.4). The external morphology is that of a strong, gently dipping (westwards) and steeply dipping (eastwards) upper boundary, with a bimodal internal structure of steeper reflectors to the east of the unit and shallower-dipping reflectors to the west. Line 261 shows a maximum time-thickness of 4 ms TWTT for unit C_2 . Although the boundary is not strongly defined by a single, discrete reflector, unit C_2 is overlain by an acoustically clear seismic unit (termed unit A), with very little internal structure (Figure 5.4). Gravity cores taken at the time of the survey indicate Unit A to be composed of fine sands, but no further geotechnical information is available. The events parallel to the seabed on the paper sections are a manifestation of ringing of the boomer source and do not reflect a layered internal structure. Unit A thins upwards towards the west, and may form a thin layer above unit B, although this is not clear from the paper records.

Beneath the Red Event (Figure 5.4), another strong, flat, sub-horizontal reflector occurs at about 56 ms TWTT, termed the 'Yellow Event' for this work. A thin structureless unit ('unit D') is bounded by the Red and Yellow events. Beneath the Yellow Event a unit of varying lateral and vertical seismic character occurs down to about 64 ms TWTT ('unit E'), where it is bound by a discrete reflector. In the central part of Line 261 unit E appears structureless to chaotic in internal character, with low-amplitude, internal reflections. To the east, the character becomes well-layered, with strong, sub-horizontal, parallel internal reflectors. Just west of the chaotic zone, unit E shows internal reflectors which appear to terminate upwards against the Yellow Event. A further two seismic units are visible beneath unit E. The first, ('unit F') occurs between 64 ms and 74 ms TWTT. It is characterised by discontinuous sub-parallel internal reflections, and has a sub-horizontal base. The deepest discrete seismic unit occurs below 74 ms TWTT and consists of laterally continuous, parallel-layered internal reflectors, but below 88 ms very little structure is seen in the seismic sections. The last 40 ms or so of the records are masked by the arrival of the seabed multiple and multiples of the near-surface events.

Perhaps the most striking feature seen in line 261 is the abrupt loss of reflection strength west of a line dividing seismic units A and B (Figure 5.5). The internal reflections,

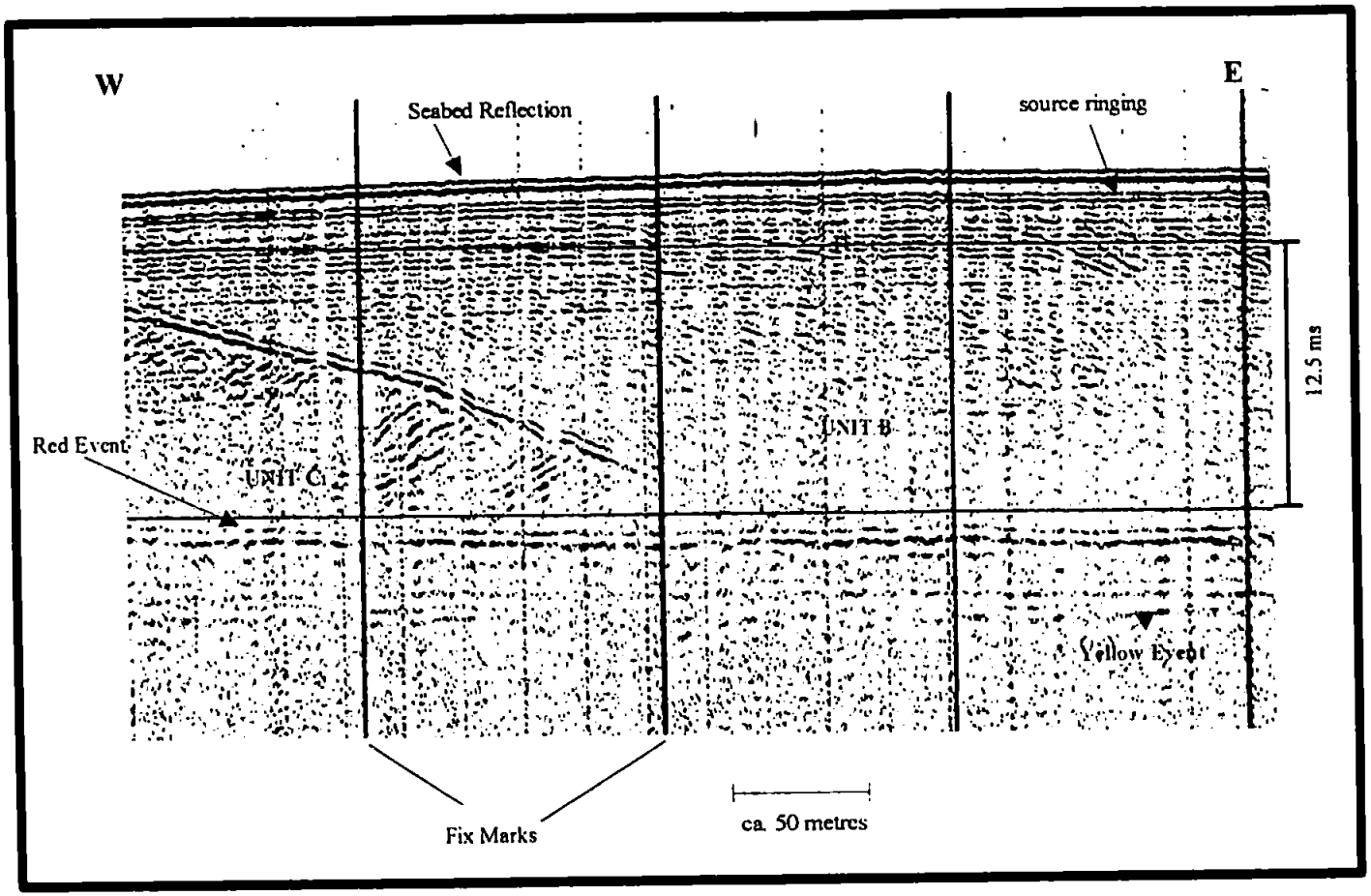

Figure 5.2 Seismic line 261 (west section) of 49/10 survey area

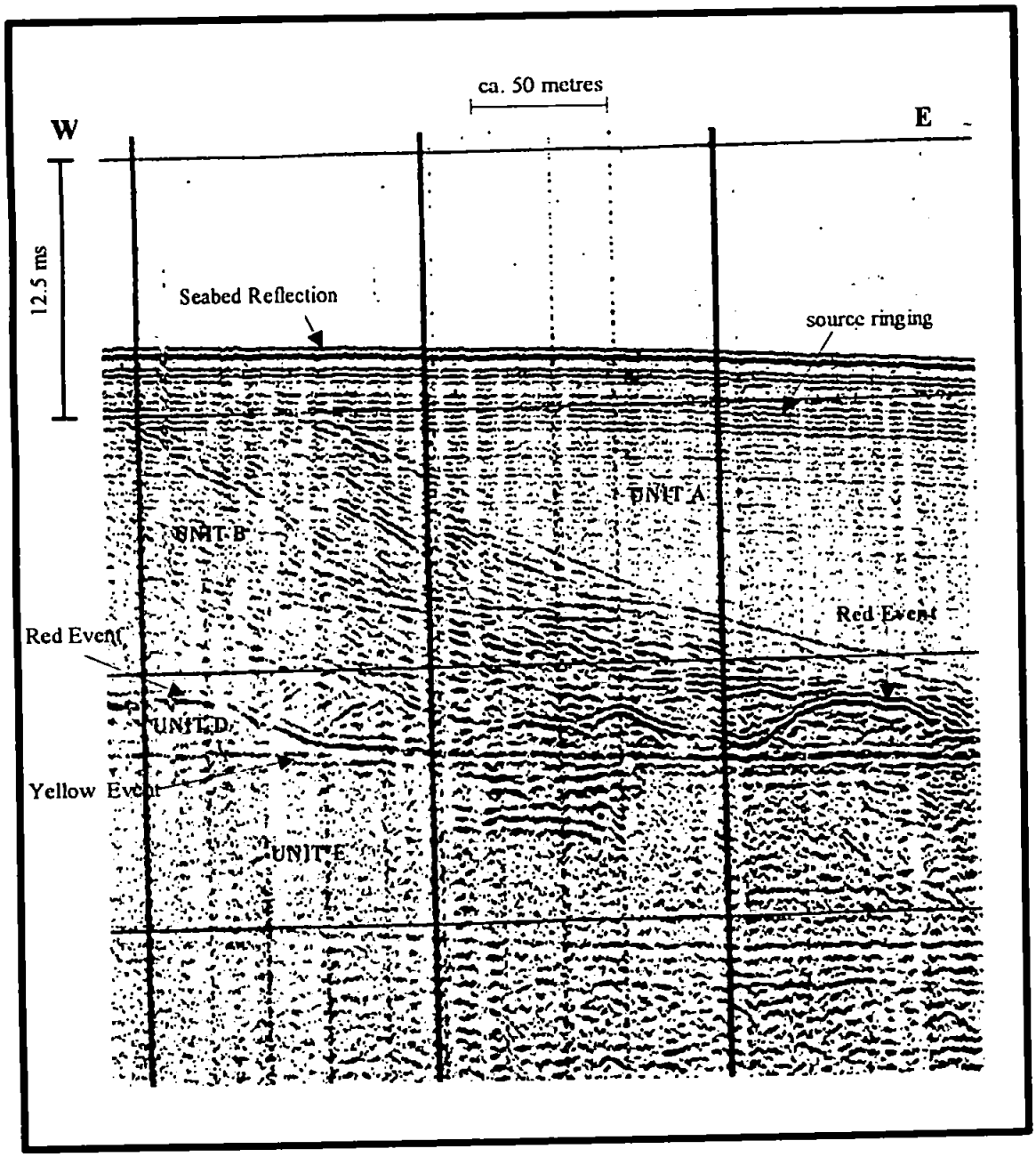

Figure 5.3 Seismic line 261(middle section) of 49/10 survey area

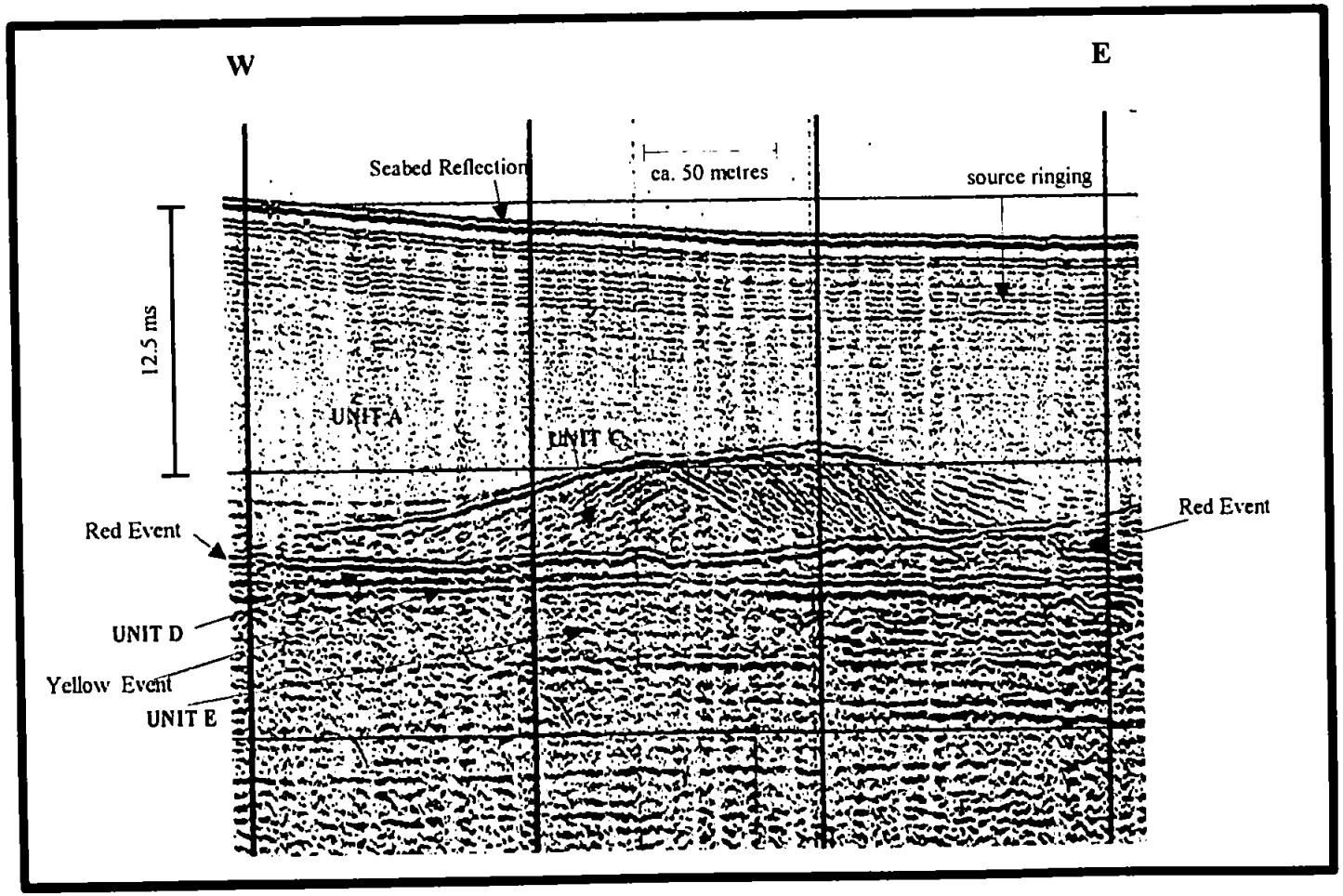

Figure 5.4 Seismic line 261 (east section) of 49/10 survey area

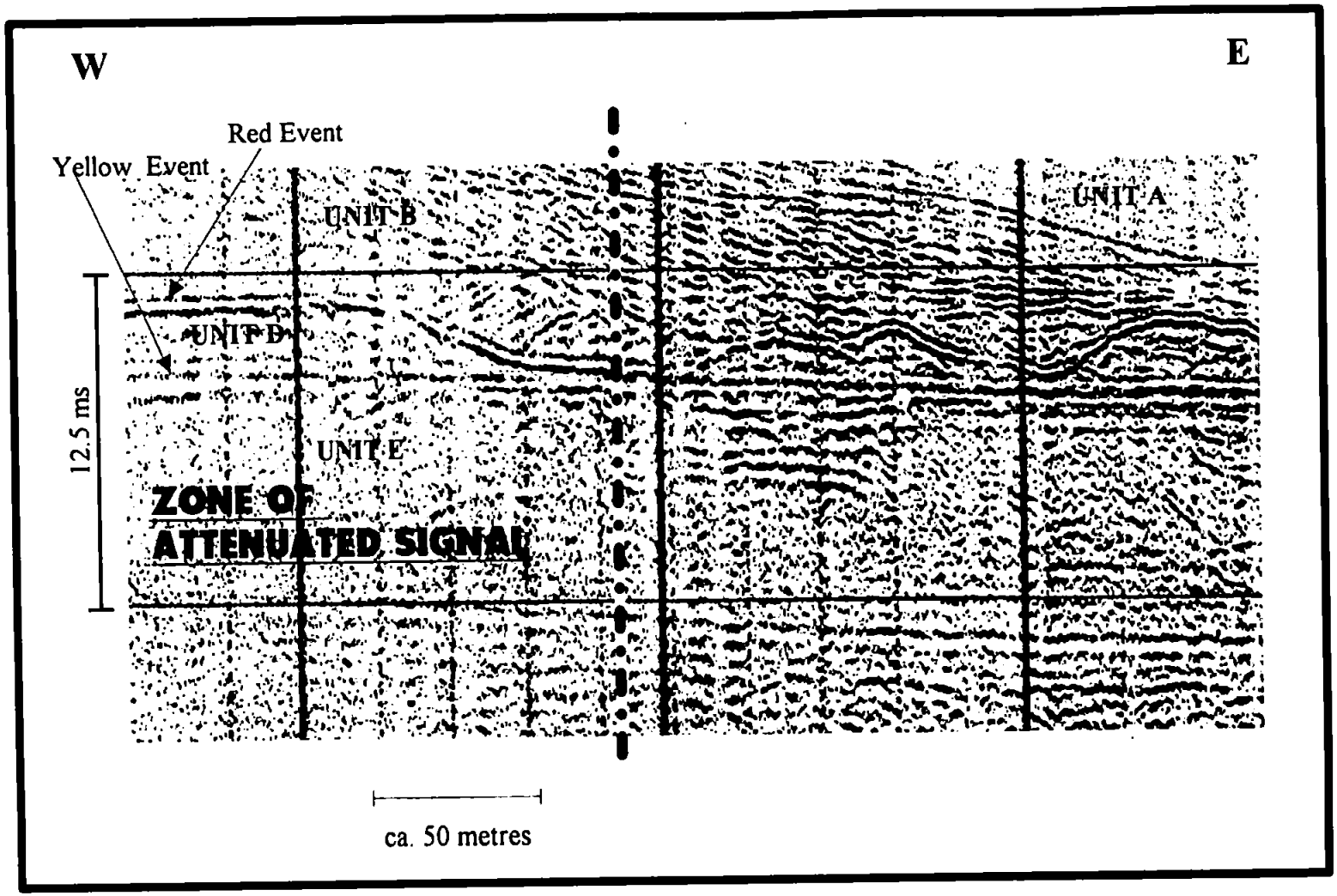

Figure 5.5 Zone of attenuated signal, line 261, 49/10 survey area.

and major reflectors of all the seismic units are weaker in this zone than to the east, and the Red and Yellow events appear somewhat broader (time thickness) in character. It is this feature of the data set that provides the potential for the analysis of spectral content of reflected events in the examination of frequency-selective attenuation. Further discussion of this feature is in section 5.5.

Line 247a (Figure 5.6) was run as a cross line to Line 261. All the seismic units mentioned above are visible on the section, with the exception of units B and C_1, which occur further west. Line 247a shows a more complete development of unit C_2 as discrete seismic features resting directly on the Red Event. Line 238a (Figure 5.7) intersects Line 261 towards the western end of line 262.Units B and C_1 are clearly identifiable above the Red and Yellow events, as is the amplitude loss beneath the Yellow Event.

The survey area is shown in Figure 5.8 in relation to the distribution of the major sub-Holocene Quaternary units in the region (after Cameron *et al.*,1986). The survey area lies across the sub-Holocene boundary between the Eem Formation to the south-east and the overlying Bolders Bank Formation to the north-west. The latter is known to be a blanket deposit of Weichselian till up to 15 metres thick, to be chaotic to poorly ordered on seismic profiles , and be between 39 and 45 metres below sea level (Cameron *et al.*, 1986). This base is characterised by a high-amplitude, flat or gently undulating reflector. In addition, where Holocene sediments overlie the Bolders Bank Formation, they comprise clean sand or sandy gravel, and are known to be less than 2 metres thick. None of the units lying above the Red Event (A,B,C_1 and C_2) are considered to have those seismic characteristics that would arise from such a till deposit *i.e.* having a chaotic internal structure with numerous scatterers. Given a minimum average velocity of 1500 ms^{-1} and a maximum of 1700 ms^{-1} the Red Event occurs at between 38.5 m and 43.5 m below sea level, whilst the Yellow Event occurs between 40 m and 45.5 m below sea level. Both events are at a depth at which the major subglacial erosion surface could have occurred. Seismic unit D, although thin, has a structureless to chaotic internal structure. Thus the Red and Yellow events may represent strong, sub-horizontal acoustic boundaries of a thin seismic unit corresponding to the eastern outlier of the Bolders Bank Formation, or the

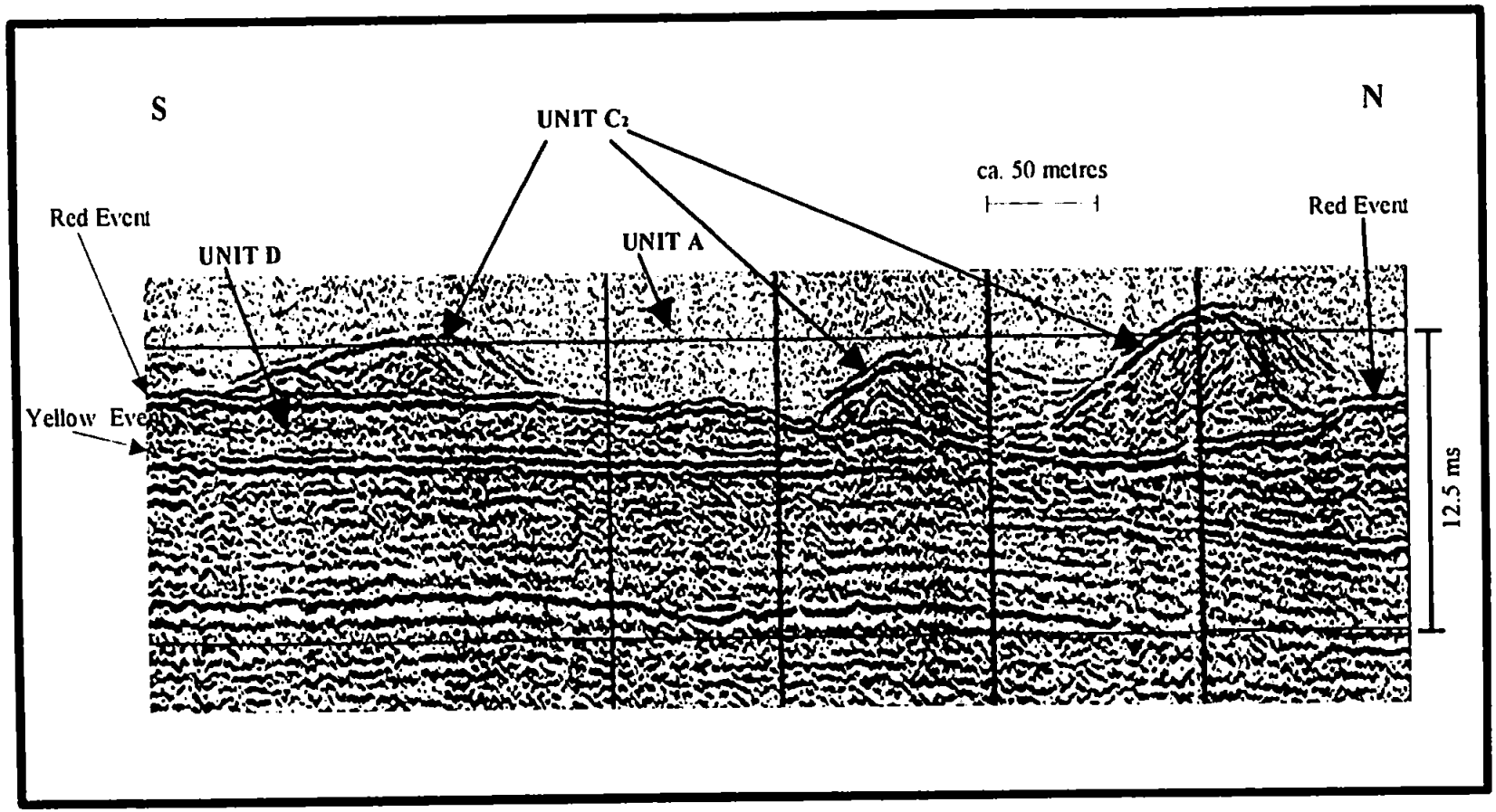

Figure 5.6 Part of seismic line 247a, 49/10 survey area.

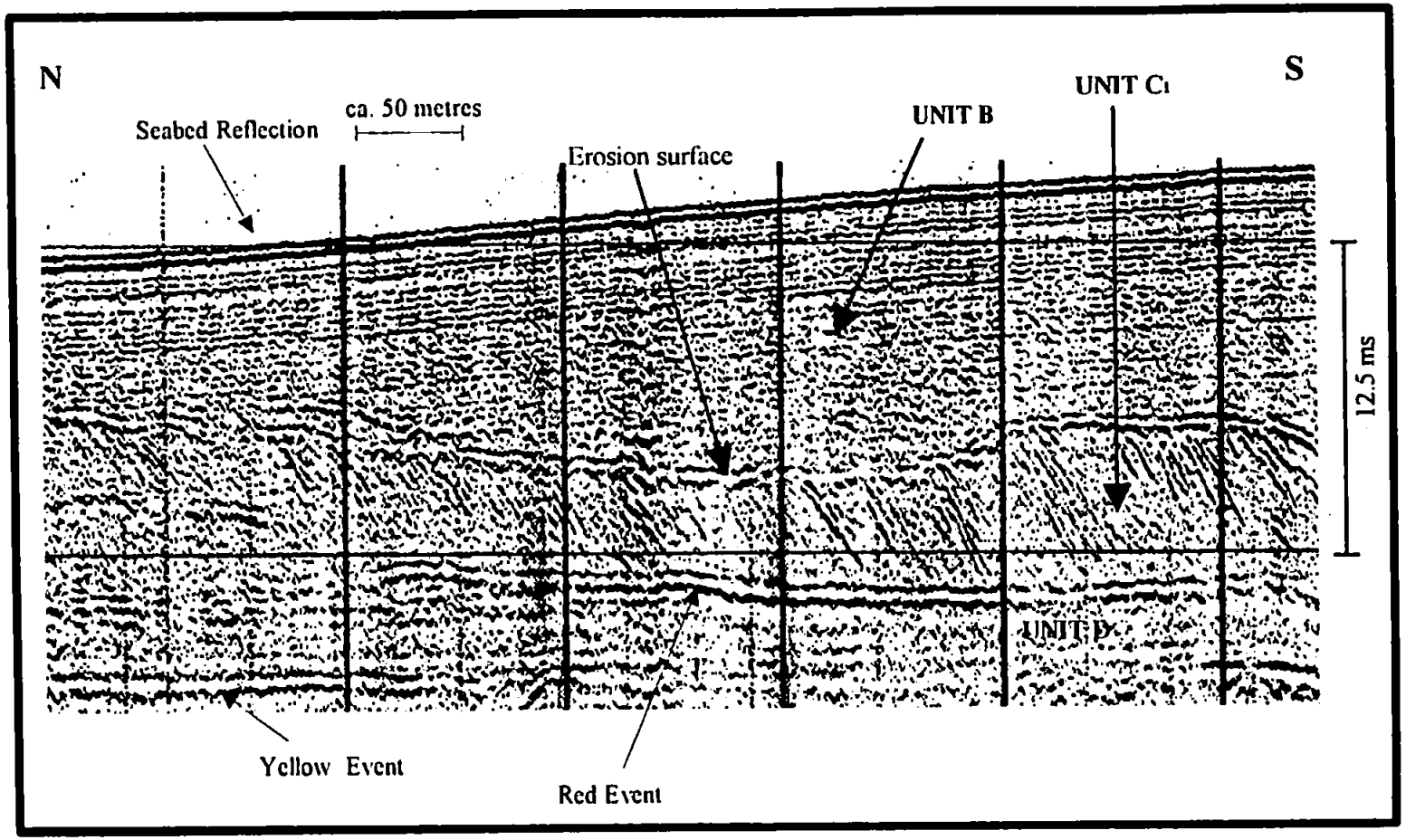

Figure 5.7 Part of seismic line 238a, 49/10 survey area.

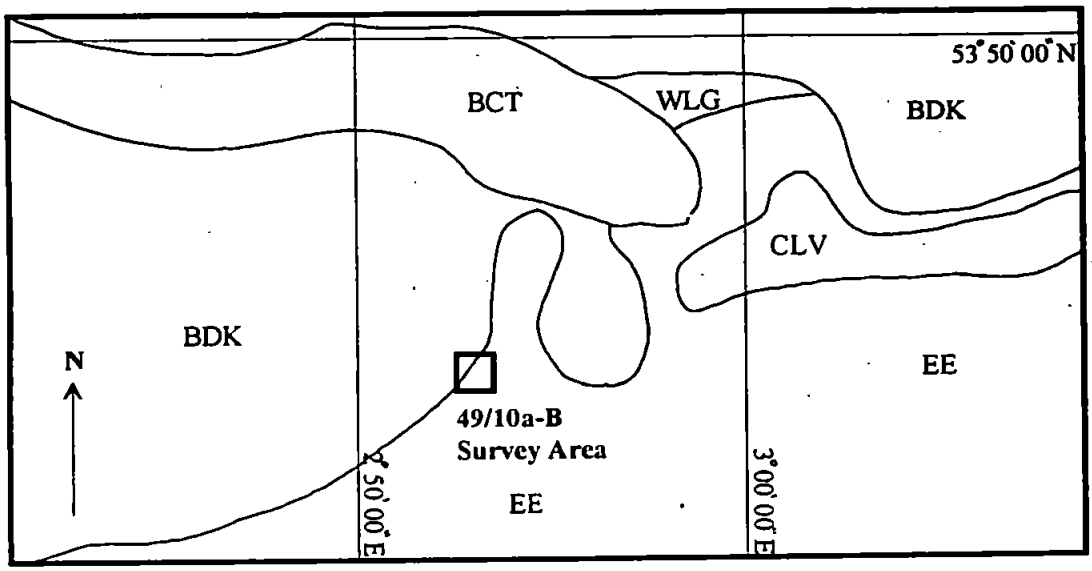

BCT Botney Cut Formation
BDK Boulders Bank Formation
EE Eem Formation
CLV Cleaver Bank Formation
WLG Well Ground Formation

Figure 5.8 Position of 49/10 survey area relative to Quaternary geological formations of the region.

Red Event may represent a terrestrial surface upon which units C_1 and C_2 were developed. The seismic data shows the dune-like C_2 unit clearly developed on the Red Event. The dune-like features are between 50 and 200 metres in apparent length, and up to about 4.5 m in apparent height. The dune-shaped external morphology, and the internal structure suggest an aeolian or a fluvial genesis for these structures. These features may be a result of winds blowing around and over the ice sheet, being equivalent to the Twente Formation (Cameron et al.,1989), or may be a result of meltwater streams around the limits of the ice sheet (Well Ground Formation). This interpretation would be consistent with the survey area lying within a periglacial plain (Cameron et al., 1992) at the time of deposition of the Bolders Bank Formation. The survey area lay within a periglacial plain (dry land) at the maximum extent of the Weichselian ice maximum (Figure 5.1), that is at the time of deposition of the Bolders Bank Formation. Within this geological framework, units D, E and F would therefore be older than the Bolders Bank Formation, and would be geological units of the Eem Formation and older. Lines 261,262 and cross-line 238a show unit C_1 has well developed internal reflectors dipping steeply to the south-west, capped by an erosion surface (*e.g.* Figure 5.7). Whilst unit B indicates an eastwards sediment transport direction, C_1 shows foreset development which suggests a south-westwards transport direction. The internal structure of unit C_2 is insufficiently defined to determine a direction of development and the external morphology may be a result of erosion prior to the deposition of unit A rather than a dune-shape resulting from fluvial or aeolian deposition. Units B and A are interpreted as water-lain deposits following the general sea-level rise associated with the decay of the late Weichselian ice sheets. The genetic aspect of unit B is difficult to determine, but it does appear to have an erosive contact with C_1 indicating a non-terrestrial origin. Unit B may have been deposited either as a result of meltwater stream deposition or been deposited at a later (transgressive) time , perhaps within an intertidal channel. If the Red Event is taken to be the Weichselian land surface (periglacial plain), then units D, E and F are likely to represent marine or lacustrine sediments deposited during the Eemian stage.

5.4.4 Geological Summary

A basic geological model has been developed for the seismic stratigraphy of the limited survey area. The Red Event on the seismic sections is interpreted as representing a terrestrial surface upon which dune formation took place during periglacial conditions to the south-east of a Weichselian ice-sheet. The seismic units beneath the Red Event are likely to be of pre-Weichselian marine or lacustrine origin, whilst those above are related to the sea-level rise following the decay of the ice sheet. This is a general interpretation based on a data set with little geological sampling, which largely arises from the identification of a terrestrial erosion surface coupled with terrestrial deposition at a depth corresponding to the periglacial plain proposed by Cameron et al., (1992).

5.5 Numerical Analysis

5.5.1 Introduction

Units A and B differ in seismic character in two ways. Firstly, unit A is devoid of internal structure whereas unit B is visibly layered. Secondly, the lower bounding reflector of unit A is relatively narrow in time thickness (0.5 ms TWTT), in contrast to the broader appearance of that beneath unit B (0.7 ms TWTT). In addition, the general amplitudes of reflected events tend to be much lower beneath unit B than beneath unit A. The aim of the following numerical analysis to examine the data in order to obtain an estimate of the spectral characteristics of the upper and lower bounding reflections of units A and B. In turn, the frequency-selective attenuation characteristics (if any) of the sediments making up these units will be determined using the methods previously outlined in Chapter 4.

A total of 18 stations ('areas') are used, 8 for the spectral analysis of unit A and a further 10 for Unit B. Area 1 will be discussed in detail to show the method of data analysis.

5.5.2 Area 1 - Spectral Measurements

Figure 5.9 shows the western end of Line 262 from the survey area. The digital data from the zone marked A-A' was selected to represent the upper and lower bounding reflectors for unit B. For the analysis, the data was windowed from just above the seabed reflector, to 25 ms later in the section. In this instance, the lower bounding reflector is the Red Event described in section 5.4. The seabed and Red Event reflection events are separated by about 16 ms TWTT, representing a sediment thickness of about 12 to 13 metres. The digital data are represented in Figures 5.10. The seabed reflection is clearly very high in amplitude (ca. 2000 units arbitrary units peak to peak) whilst the Red Event is much lower (ca. 150 units peak to peak). Each of the 40 traces were used as input into the computer programs described in Chapter 4.

The appearance of the Red Event in Figure 5.10 is one of a discrete, but laterally

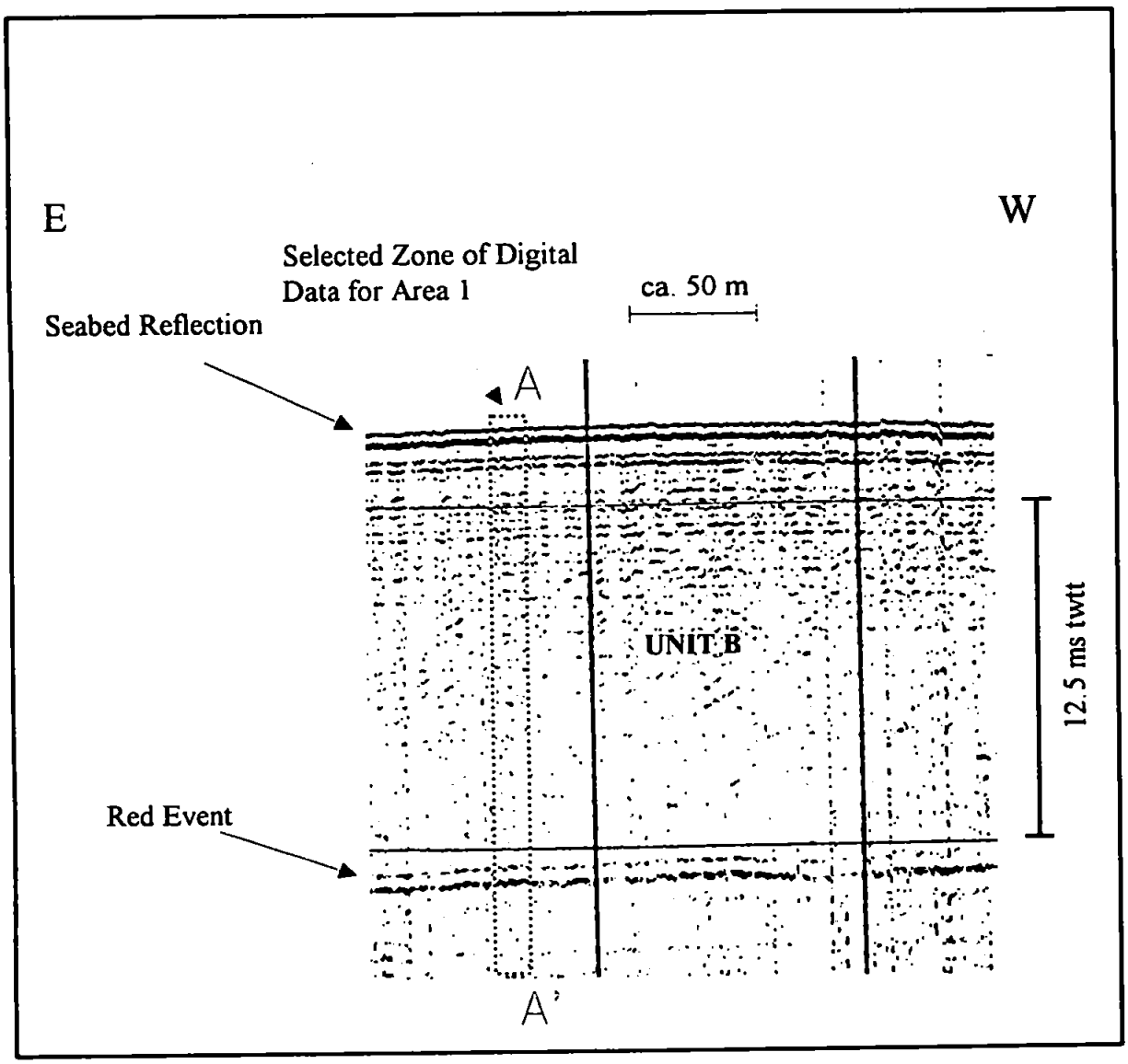

Figure 5.9. Western end of line 262, Area1, 49/10 survey area.

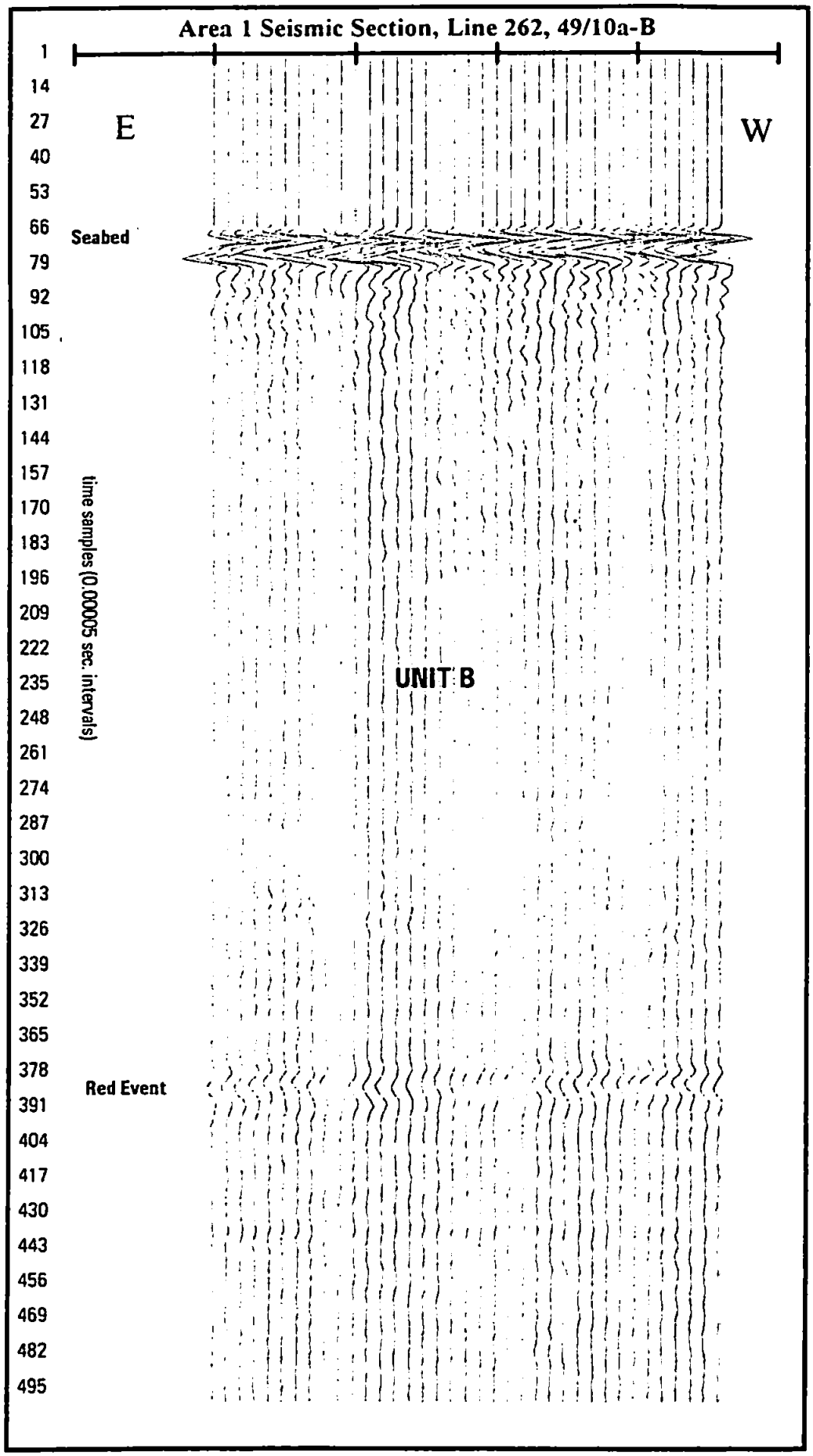

Figure 5.10 Detail of seismic line 262, Area 1, 49/10 survey area.

variable reflected event. The reflected pulse appears to be weaker within the middle section and stronger towards the margins, particularly to the east.

The data were analysed using the wavelet modelling, spectrum modelling and matching methods. The data was processed on a trace-by-trace basis to yield individual Q measurements. These measurements were summed to give a mean Q estimate for each particular method.

Three example traces, numbers 2, 3 and 4 are shown to show the computational procedure used. Figures 5.11a to 5.11c shows the results of wavelet modelling of the three traces, which yields a synthetic pulse, a Q-estimate, and a value for the TWTT of the Red Event relative to the seabed event. The original traces are shown, along with the optimum-fit synthesised wavelets. A detailed comparison of the observed and synthesised Red Event wavelets is shown in Figure 5.12 . The amplitude spectra of the two events were then determined using the FFT. The signal-to-noise ratios of the two events were estimated by dividing the spectral amplitudes across the complete spectra by the mean amplitudes of the non-signal, high-frequency parts of the spectra (Figure 5.13a to 5.13c). The noise-tail was taken to be from 8 kHz to 10 kHz for the seabed, and 6 kHz to 10 kHz for the Red Event. An estimation of the spectral coherence between the two events was then calculated (Figure 5.14a to 5.14c). From the spectral coherence, the band across which spectrum modelling and the matching technique could be applied was determined. The results of spectrum modelling of the three example traces, showing the seabed, Red Event and synthetic spectra up to 3 kHz are shown in Figures 5.15a to 5.15c. Figures 5.16a to 5.16c show the smoothed spectral ratios for the example traces. For this case study, a spectral smoothing factor of 16 was used; the spectrum being averaged over 16 frequency 'bins', each having a width of 625 Hz. The 95% and 5% confidence limits for the resulting spectral ratios are shown in Figures 5.16a to 5.16c. A line was fitted to a selected part of the spectrum chosen for its high spectral coherence, the slope of which yielded the quality factor, Q. The above procedure was carried out for all of the traces for Area 1. The estimates of Q determined from the wavelet and spectrum modelling and matching are presented in Figure 5.17 .

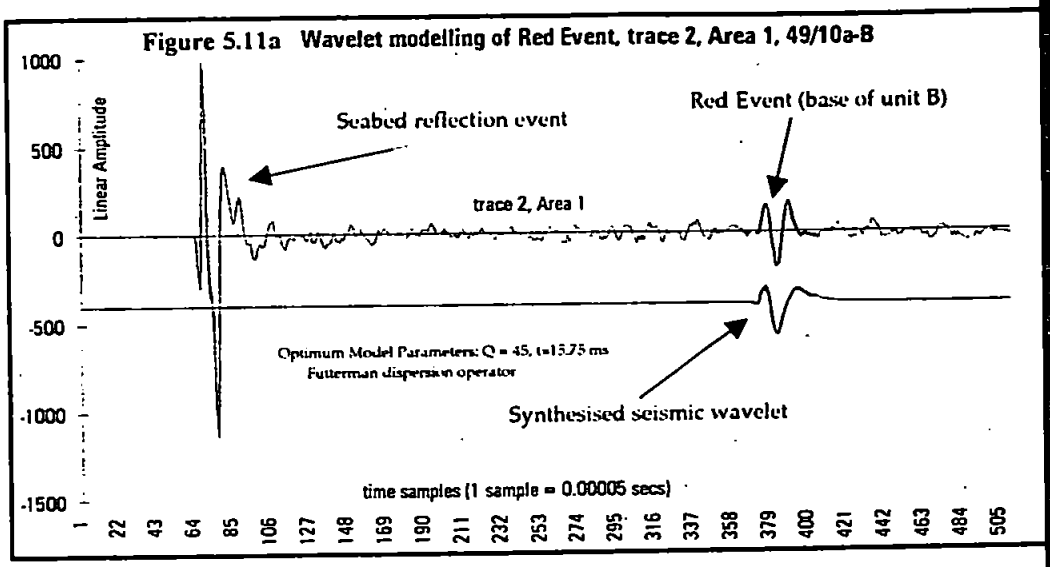
Figure 5.11a Wavelet modelling of Red Event, trace 2, Area 1, 49/10a-B
Seabed reflection event
Red Event (base of unit B)
trace 2, Area 1
Linear Amplitude
Optimum Model Parameters: Q = 45, t=15.75 ms
Futterman dispersion operator
Synthesised seismic wavelet
time samples (1 sample = 0.00005 secs)

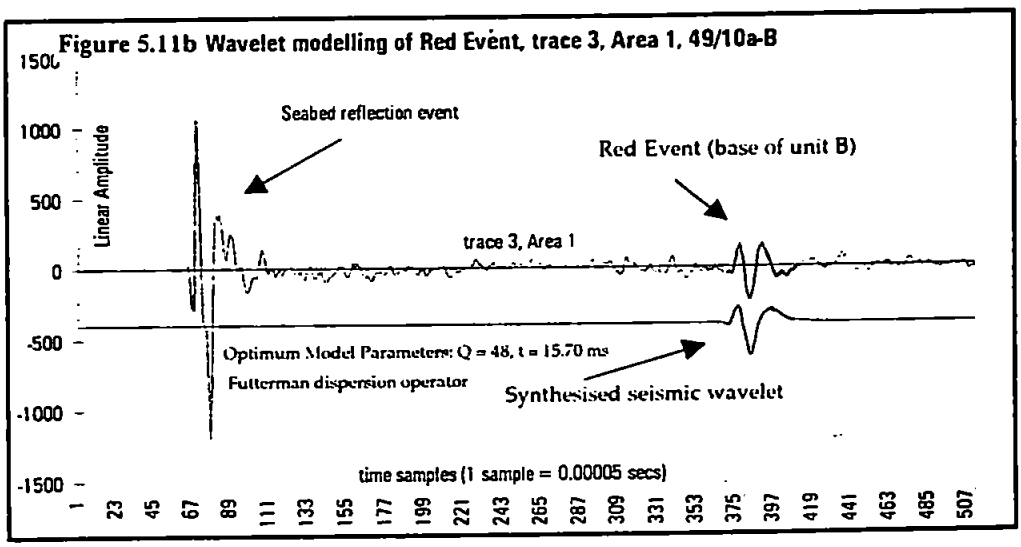
Figure 5.11b Wavelet modelling of Red Event, trace 3, Area 1, 49/10a-B
Seabed reflection event
Red Event (base of unit B)
trace 3, Area 1
Linear Amplitude
Optimum Model Parameters: Q = 48, t = 15.70 ms
Futterman dispersion operator
Synthesised seismic wavelet
time samples (1 sample = 0.00005 secs)

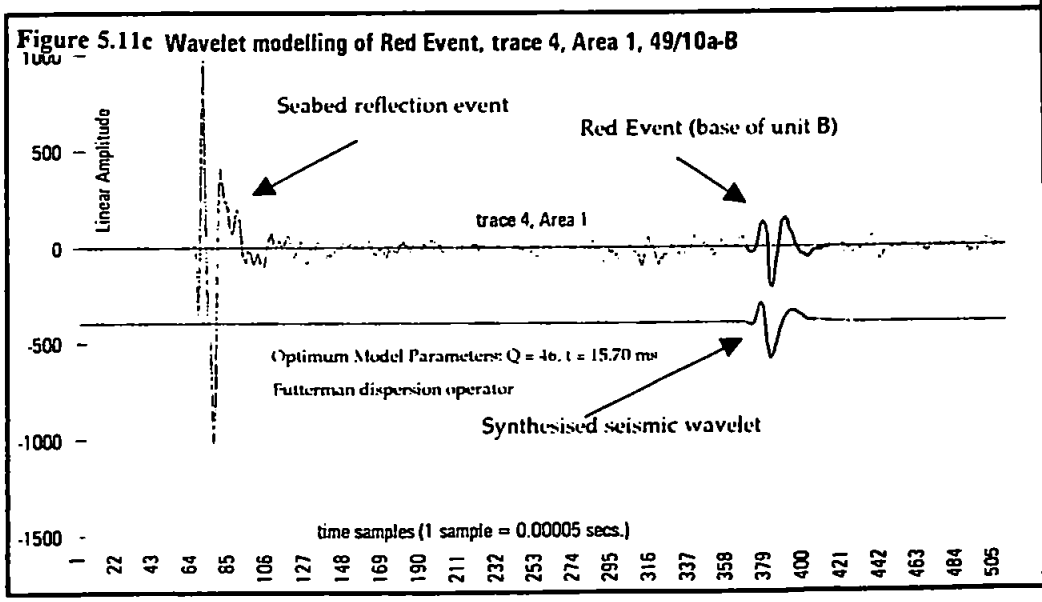
Figure 5.11c Wavelet modelling of Red Event, trace 4, Area 1, 49/10a-B
Seabed reflection event
Red Event (base of unit B)
trace 4, Area 1
Linear Amplitude
Optimum Model Parameters: Q = 46, t = 15.70 ms
Futterman dispersion operator
Synthesised seismic wavelet
time samples (1 sample = 0.00005 secs.)

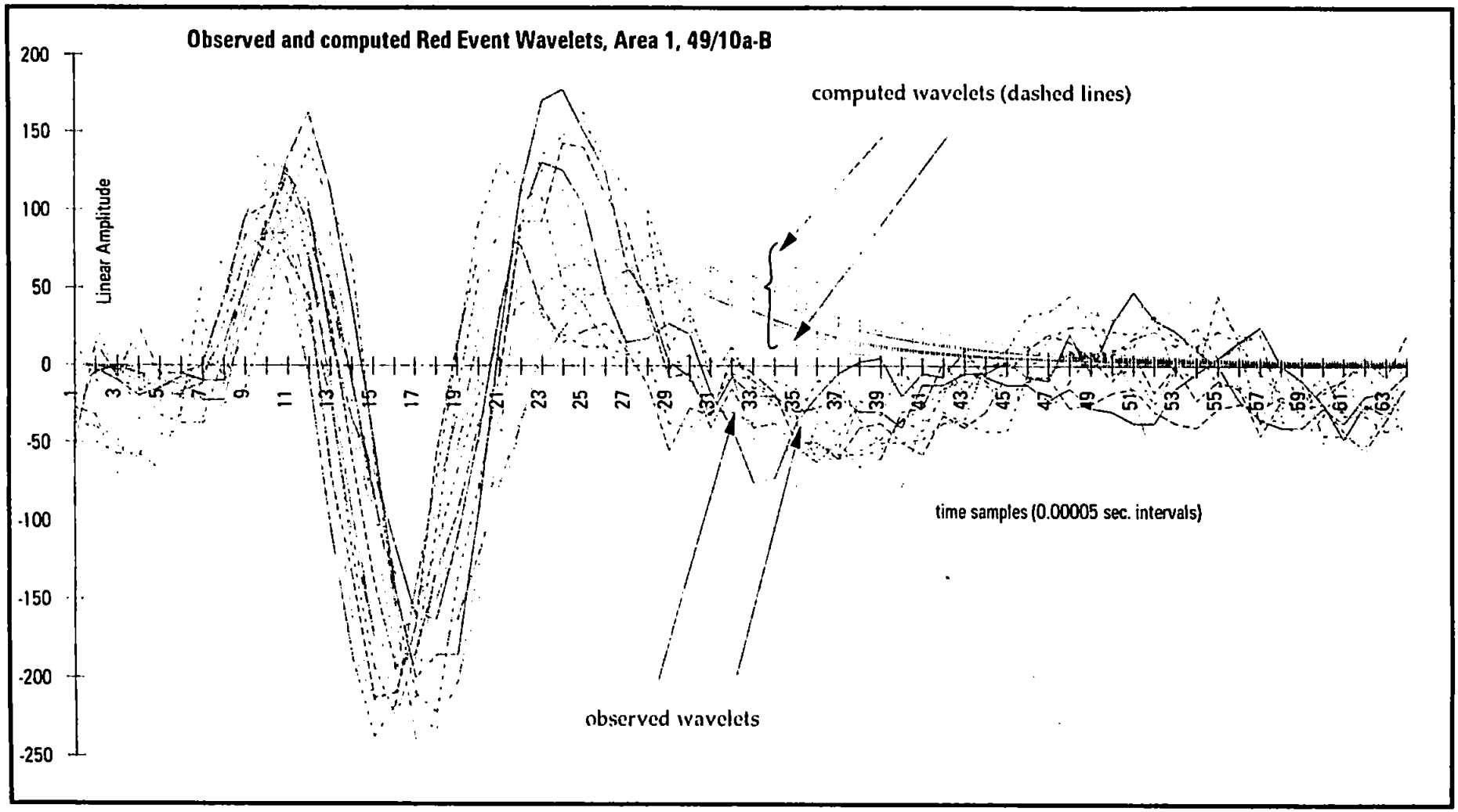

Figure 5.12 Observed and computed Red Event wavelets, Area 1, 49/10 survey area.

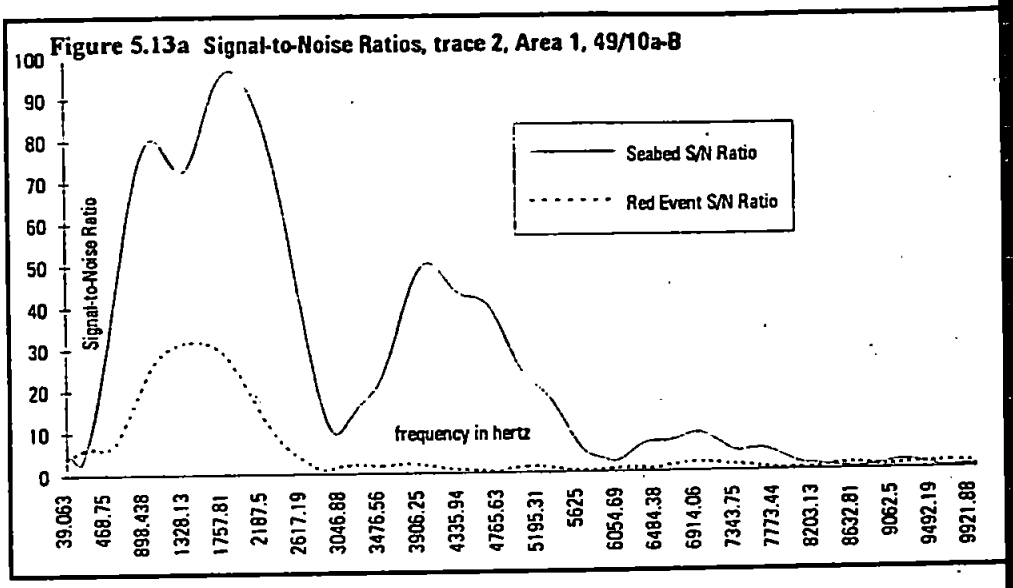
Figure 5.13a Signal-to-Noise Ratios, trace 2, Area 1, 49/10a-B
Seabed S/N Ratio
Red Event S/N Ratio
Signal-to-Noise Ratio
frequency in hertz
100
90
80
70
60
50
40
30
20
10
0
39.063
468.75
898.438
1328.13
1757.81
2187.5
2617.19
3046.88
3476.56
3906.25
4335.94
4765.63
5195.31
5625
6054.69
6484.38
6914.06
7343.75
7773.44
8203.13
8632.81
9062.5
9492.19
9921.88

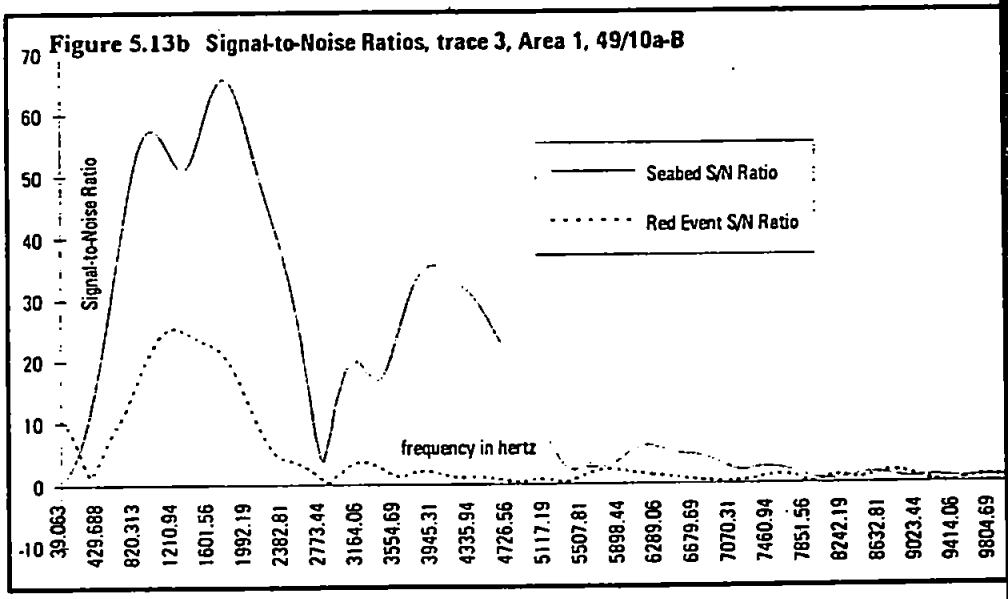
Figure 5.13b Signal-to-Noise Ratios, trace 3, Area 1, 49/10a-B
Seabed S/N Ratio
Red Event S/N Ratio
Signal-to-Noise Ratio
frequency in hertz
70
60
50
40
30
20
10
0
-10
39.063
429.688
820.313
1210.94
1601.56
1992.19
2382.81
2773.44
3164.06
3554.69
3945.31
4335.94
4726.56
5117.19
5507.81
5898.44
6289.06
6679.69
7070.31
7460.94
7851.56
8242.19
8632.81
9023.44
9414.06
9804.69

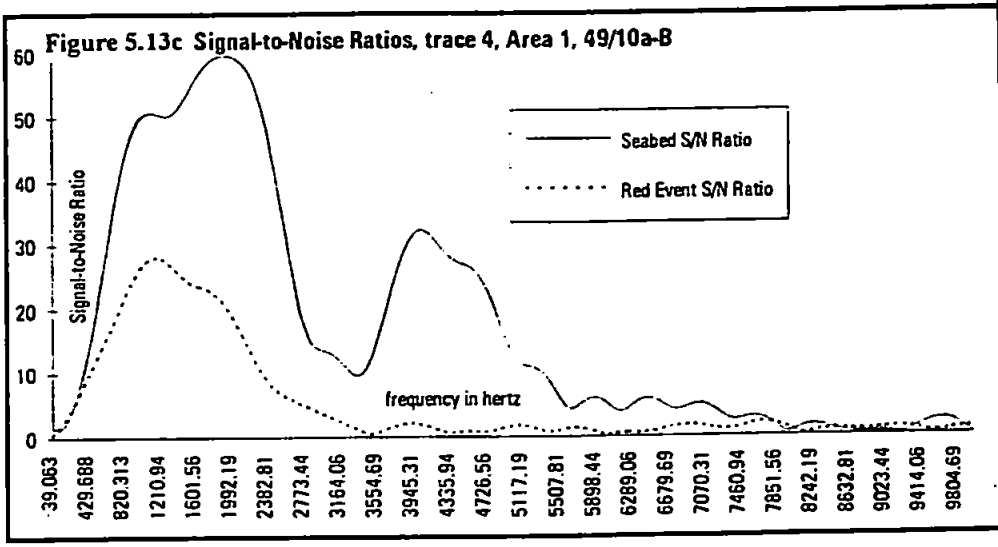
Figure 5.13c Signal-to-Noise Ratios, trace 4, Area 1, 49/10a-B
Seabed S/N Ratio
Red Event S/N Ratio
Signal-to-Noise Ratio
frequency in hertz
60
50
40
30
20
10
0
39.063
429.688
820.313
1210.94
1601.56
1992.19
2382.81
2773.44
3164.06
3554.69
3945.31
4335.94
4726.56
5117.19
5507.81
5898.44
6289.06
6679.69
7070.31
7460.94
7851.56
8242.19
8632.81
9023.44
9414.06
9804.69

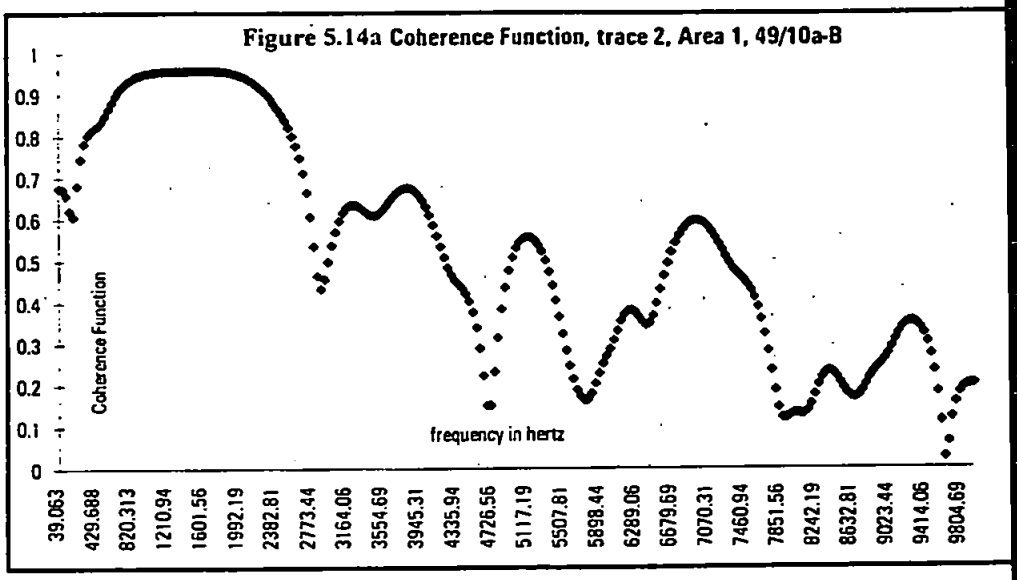

Figure 5.14a Coherence Function, trace 2, Area 1, 49/10a-B

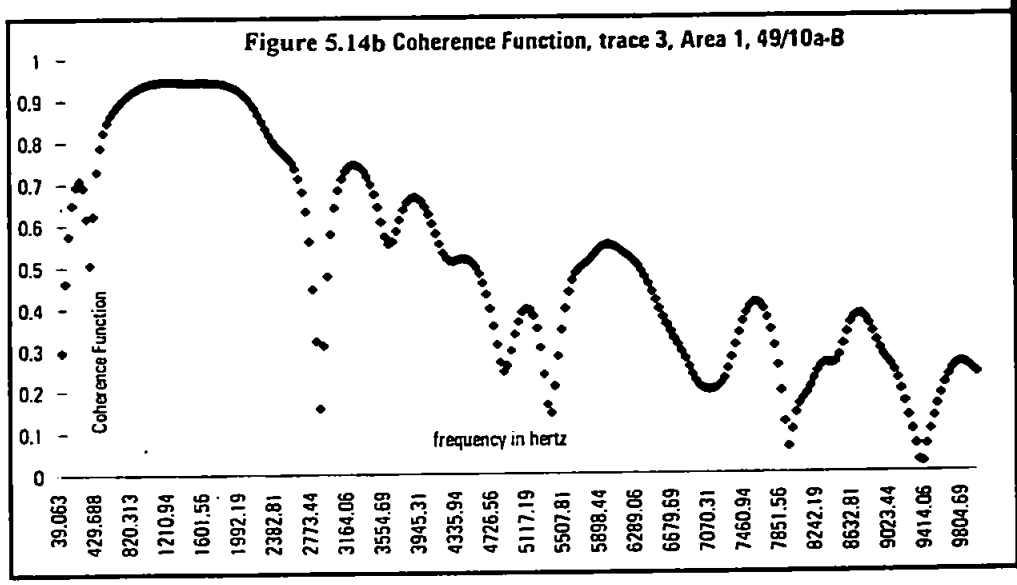

Figure 5.14b Coherence Function, trace 3, Area 1, 49/10a-B

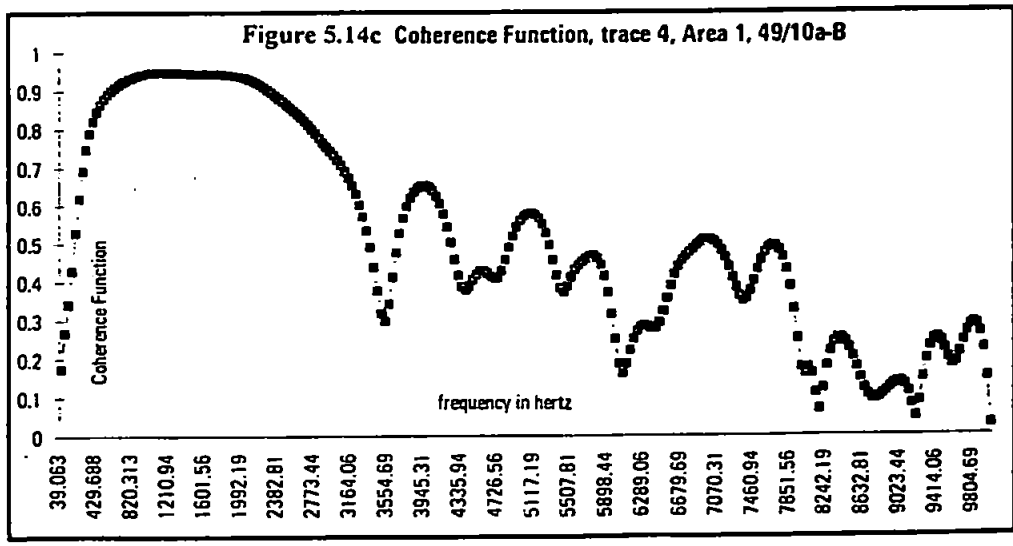

Figure 5.14c Coherence Function, trace 4, Area 1, 49/10a-B

Figure 5.15a Spectrum modelling of Red Event, trace 2, Area 1, 49/10 survey area.

Figure 5.15b Spectrum modelling of Red Event, trace 3, Area 1, 49/10 survey area.

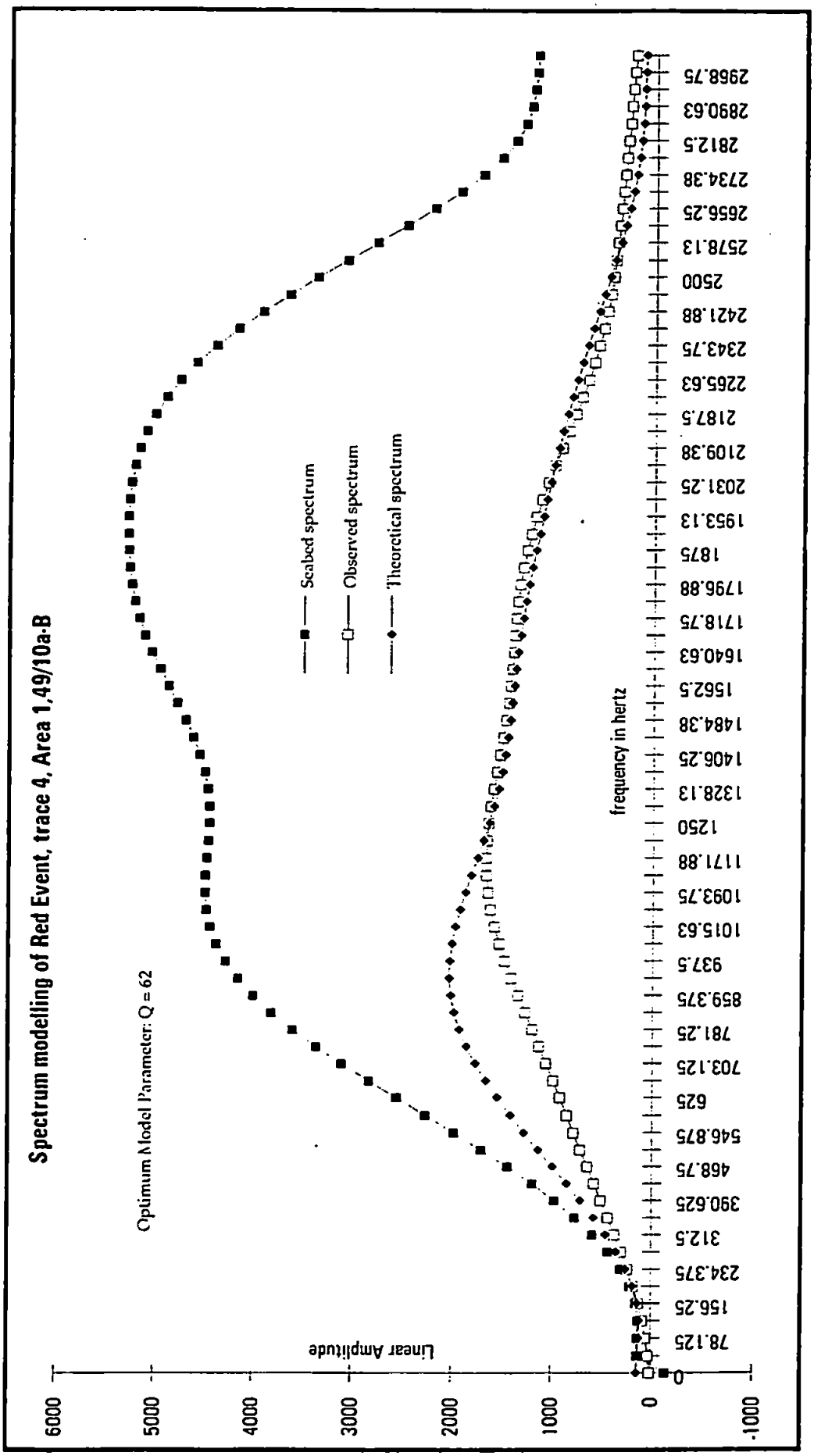

Figure 5.15c Spectrum modelling of Red Event, trace 4, Area 1, 49/10 survey area.

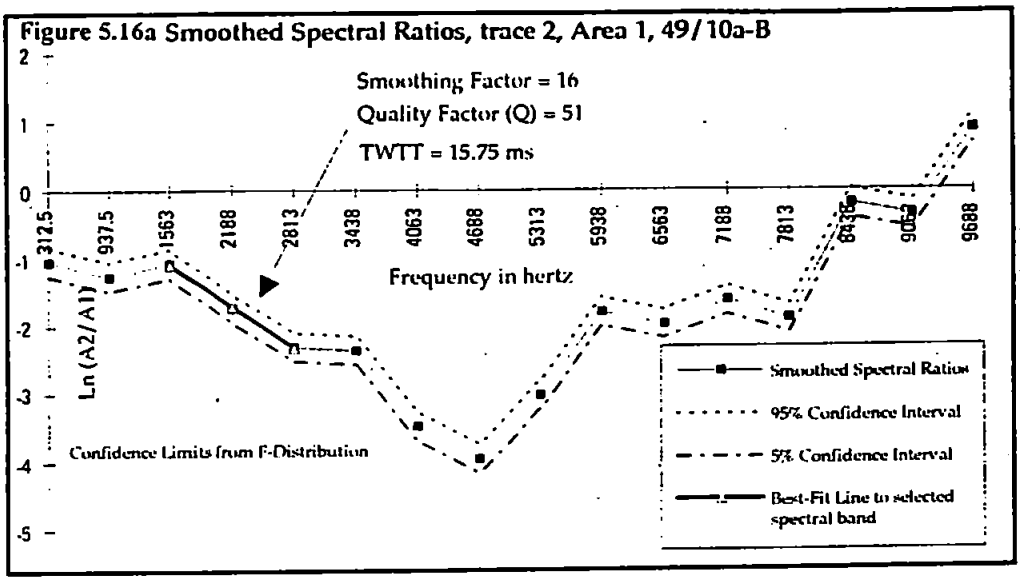
Figure 5.16a Smoothed Spectral Ratios, trace 2, Area 1, 49/10a-B
Smoothing Factor = 16
Quality Factor (Q) = 51
TWTT = 15.75 ms
Frequency in hertz
Ln (A2/A1)
Confidence Limits from F-Distribution
Smoothed Spectral Ratios
95% Confidence Interval
5% Confidence Interval
Best-Fit Line to selected spectral band

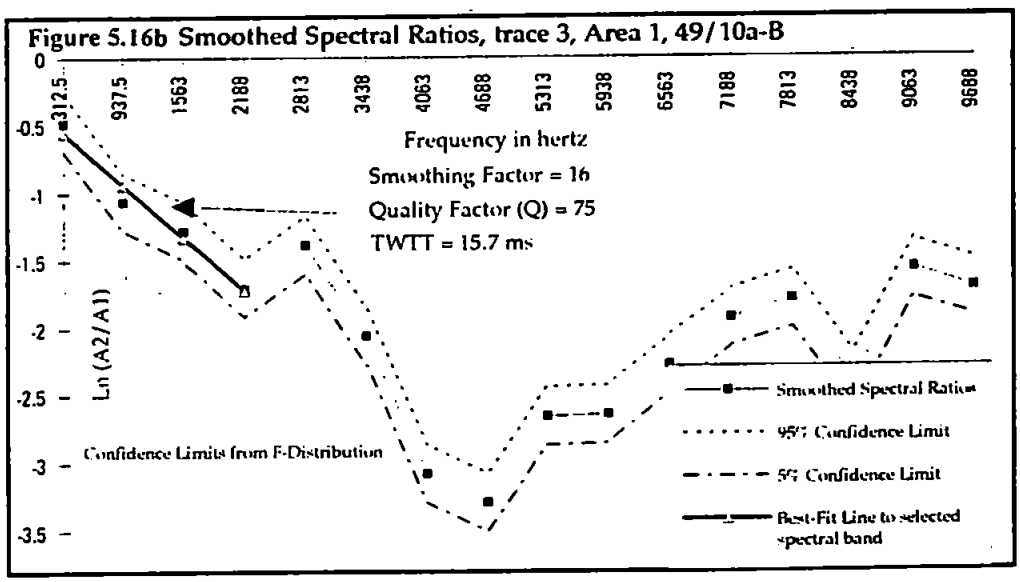
Figure 5.16b Smoothed Spectral Ratios, trace 3, Area 1, 49/10a-B
Frequency in hertz
Smoothing Factor = 16
Quality Factor (Q) = 75
TWTT = 15.7 ms
Ln (A2/A1)
Confidence Limits from F-Distribution
Smoothed Spectral Ratios
95% Confidence Limit
5% Confidence Limit
Best-Fit Line to selected spectral band

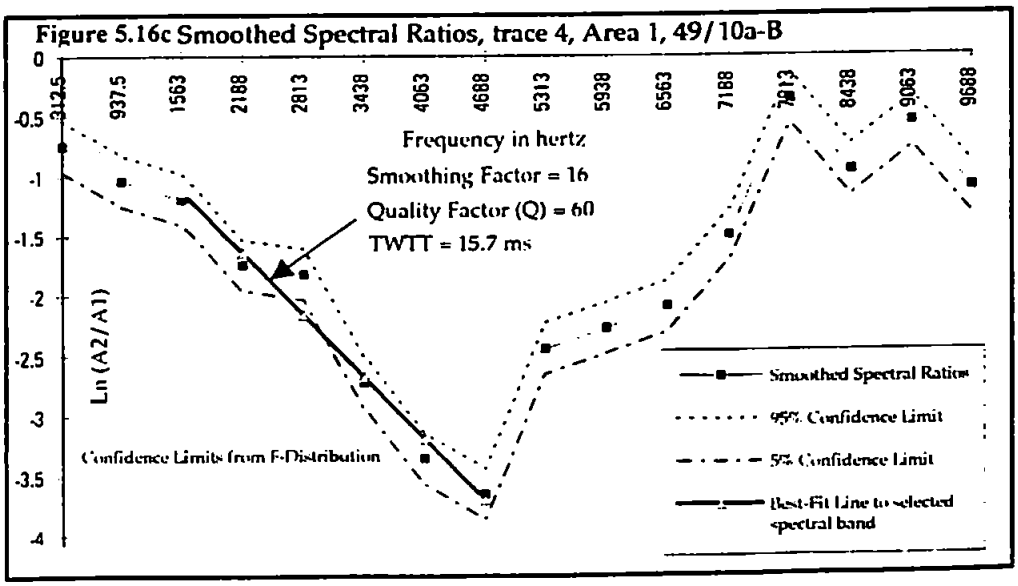
Figure 5.16c Smoothed Spectral Ratios, trace 4, Area 1, 49/10a-B
Frequency in hertz
Smoothing Factor = 16
Quality Factor (Q) = 60
TWTT = 15.7 ms
Ln (A2/A1)
Confidence Limits from F-Distribution
Smoothed Spectral Ratios
95% Confidence Limit
5% Confidence Limit
Best-Fit Line to selected spectral band

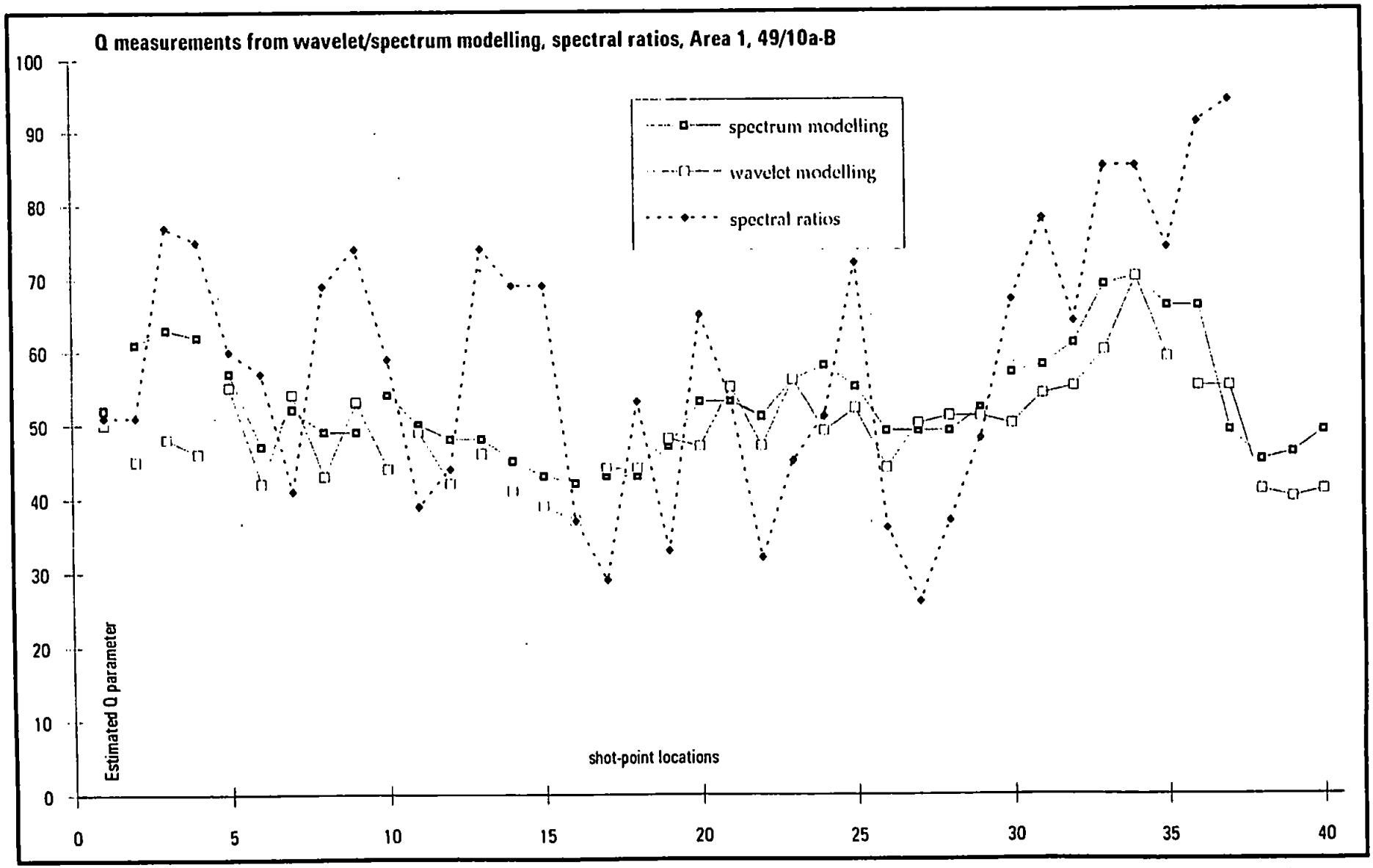

Figure 5.17 Q measurements from wavelet/spectrum modelling and spectral ratios, Area 1, 49/10 survey area.

Across Area 1, the mean quality factor value for individual wavelet modelling of each trace was 49 (see Figure 5.12 for observed and synthetic wavelets), with a standard deviation of 6.7 . The mean value from spectrum modelling was 53 with a standard deviation of 7.3 . Fifteen observed Red Event spectra are presented in Figure 5.18. The results of the matching technique show a mean quality factor of 53, with a standard deviation of 19.1 . The traces were then aligned and stacked into one normalised trace to provide an average trace to represent Area 1. Wavelet modelling (Figure 5.19) yielded a value of 51 for Q. Spectrum modelling (Figure 5.20) yielded a value for Q of 58, whilst the matching technique yielded a value for Q of 50 (Figure 5.21). The results are summarised below in Table 5.2 .

Table 5.2: Comparison of Q measurements, Area 1, 49/10

Method	***Q*-estimate**
Wavelet Modelling (mean of individual traces)	49
Spectrum Modelling (mean of individual traces)	53
Matching Technique (mean of individual traces)	53
Wavelet Modelling (stacked trace)	51
Spectrum Modelling (stacked trace)	58
Matching Technique (stacked trace)	50
Overall mean Q^{-1}	**0.0192**
Overall mean Q	**52**

Figure 5.18 Red Event spectra (15 traces), Area 1, 49/10 survey area.

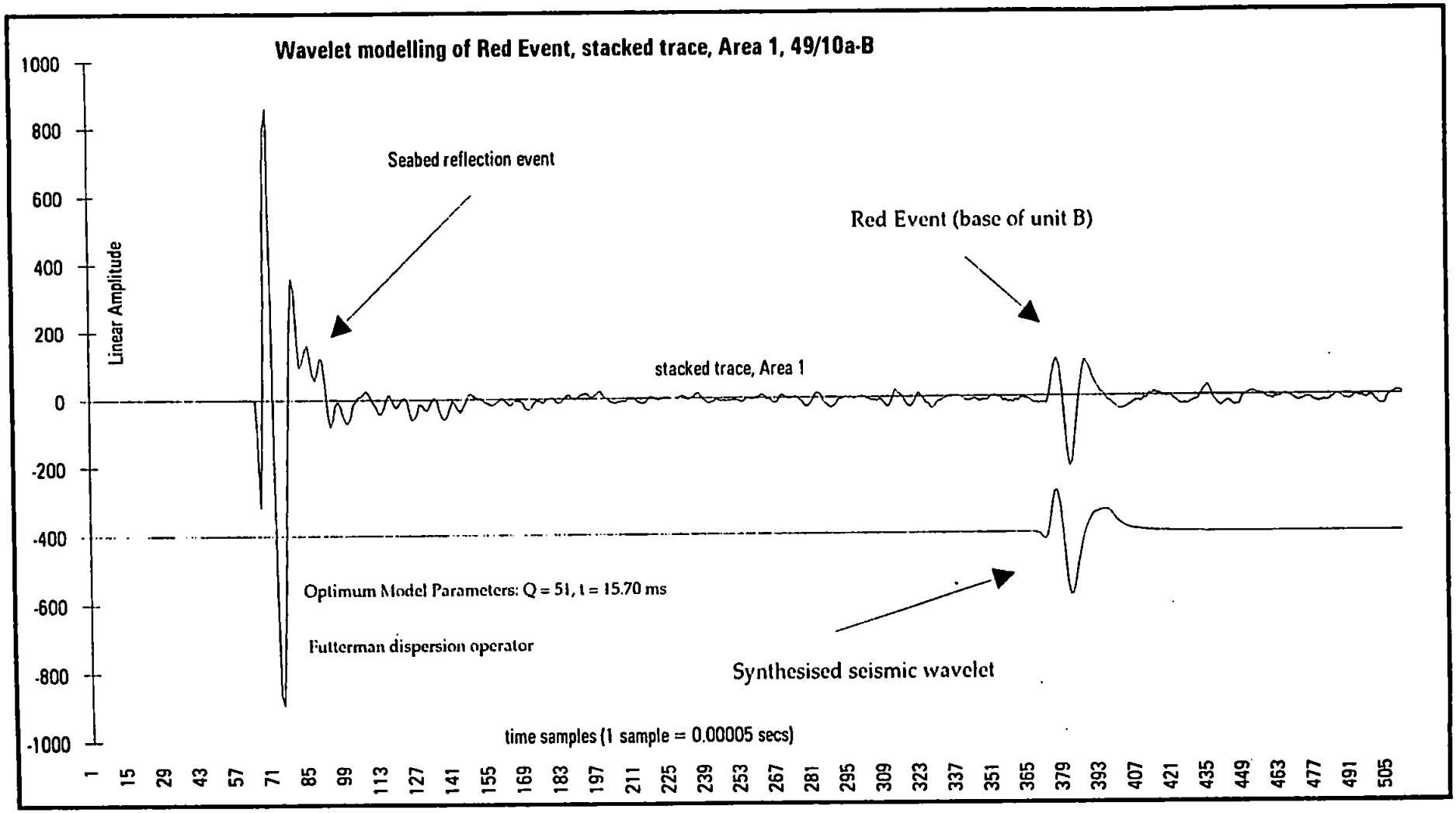

Figure 5.19 Wavelet modelling of Red Event, stacked trace, Area 1, 49/10 survey area.

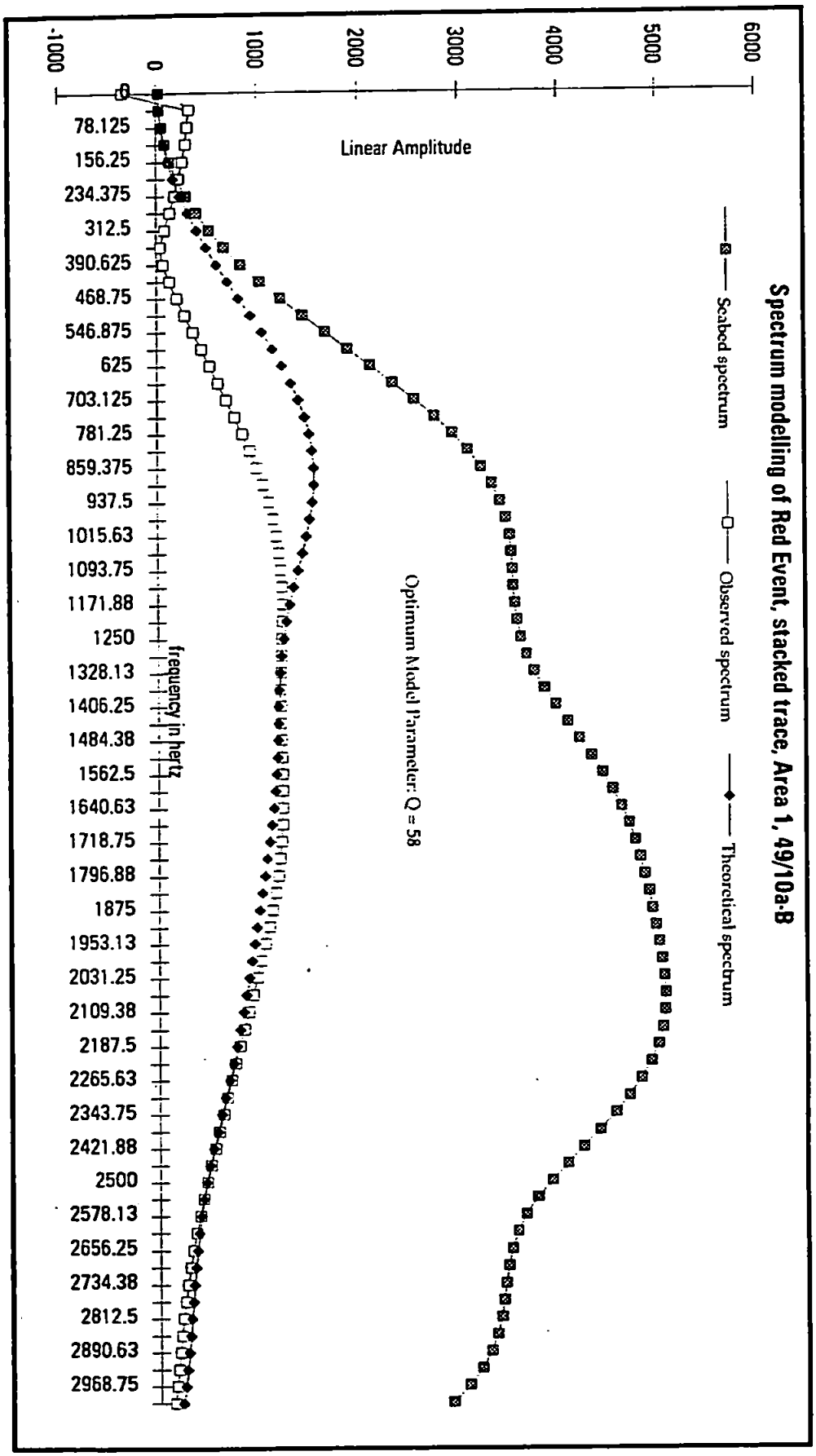

Figure 5.20 Spectrum modelling of Red Event, stacked trace, Area 1, 49/10 survey area.

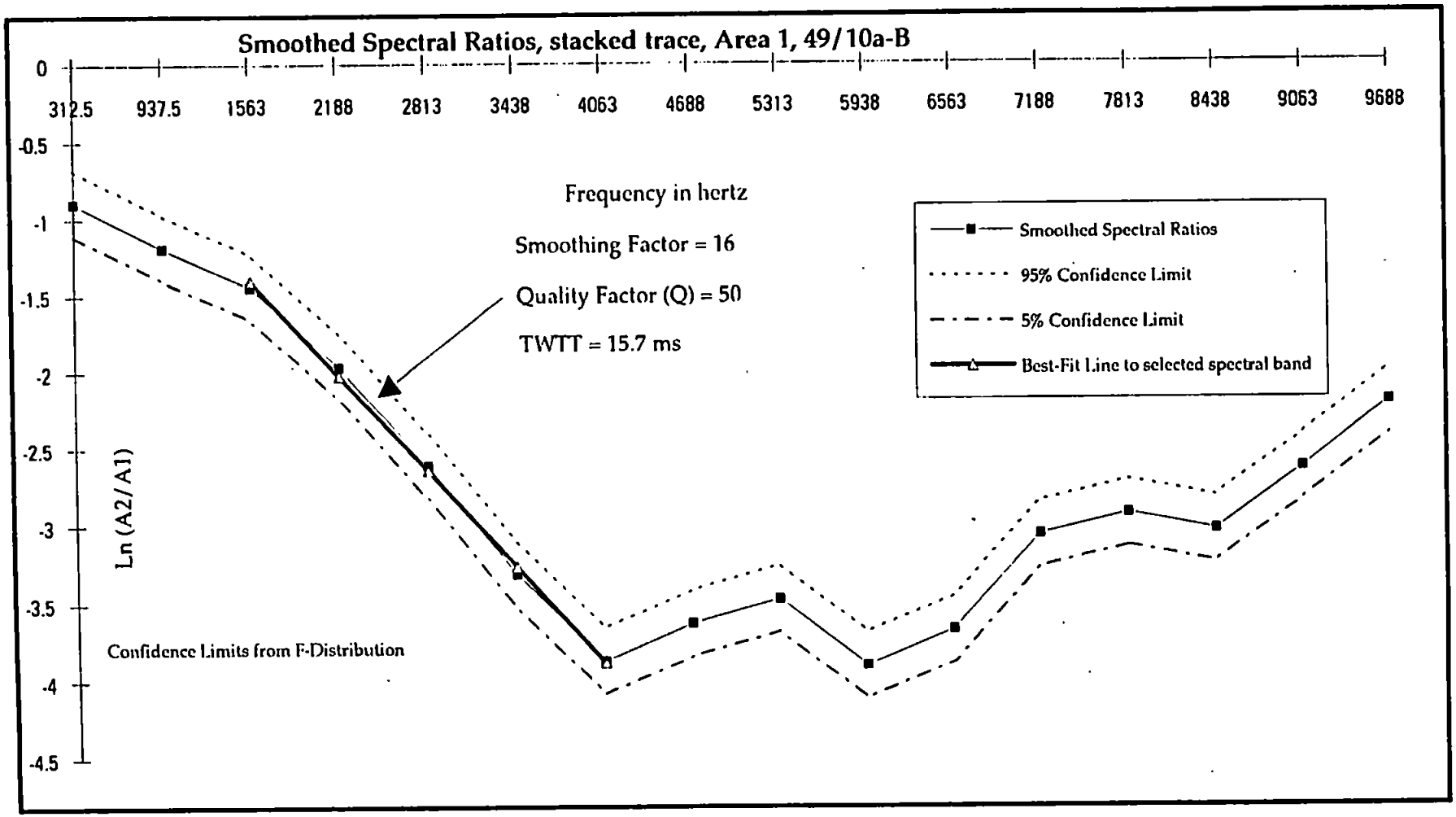

Figure 5.21 Smoothed spectral ratios, stacked trace, Area 1, 49/10 survey area.

5.5.3 Discussion - Area 1

The signal-to-noise plots of Figures 5.14a to 5.14c are typical of the spectral character of the seabed and Red Events across Area 1. The peak frequency of the seabed varies from 1.5 kHz to 2 kHz, whilst the Red Event displays a peak frequency of 1.1 kHz to 1.4 kHz. The seabed spectrum exhibits a strong notch centred at about 2.8 kHz to 3.1 kHz, and extends out to 6 kHz to 8 kHz before flattening out to background noise amplitudes. The Red Event extends out to about 3 kHz before flattening out to background noise levels. For the chosen bands for Q estimation, the signal-to-noise (S/N) ratio of the seabed reflection varied from about 10:1 to 65:1. The S/N ratio of the Red Event varied from 5:1 up to 25:1.

The mean spectral coherence estimated from the signal-to-noise ratios shows a broad zone extending from about 900 Hz to about 3 kHz with coherence > 0.7 . This threshold appears to indicate the band across which a reasonable signal-to-noise ratio for both spectra occurs, the high-frequency limit being controlled by the upper limit of the signal part of the Red Event spectrum.

Wavelet modelling of the Red Event across Area 1 was reasonably successful at modelling the (earlier) front end of the Red Event wavelet; this can be seen in Figure 5.22 which compares the mean observed and computed Red Event wavelets. However, the latter third of the synthetic wavelet could not be fitted to the Red Event using the expressions for absorption and dispersion. This is reflected in the results of spectrum modelling and matching. Figure 5.18 shows the spectra for 15 traces across Area 1, from 0 Hz to 3 kHz. The spectra are plotted as a percentage of the 'ideal' spectral amplitude of the synthetic absorbed spectrum for each trace. The mean spectrum for the 40 traces is shown and indicates that the mean spectrum models the 'ideal' spectrum well from about 3000 Hz down to about 1200 Hz. Below this frequency, the mean observed spectrum is deficient in amplitude in comparison to that which would be expected if the constant-Q model is correct. The smoothed spectral ratios plot of the stacked trace (Figure 5.21) shows a linear spectral ratio from greater than 3.5 kHz down to about 1.5 kHz, but with a change in slope below this frequency.

The arrival times for the Red Event were calculated using wavelet modelling. Figure 5.23 shows a slight variation in the estimated arrival times across Area 1.

The variation of Q measurements using the modelling and matching methods are shown in Figure 5.17. The Q estimates from wavelet and spectrum modelling appear to vary in a systematic manner with each other across Area 1, that is, when wavelet modelling shows a high Q, spectrum modelling also shows a high Q. The matching method yielded Q estimates with a much higher standard deviation of the distribution of the measurements about a mean. Further use of the matching technique will be restricted to application with stacked traces from areas rather than using individual measurements.

The overall mean Q estimate for Unit B was found to be 52. This figure was obtained from the means of individual measurements on separate traces and measurements on stacked traces.

Figure 5.24 shows the mean coherence function for Area 1. This function defines a bandwidth from 800 Hz to about 3 kHz across which the coherence is greater than 0.7 . For the other areas within the 49/10 data set, a threshold of 0.7 for the spectral coherence calculated from the signal-to-noise ratios will be used to define the spectral limits for spectrum modelling and the matching method.

6.5.4 Summary of Numerical Analysis

The wavelet and spectrum modelling techniques were applied to 18 small data sets within the 49/10 data. Eight of the areas measured Q within unit A whilst the other ten measured Q within unit B. In all cases the data (minimum 15 traces per area) was limited to those traces showing reasonably strong lateral continuity and minimal dip. The traces were stacked horizontally to form a representative trace for each area. The optimal stack for each area was found by performing a running cross-correlation through the data in order to determine the degree of time adjustment each trace required relative to its neighbour.

Following the processing of areas 1,2,3,4 and 5, a comparison between the mean of individual Q measurements from the modelling techniques with the Q measurements revealed very little difference between the mean Q and stacked trace Q results (see Table

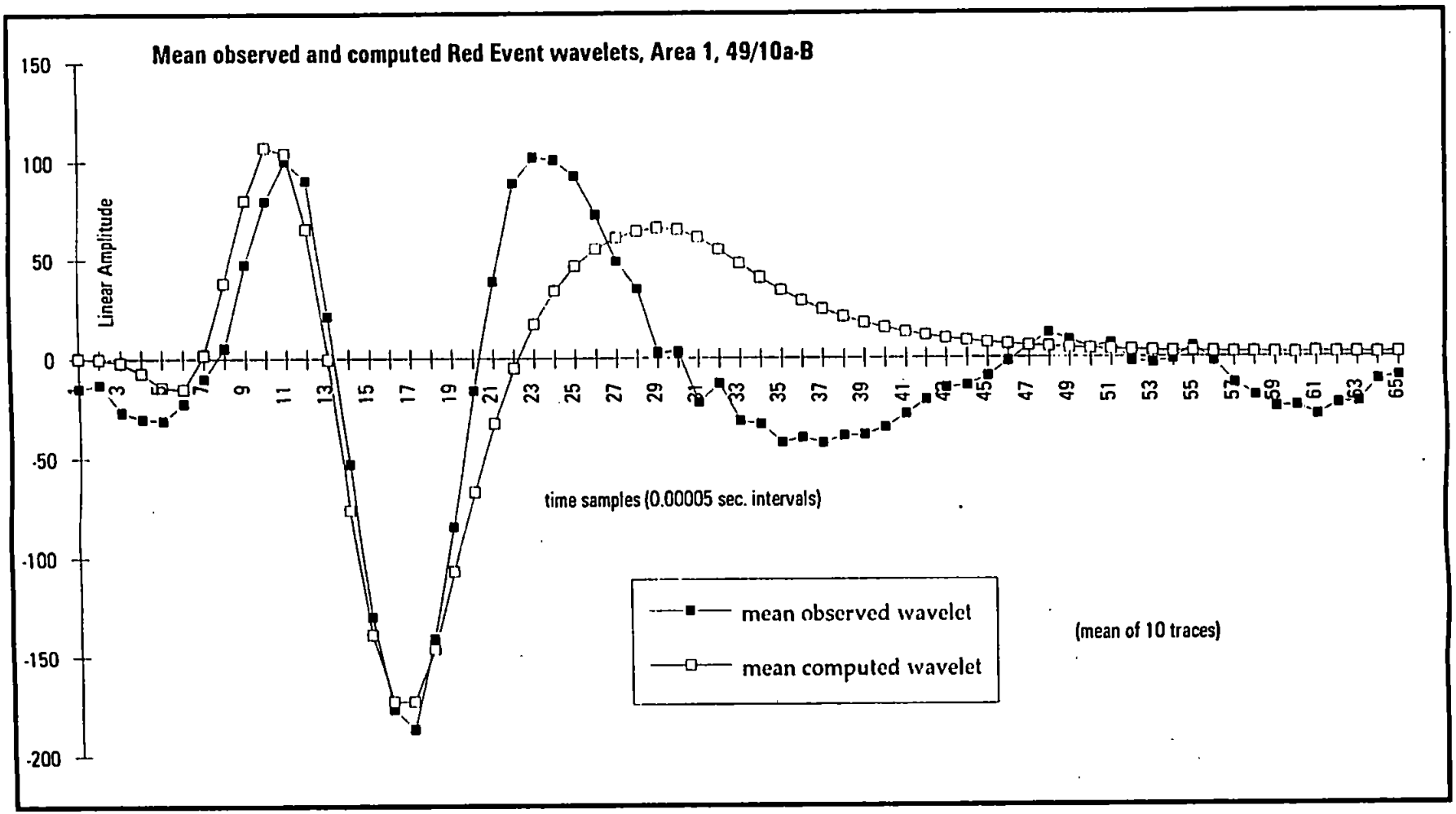

Figure 5.22 Mean observed and computed Red Event wavelets, Area 1, 49/10 survey area.

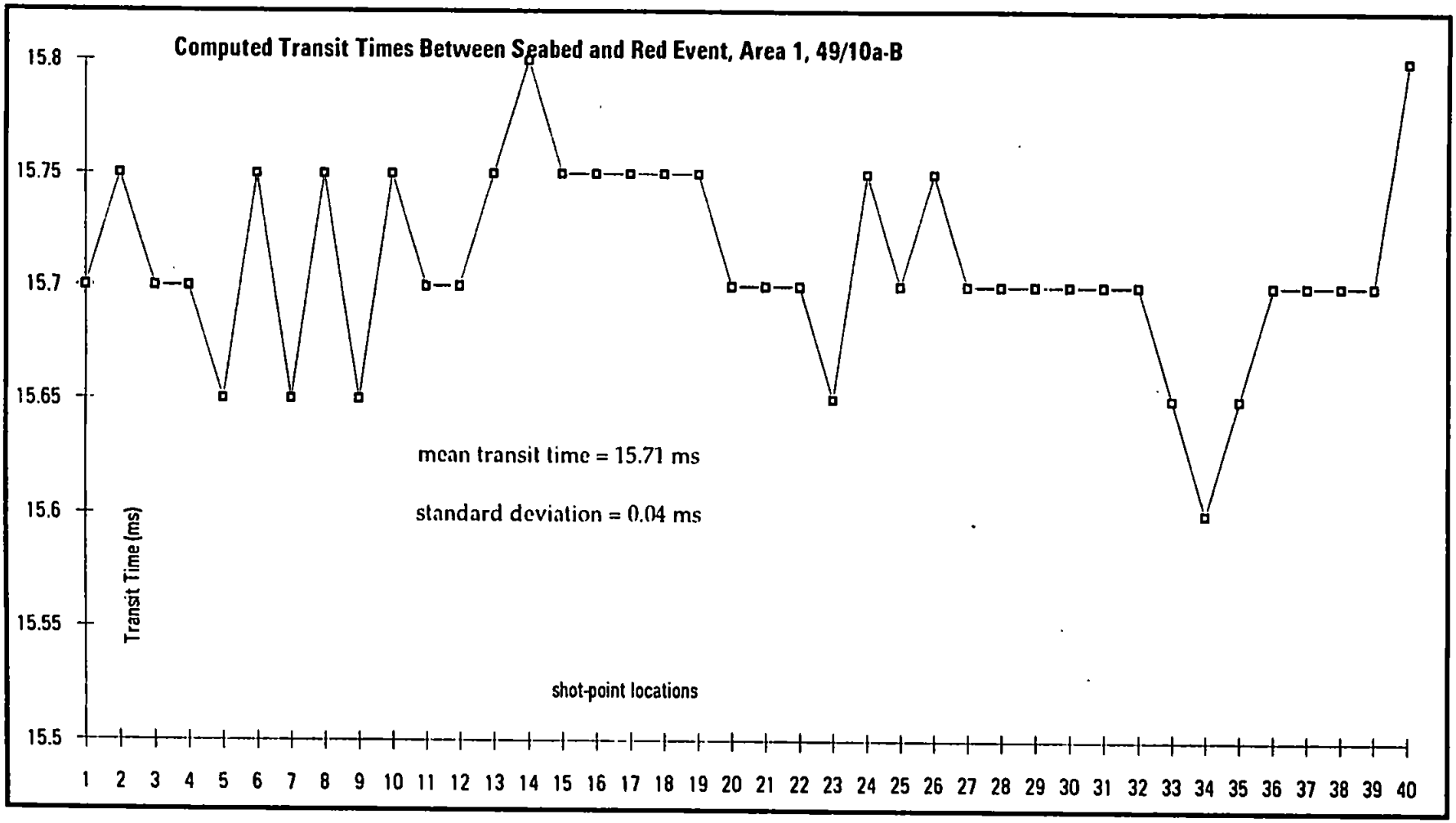

Figure 5.23 Computed transit times between seabed and Red Event, Area 1, 49/10.

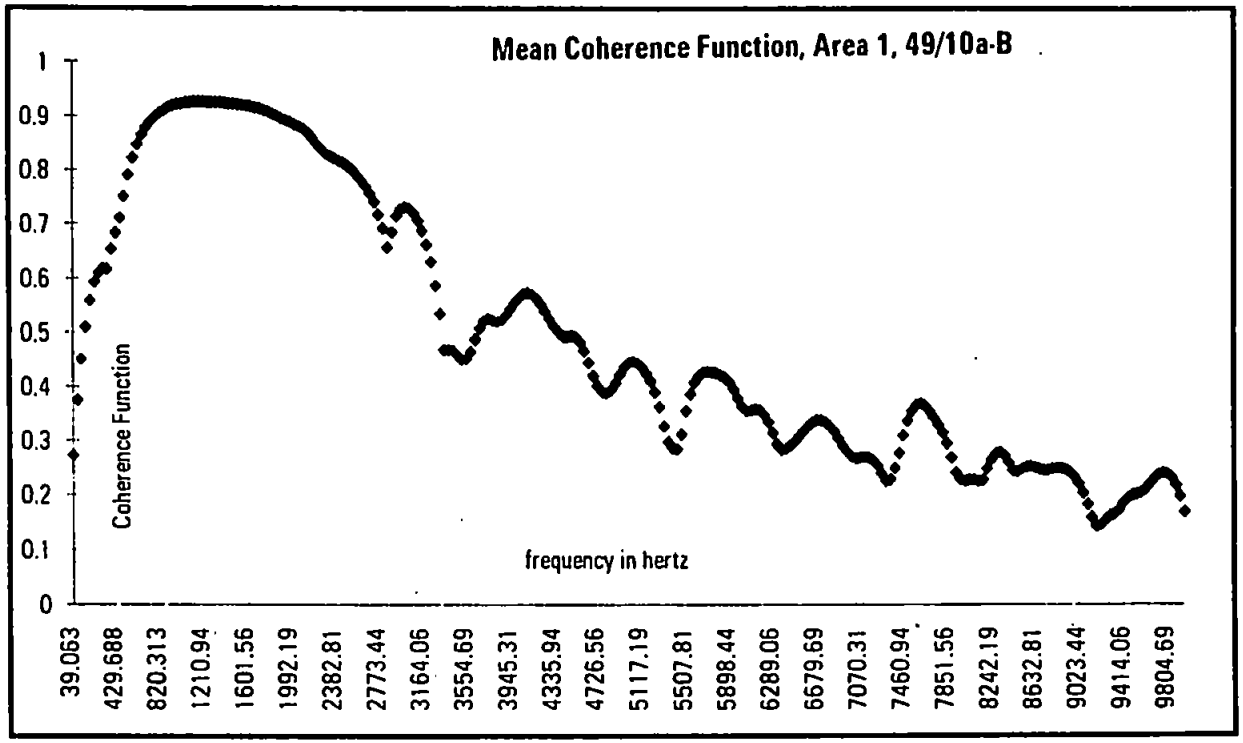

Figure 5.24 Mean coherence function, Area 1, 49/10 survey area.

5.3), despite a processing time factor of about 25 between the slower individual measurments and the much more efficient stacked trace measurements.

Table 5.3: Comparison between mean of individual and stacked measurements for Areas 1 to 5 (Unit B measurement), 49/10

Area	mean Q(sm)	mean Q(wm)	stacked Q(sm)	stacked Q(wm)
1	53	49	58	51
2	50	43	45	41
3	46	45	49	47
4	48	44	51	42
5	43	41	46	46

wm = wavelet modelling, sm = spectrum modelling

Accordingly, individual trace processing was discontinued following the processing of Area 5. In addition the matching technique was found to provide very similar results to spectrum modelling. This is because the spectrum modelling and matching methods both used the same high-coherence portion of the spectra. As will be shown (Figures 5.30 - 5.33), across much of this band there is a good fit between the observed and the theoretical spectra for the events forming the base of both Units A and B. The two methods will therefore tend to yield similar results, as is illustrated in Table 5.4. The matching method was therefore not used following the processing of Areas 1 through to 5.

Table 5.4: Comparison of spectrum modelling vs. matching method measurements for Areas 1 to 5 (Unit B measurement, stacked traces), 49/10.

Area	Q(sm)	Q(match)
1	58	50
2	45	47
3	49	47
4	51	52
5	46	48

sm = spectrum modelling, match = matching method

For unit A the TWTT varied between 14.2 ms and 17.8 ms, whilst within unit B the TWTT varied between 11.9 ms and 19.85 ms. These figures represent a minimum depth of investigation of about 11.5 m and a maximum depth of 16 m respectively below the seabed.

The summary of modelling results for all 18 areas within the 49/10 study area are shown in Figure 5.25 .

For Unit A, the mean Q measurement was 56 (±3.6) from wavelet modelling and 63 (±6.9) from spectrum modelling, yielding an overall averaged Q of 60 for both methods from 8 different areas within the survey area.

For Unit B the mean Q measurement was 44 (±3.4) from wavelet modelling and 50 (±5.1) from spectrum modelling, yielding an overall averaged Q of 47 for both methods from 10 different areas within the survey area. Figures 5.26a to 5.26b (Appendix B) show three digital seismic section examples (areas 6,12 and 14) of Unit A whilst Figures 5.27a to 5.27c (Appendix B) show three of Unit B (areas 9, 11 and 17). With such a small sample of data for each area, very little internal structure can be seen within either seismic unit.

The time-domain results of the wavelet modelling are summarised in Figures 5.28 and 5.29. Figure 5.28 (area 12) shows an example of wavelet modelling for the reflector bounding the top of the C_2 seismic unit. The general fit of the theoretical to the observed wavelet confirms the reflector as being of the same polarity as that of the seabed. The observed wavelet clearly lacks the low frequency content of the modelled wavelet. Figure 5.29 (Area 11) shows an observed wavelet (the Red Event) again lacking the low frequency content of the modelled wavelet.

Figures 5.30 and 5.31 are representative of the frequency domain modelling for Unit A. The seabed spectrum peaks at about 3 kHz whilst the observed spectrum peaks near 2.3 kHz. The observed spectrum fits the theoretical spectrum well from 3 kHz down to about 1.3 kHz. Below this threshold, the observed spectrum is deficient in low frequency amplitude (*c.f.* time domain modelling).

This effect is more pronounced for Unit B (Figures 5.32 and 5.33) where again, there is a low frequency 'hole' in the observed spectrum relative to the theoretical spectrum calculated from spectrum modelling of the seabed reflector. The seabed reflector has a spectral peak at about 2.1 kHz whilst the observed wavelet spectrum peaks between 1.4 kHz to 1.8 kHz. The threshold below which there is a lack of low frequency amplitude occurs between 1.1 kHz and 1.4 kHz.

5.6 Summary of Results

1. Using spectrum and wavelet modelling, Unit A has a measured Q of 60.
2. Using the same procedures, Unit B has a measured Q of 47.
3. The peak frequency of the target events (Red Event and top of C2) is centred around 2.3 kHz to 2.5 kHz for Unit A and 1.3 kHz to 1.8 kHz for Unit B)
4. Spectrum modelling yielded Q estimates which were, on average, 13% higher than that obtained by wavelet modelling for Unit A and 14% higher than wavelet modelling for Unit B.
5. The observed wavelets from the reflectors that form the base of Units A and B are deficient in low frequency amplitude below a threshold frequency of about 1.3 kHz. Above this frequency the theoretical wavelets predicted from modelling fitted the observed wavelets well up to around 3 kHz.
6. Using a stacked trace for single channel data yields effectively the same results as processing a number of individual unstacked traces for Q measurement, providing the number of traces is well aligned to not cause any smearing effects on either the seabed or the target events which would lead to spectral distortion.
7. Signal to noise ratios, based on comparing the high-frequency noise tail of the data spectrum to the signal portion can yield an approximation of spectral coherence which can be used to assess which part of the spectrum has enough amplitude for comparing a reference wavelet to one with an attenuated spectrum.
8. The matching and spectrum modelling methods yield essentially the same Q measurement for any given stacked trace, as there was a good predictability of the observed wavelet from the seabed event.

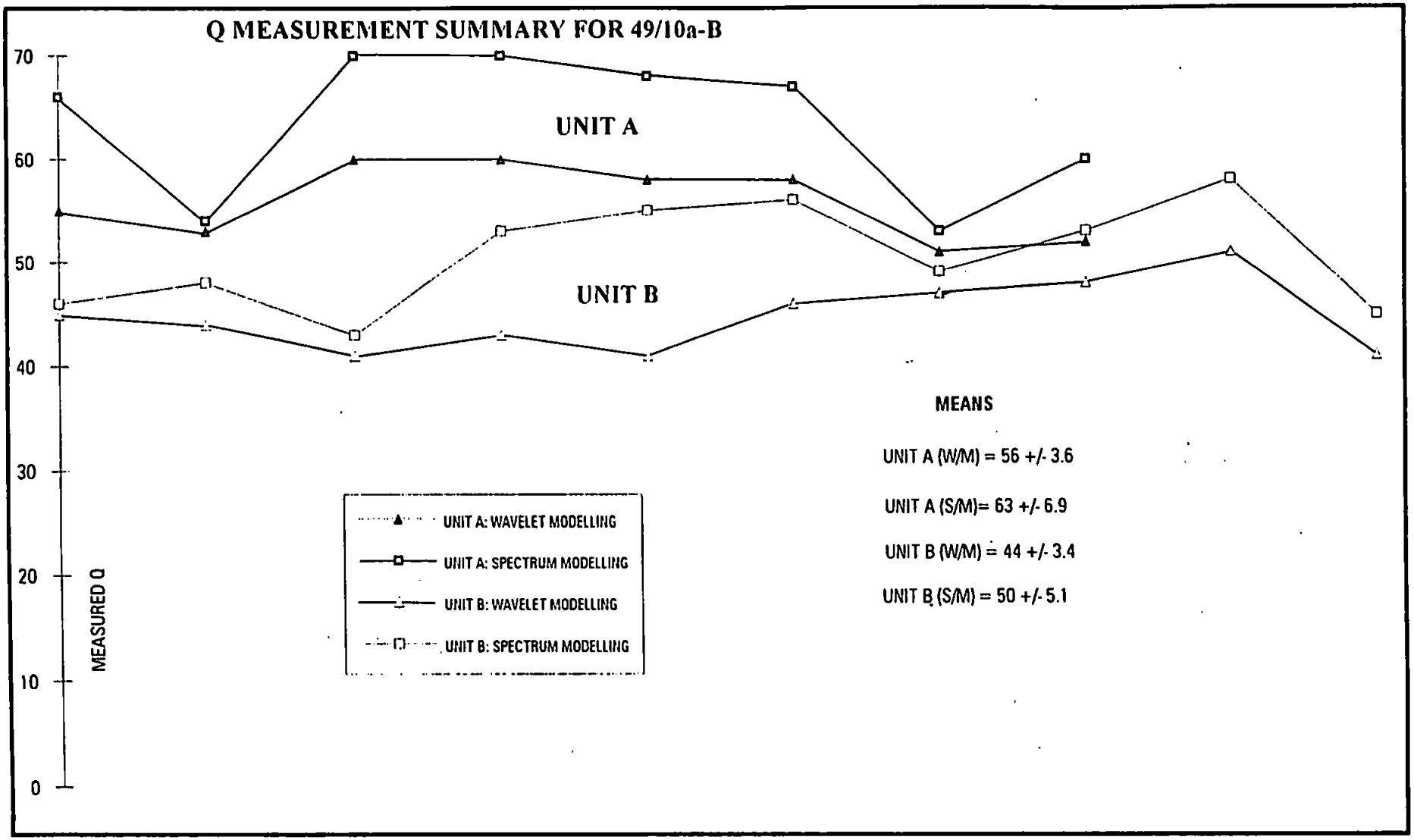

Figure 5.25 Q measurement summary for 49/10 survey area.

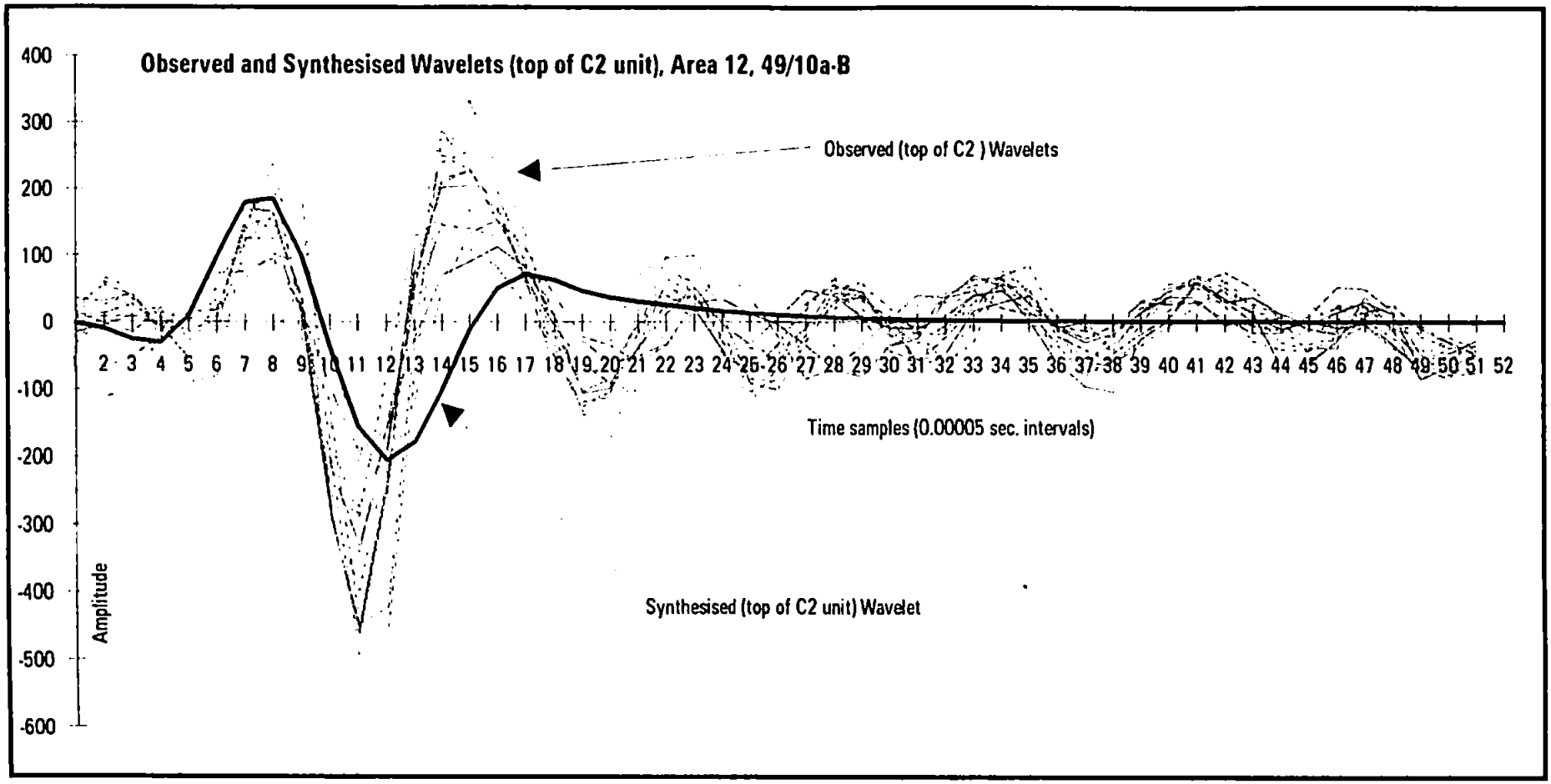

Figure 5.28 Observed and synthesised wavelets (top of C_2 unit), Area 12, 49/10 survey area.

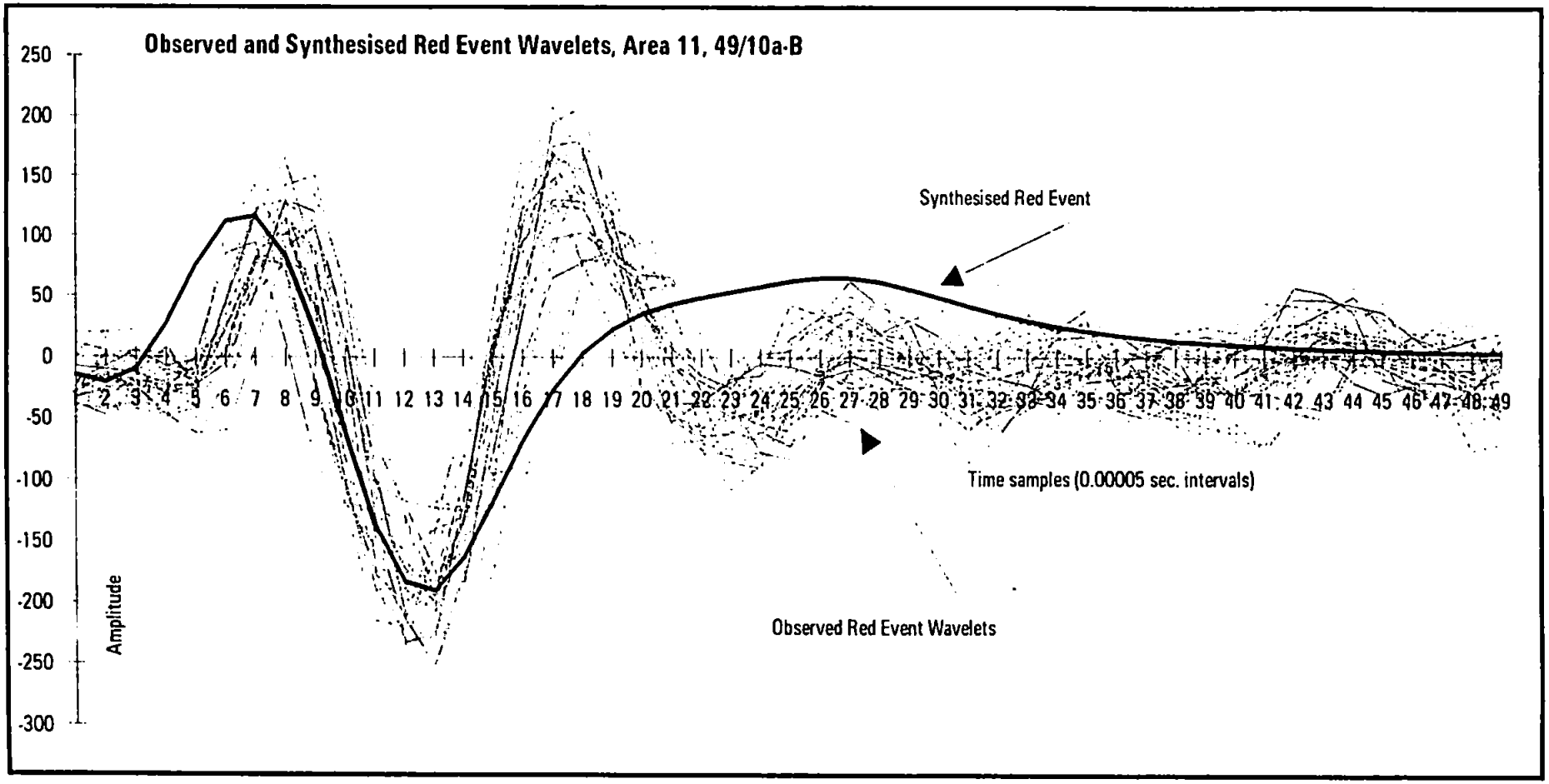

Figure 5.29 Observed and synthesised Red Event wavelets (top of C2 unit), Area 11, 49/10 survey area.

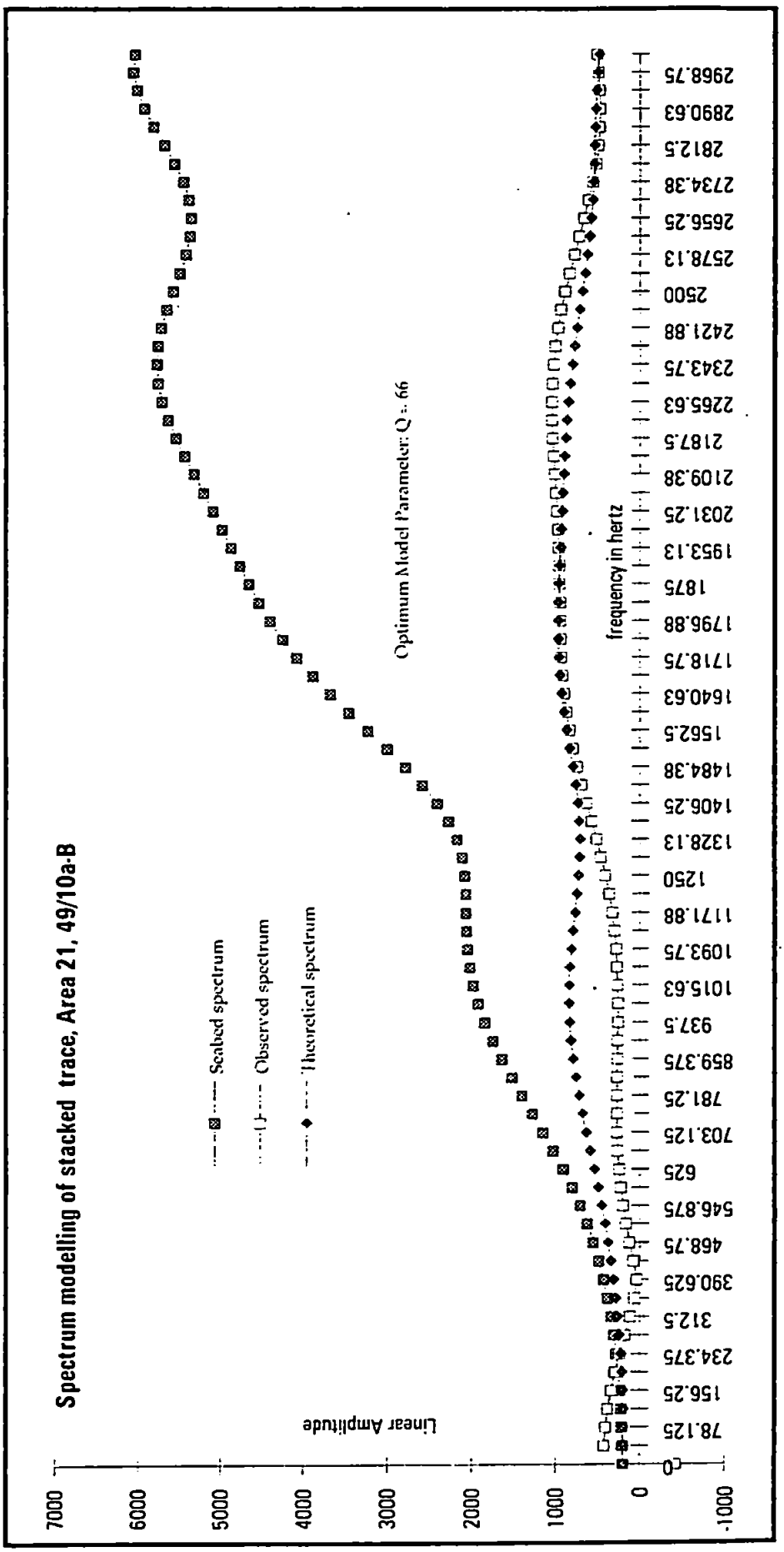

Figure 5.30 Spectrum modelling of stacked trace, Area 21, 49/10 survey area.

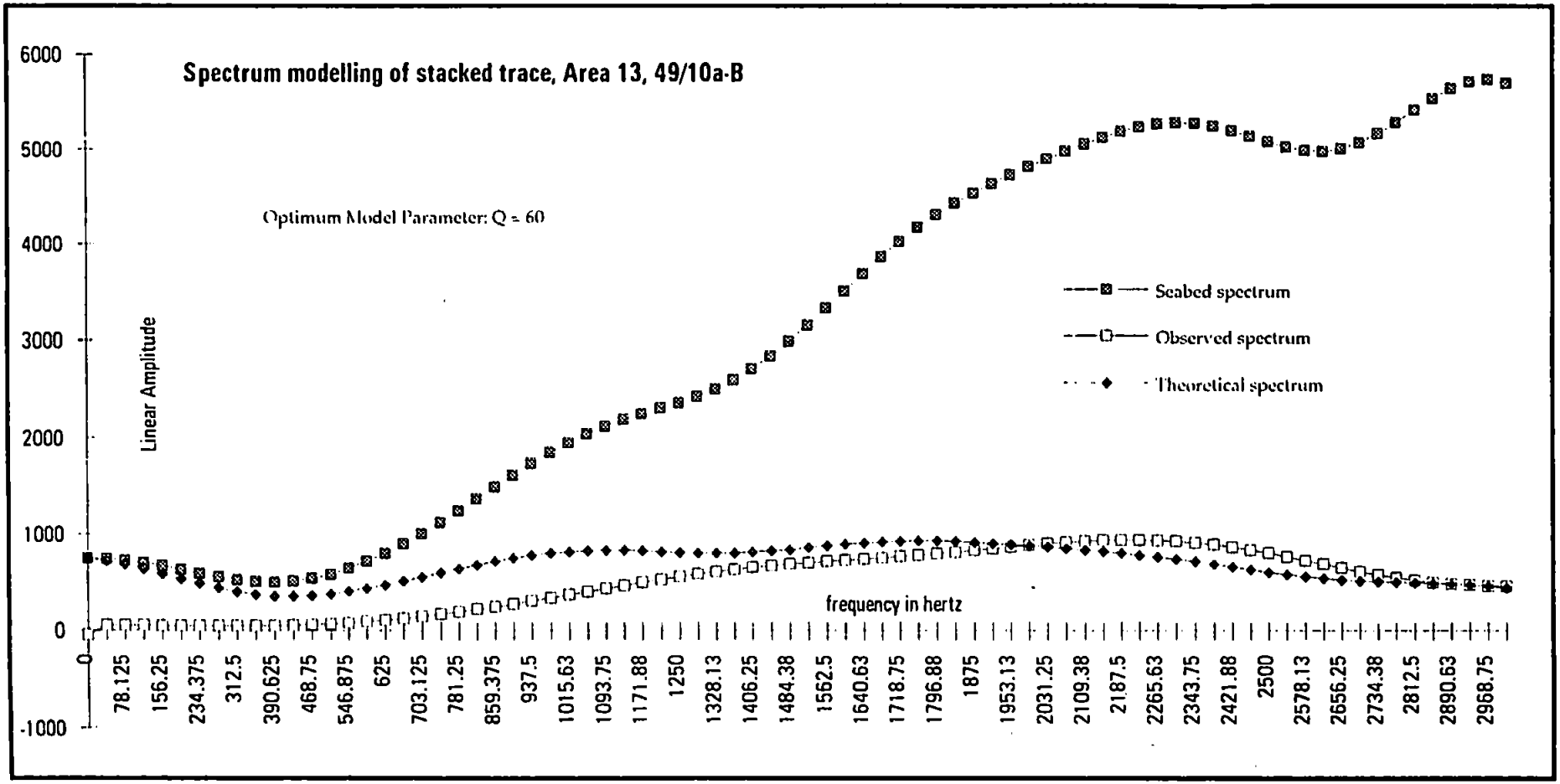

Figure 5.31 Spectrum modelling of stacked trace, Area 13, 49/10 survey area.

Figure 5.32 Spectrum modelling of stacked trace, Area 11, 49/10 survey area.

Figure 5.33 Spectrum modelling of stacked trace, Area 1, 49/10 survey area.

Chapter 6: Bruce and Atlantic Frontiers Case Studies

BRUCE CASE STUDY

6.1 Introduction - Bruce Case Study

The Bruce case study was undertaken to compare the spectral characteristics of a reflected signal from the seabed to that of the first seabed multiple. Given a constant source-receiver geometry between the arrival of the seabed reflection and the arrival of the first seabed multiple, any frequency-dependant effects observed between the two events will be due to the effects of the second bounce from the seabed, the twin extra seawater passage and the reflection at the sea surface.

The Bruce data set was chosen as the first seabed multiple occurs at a TWTT at which there appears to be no reflected events from the sub-surface sediments, and would not, therefore, suffer from interference effects.

The Bruce case study uses data from Quadrant 9, Block 9 of the northern North Sea, in the proximity of the Bruce oil field (Figure 6.1). The data was acquired by Geoteam UK Ltd. on behalf of BP in 1991. The data set comprises six seismic lines acquired using an array of three mini-airguns. The digital data were acquired with a 0.5 ms sampling interval.

6.2 Bruce Data Processing

The demultiplexed survey data were reprocessed to be used in amplitude studies. The raw data was acquired with 24 channels. Only the first 12 channels (near offset) were used to minimise moveout effects (mainly smearing of the pulse shape from the far offsets). The data were sorted into separate common depth points (CDP sort). A basic normal moveout (NMO) correction was applied using pre-determined velocity functions (details unavailable),

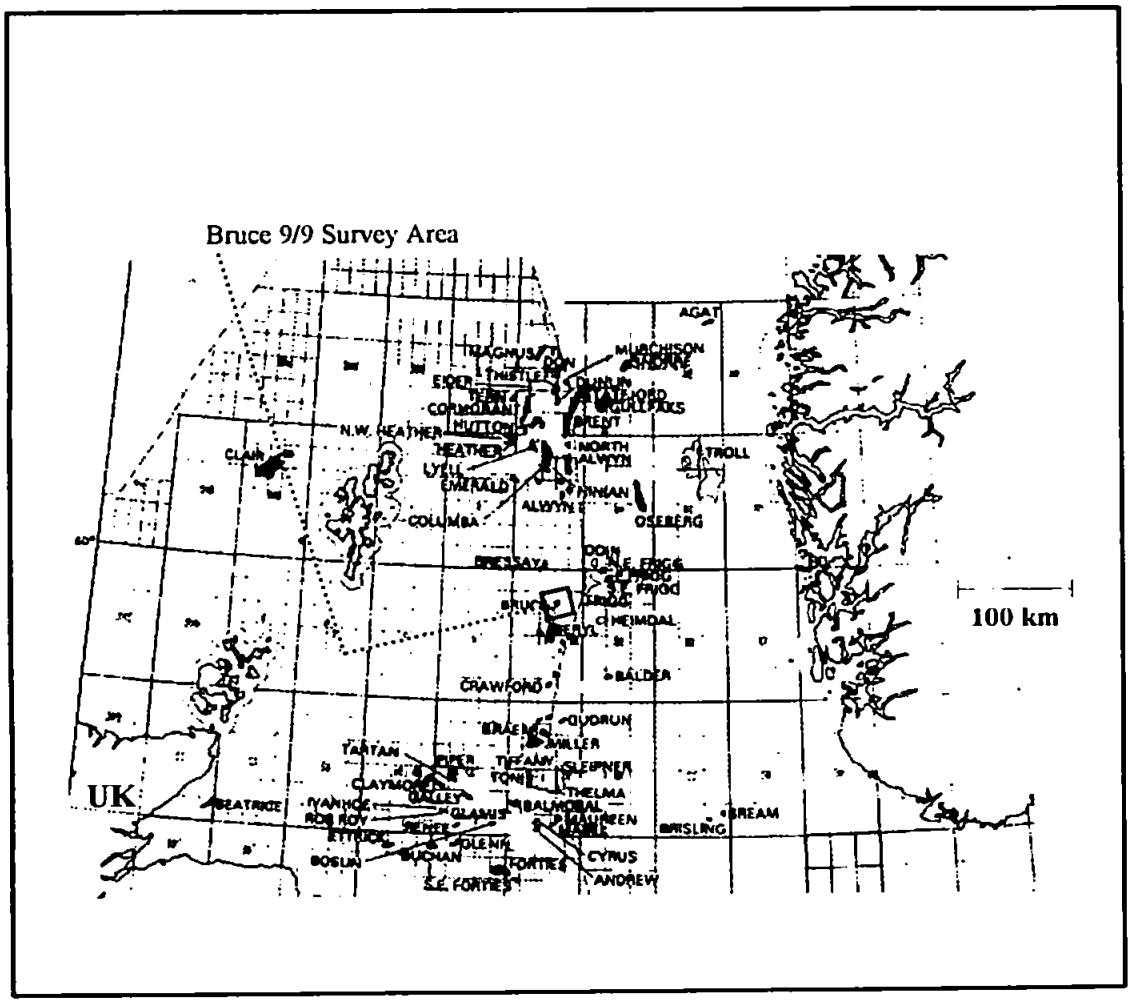

Figure 6.1 Bruce 9/9 Survey Area Location Map

followed by a 6-fold stack. The data was then output to floppy disks in a trace-by-trace floating point format. The time range of the data was restricted to 151 ms to 400 ms TWTT. Each line was originally shot with 512 CDP's. In order to reduce the data to a practical volume, the first and last 40 CDP's were not used, giving a total of 432 CDP's per seismic line.

Each line was then processed to give 'condensed' seismic sections. Groups of CDP's were horizontally stacked and corrected for spherical spreading to give one representative trace for each group of 20 CDP's. Therefore each line was represented by a condensed seismic section of 21 stacked traces. This procedure was carried out in order to reduce the effects of differing localised wavelet shape along the seabed.

6.3 Bruce Qualitative Data Description

The five seismic lines (UHR-304,-307,-308,-309,-320) show broadly similar seismic characteristics. The seabed reflection occurs at about 165 ms TWTT (c. 132 metres water depth). The strong seabed reflection is horizontal and laterally consistent in character. Two sub-parallel, laterally consistent but irregular reflectors occur at 175 ms and 183 ms TWTT. From 190 ms down to 258 ms TWTT the seismic character changes to one of sub-parallel, laterally persistent reflections of lower amplitude. Below this zone the seismic section is virtually featureless down to about 330 ms TWTT, where the first seabed multiple occurs, hereafter known as the "Green Event".

6.4 Bruce Background Geology

The Quaternary geology of the area around the Bruce oil field is summarised in the 1:250 000 scale 'Bressay Bank' Sheet 59°N-00° ,(1990) Quaternary Geology Map published by

the British Geological Survey, Long (1990). The map was drawn up from the interpretation of sparker and boomer seismic profiles run by the BGS in 1982.

The area of the Bruce oil field has a very smooth, flat bathymetry, with a water depth of about 120 m, or a TWTT of 160 ms for the seabed reflection. The youngest unit is that of the Ferder Formation (late Quaternary). The sediments consist of sandy muds, muddy sands and sands with small rock and shell fragments with undrained shear strengths of up to 500 kPa (Long, 1990). The lower boundary of this unit corresponds with the strong reflector some 9 ms below the seabed reflection, giving a thickness of about 8 m for this unit.

6.5 Bruce Wavelet and Spectrum Modelling

The 49/10 case study in Chapter 5 examined seismic data whose bandwidth was limited to the 400 Hz to 3 kHz range. The Bruce data set was selected to analyse data in the 70 Hz to 400 Hz range. The dominant frequency of the boomer-sourced 49/10 data was around 1500 Hz; in the case of Bruce, the mini-airgun array produced a source whose dominant frequency was around 150 Hz.

The wavelet modelling software designed for this project obtains an initial estimation of the transit time of the target reflector using a simple autocorrelation algorithm. In order that the software did not detect events between the seabed and the Green event, a degree of trace muting (amplitudes set to zero) was carried out. The seabed wavelet on each of the seismic sections was taken to be the first 40 time samples (20 ms in duration). No muting was carried out within this window or on the trace following the onset of the seabed multiple. In addition, the seabed wavelet was reversed in polarity for the wavelet modelling (sign of amplitude changed) as the wavelet modelling software carries out observed versus synthesised wavelet comparison in the time domain, that is, similarity of shape. This polarity reversal did not effect the spectral content of the data.

6.5.1 Bruce UHR-304 Modelling

The relative amplitude stack of UHR-304 (Enclosure 6a) shows a Green Event at about 330 ms TWTT. The event is of relatively high amplitude between CDP 400 and CDP 300 and between CDP 170 and CDP 50. Three stacks on the condensed line of UHR-304 (numbers 3, 12 and 15, Figure 6.2) from the 21 stacks are used to illustrate wavelet and spectrum modelling of the data. As might be expected, stacks 8 to 11 and 19 to 21 are lower in amplitude than the others as they are formed from the data segments displaying a lower amplitude. The seabed reflection (Figure 6.2) varies in shape, primarily in the latter part of the wavelet. The modelling of stacks 3, 12 and 15 are shown in Figures 6.3a to 6.3f).

For the three traces, the wavelet and spectrum modelling software fitted theoretical wavelets and spectra well to the observed Green Event. Typically, the seabed event has a spectrum ranging from about 60 Hz ±10Hz up to 400 Hz ±30Hz. These limits are arbitarily defined as 20% of the dominant frequency at either end of the spectrum. For this case study, the dominant frequency is taken to be that at which the highest spectral amplitude occurs, and does not involve other considerations such as the centre of gravity of the spectrum. The UHR-304 data show a double peak spectral shape centred on 110 Hz ±15 Hz and 230 Hz ±15 Hz for the seabed event, with a deep spectral notch centred around 170 Hz ±10Hz. The notch becomes less pronounced and the higher frequency peak becomes lower in amplitude with higher stack numbers. The observed spectrum of the Green Event clearly displays the same deep notch in the examples given. The theoretical spectrum determined from the seabed event using spectrum modelling shows a close match between the theoretical and observed spectra between about 100 Hz and 250 Hz. Above this band, the observed spectrum consistently shows an excess of high-frequency amplitudes relative to the theoretical spectrum. Below 100 Hz there is a deficiency of low frequency amplitudes in the observed spectrum.

In the time-domain, the theoretical seabed multiple wavelets were determined using wavelet modelling. To obtain the optimum fit, the theoretical and observed wavelets were compared over 40 time samples (20 ms). The fit between the observed and theoretical

wavelets is generally good, but particularly in the central 50% of the wavelet which contains the highest amplitudes. The compressional phase (centred around time sample 15) is modelled very well, but with the theoretical compression consistently being slightly broader than the observed compression. The onset of the seabed multiple is modelled reasonably well, but the onset of the theoretical wavelet consistently occurs before the onset of the observed seabed multiple reflection.

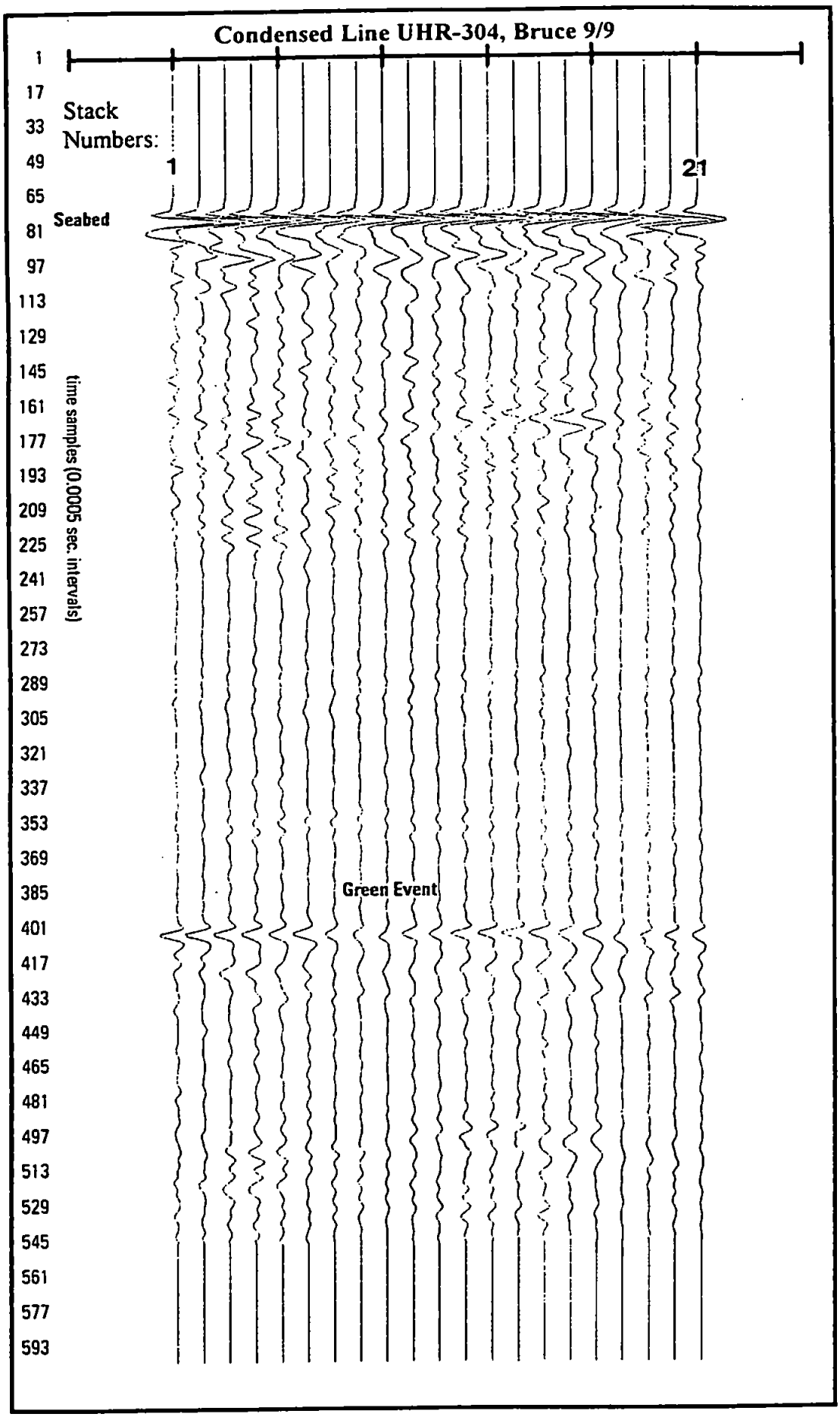

Figure 6.2 Condensed line UHR-304, Bruce 9/9.

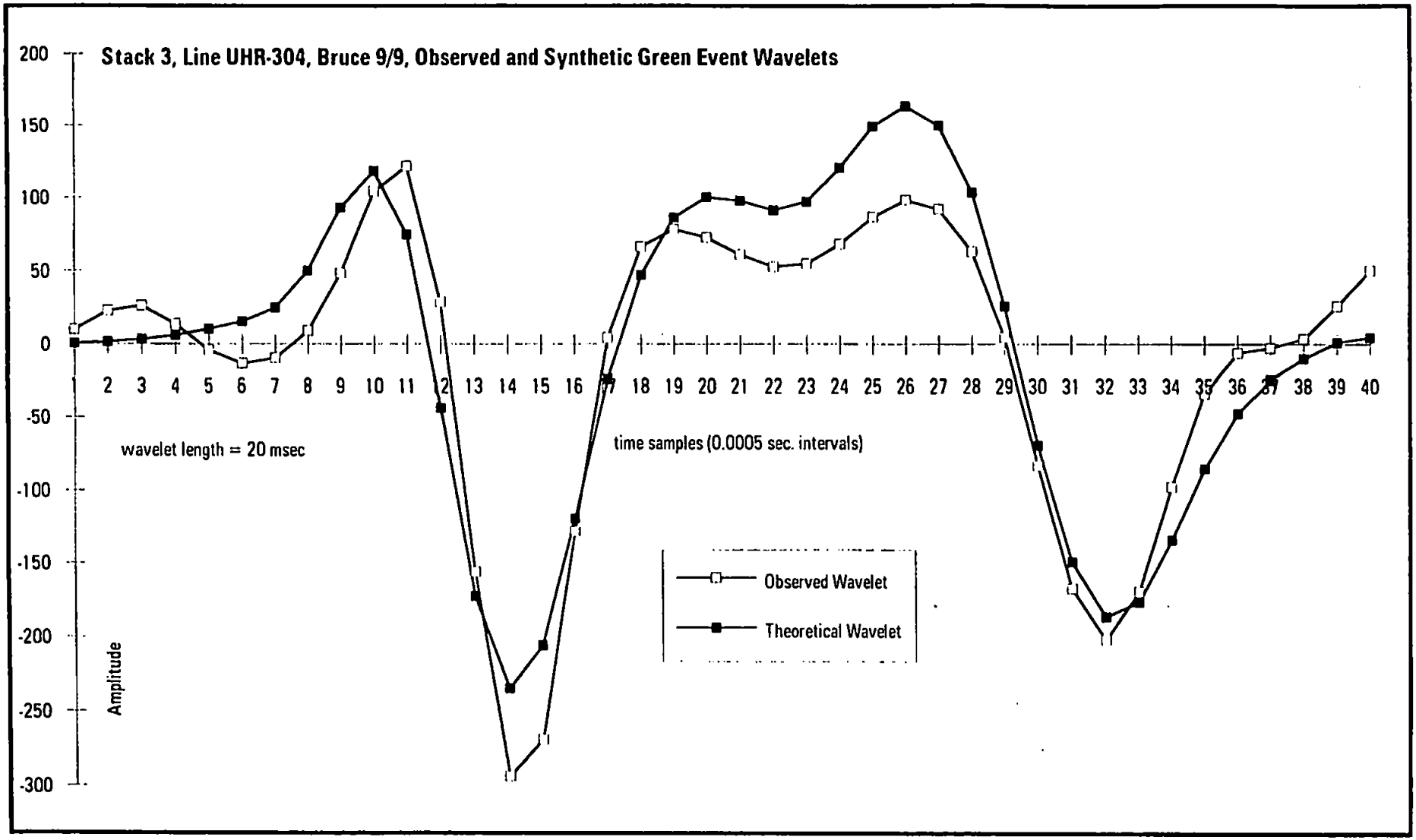

Figure 6.3a Stack 3, line UHR-304, Bruce 9/9, observed and synthetic Green Event wavelets.

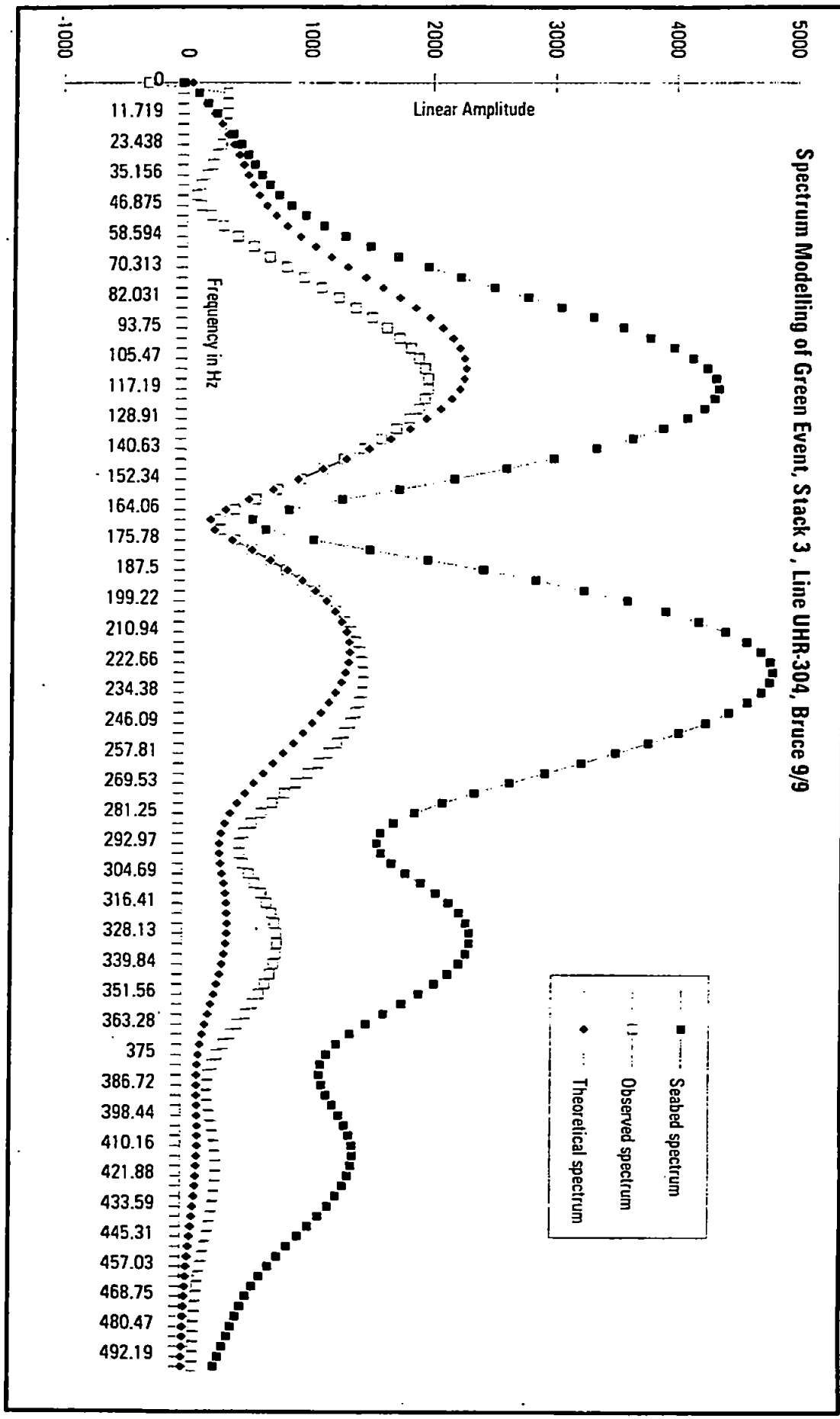

Figure 6.3b Spectrum modelling of Green Event, stack 3, line UHR-304, Bruce 9/9.

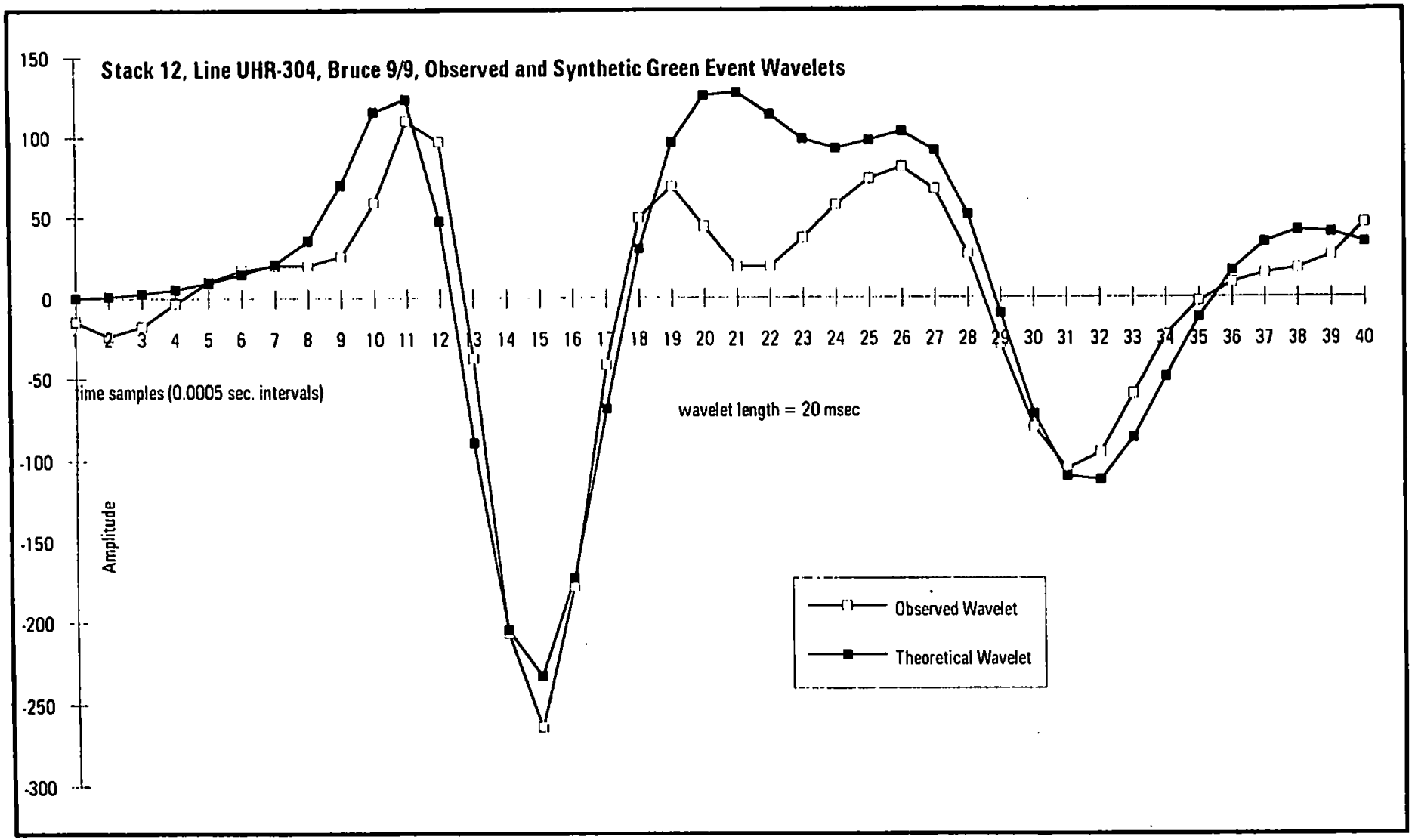

Figure 6.3c Stack 12, line UHR-304, Bruce 9/9, observed and synthetic Green Event wavelets.

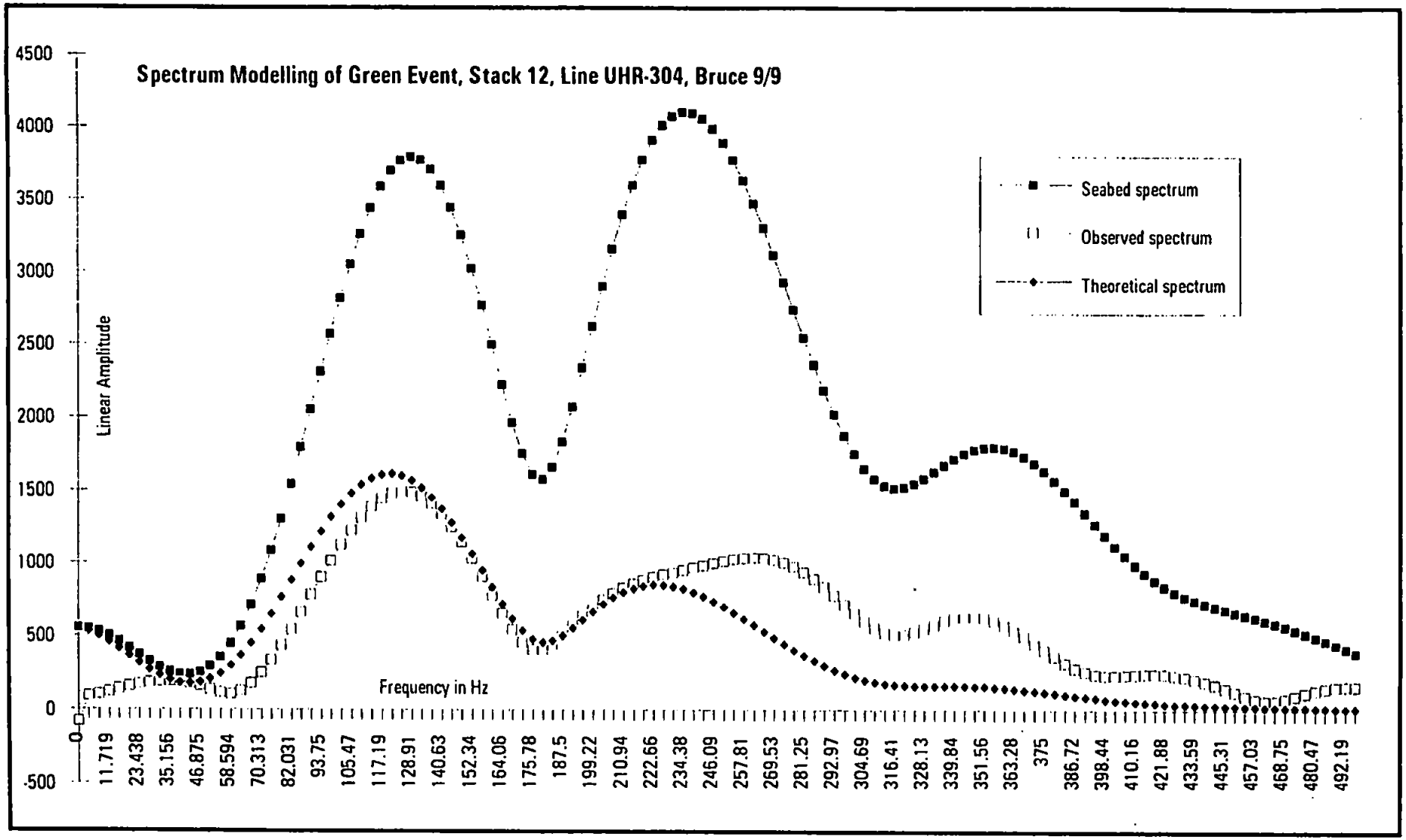

Figure 6.3d Spectrum modelling of Green Event, stack 12, line UHR-304, Bruce 9/9.

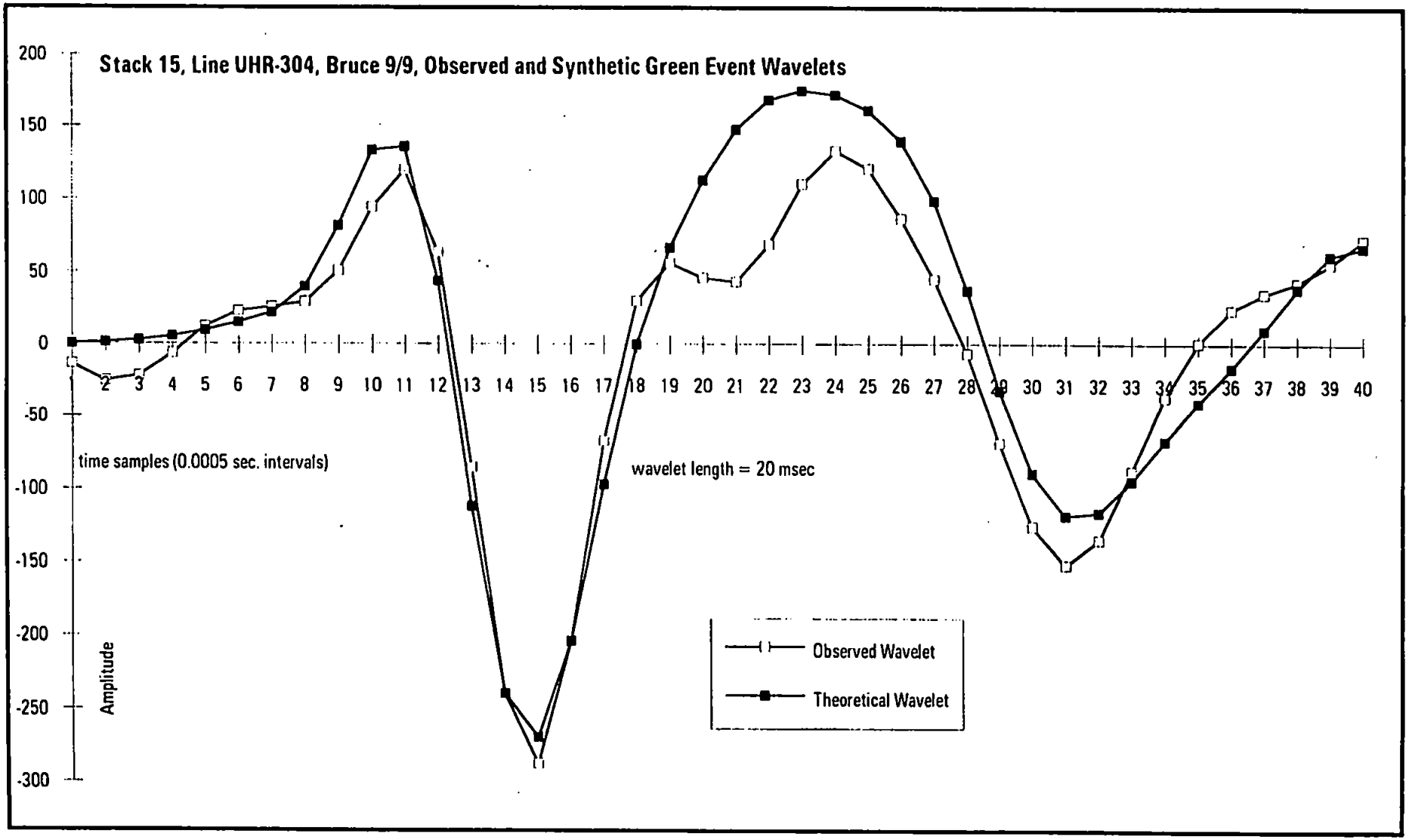

Figure 6.3e Stack 15, line UHR-304, Bruce 9/9, observed and synthetic Green Event wavelets.

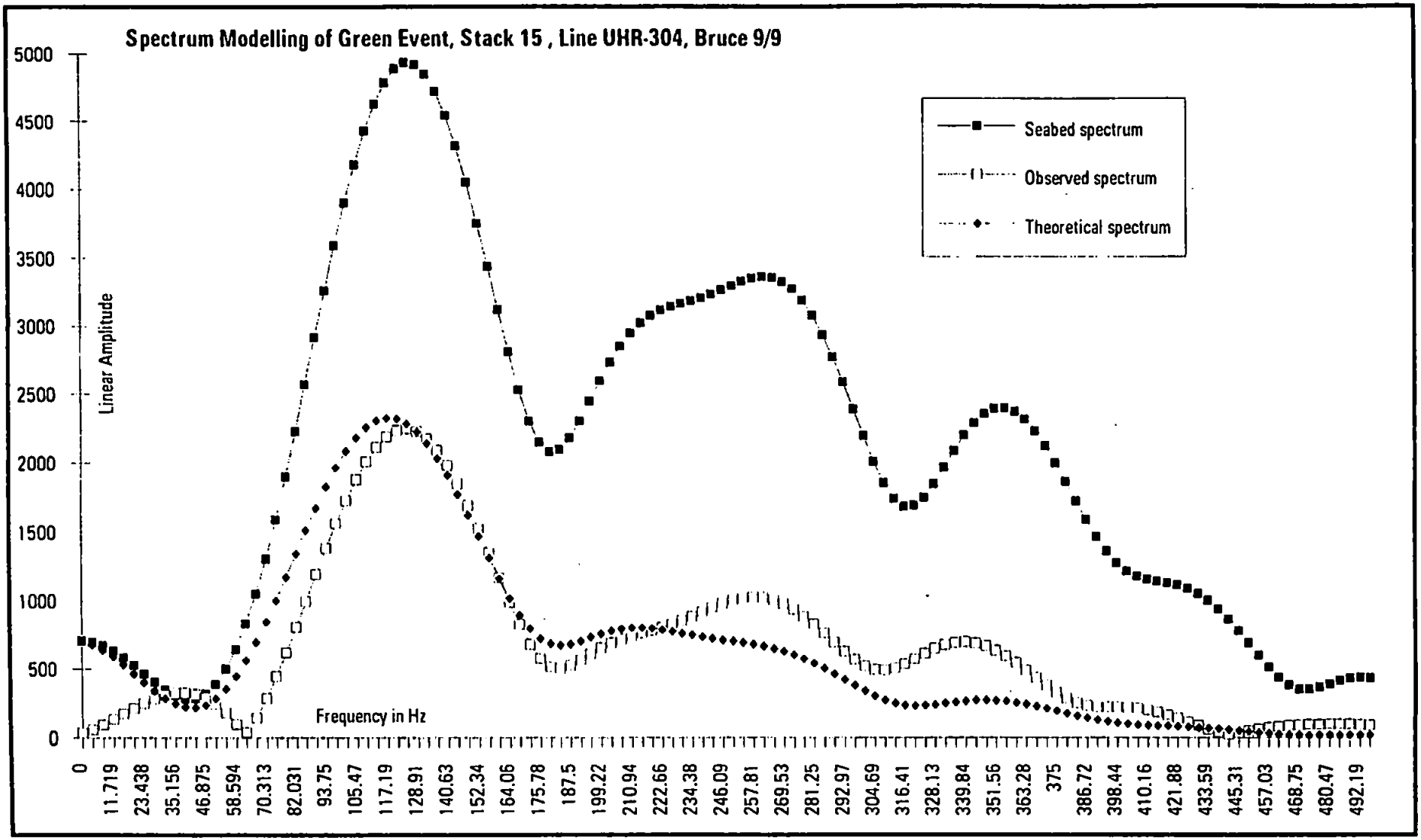

Figure 6.3f Spectrum modelling of Green Event, stack 15, line UHR-304, Bruce 9/9.

6.5.2 Bruce UHR-307 Modelling

The relative amplitude stack of UHR-307 (Enclosure 6b) shows the Green Event at about 330 ms TWTT. The event is of relatively high amplitude between CDP 40 and CDP 110, and between CDP 250 and CDP 512. The condensed section of UHR-307 (Figure 6.4) shows the Green Event to be relatively high in amplitude for stacks 1 to 4, and 10 to 21 respectively. In addition the stacks also show a variation in the shape of the seabed and Green reflection events across the section. The modelling of stacks 14, 17, 18, 19 and stack 21 is shown in Figures 6.5a to 6.5h.

The UHR-307 data show a seabed spectrum centred around 150 Hz ± 15 Hz. The seabed spectrum ranges from about 60 Hz ± 10 Hz to 380 Hz ± 30 Hz. A minor spectral peak occurs at 290 Hz ± 10 Hz. Clearly, there is a great variation in the shape of the seabed spectrum in the examples shown. This is manifested by changes in the position and depth of the spectral notch and height of the secondary spectral peak.

The observed spectrum of the Green Event is centred on 140 Hz ±10 Hz. The peak of the observed spectrum is consistently lower than the peak of the seabed spectrum. The form of the observed spectrum of the Green Event follows the variation in shape seen in the seabed event. Where a pronounced spectral notch occurs in the seabed spectrum, the same feature is seen in the observed Green Event spectrum, for example in stack 18 (Figure 6.5d). Conversely a smoother observed spectrum occurs when the seabed spectrum is smooth, for example in stack 19 (Figure 6.5f). The theoretical spectrum determined from the seabed response shows a good match to the observed spectrum of the Green Event, particularly in the 140 Hz to 250 Hz band. As with the UHR-304 data, there is a fairly consistent lack of observed spectral amplitudes in the 60 Hz to 140 Hz band.

Wavelet modelling of the data shows a good match between the observed seabed multiple and the synthesised wavelet. As with UHR-304, the central trough of the wavelet is very well reproduced. The theoretical wavelet is consistently slightly broader than the observed central trough. The theoretical initial peak consistently occurs one time sample prior to the observed initial peak, and the build-up of the energy occurs earlier in the

theoretical wavelet. Overall, the theoretical wavelets appear to be slightly longer in time duration than the observed wavelets.

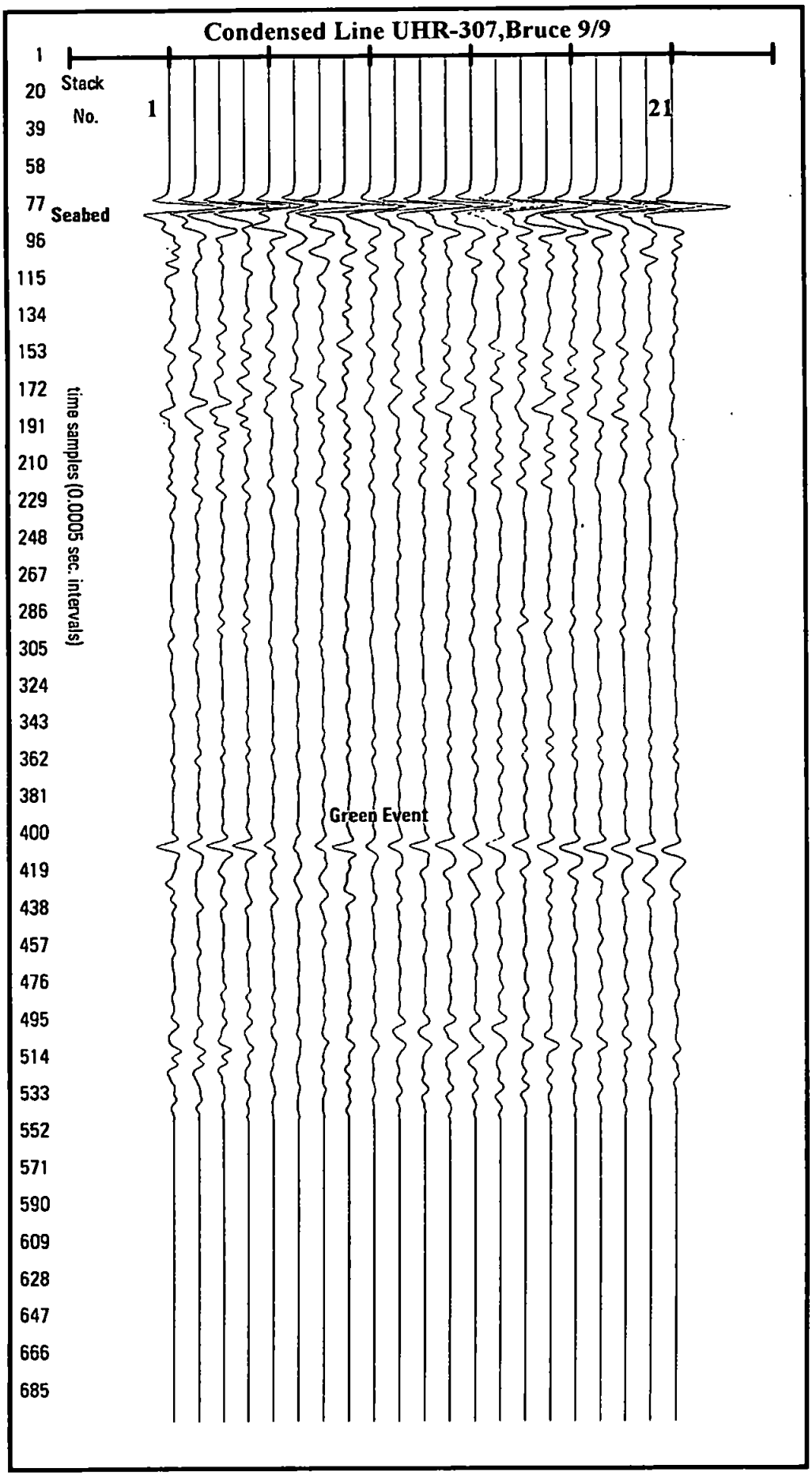

Figure 6.4 Condensed line UHR-307, Bruce 9/9

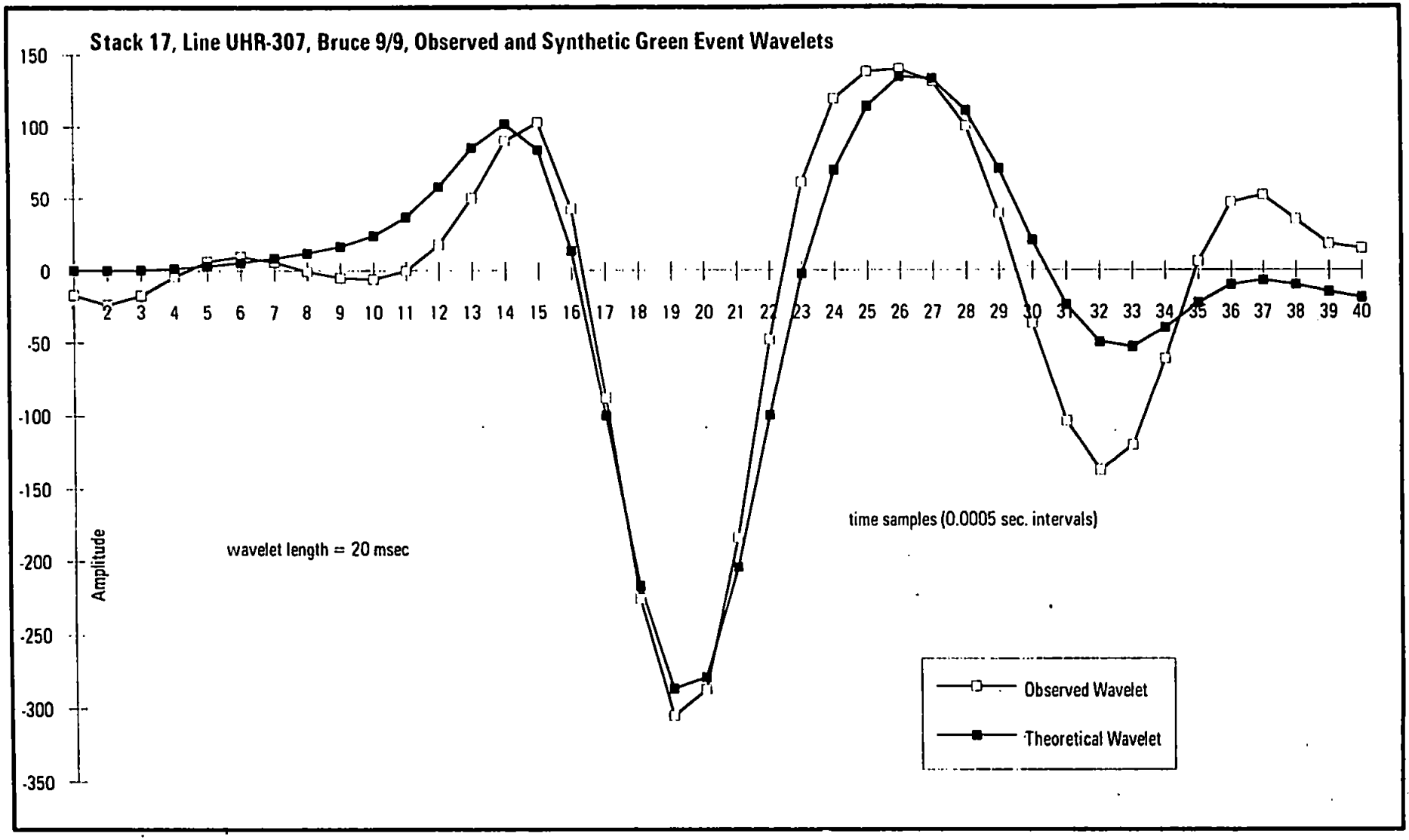

Figure 6.5a Stack 17, line UHR-307, Bruce 9/9, observed and synthetic Green Event wavelets.

Figure 6.5b Spectrum modelling of Green Event, stack 17, line UHR-307, Bruce 9/9.

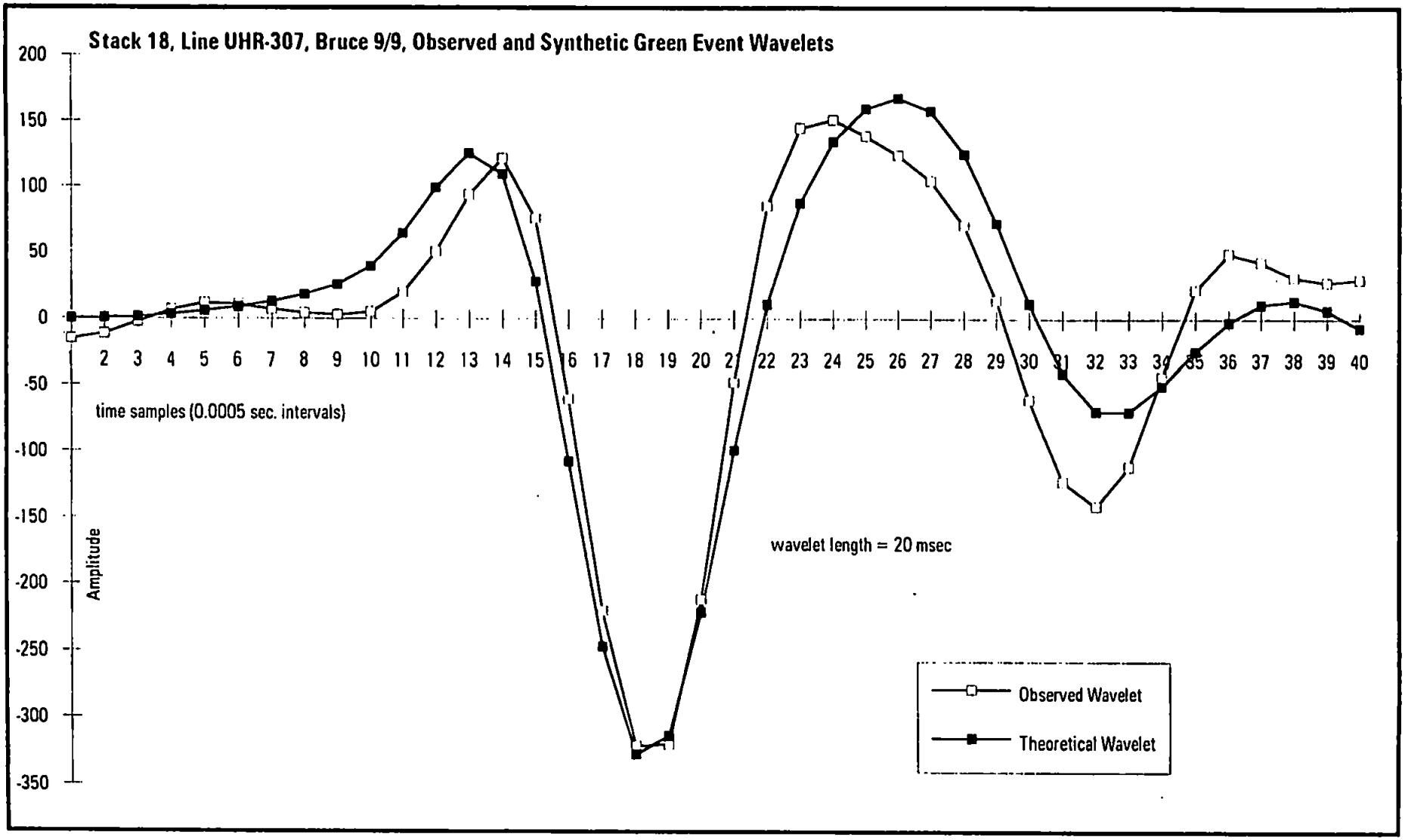

Figure 6.5c Stack 18, line UHR-307, Bruce 9/9, observed and synthetic Green Event wavelets.

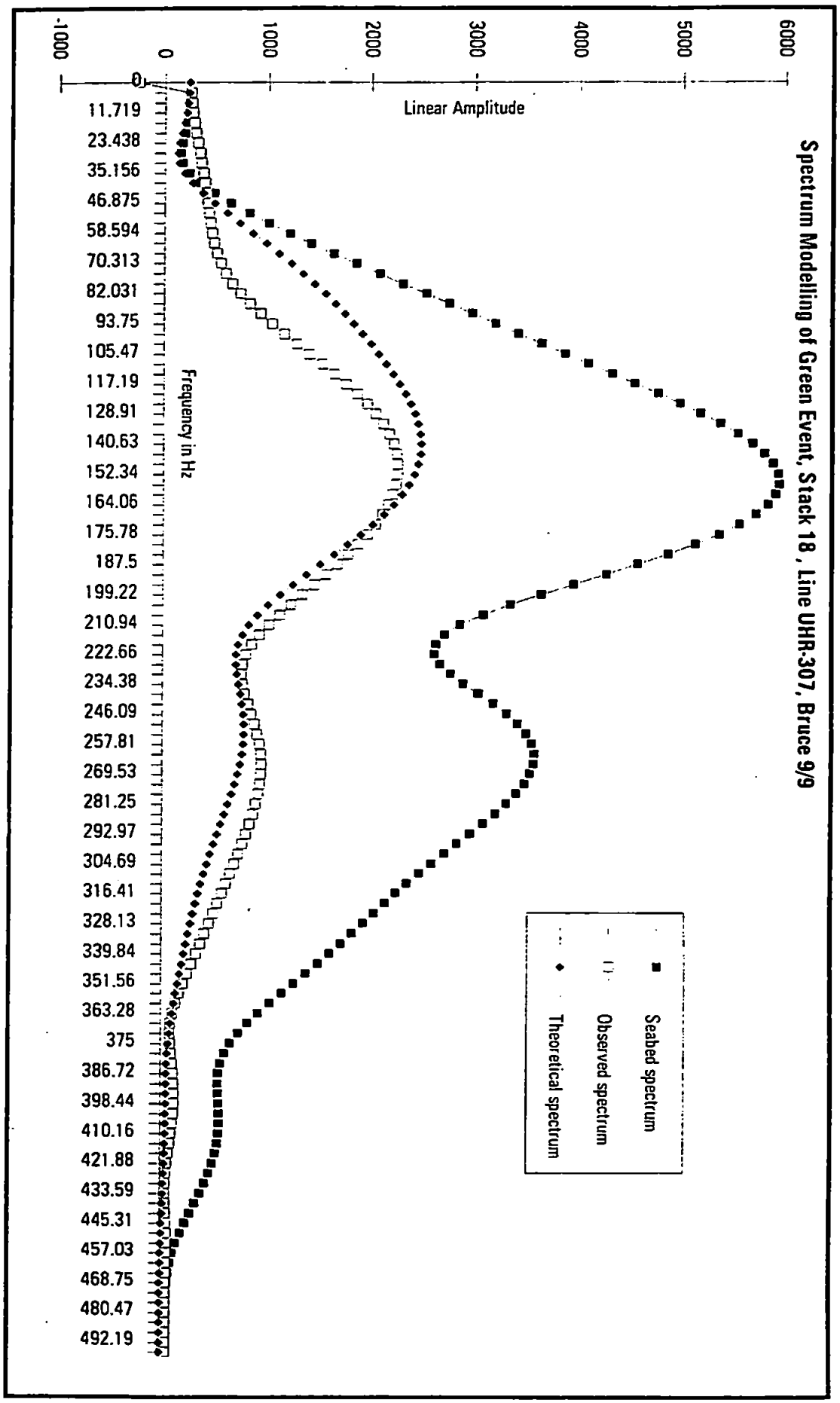

Figure 6.5d Spectrum modelling of Green Event, stack 18, line UHR-307, Bruce 9/9.

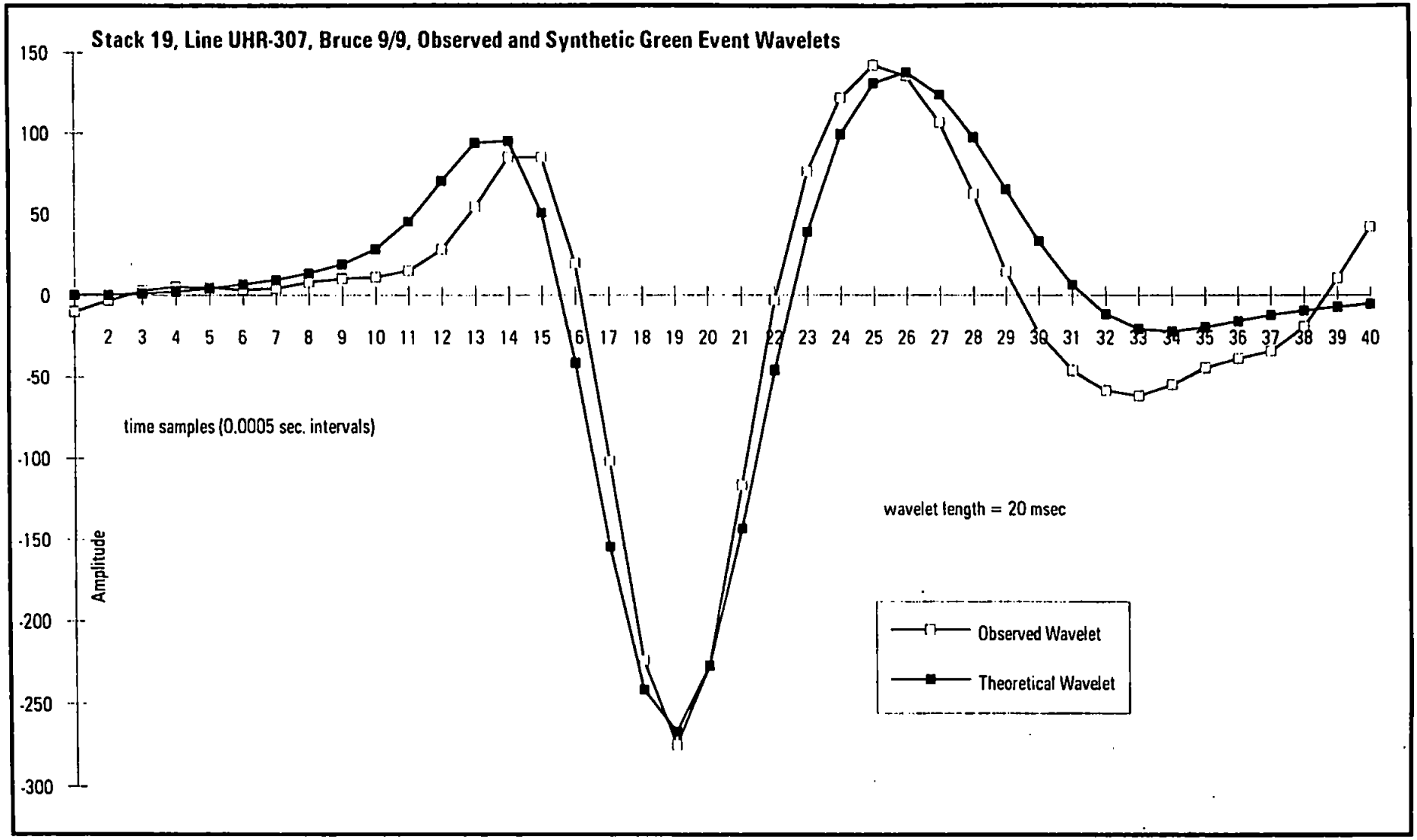

Figure 6.5e Stack 19, line UHR-307, Bruce 9/9, observed and synthetic Green Event wavelets.

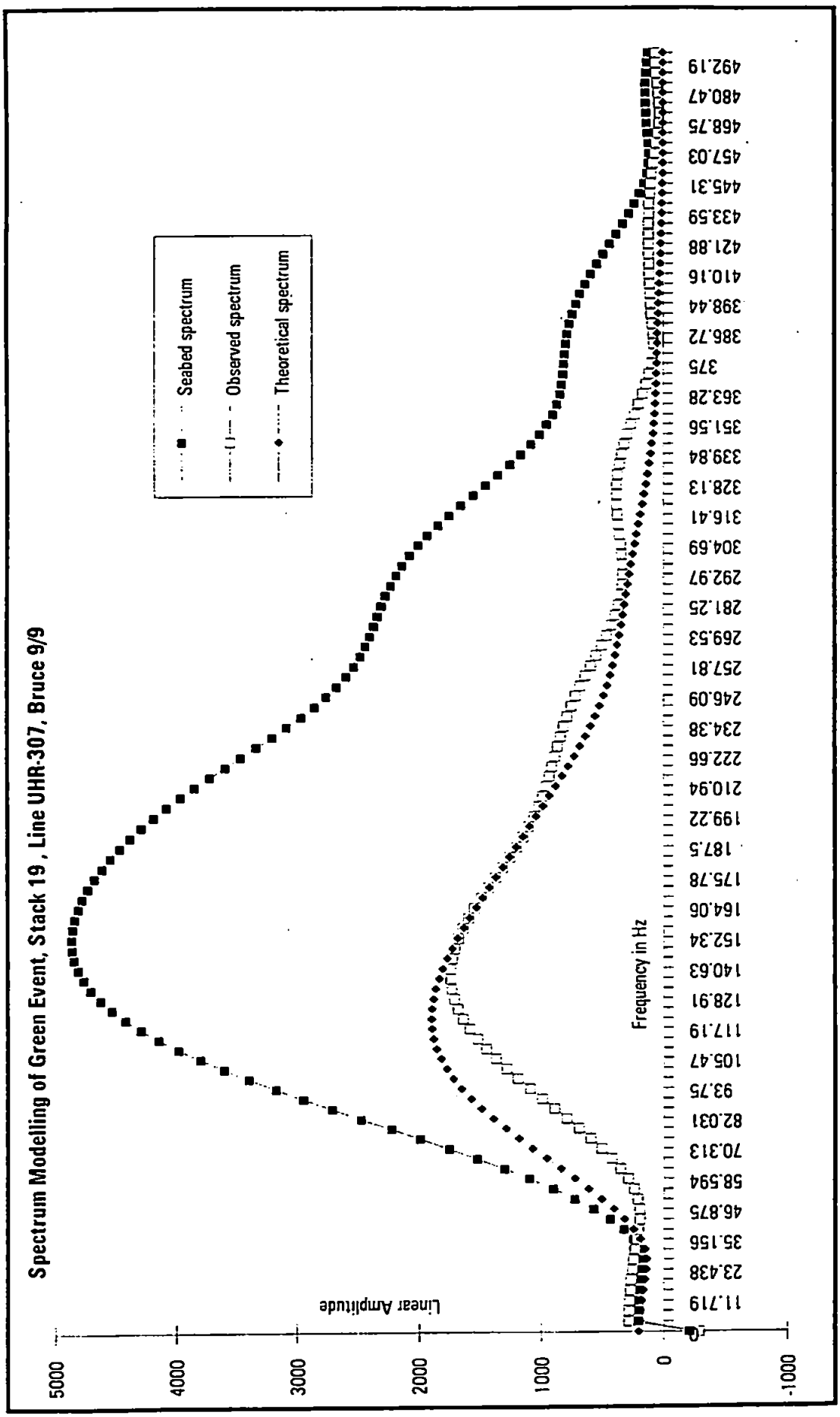

Figure 6.5f Spectrum modelling of Green Event, stack 19, line UHR-307, Bruce 9/9.

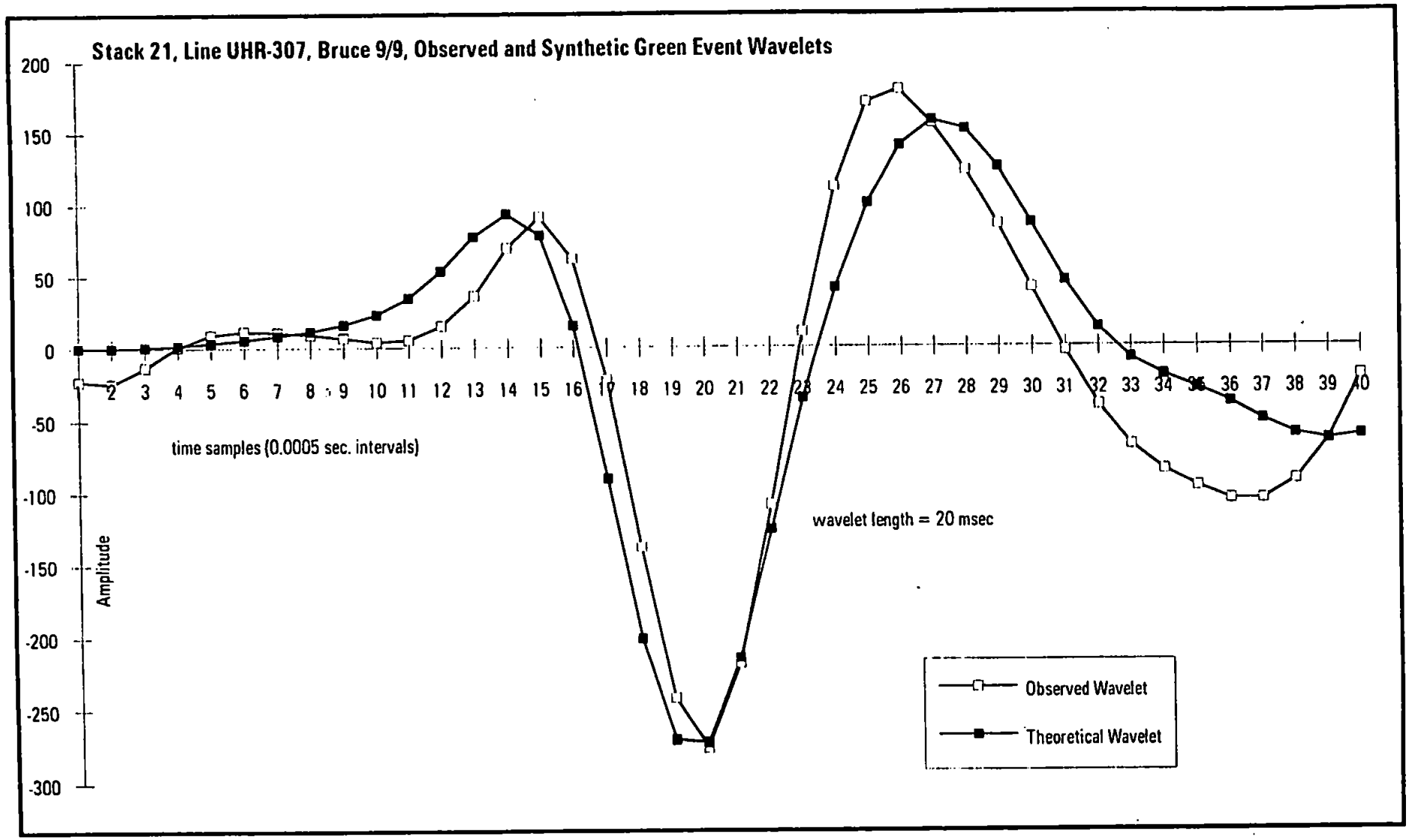

Figure 6.5g Stack 21, line UHR-307, Bruce 9/9, observed and synthetic Green Event wavelets.

Figure 6.5h Spectrum modelling of Green Event, stack 21, line UHR-307, Bruce 9/9.

6.5.3 Bruce UHR-308 Modelling

The relative amplitude stack of UHR-308 (Enclosure 6c) shows more variation in the Green Event than for lines UHR-304 and UHR-306. This results in a poorer (lower Green Event amplitude) condensed section of UHR-308 (Figure 6.6), with the exception of stacks 8, and 11 to 13. The modelling of stacks 8, 11, 12 and 13 are shown in Figures 6.7a to 6.7h.

Even within the four example traces, there is much variation of the seabed spectrum from stack to stack. For example, stacks 8 and 13 show a double peaked spectrum centred around 130 Hz, whilst stacks 11 and 12 show a triple peaked spectrum. These characteristical spectral shapes are also seen in the observed spectra of the Green Event. The bandwidths of both events are similar to that of UHR-307, but with the seabed spectrum extending to 410 Hz ±10 Hz. Spectrum modelling fitted a theoretical spectrum well to the observed Green Event spectrum over a bandwidth of 130 Hz to 300 Hz. Below 130 Hz there is a lack of low-frequency amplitude in the observed spectrum of the seabed multiple.

Time-domain modelling again matched the observed seabed multiple to a synthesised wavelet. As with the previous two lines, the theoretical wavelet is consistently broader in appearance, but very similar in shape, despite the spectral variation in the seabed reflector from stack to stack.

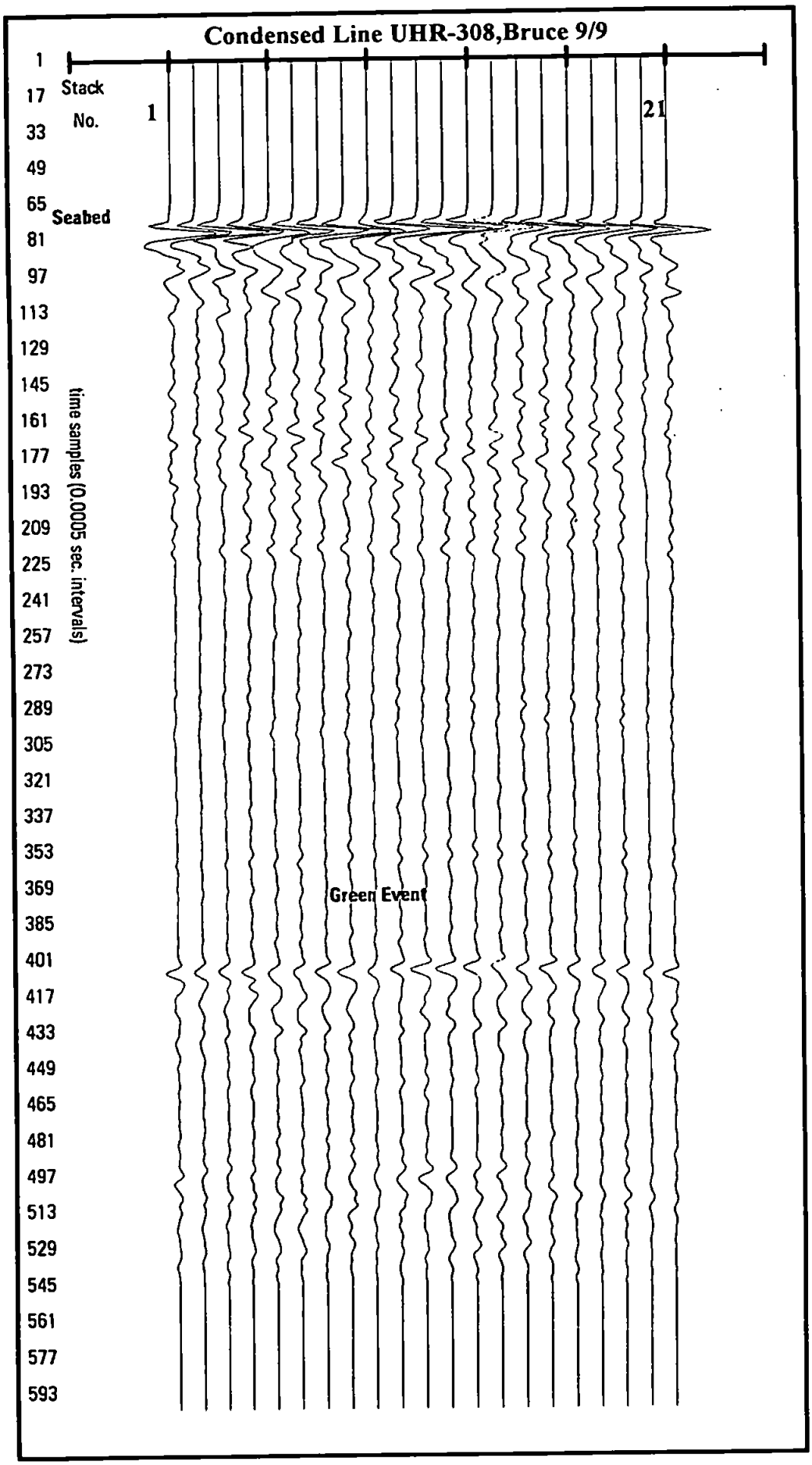

Figure 6.6 Condensed line UHR-308, Bruce 9/9

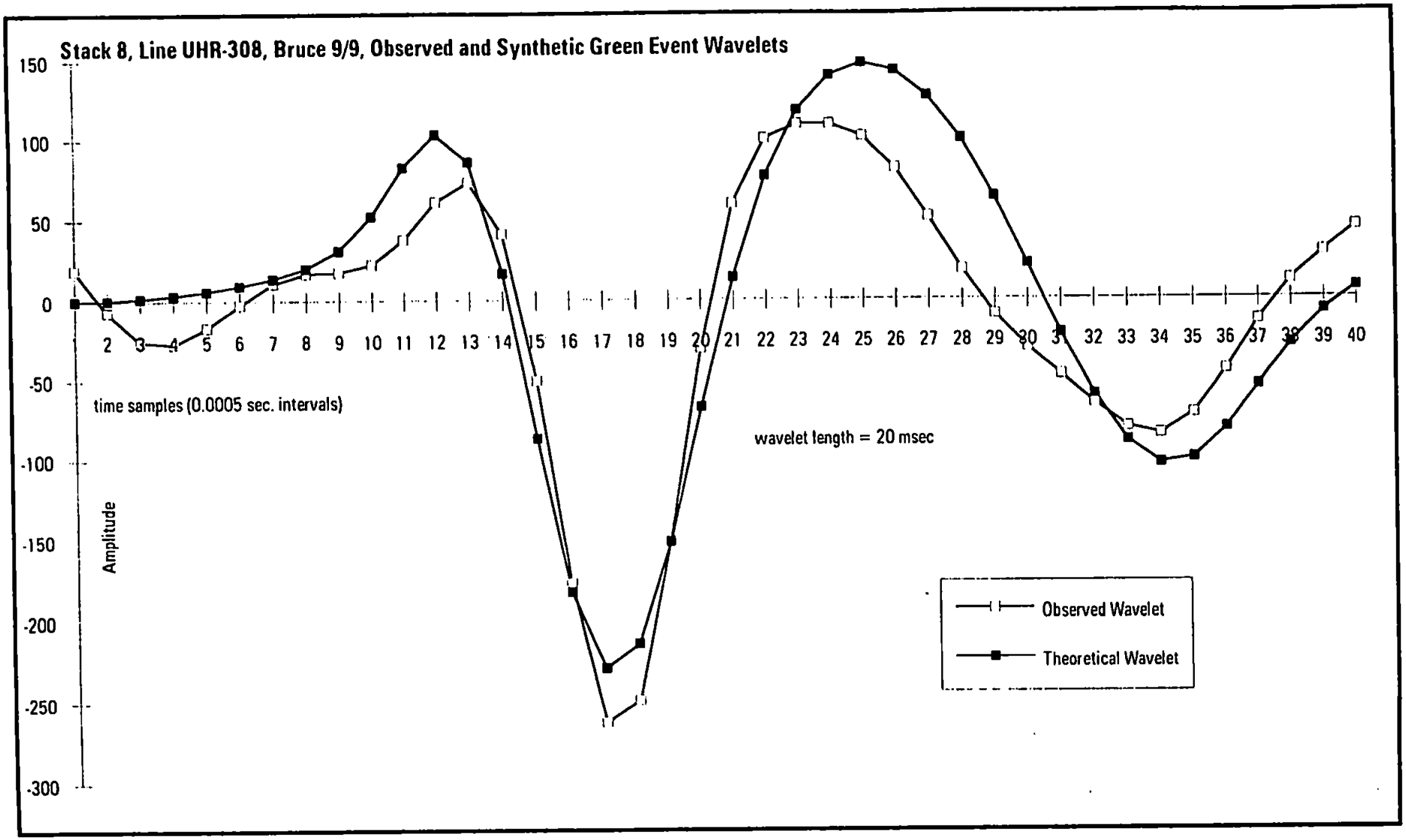

Figure 6.7a Stack 8, line UHR-308, Bruce 9/9, observed and synthetic Green Event wavelets.

Figure 6.7b Spectrum modelling of Green Event, stack 8, line UHR-308, Bruce 9/9.

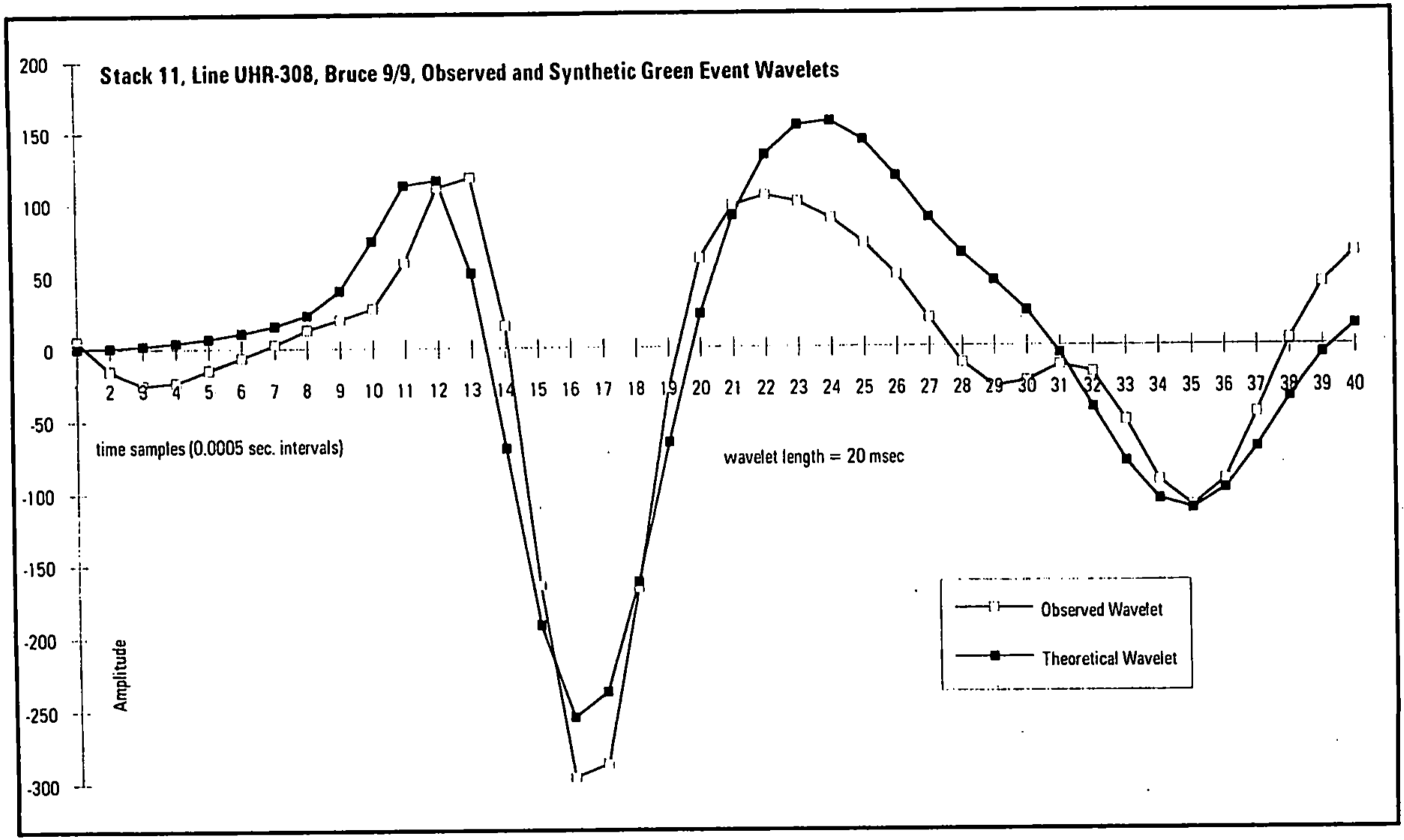

Figure 6.7c Stack 11 line UHR-308, Bruce 9/9, observed and synthetic Green Event wavelets.

Figure 6.7d Spectrum modelling of Green Event, stack 11, line UHR-308, Bruce 9/9.

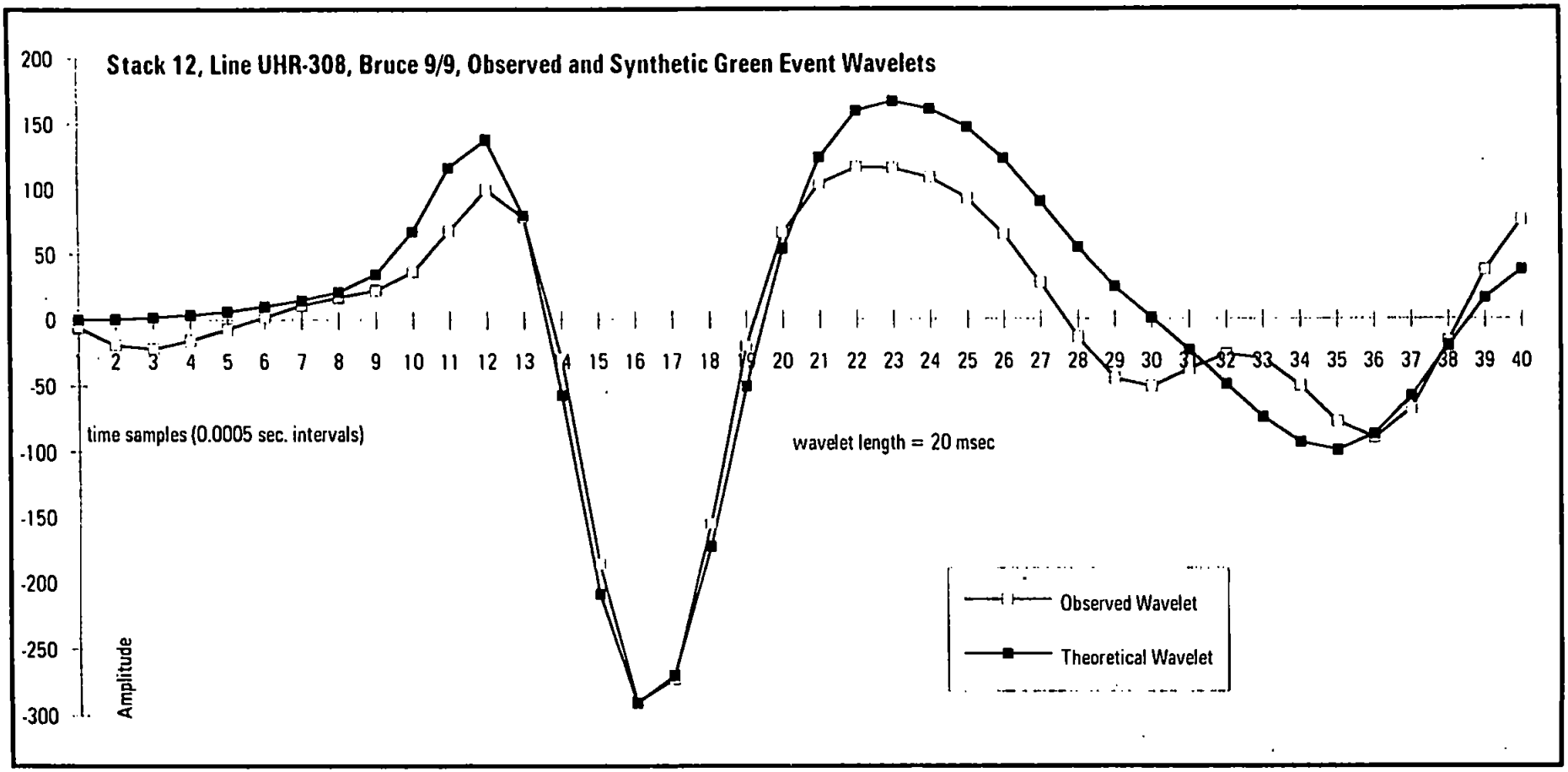

Figure 6.7e Stack 12, line UHR-308, Bruce 9/9, observed and synthetic Green Event wavelets.

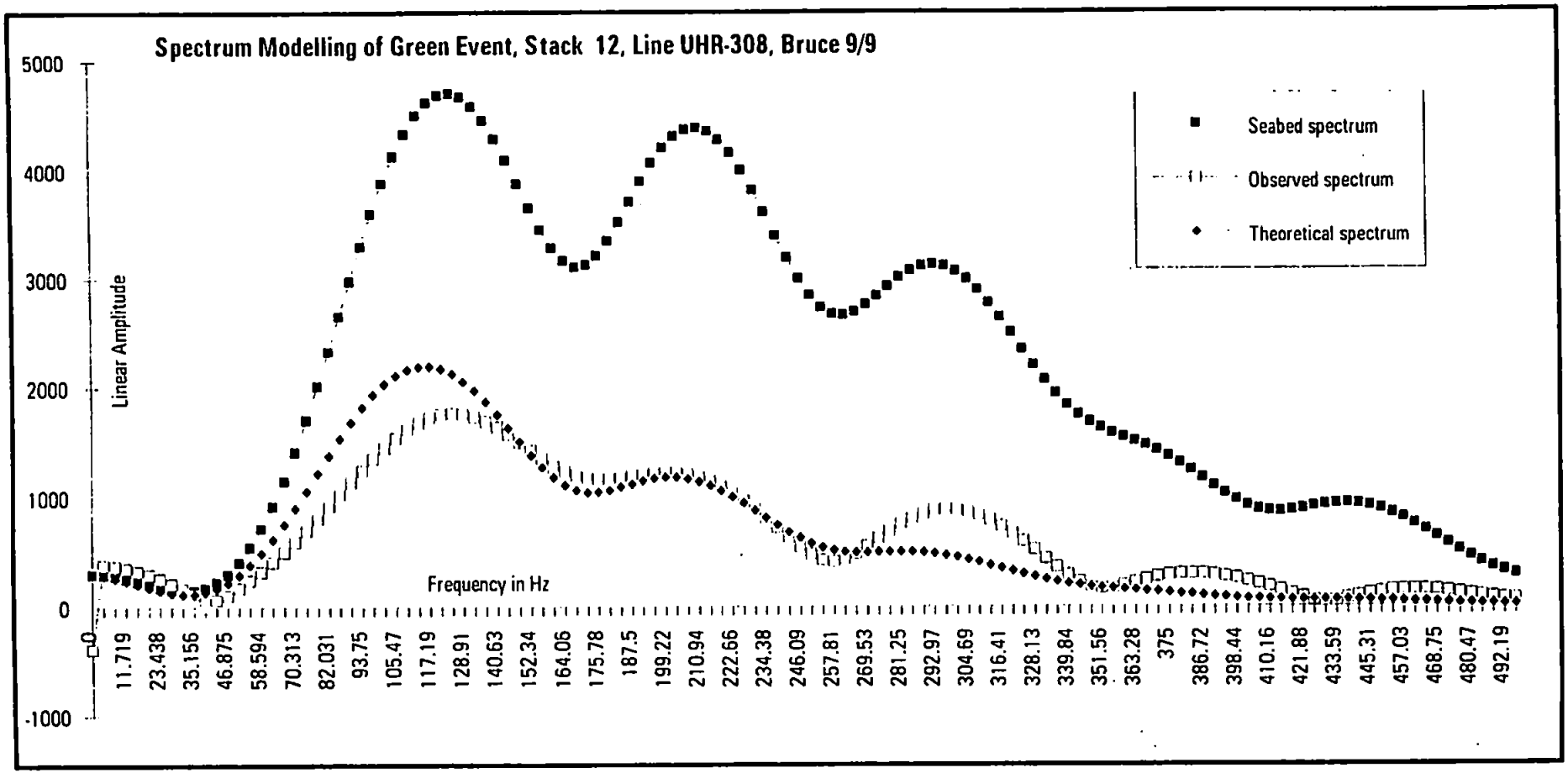

Figure 6.7f Spectrum modelling of Green Event, stack 12, line UHR-308, Bruce 9/9.

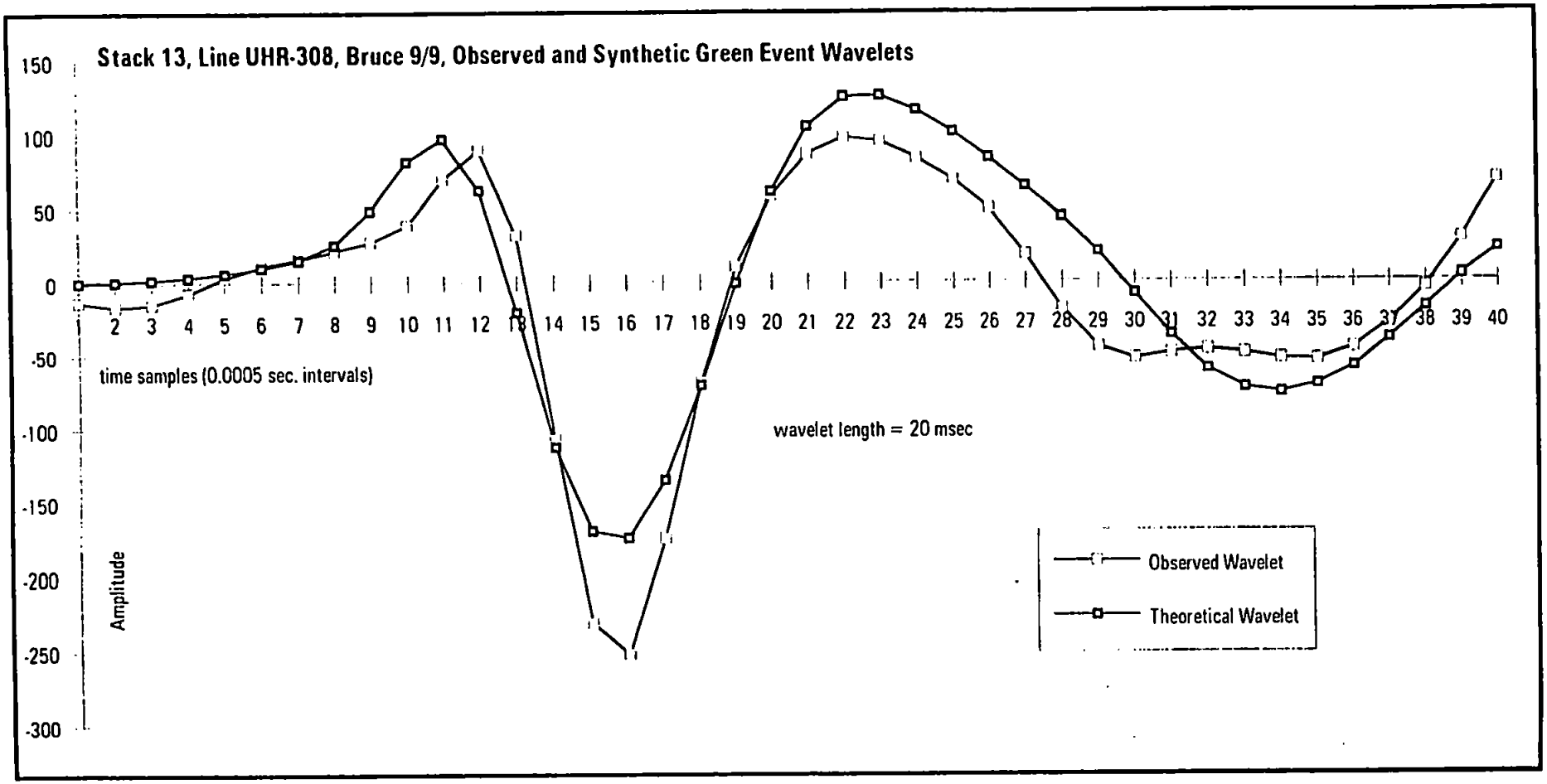

Figure 6.7g Stack 13, line UHR-308, Bruce 9/9, observed and synthetic Green Event wavelets.

Figure 6.7h Spectrum modelling of Green Event, stack 13, line UHR-308, Bruce 9/9.

6.5.4 Bruce UHR-309 Modelling

The relative amplitude stack of UHR-309 (Enclosure 6d) shows a consistently strong Green Event reflection at 330 ms TWTT. The event is particularly strong between CDP 410 and CDP 240, and between CDP 100 and CDP 1. The condensed line of UHR-309 again shows high amplitude stacked traces across the section (Figure 6.8). Five stacks are presented as modelling examples, stacks 7, 11, 12, 14 and 18 (Figures 6.9a to 6.9f).

The seabed spectra show a bandwidth ranging from 60 Hz ±10 Hz to 350 Hz ±30 Hz, with a dominant central peak at 150 Hz ±10 Hz. In some cases a secondary peak is developed at 290 Hz ±15 Hz. The observed Green Event spectrum has a peak at 135 Hz ± 10 Hz. In the examples presented, the theoretical spectrum fitted the observed spectrum very well up to about 350 Hz . The amplitude deficiency in the observed spectrum seen in the previous lines is less well developed in these examples.

The wavelet modelling results mirror the results of the spectral modelling, in that there is a very good fit between the observed and the synthesised seabed multiple wavelets. The best example of this can be seen in stack 7, where a very close fit has been achieved for all but the first 13 time samples (Figure 6.9a). Over the complete duration of the wavelet, the synthesised seabed multiple still appears slightly broader in appearance than the observed equivalent, as with the lines previously discussed.

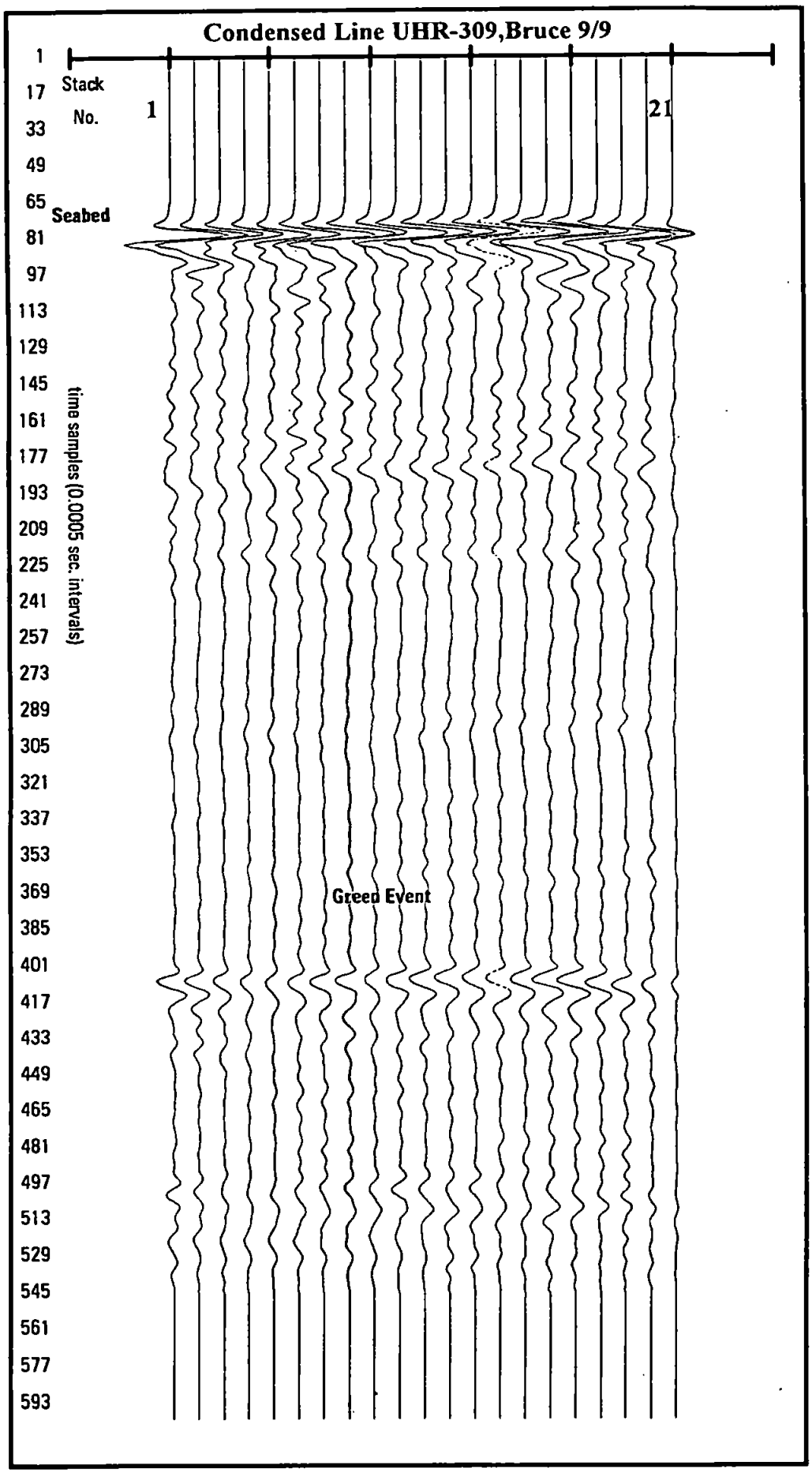

Figure 6.8 Condensed line UHR-309, Bruce 9/9

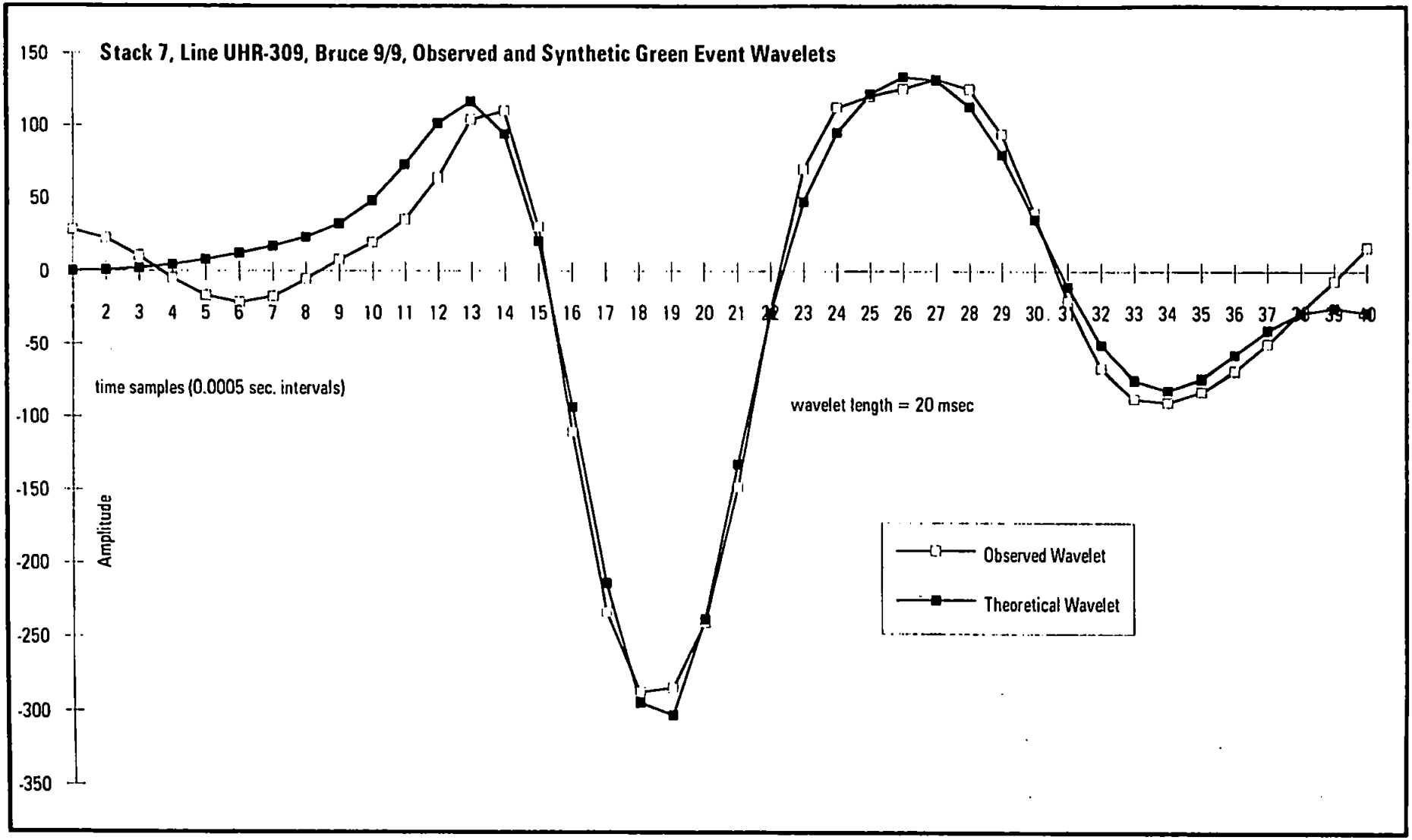

Figure 6.9a Stack 7, line UHR-309, Bruce 9/9, observed and synthetic Green Event wavelets.

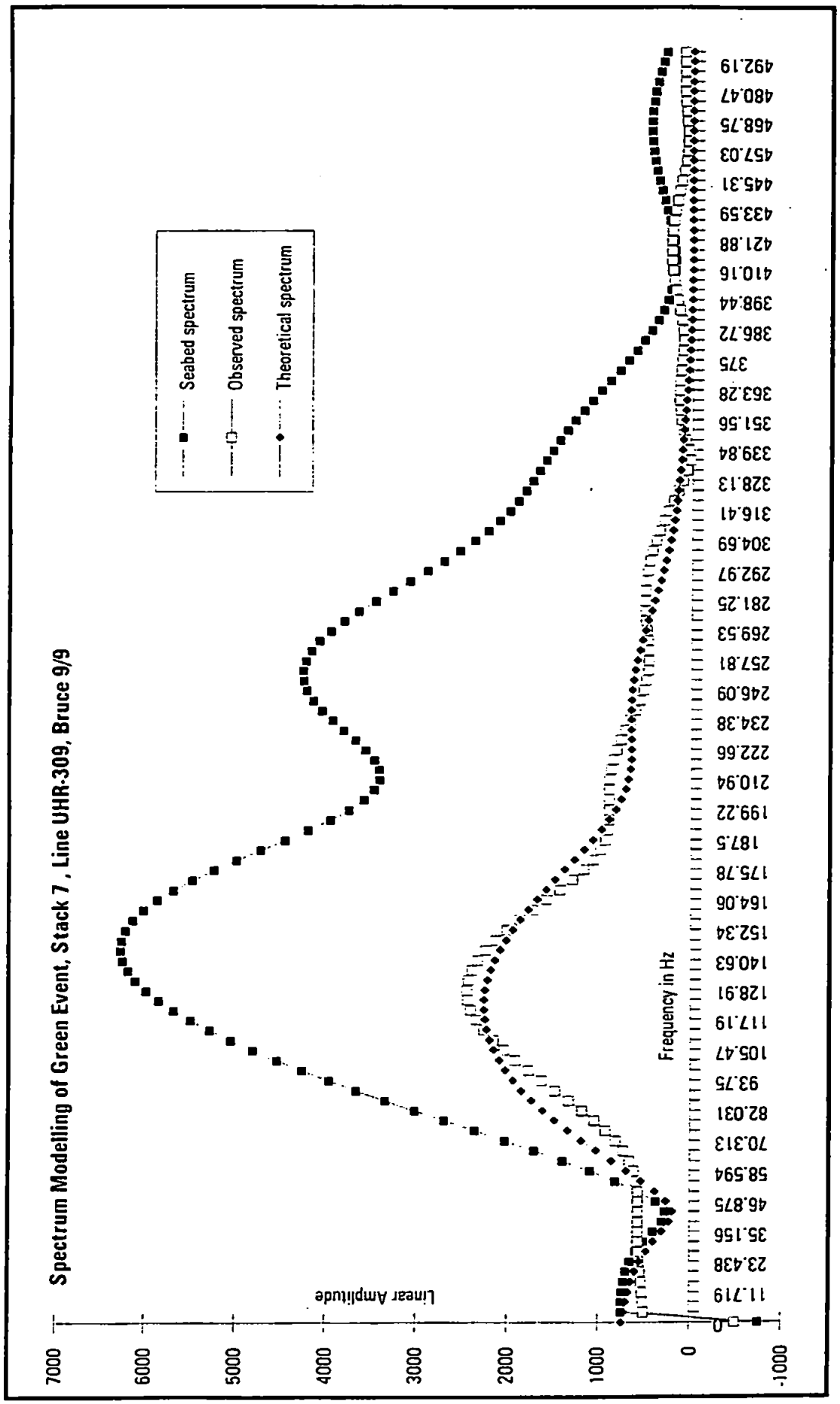

Figure 6.9b Spectrum modelling of Green Event, stack 7, line UHR-309, Bruce 9/9.

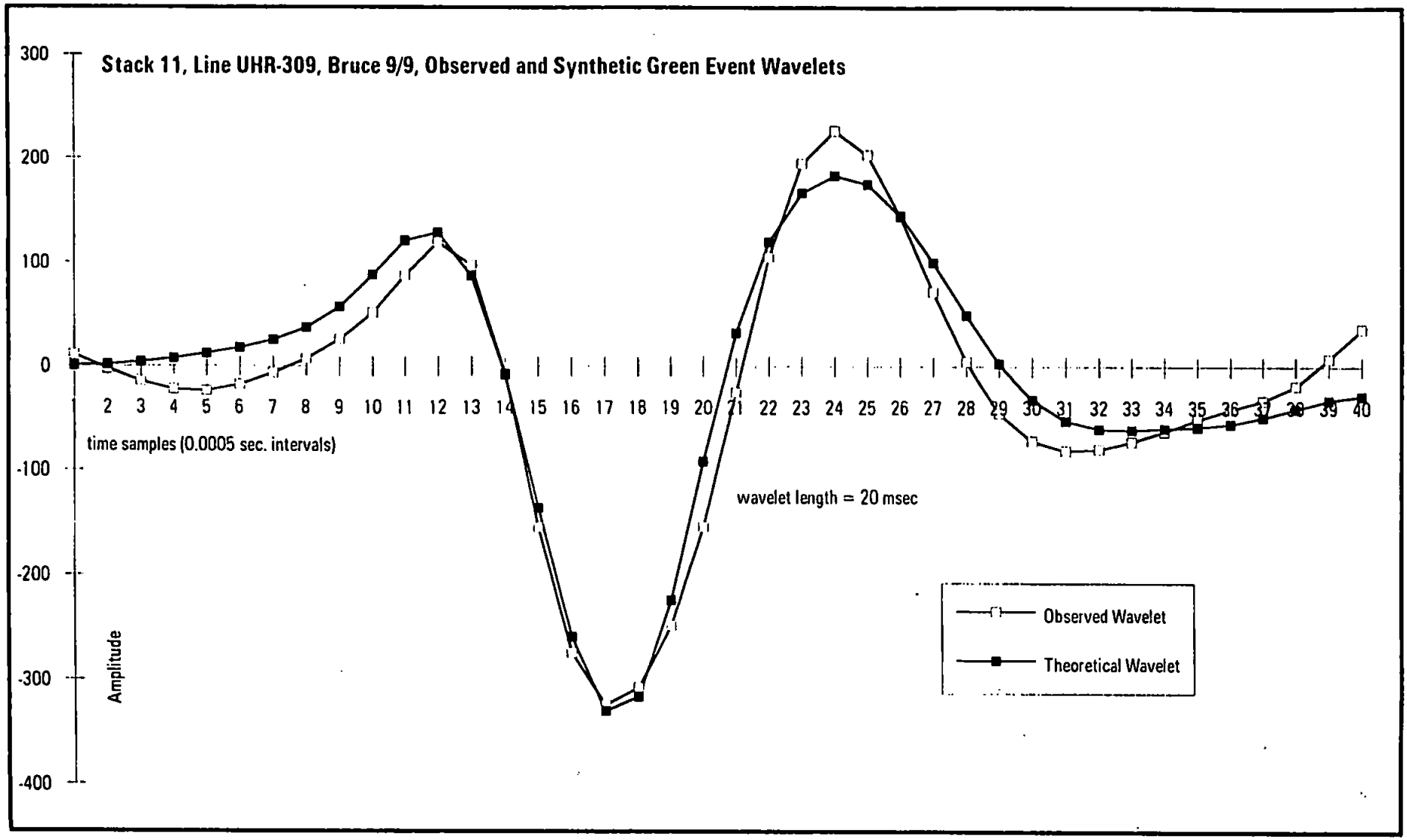

Figure 6.9c Stack 11 line UHR-309, Bruce 9/9, observed and synthetic Green Event wavelets.

Figure 6.9d Spectrum modelling of Green Event, stack 11, line UHR-309, Bruce 9/9.

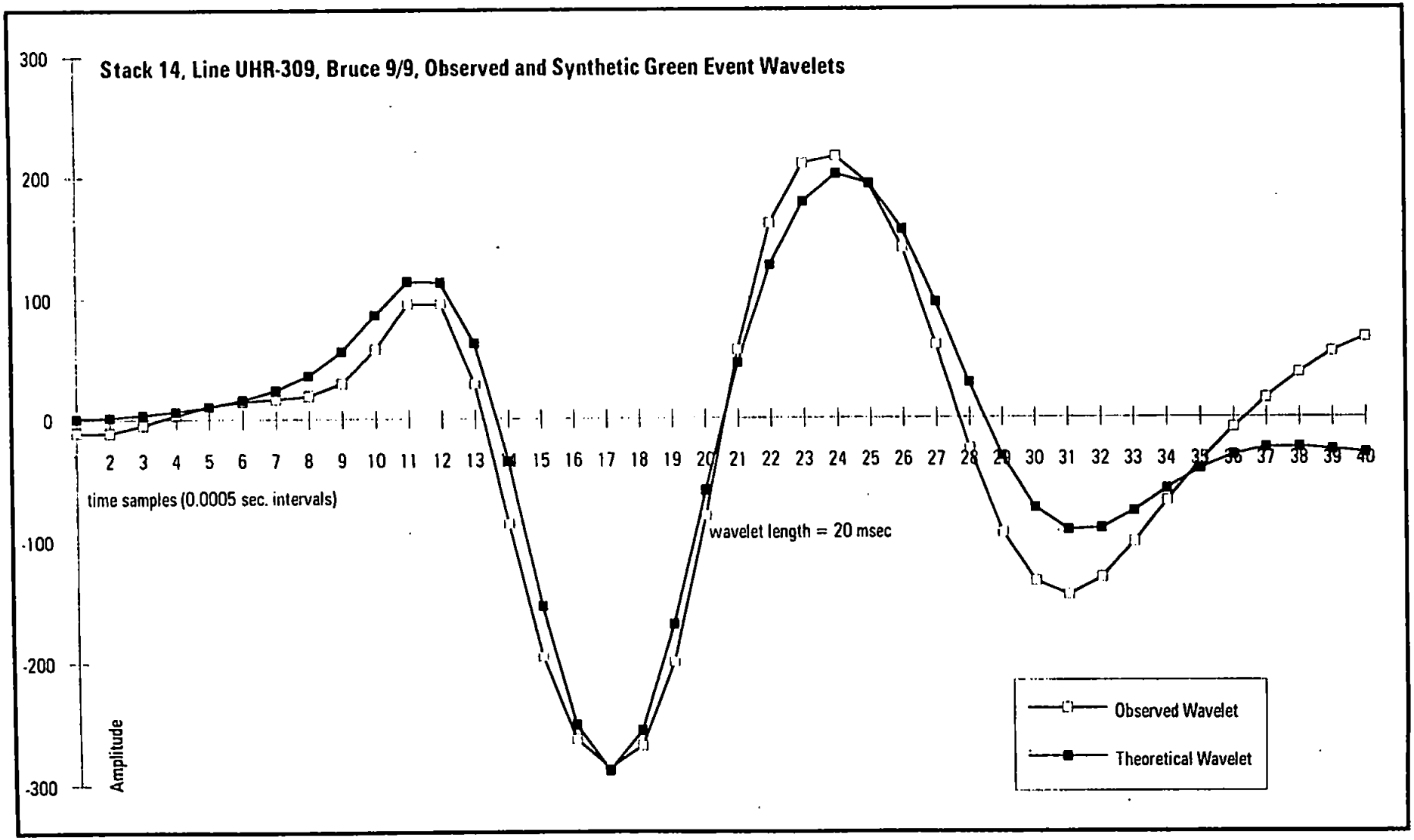

Figure 6.9e Stack 14, line UHR-309, Bruce 9/9, observed and synthetic Green Event wavelets.

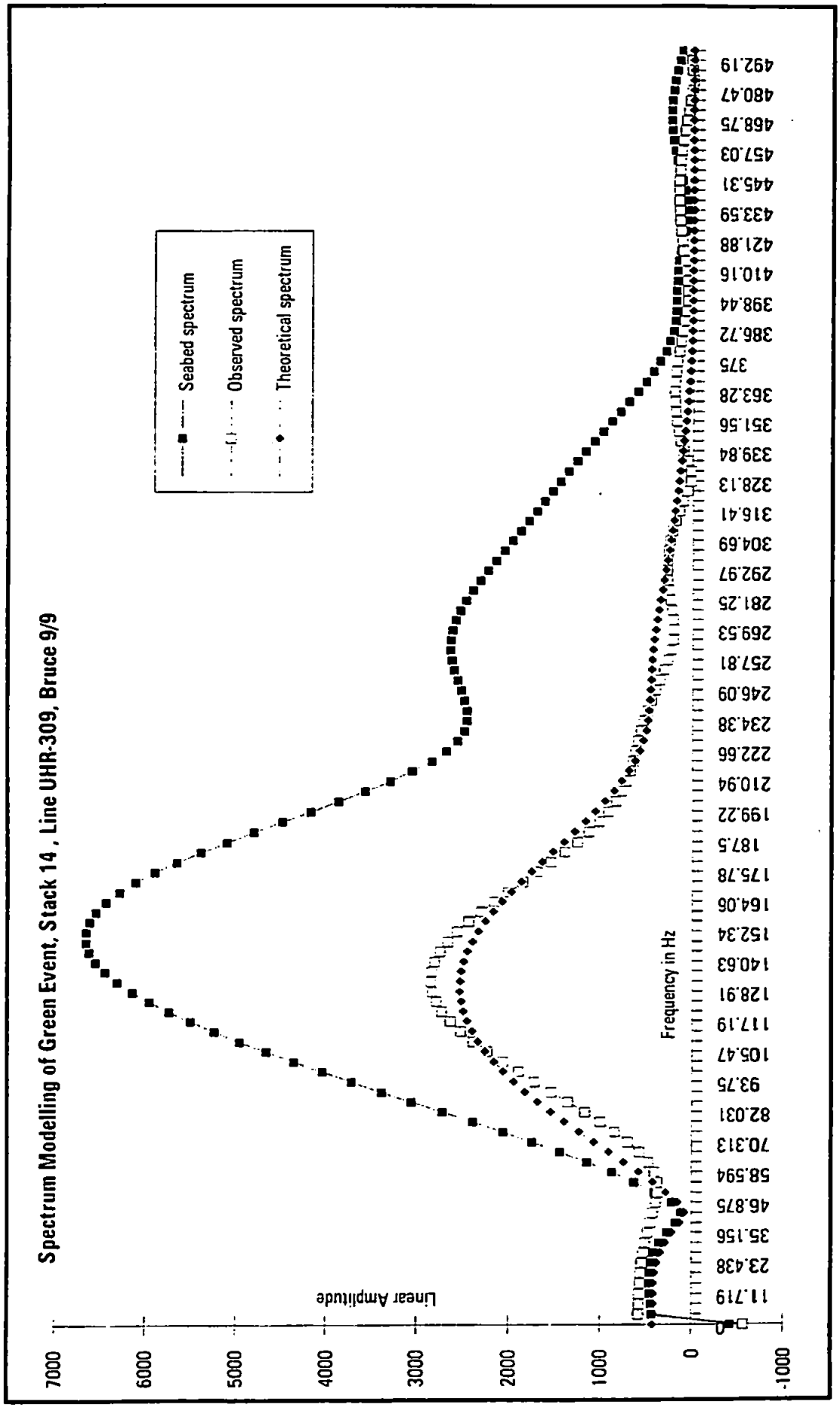

Figure 6.9f Spectrum modelling of Green Event, stack 14, line UHR-309, Bruce 9/9.

6.5.5 Bruce UHR-320 Modelling

The relative amplitude stack of UHR-320 (Enclosure 6e) shows a very well developed Green Event in the middle of the section between CDP 350 and CDP 140 at about 330 ms TWTT (Figure 6.10). The spectrum of the seabed ranges from 60 Hz ±10 Hz to 390 Hz ± 20 Hz, peaking at 150 Hz ±10 Hz. A secondary peak is developed at 270 Hz ±10 Hz. The observed seabed multiple spectrum peaks at 130 Hz ±10 Hz. Stacks 8 to 11 and 14 are used as modelling examples (Figures 6.11a to 6.11j).

Within the examples presented (Figures 6.11a to 6.11j), the theoretical spectrum models the observed spectrum well up to 400 Hz. As seen before, there is a consistent lack of low frequency amplitude in the observed spectrum relative to the theoretical spectrum below 130 Hz.

Wavelet modelling yielded synthetic wavelets which fitted the observed Green Event wavelets well. The synthetic wavelets were consistently slightly longer in duration than their observed equivalents. Once more, the onset of the initial peak occurs slightly earlier and more gently for the synthetic wavelets, whilst the central trough is slightly broader and the second peak is slightly delayed.

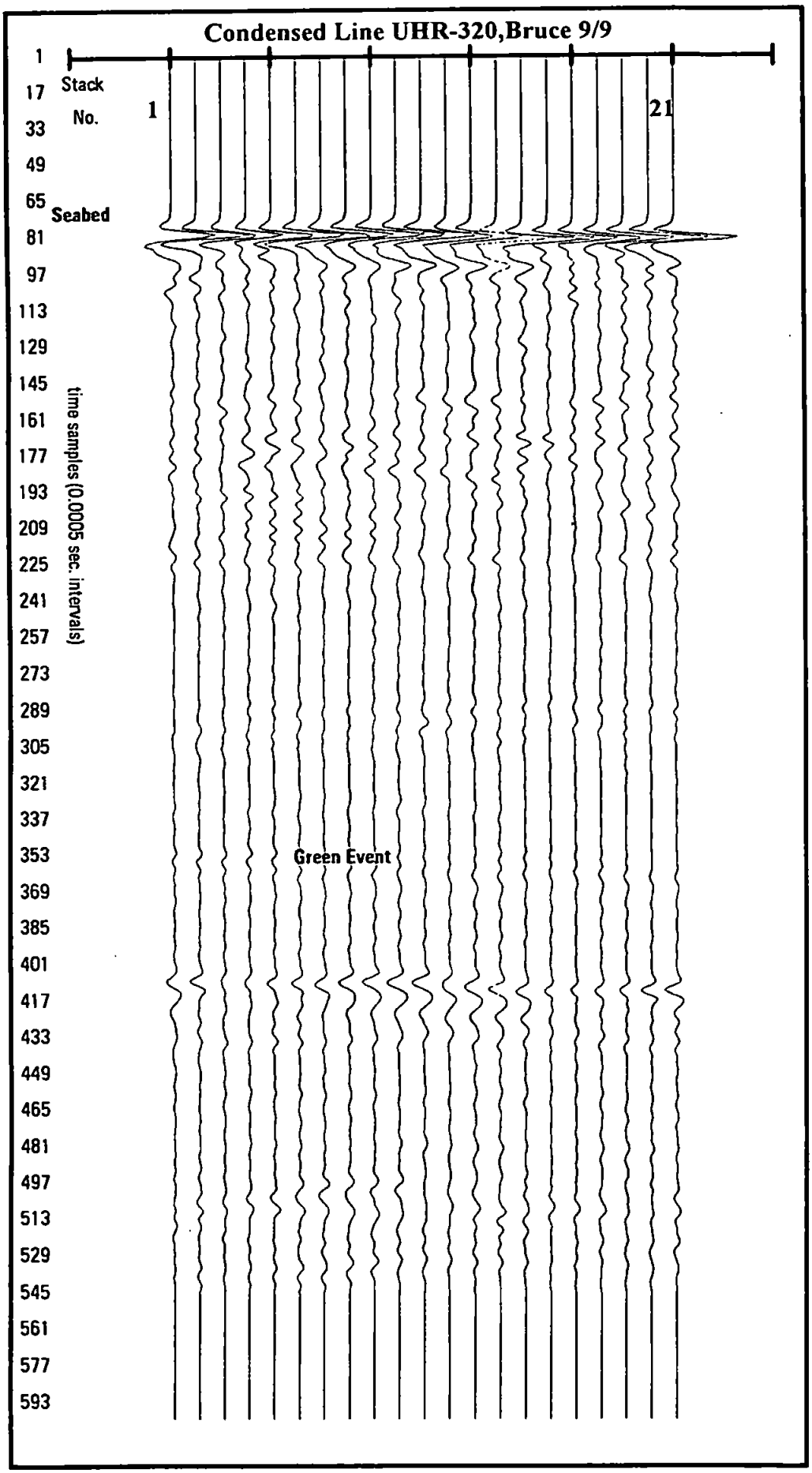

Figure 6.10 Condensed line UHR-320, Bruce 9/9

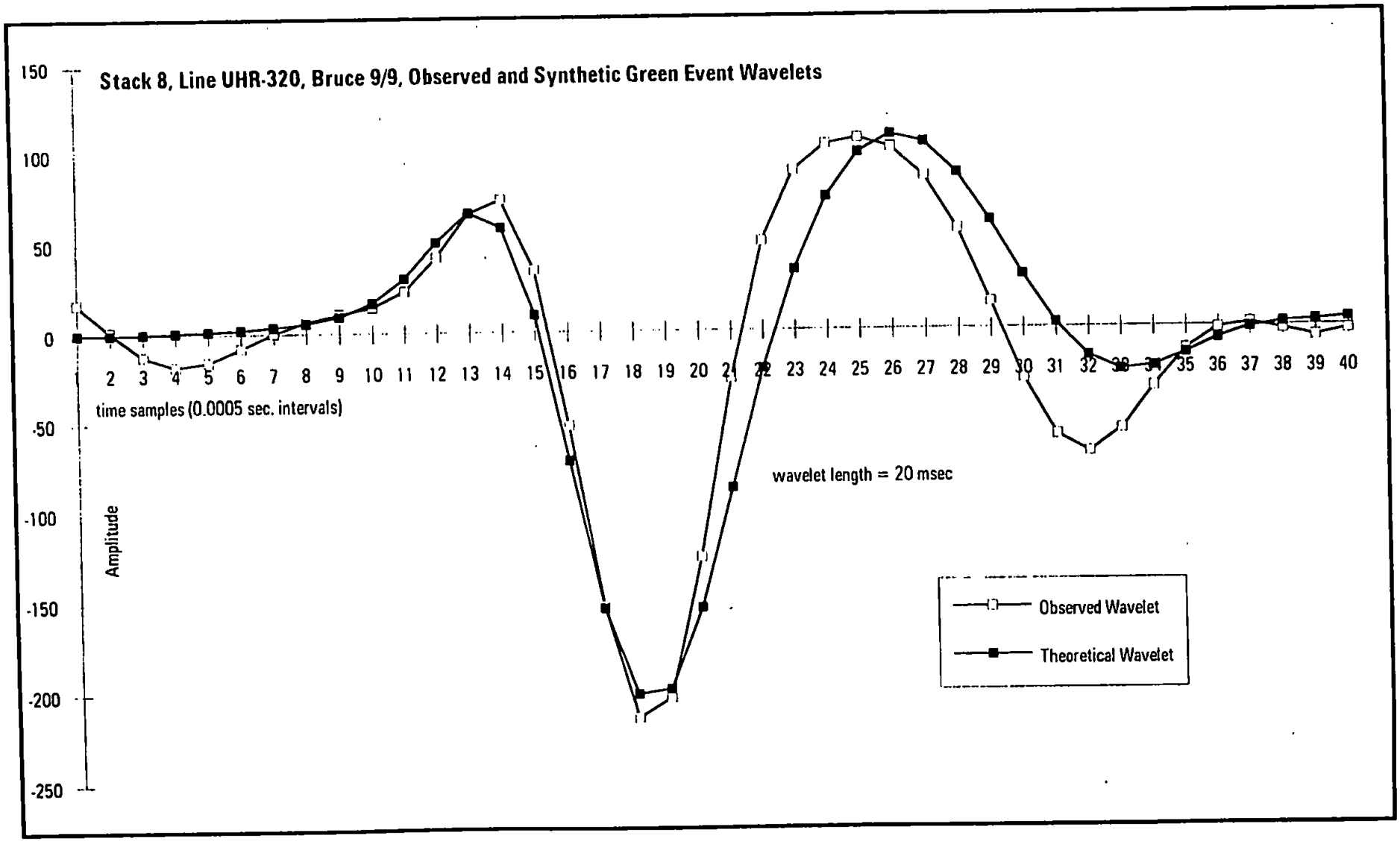

Figure 6.11a Stack 8, line UHR-320, Bruce 9/9, observed and synthetic Green Event wavelets.

Figure 6.11b Spectrum modelling of Green Event, stack 8, line UHR-320, Bruce 9/9.

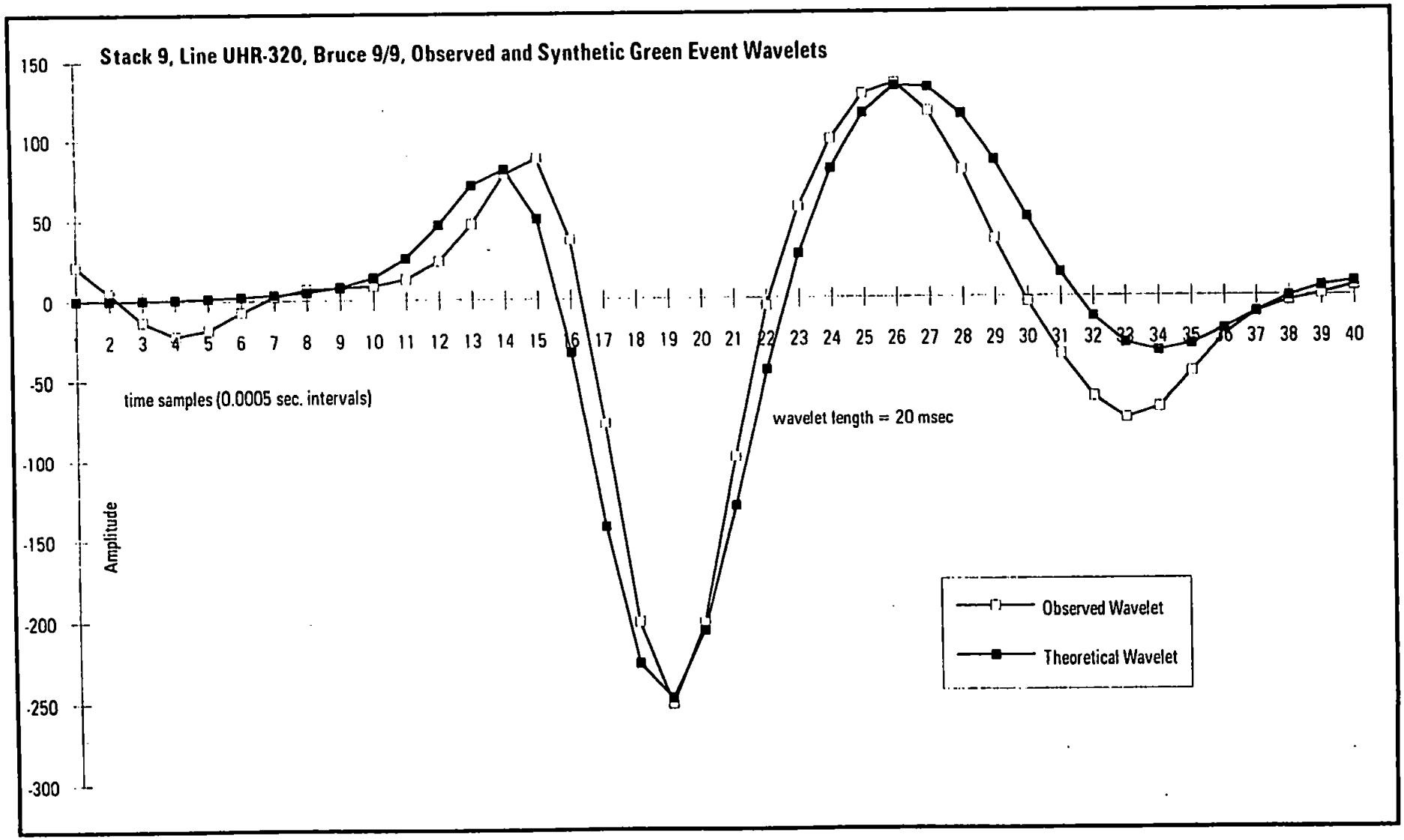

Figure 6.11c Stack 9 line UHR-320, Bruce 9/9, observed and synthetic Green Event wavelets.

Figure 6.11d Spectrum modelling of Green Event, stack 9, line UHR-320, Bruce 9/9.

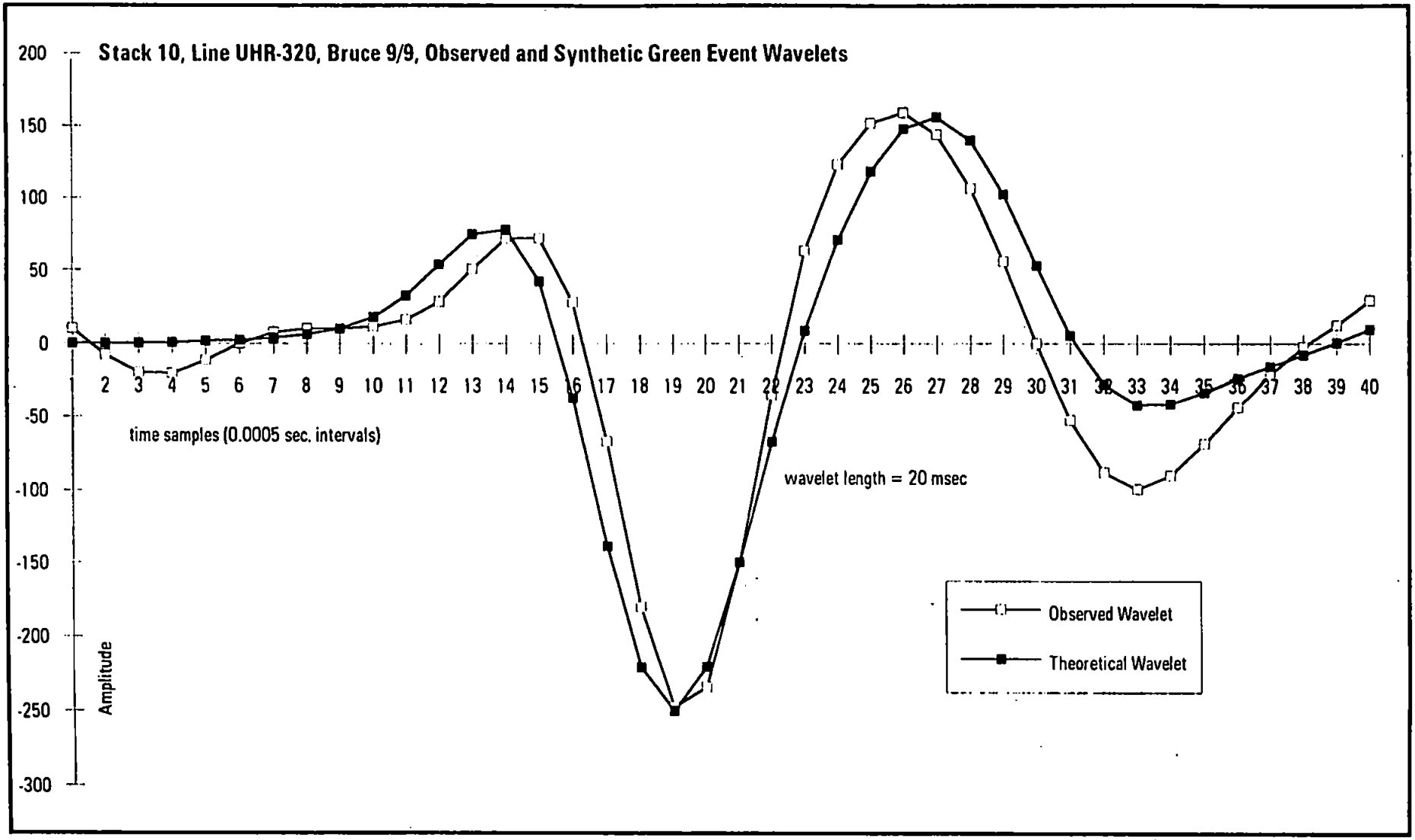

Figure 6.11e Stack 10, line UHR-320, Bruce 9/9, observed and synthetic Green Event wavelets.

Figure 6.11f Spectrum modelling of Green Event, stack 10, line UHR-320, Bruce 9/9.

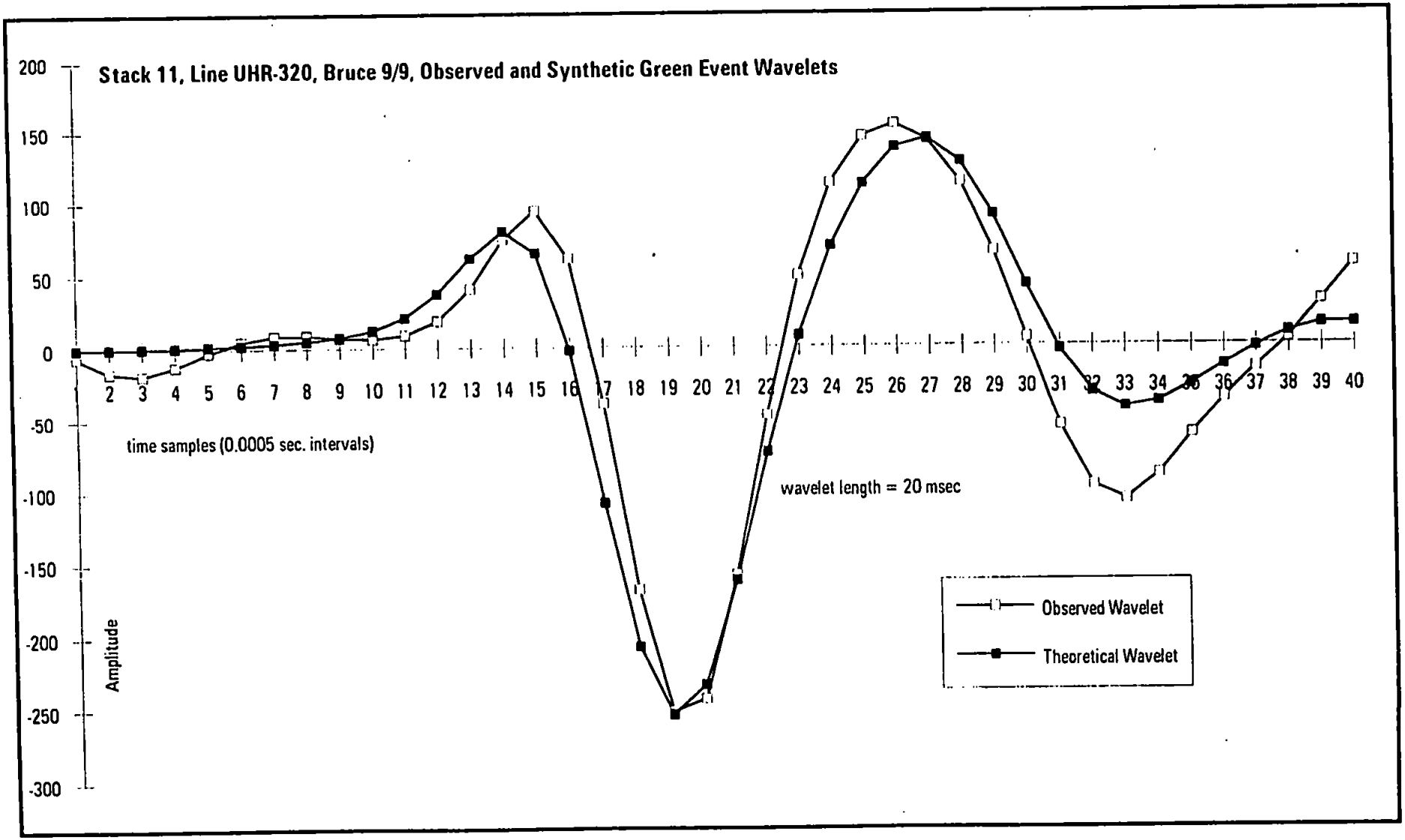

Figure 6.11g Stack 11, line UHR-320, Bruce 9/9, observed and synthetic Green Event wavelets.

Figure 6.11h Spectrum modelling of Green Event, stack 11, line UHR-320, Bruce 9/9.

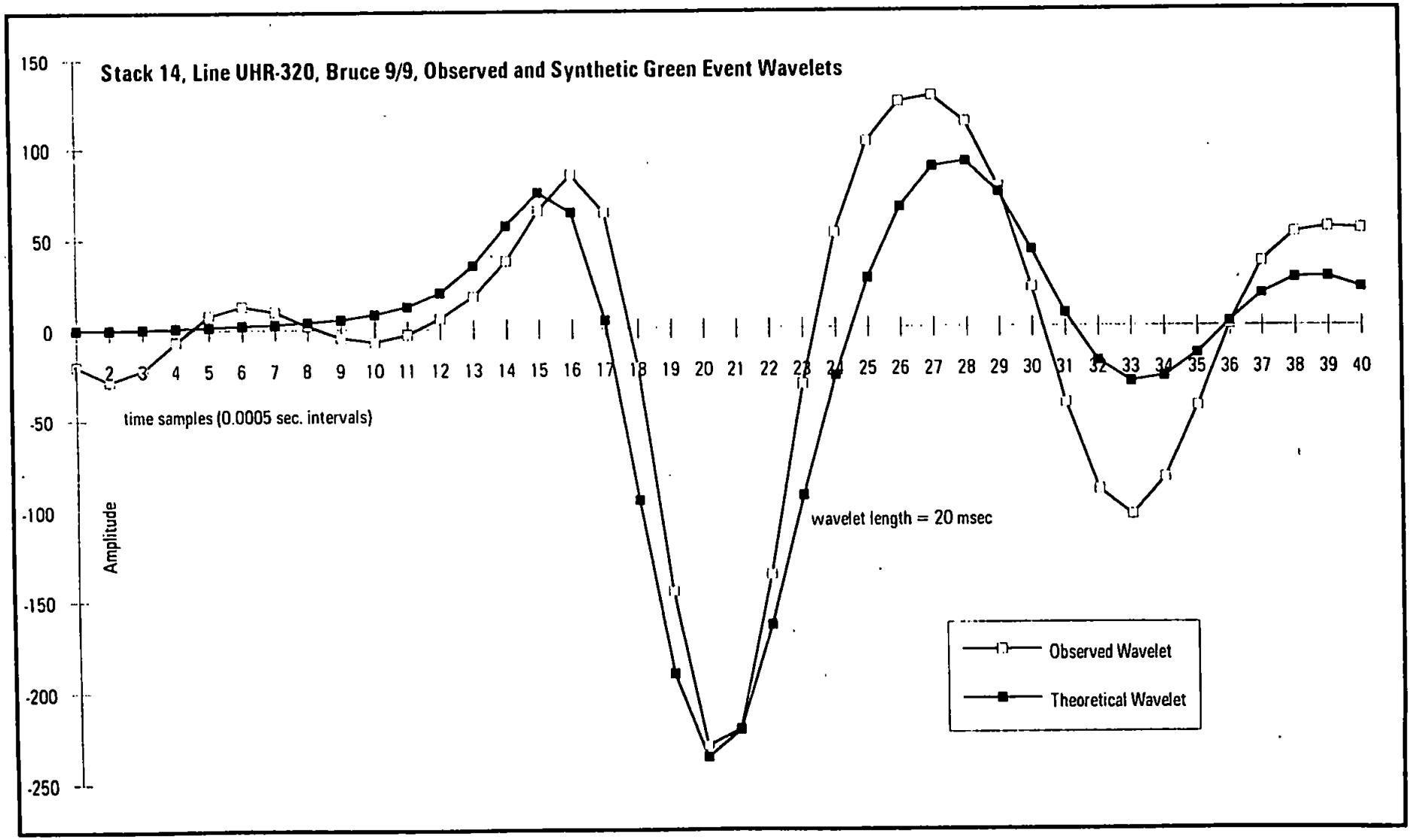

Figure 6.11i Stack 14, line UHR-320, Bruce 9/9, observed and synthetic Green Event wavelets.

Figure 6.11j Spectrum modelling of Green Event, stack 14, line UHR-320, Bruce 9/9.

6.6 Discussion - Bruce Case Study

The modelling carried out has assumed normal incidence of both the event reflected from the seabed and the Green Event. The spectral response of the receiver is assumed to be constant from the beginning of the seabed arrival to the end of the arrival of the Green Event. In practice, this means a constant depth for the receiver groups of the hydrophone as well as no dramatic changes in the sea state.

Spectrum and wavelet modelling shows that the Green Event is deficient in amplitude at the lower end of the signal spectrum (< c. 130 Hz), in comparison to the seabed reflection, and that the equivalent time-domain reflected event is slightly sharper in appearance. An analysis of the spectra of the two events shows that the amplitude loss between the two events is broadly proportional to the first power of frequency in the 130 Hz to 300 Hz frequency band. Clearly a process has consistently occurred across the seismic lines which has filtered the propagating pulse between the two arrivals in a low-pass manner below a certain frequency threshold.

The seabed is considered as having a filtering effect on the second incidence of the propagating source pulse. This filtering effect is fairly consistent across the seismic lines considered here. This filtering effect is likely to have arisen from a layer that is thin relative to the period of the incident source wavelet at the seabed. This implies that the first incidence of the downgoing pulse will also be filtered at the seabed. The low-pass transmission effects of a thin layer have been described in Chapter 2. In this example, frequencies below c. 130 Hz have been preferentially transmitted at the seabed, and in doing so, have left the spectrum of the reflected part of the pulse deficient in that band to be recorded at the hydrophone. This amplitude deficiency is not considered to arise from the hydrophone; any spectral notches in the response characteristics of the receiver would be seen in the seabed spectrum as well as in the spectrum of the Green Event, given a constant hydrophone depth in the c. 1/3 sec. between the onset of the seabed arrival and that of the Green Event.

A variation in the spectral shape of both events does occur throughout the seismic lines. For example stack 3 of UHR-304 displays a deep spectral notch at c. 170 Hz (Figure 6.3b) whilst stack 11 of UHR-320 shows a rather smooth spectrum across the 50 Hz to 400 Hz band without any notching (Figure 6.11h). This variation may be due to differing source/receiver orientations between particular shots, or to lateral variations in the near-surface layering, but will not be due to variation in source/receiver geometry between the arrival of the two reflected events. This is shown in both of the examples; the Green Event shows a similar spectral notch at c. 170 ms in the first example, and similarly, the spectrum of the Green Event is smooth across the 70 Hz to 380 Hz range without notching in the second example.

Without consideration of the specific details of the thin seabed layer, this case example has implications for other absorption studies using the seabed as the reference (unattenuated/unabsorbed source) pulse. If near-seabed layering can be shown to have a filtering effect (high-pass reflection response) between the arrival of the seabed return and the first multiple, the low-pass transmission response of the same layering is clearly going to be an important factor when comparing the seabed event to an event from a deeper interface. This is because the propagating pulse will be subject to low pass filtering twice, once from above the seabed and once from below following reflection from the deeper event.

As was shown in Chapter 2, section 2.3, this thin-layer response is partly a function of the reflection coefficients bounding the thin layer, with a greater low-pass transmission response occurring with higher reflection coefficients. Excepting the case of near-surface gassy sands the strongest reflection coefficients are likely to be found at or very near the sediment-water interface for a sequence of unconsolidated sediments. A thin layer at the seabed, therefore, may have a strong influence on the spectral properties of the downgoing and upgoing pulses, which will mask the frequency-dependant effects of absorption measured by comparing the seabed event to a deeper reflector. The situation is obviously even more complex if the deeper event is not a single interface, or if there are thin layers between the seabed and the deeper event.

A comparison between the observed and the synthetic Green Event shows that, in general, there is a frequency-dependent decay of amplitude above c. 130 Hz that appears close to a first-power relationship, that is, between 130 Hz and c. 280 Hz the observed spectrum is predictable from the seabed spectrum given a 'linear absorption mechanism'. But, this is a waveform that has not propagated through sediments but through the water column, with one bounce from the seabed in between. The average quality factor was calculated as 2050 (±401) for wavelet modelling and 2290 (±365) for spectrum modelling across the whole of the data set. It should be noted that these values are a gross approximation as the methods used to obtain these measurements are not reliable for quality factors greater than 150 even at noise levels as low as 5% (Jannsen *et al.*, 1985). The results are just below the quality factor for water (2300-19,000) reported in the literature (Albers, 1960). The presence of the low-frequency 'hole' in the spectrum of the seabed multiple in addition to the decay of amplitudes at the high end of the spectrum cannot be explained by a simple near-surface layering model. If such spectral effects are a result of the reflection response of the seabed, then clearly there will be a corresponding set of filtering effects as a result of the transmission response. The filtering effects of the reflection and transmission response of the seabed are likely to mask and interfere with the spectral effects of absorption measured from deeper reflection events.

The identification of near-seabed layering effects may be possible given the far-field measurement of the direct wave, and its spectral comparison to the waveform reflected from the seabed, again recorded deep enough to avoid complications with the spectral effects of the sea-surface ghost.

6.7 Summary of Results - Bruce Case Study

1. A spectral comparison between the seabed reflection event and its first multiple has indicated that prior to an acoustic pulse entering a sequence of sediments, certain changes in the spectrum of the pulse may occur which are not a result of any absorption process. In the Bruce study these changes are manifested in two ways. Firstly, there is a

decay of amplitudes above 130 Hz that is explained by very low absorption rates within the water column owing to the very low damping capacity of the medium. This results in very high estimates of the quality factor, Q.

2. The seabed multiple (Green Event) is lacking in amplitude at frequencies below a threshold of about 130 Hz. This feature may be due to the low-pass transmission response (or high-pass reflection response) of a thin layer or thin layers immediately below the seabed. If a technique meant to measure absorption (such as spectrum or wavelet modelling) compares the seabed to a deeper event, then it will not only be the effects of absorption that will be measured. They will be accompanied by the reflection response of the seabed (for the reference wavelet) and the transmission response of the seabed (squared) for the deeper event.

6.8 Atlantic Frontiers Case Study - Introduction

The third case study uses data supplied for BP Exploration. The seismic data were acquired in 1993 off the north-western continental shelf of the UK. The survey data are commercially sensitive and thus the precise location has not been given. The water depth and the time of the survey would strongly suggest that the location is within Quadrant 204, Block 24. This data set was chosen so as to provide a lower frequency band for the seismic source compared to that of the 49/10 survey (Chapter 5). The Atlantic Frontiers survey enables an investigation into the seismic characteristics of unconsolidated sediments in the sub - 300 Hz band.

6.9 Atlantic Frontiers Survey Details

The Atlantic Frontiers survey was carried out by BP in approximately 360 m of water. The seismic source consisted of three mini-airguns which provided a source pulse with a peak frequency of 100 to 120 Hz (Grieves, 1993). The receiver was a 4-channel digital hydrophone streamer. Given the depth of water and the source-receiver spacing of only a few metres, the data can be considered as vertically incident on the seabed and deeper reflectors. The incoming data were digitised at a frequency of 1 kHz or a sample interval of 1 ms. For visual clarity and qualitative interpretation, a 30 dB/second gain was applied to the field data by Geoteam UK Ltd., the seismic survey contractor. In addition, a diversity stack was made from each channel of data, essentially making a stack of the four single channels of data acquired from each seismic shot. Finally, a bandpass filter of 20 to 300 Hz was applied to the data.

6.10 Atlantic Frontiers Data Preparation and Processing

In order to prepare the data for frequency- and time-domain absorption analysis, a -30 dB/second gain was applied to the data thus reversing the amplitude manipulation applied by Geoteam. The diversity stacks were treated as single channel traces from a single shot with a vertical source-receiver geometry. Line BPAT-054 (Figure 6.12) was selected for processing as the seabed is strong and predominantly horizontal at about 490 ms TWTT. The target seismic event can be seen as a strong reverse-polarity event at about 570 ms TWTT (hereafter termed the 'Blue Event'). The sediment type of the seismic unit between the two events is not known. The unit has a thickness of about 70 m given an interval velocity of 1700 ms^{-1}. Seven batches of 15 shots were selected from Line BPAT-054 taking care that there was as little apparent interference on the Blue Event as was possible. Such zones included shots #1 to #80, #30 to #330 and #470 to #500. From each batch of 15 shots a normalised stack or average trace was made, using a crosscorrelation algorithm to obtain the most coherent result. The final data preparation inverted the polarity of the Blue Event for wavelet processing as the program compares the time-domain shape of the reflected amplitudes for similarity with the positive seabed pulse. The resulting seven stacked traces were then input into the same spectrum and wavelet modelling computer programs that were used in the previous two case studies.

6.11 Summary of Results - Atlantic Frontiers Case Study

The results of wavelet modelling of the Blue Event are summarised in Figures 6.13a to 6.13g. The computed and observed wavelets were compared over a time window varying in length between 25 ms and 34 ms. In general the computed wavelets fitted the observed wavelets well in the earlier half of the observed Blue Event, containing the high amplitude, high frequency components. The computed wavelets did not fit the latter half of the

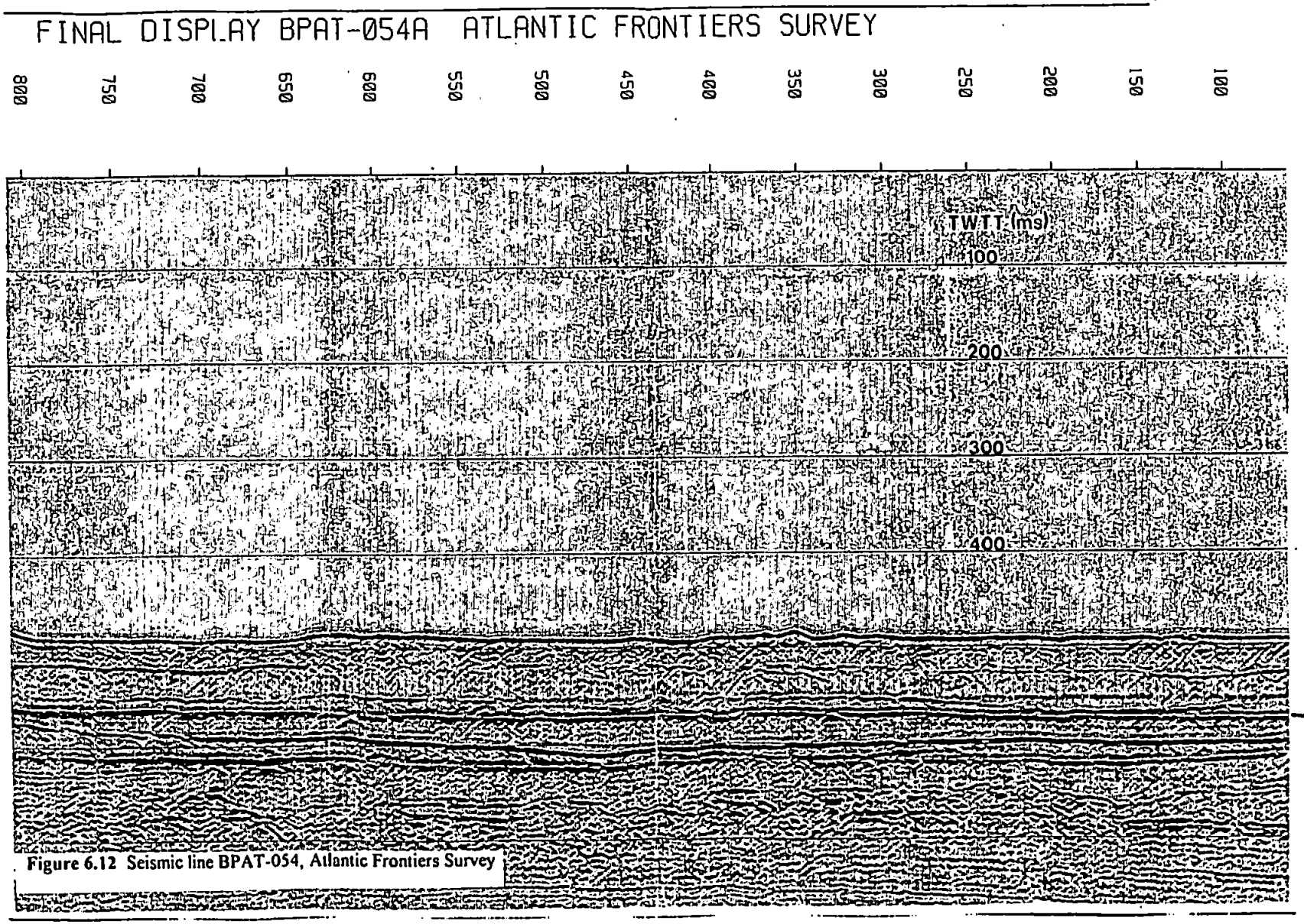

Figure 6.12 Seismic line BPAT-054, Atlantic Frontiers Survey

observed Blue Event well, with the former showing a lower frequency tail than the observed Blue Event. The quality factor,Q was found to range between 42 and 63 (Table 6.1) for the stacked traces, with a mean value for Q of 54 ±9.

The spectra of the seabed and Blue Event reflections are presented in Figures 6.14a to 6.14g. The seabed has a spectral peak centred around 100 Hz whilst the peak of the Blue Event is centred around 107 Hz. The best-fit theoretical spectrum is also shown in figures 8.4.8 to 8.4.14. Q was measured for the seven traces (Table 6.1) ranging from 50 to 74, and a mean of $Q = 63 \pm 9$. The fit of the theoretical to the observed spectra was generally good between about 240 Hz and 100 Hz. Below 100 Hz the observed spectra were deficient in amplitude relative to the theoretical spectra in all of the stacked traces.

Table 6.1 Summary of Q measurements, Atlantic Frontiers Case Study

Stack	Q (wavelet modelling)	Q(spectrum modelling)
1	63	74
2	54	63
3	43	53
4	58	66
5	42	50
6	63	72
7	57	69
mean Q^{-1}	**0.0189**	**0.0160**
mean Q	**53** ±9	**63** ±9

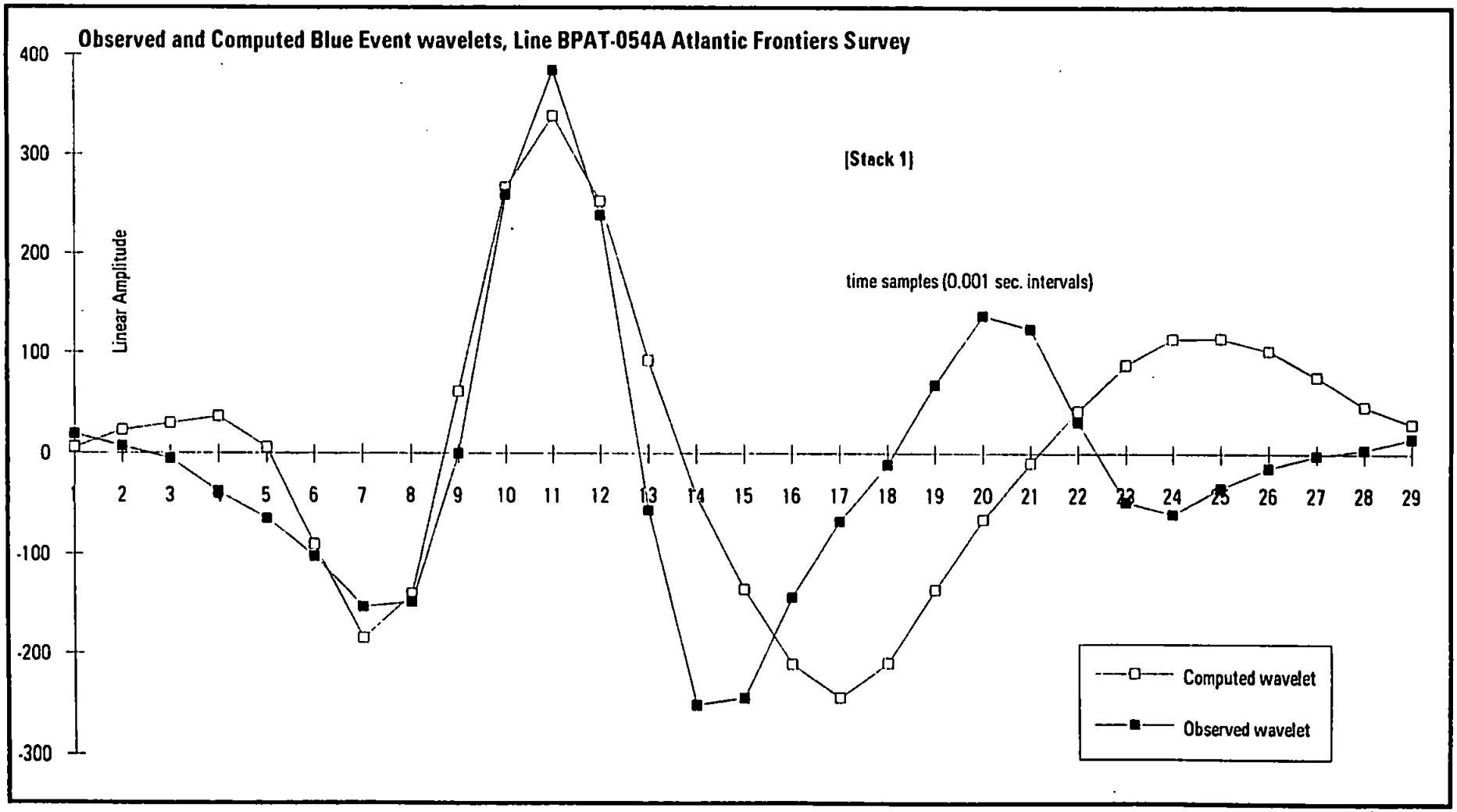

Figure 6.13a Observed and computed Blue Event wavelets, stack 1, line BPAT-054A, Atlantic Frontiers Survey

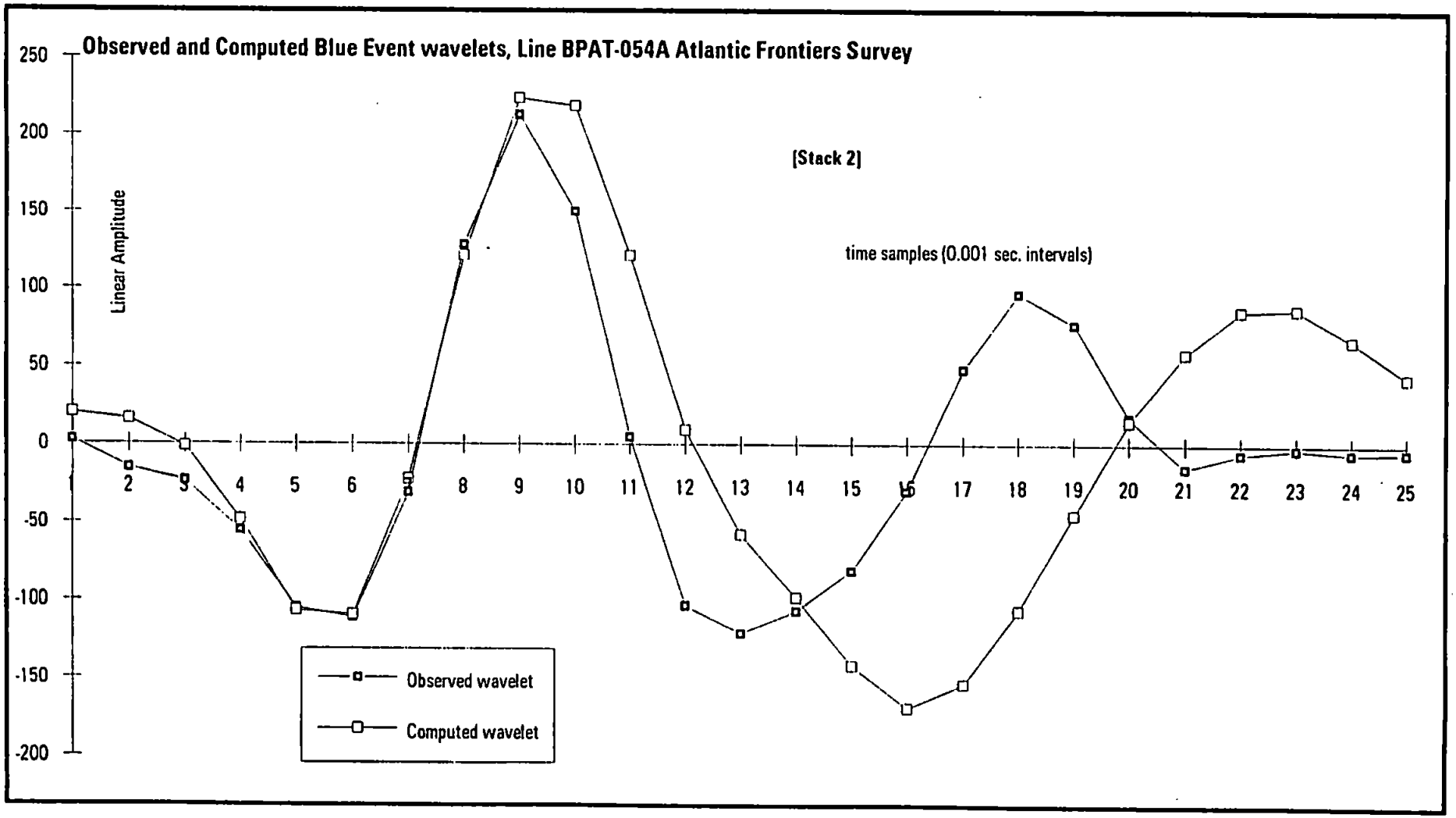

Figure 6.13b Observed and computed Blue Event wavelets, stack 2, line BPAT-054A, Atlantic Frontiers Survey

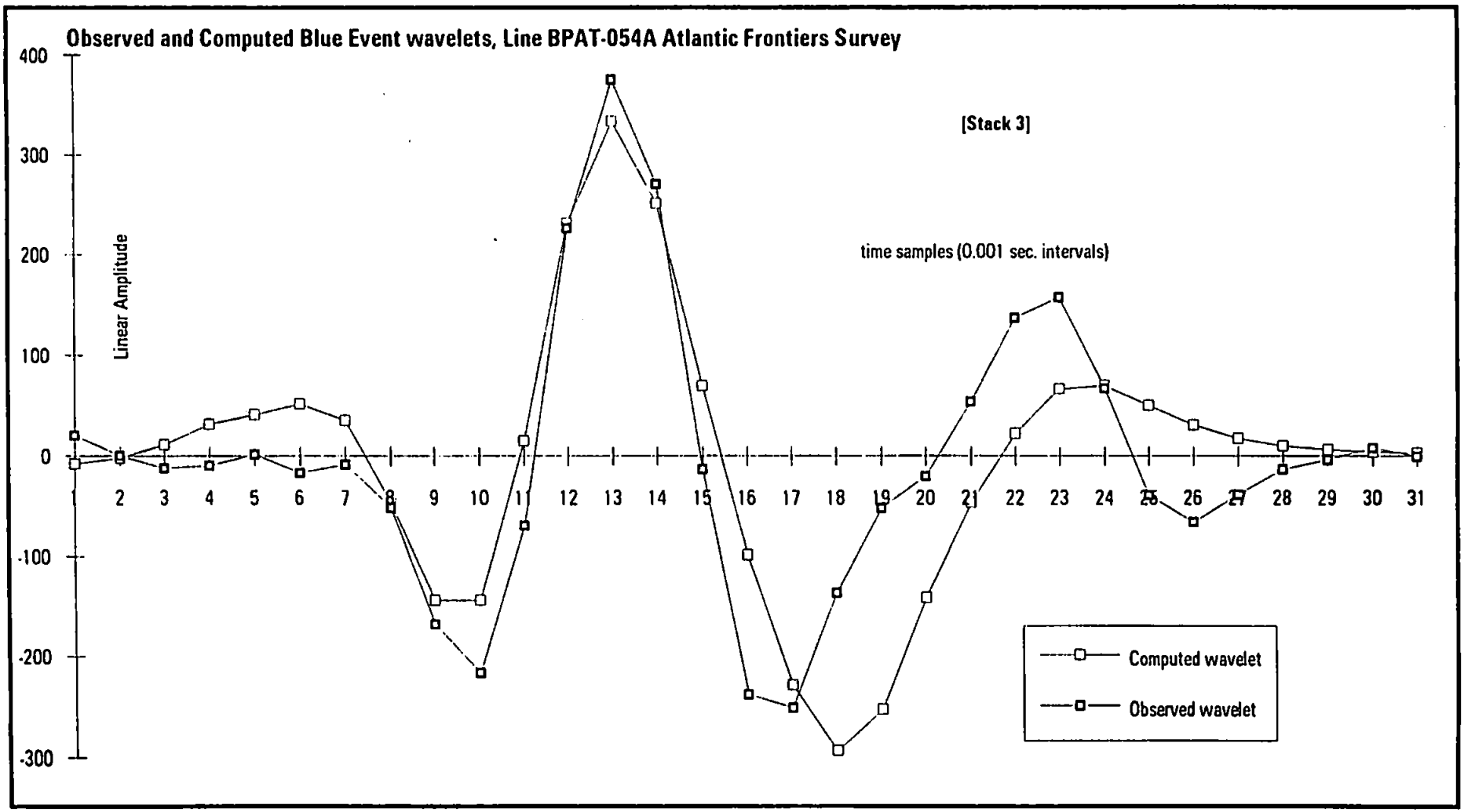

Figure 6.13c Observed and computed Blue Event wavelets, stack 3, line BPAT-054A, Atlantic Frontiers Survey

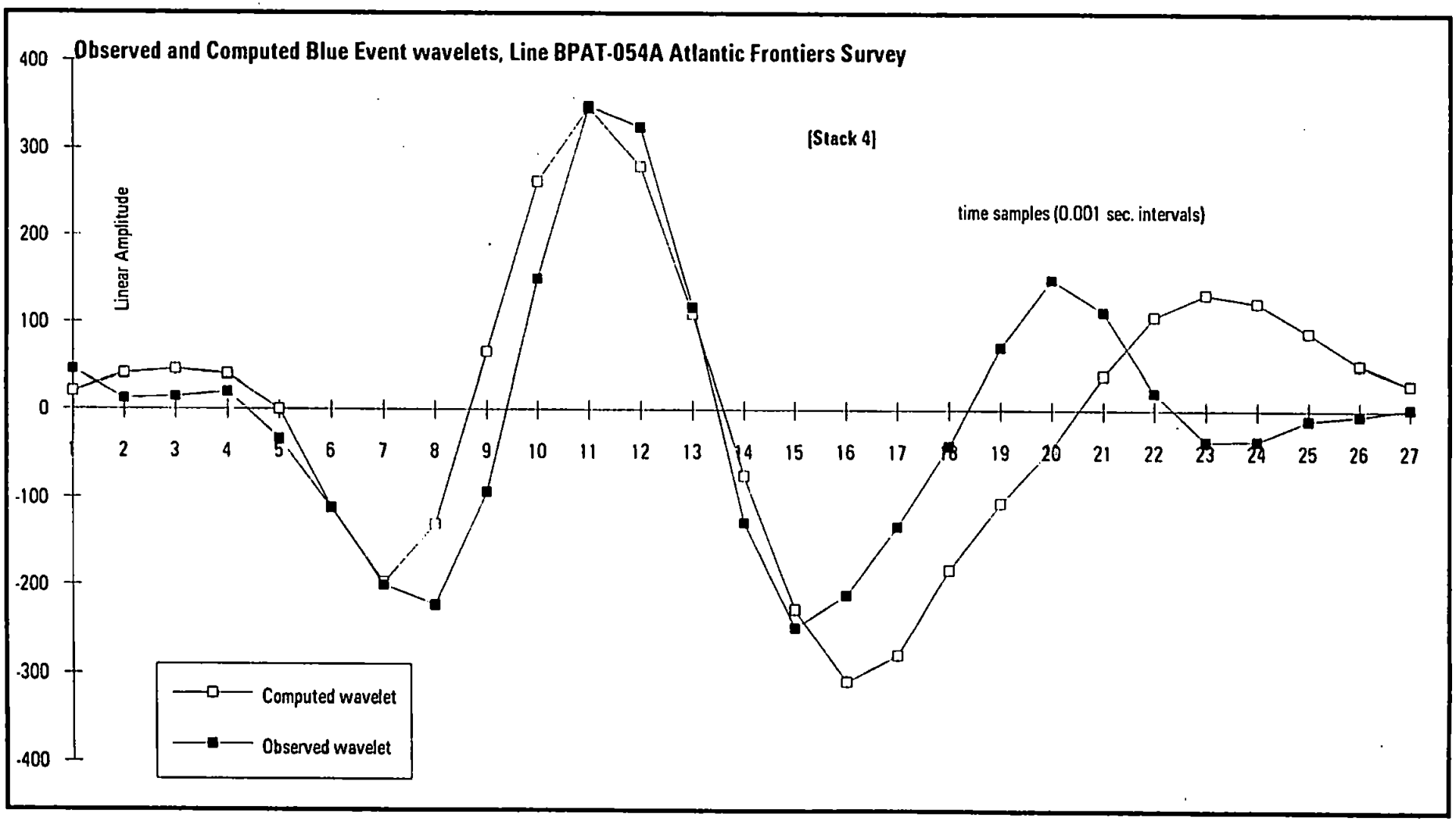

Figure 6.13d Observed and computed Blue Event wavelets, stack 4, line BPAT-054A, Atlantic Frontiers Survey

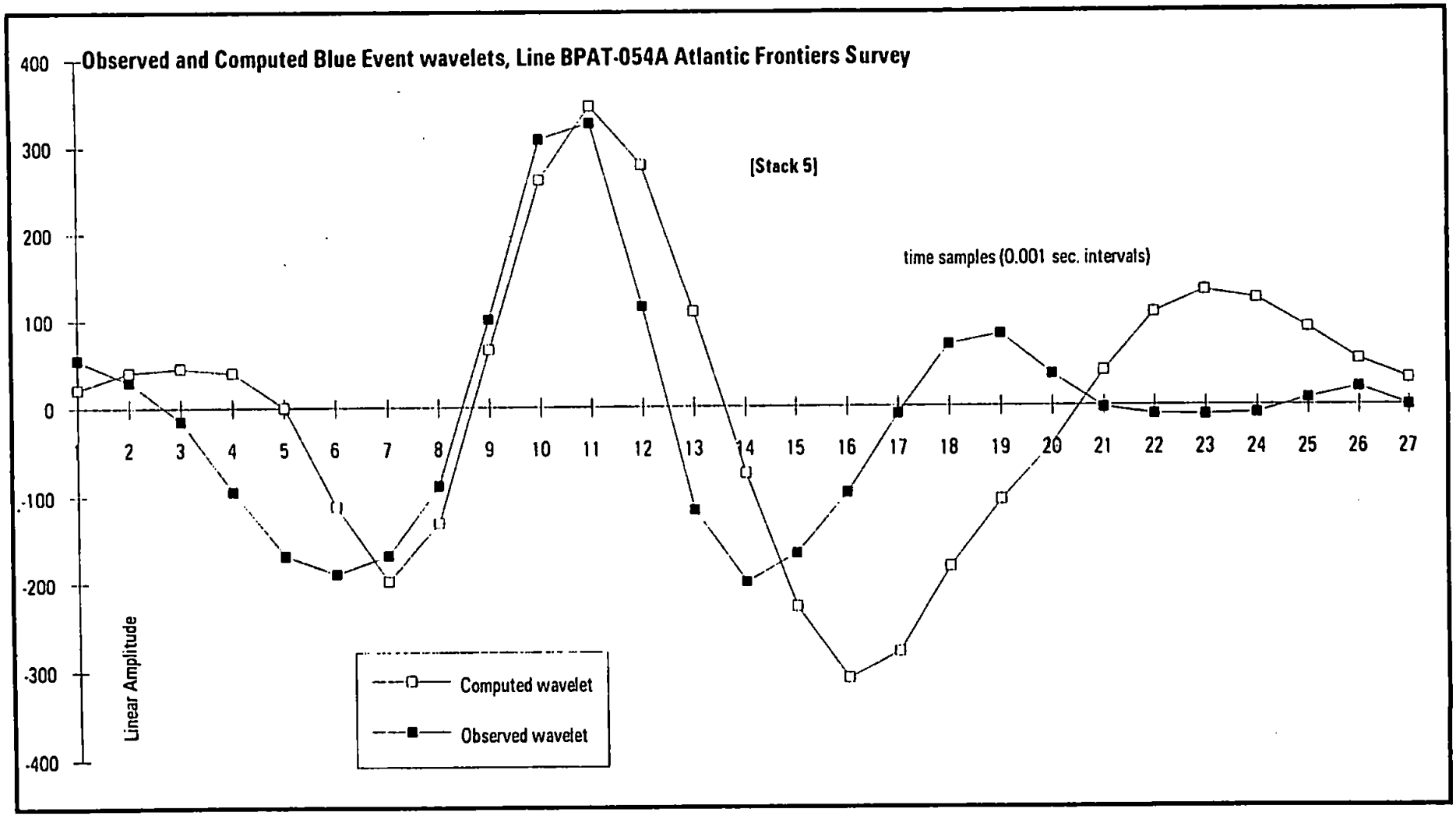

Figure 6.13e Observed and computed Blue Event wavelets, stack 5, line BPAT-054A, Atlantic Frontiers Survey

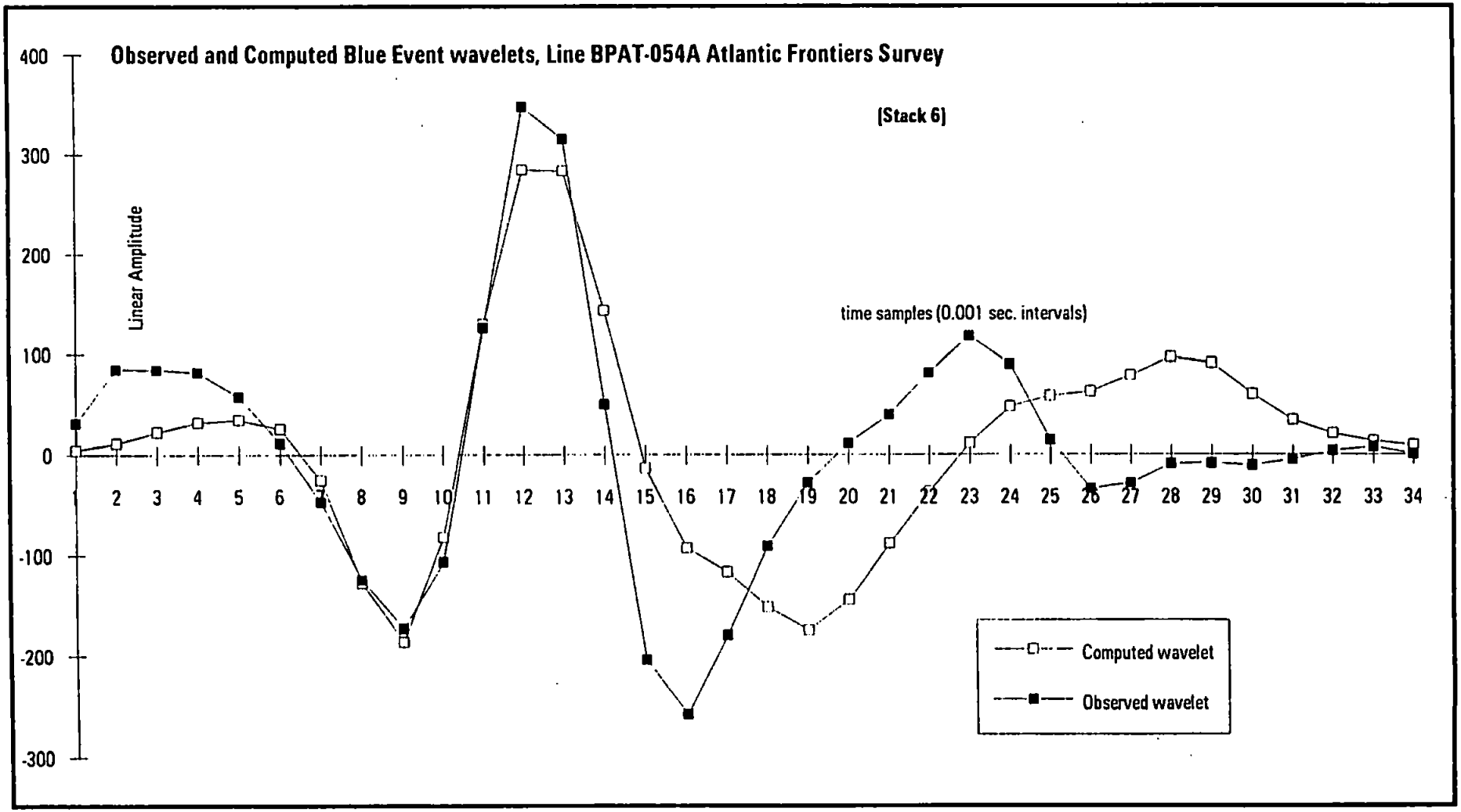

Figure 6.13f Observed and computed Blue Event wavelets, stack 6, line BPAT-054A, Atlantic Frontiers Survey

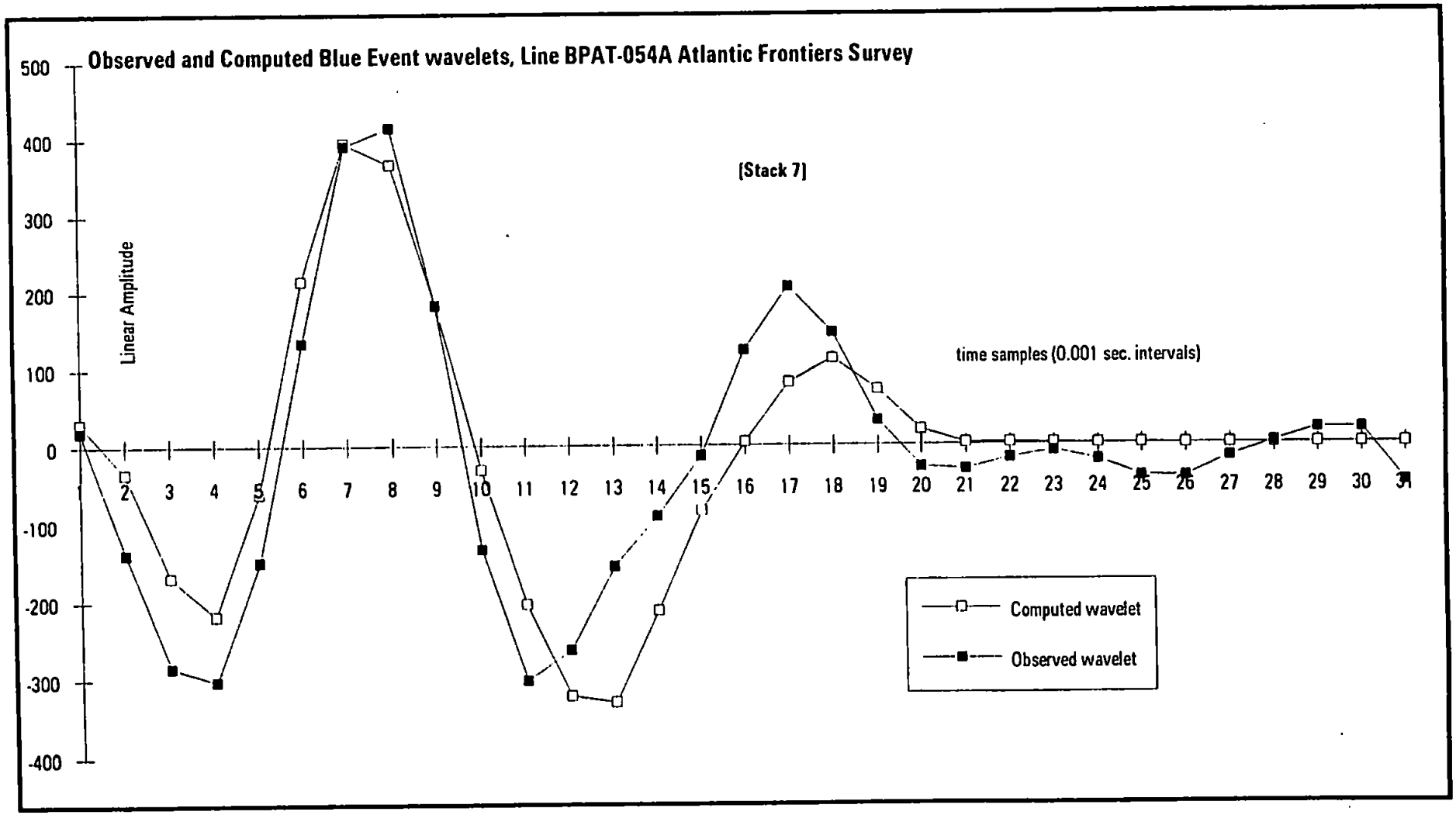

Figure 6.13g Observed and computed Blue Event wavelets, stack 7, line BPAT-054A, Atlantic Frontiers Survey

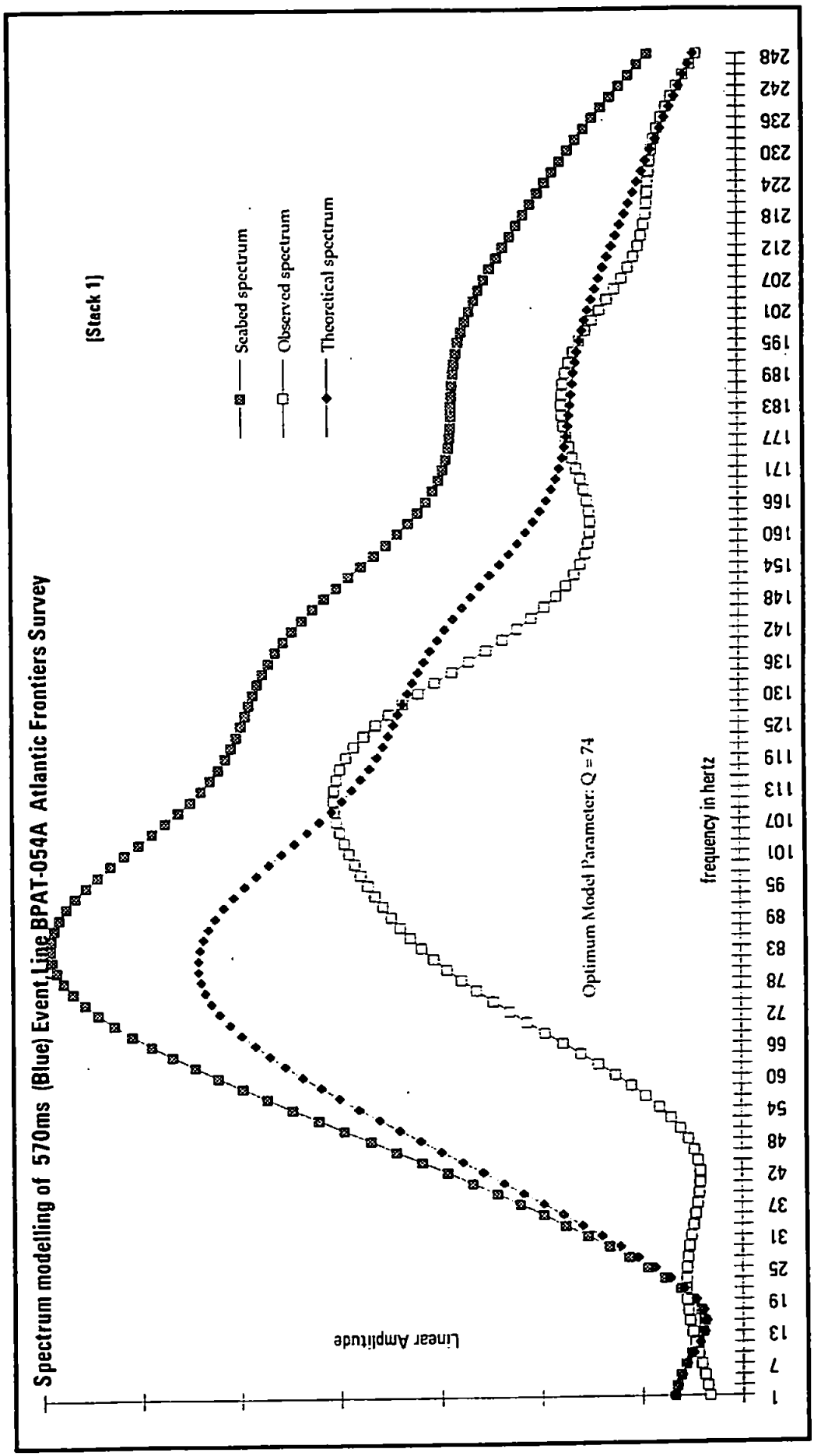

Figure 6.14a Spectrum modelling of 570 ms (Blue) Event, stack 1, line BPAT-054, Atlantic Frontiers Survey

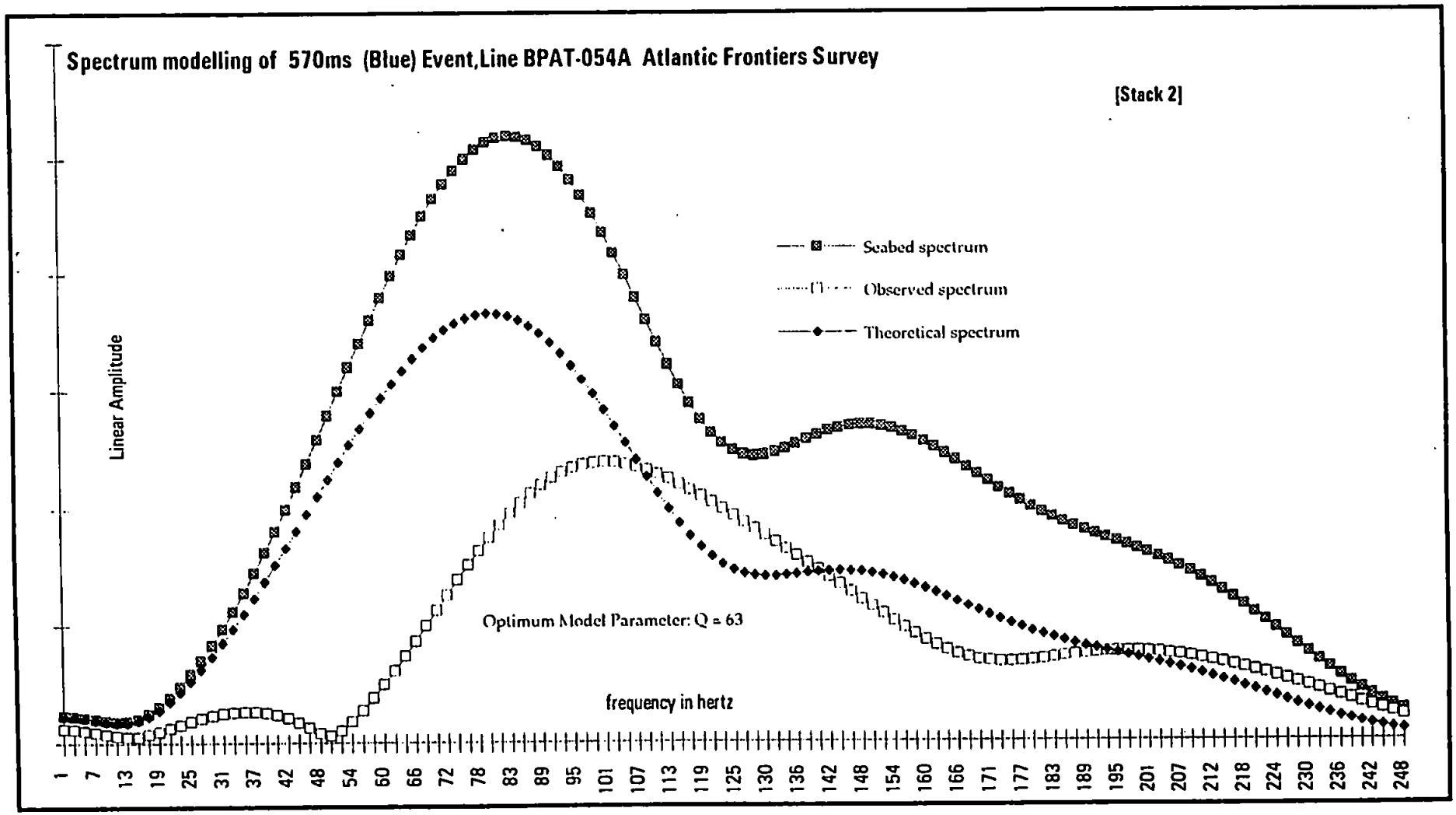

Figure 6.14b Spectrum modelling of 570 ms (Blue) Event, stack 2, line BPAT-054, Atlantic Frontiers Survey

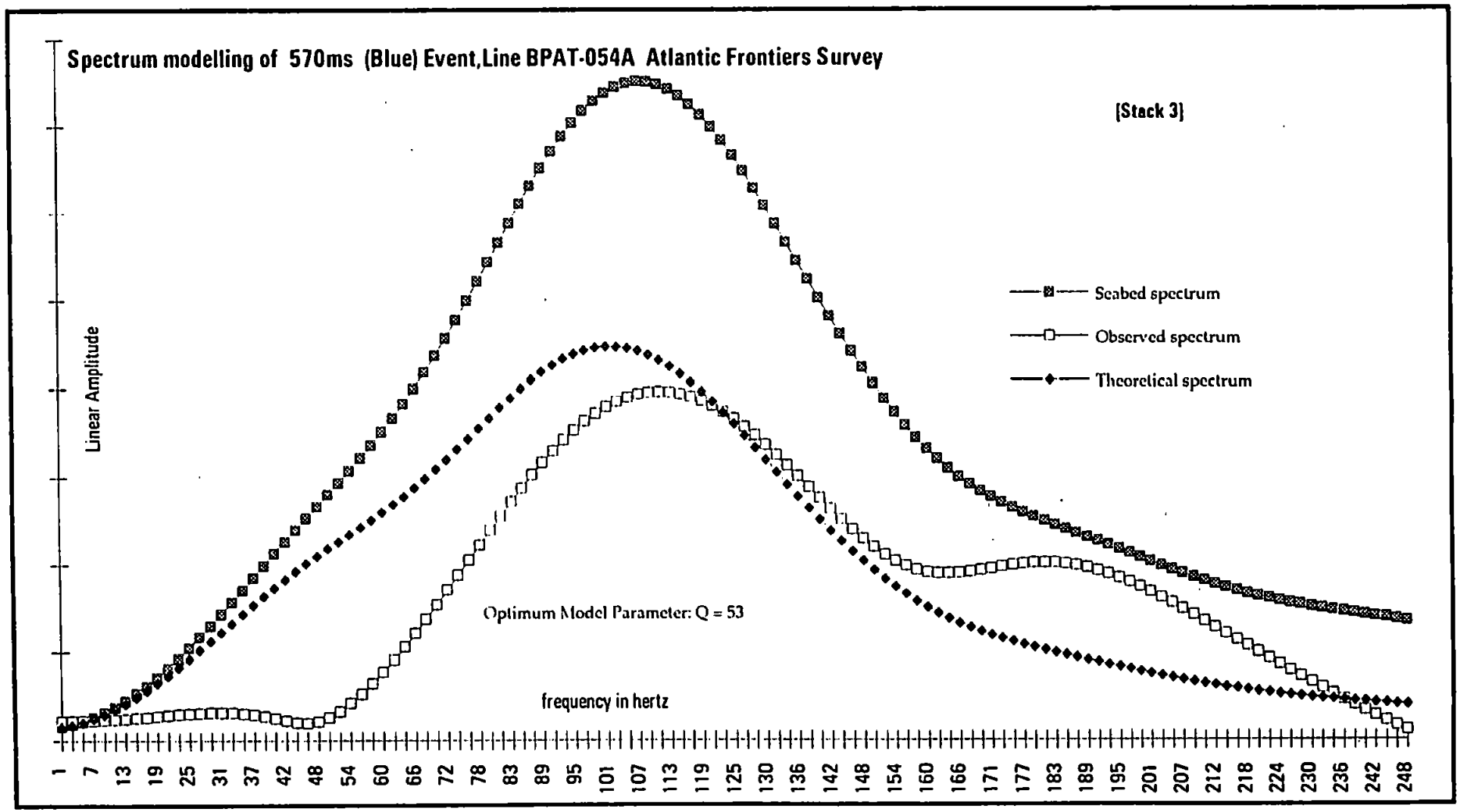

Figure 6.14c Spectrum modelling of 570 ms (Blue) Event, stack 3, line BPAT-054, Atlantic Frontiers Survey

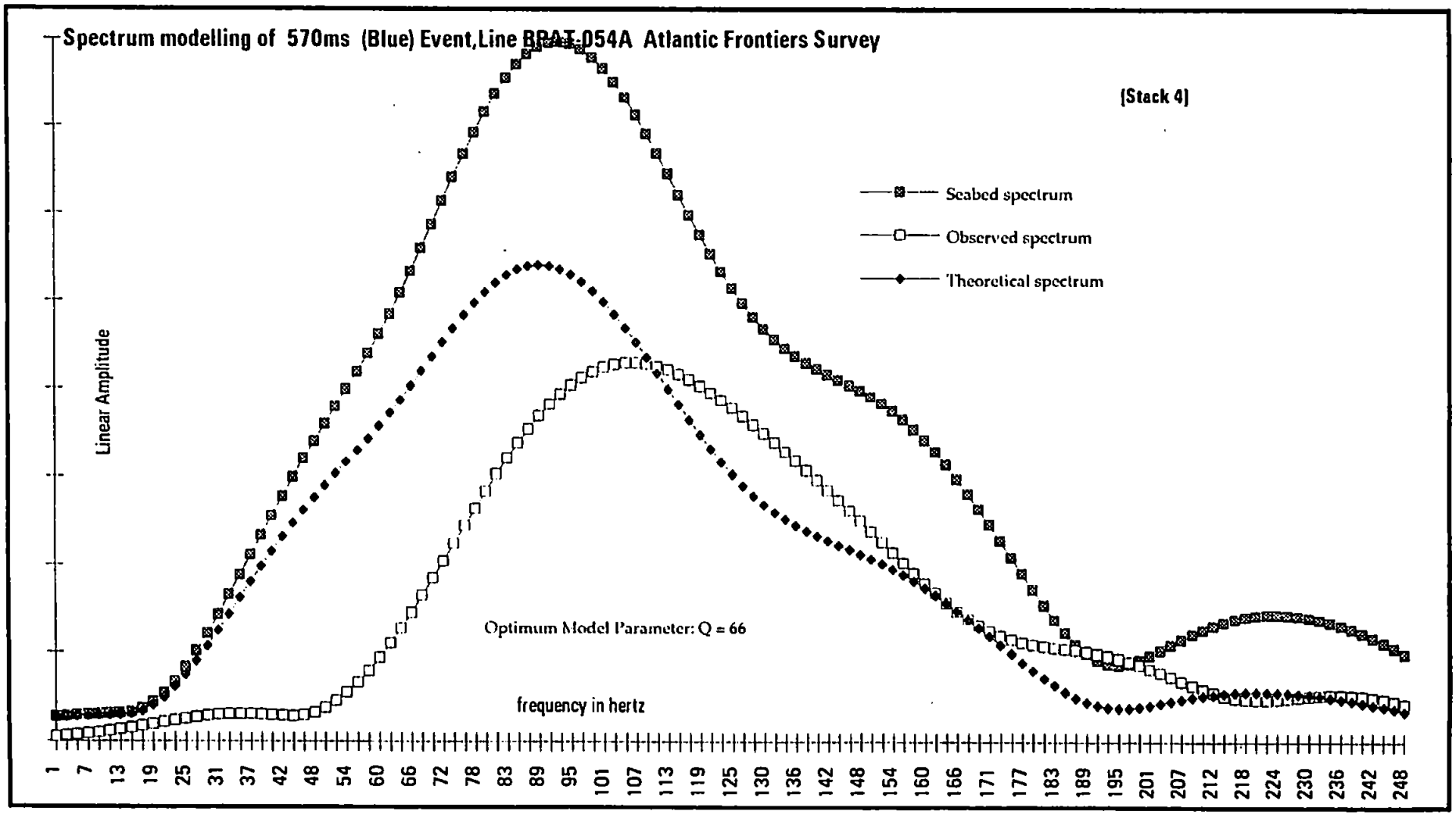

Figure 6.14d Spectrum modelling of 570 ms (Blue) Event, stack 4, line BPAT-054, Atlantic Frontiers Survey

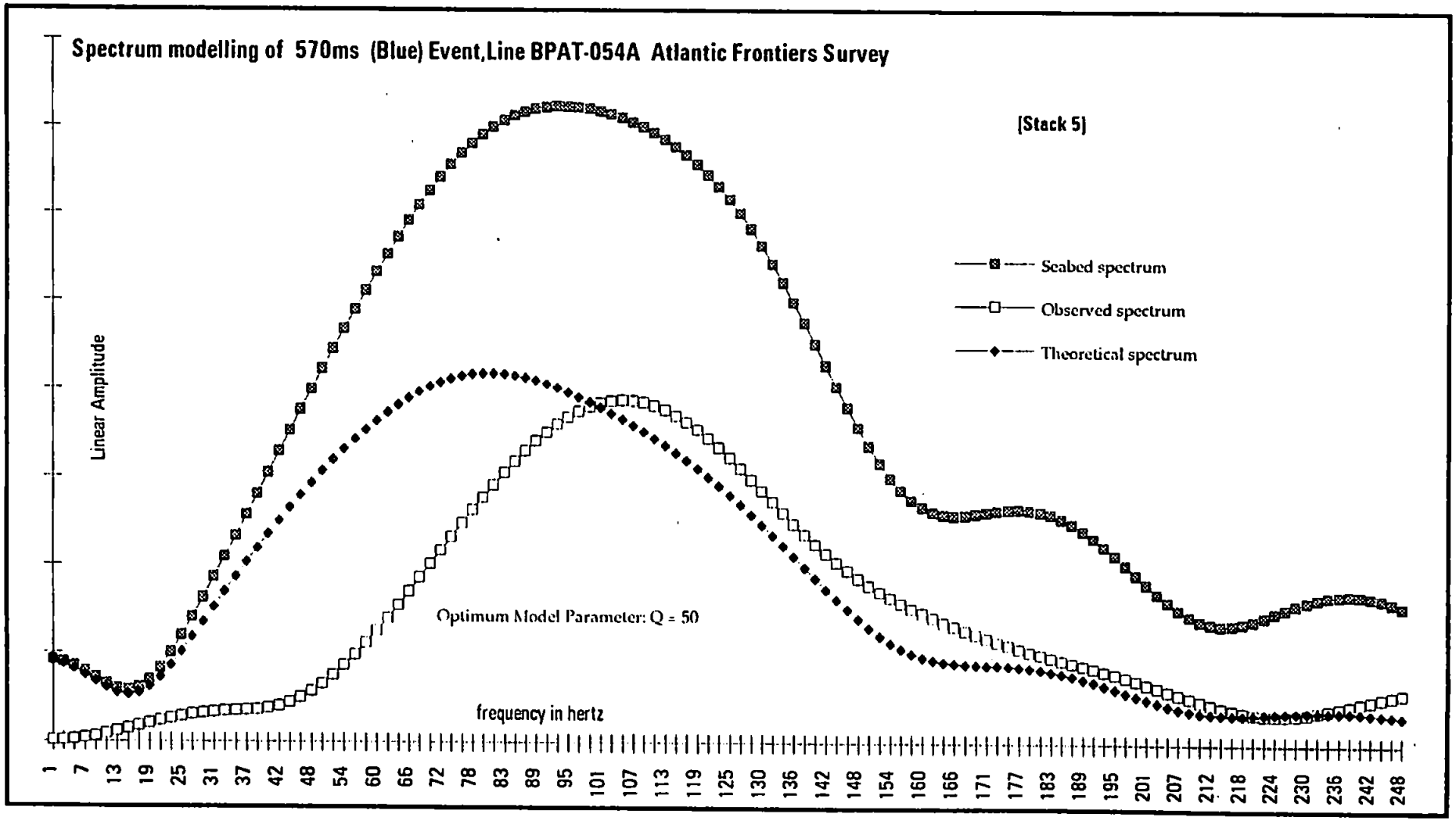

Figure 6.14e Spectrum modelling of 570 ms (Blue) Event, stack 5, line BPAT-054, Atlantic Frontiers Survey

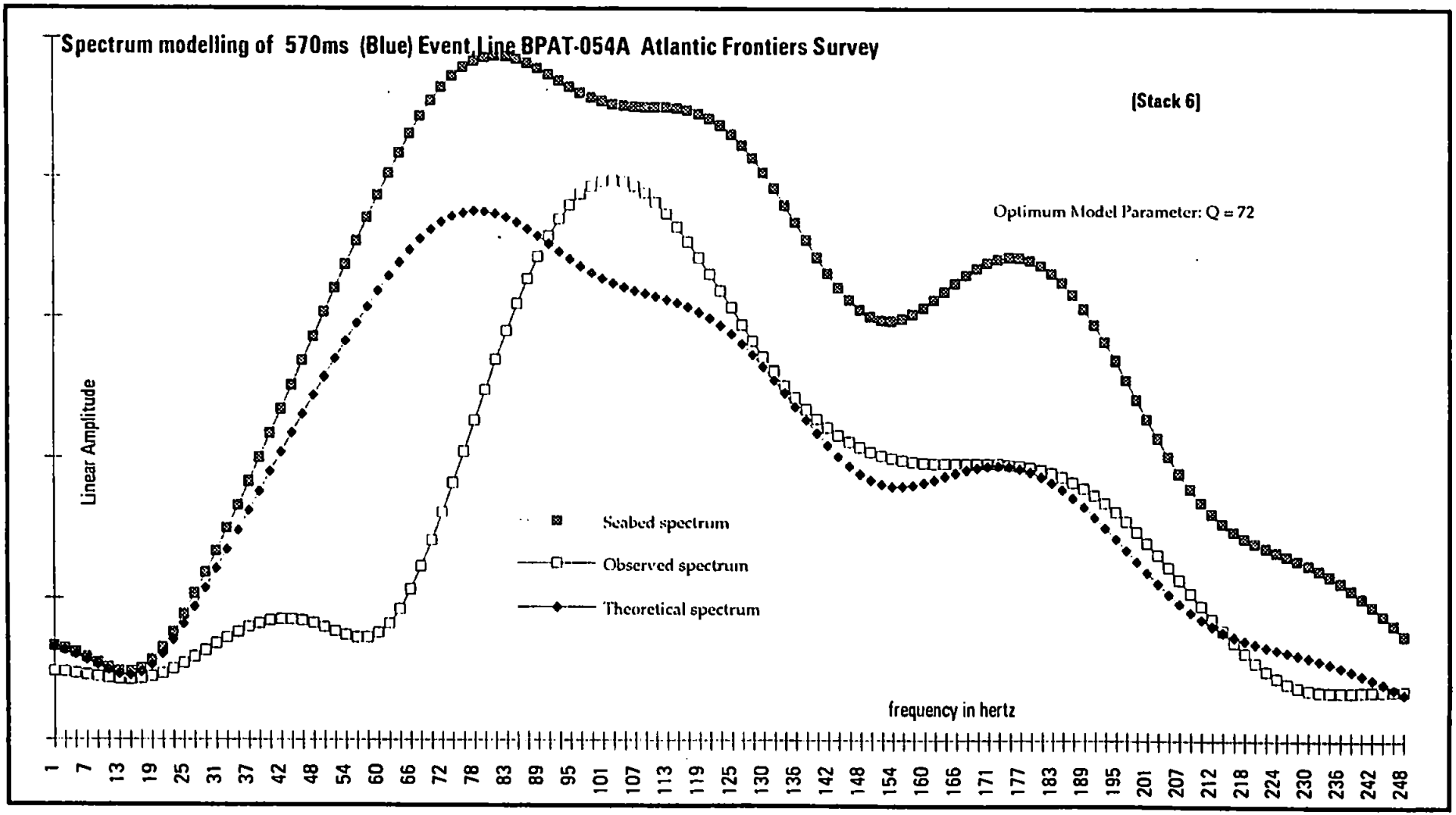

Figure 6.14f Spectrum modelling of 570 ms (Blue) Event, stack 6, line BPAT-054, Atlantic Frontiers Survey

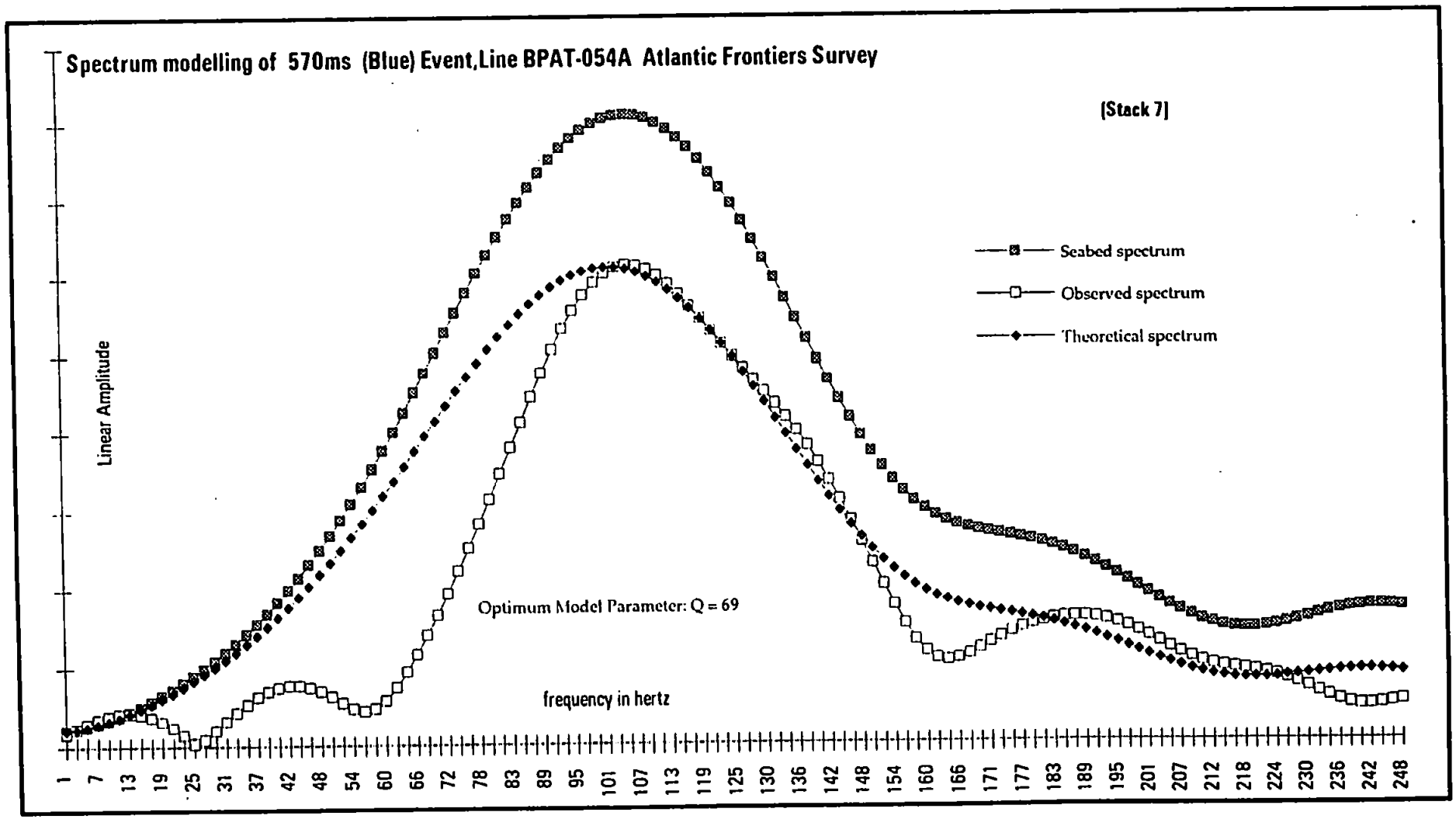

Figure 6.14g Spectrum modelling of 570 ms (Blue) Event, stack 7, line BPAT-054, Atlantic Frontiers Survey

6.12 Discussion - Atlantic Frontiers Case Study

The seismic unit bound between the seabed and the Blue Event on Line BPAT-054 (Figure 6.12) has a Q somewhere between 54 and 63 determined from wavelet and spectrum modelling. Whilst this is a limited data set, each analysed trace has been formed from summing 15 diversity stacks, each stack containing four single-channel traces.

There is clear evidence that the low-frequency part of the spectrum of the downgoing pulse that has been reflected from the Blue Event reflector is deficient to that which would be expected if the Blue Event was a perfect all-pass (white) reflector, when compared to the spectrum of the seabed event. This is manifested as a lack of a low-frequency tail in the time-domain (*e.g.* Figure 6.13b) and a spectral hole at low frequencies in the frequency-domain (*e.g.* Figure 6.14e). Between frequencies of about 100 Hz up to about 240 Hz, the spectral shapes of the observed and computed Blue Event spectra were similar indicating a linear absorption mechanism. Peg-leg multiples are not considered to contribute to the linear loss mechanism as such a process adds a low frequency tail to the downgoing pulse. Such a tail is clearly not seen in the reflected Blue Event wavelet. The lack of low frequencies in the observed Blue Event spectra are probably a result of thin layer filtering (low-pass) by layering within the sediments in the vicinity of the Blue Event. Whilst such effects have not prevented measurement of Q in this data set, such filtering presents a clear hazard in the estimation of Q based upon spectral measurement. In more practical terms, the seabed and target reflectors which bound the seismic unit for which Q is required should have as little interference as possible. The spectrum modelling yielded Q estimates which were, on average, 14% higher than those estimates obtained from wavelet modelling.

The Q estimates obtained in this case study might indicate that the sediments in the seismic unit beneath the seabed are sandy rather than muddy in nature, when compared to Q estimates from earlier studies by other workers such as Hamilton (1972), described in Chapter 2. Further refinement of the capability of the technique to determine whether sediments are prone to be broadly sandy or muddy (based upon Q-estimation) would

require a much more extensive analysis of the survey area coupled with a shallow borehole programme.

Chapter 7: Discussion and Summary

7.1 General

This project is primarily concerned with obtaining meaningful measurements of the way in which seismic waves decay through unconsolidated, mainly sandy sediments using commercial seismic data carried out in connection with shallow penetration studies. In the study of acoustic attenuation in natural sediments, McCann and McCann (1990) and Kibblewhite (1989) indicated that there was a lack of published results in the frequency band which lies below ultrasonic measurements (*e.g.* Buchan *et al.*, 1967; Hovem and Ingram, 1979; McCann and McCann, 1985), despite the availability of modern computing technology. There is a particular lack of detailed work in the frequencies of 100 Hz and 1 MHz, the frequency band which in part covers all but standard 'deep' seismic exploration which generally uses frequencies of less than 100 Hz.

Two important groups of factors have been described which contribute to the decay of seismic waves, namely those factors which are related to absorption and those which are not (Chapter 2). The discrimination of intrinsic absorption within the medium of propagation from measured attenuation provides one of the challenges using seismic data shot at the sea surface. Only when this has been achieved can a relationship between absorption rates (perhaps parameterised as the quality factor, Q or as an attenuation expressed in the form of $\alpha = kf^n$) and sediment characteristics (such as grain size and porosity) be established. With seismic data, measured attenuation can be expected to encompass intrinsic absorption of the media as well as the effects of instrumental response, scattering, and thin-layers (peg-leg multiples).

Murphy (1982) indicated that the frictional sliding process at grain-grain boundaries was still considered by the geophysical community to be the main cause of the process known as seismic absorption. One of the major contributors to this widespread

view was Hamilton (1972, 1987) whose presentation of the results of many studies appeared to show a linear relationship between measured attenuation and frequency over a wide range of frequencies. McCann and McCann (1985) formulated a model, largely based on Biot's theory (Biot 1941, 1956a, 1956b, 1962a, 1962b) which invoked a viscous dissipation mechanism to predict absorption values for sandy sediments. For two data sets they obtained a linear absorption rate with respect to frequency, one being an artificial sand, the other a natural beach sand. In a recent review of the results of other attenuation measurements over the past 40 years, Kibblewhite (1989) suggested that the variation of absorption with frequency was linear above a certain threshold for noncohesive sediments. This threshold was thought to be about 100 Hz for sands and between 1 kHz and 10 kHz for silts. This, clearly, has implications for this study where the data is derived from seismic sources with a range of bandwidths between about 100 Hz and 4 kHz.

There have been relatively few studies using single-channel marine surface seismic data to determine rates of absorption in near-surface unconsolidated sediments. These include the work of Cole (1965) using data in the 100 Hz to 900 Hz band and Bennett (1967) using data in the 40 Hz to 900 Hz band. Both found a linear relationship between frequency and measured attenuation. Jannsen *et al.* (1985) used data in the 150 Hz to 450 Hz band to measure Q within muddy sands in the Baltic Sea. No spectra or computed wavelets were presented within this paper to illustrate the modelling techniques used.

If the relationship between absorption and frequency becomes non-linear at the lower end of the acoustic spectrum, then there is a major implication for the measurements of absorption. Certain analytical methods rely on a linear dependence in order to measure Q, the quality factor of the sediment, such as the spectral ratios technique (Båth, 1974). With a lower rate of absorption for lower frequencies, the spectral ratios technique would over-estimate the quality factor if the measured spectrum contained both the lower frequency (non-linear) and higher-frequency (linear) modes of behaviour. In effect, Q would not be constant over the measured spectrum. This forms one of the problems of estimating the quality factor for marine sediments.

7.2 Non-Absorption Loss Mechanisms

The identification of non-absorption mechanisms may provide another major obstacle to the measurement of absorption using marine surface seismic data. Some mechanisms may be accounted for without much difficulty such as raypath divergence. Losses from Rayleigh scattering occur when wavelengths are much shorter than the average grain size (Busby and Richardson, 1957). Given that the frequencies used within this study are below 4 kHz, wavelengths are likely to be no shorter than 0.5 m, using a nominal velocity of 1700 ms^{-1} . For a gravel of 5 mm grain size, scattering would be important for wavelengths of less than 5 mm, corresponding to a frequency of at least 340 kHz for a velocity of 1700 ms^{-1} . Although scattering effects will not be considered further, it should be mentioned that many of the offshore Quaternary sequences of UK waters do contain gravels such as the Morrison Formation on the West Shetland Slope (Stoker, 1990) where the Atlantic Frontiers case study was probably located. Therefore scattering may be inconsistent through a seismic unit. The effects of layering, however, cannot be discounted when attempting to determine absorption from the subsurface using marine seismic data. The work of Anstey (1960), Berzon (1967), O'Doherty and Anstey (1971), Spencer *et al.* (1977), Schöenberger and Levin (1978), and Ziolkowski and Fokkema (1986) has shown that layering can change the spectral characteristics of pulses which have propagated through a layered medium. The recognition of such spectral effects provides a key problem to the determination of intrinsic absorption as a physical characteristic of a particular sediment body or seismic unit.

The "thin-layer" problem (Widess, 1973; Ziolkowski and Fokkema, 1986) occurs when the dominant wavelength of the propagating pulse is less than one quarter of the thickness of the seismic layer under investigation. In essence, the reflection and transmission responses of thin layers are frequency-dependent, the amplitude of which is a function of both layer thickness and reflection coefficient (Koefoed and de Voogd, 1980; Ziolkowski and Fokkema, 1986). A sequence of thin layers was shown by Ziolkowski and Fokkema to have the effect of a cascaded low-pass filter. Lower frequencies would pass

preferentially through a layered sequence, while higher frequencies would be preferentially reflected. Such a process leaves the earlier part of the seismic section relatively poor in low frequencies, and the later part relatively poor in higher frequencies. The resulting amplitude decay will, therefore, have the same general effect as seismic absorption. A combination of the elastic, frequency-dependent effects outlined above, coupled with a non-linear dependence of absorption upon frequency would present a complex problem from which to extract absorption as a characteristic of a particular sediment unit.

The effects of peg-leg multiples (O'Doherty and Anstey, 1971) are intimately related to this thin-layer problem. Modelling of the transmission response of a layered earth has shown that the peg-leg amplitudes occur in the time-domain at the tail of the time window within which the downward propagating pulse is described (shown in section 2.4) . If the amplitude spectrum of this window could be measured, then the lower part of the spectrum would be richer in lower frequencies than a pulse which has returned to surface having been transmitted through the layered sequence of low-pass filters. The transmission responses of single- and multi-layer models were calculated in Chapter 2. A pulse with a nominal spectrum of 500 Hz to 2.4 kHz was synthetically propagated through a layered sequence (section 2.3). For any combination of layer thickness and reflection coefficient there will be nodes and antinodes in the transmission (and reflection) response (e.g. Spencer *et al.*, 1977). The position of the lowest frequency node where the wavelength is equal to four times the layer thickness dictates the frequency band within which there will be a monotonic decrease in the transmission response. This is the band below which lower frequencies are preferentially transmitted. For example, there will be a monotonic decrease for a single layer that is 0.25 m thick from 0 Hz to 1700 Hz (given a seismic velocity of 1700 ms^{-1} and a reflection coefficient of 0.25) and from 0 Hz to 850 Hz for a layer that is 0.50 m thick. When the numbers of layers are increased, or the reflection coefficient is increased, the positions of the nodes of the transmission response are not affected, but the decrease in the transmission response with increasing frequency becomes more pronounced. This effect was also modelled in the time domain (section 2.4). It was shown that the peg-leg multiples are the cause of the modifications to the

spectrum of the incident pulse. If the peg-leg multiples could be separated from the primary pulse, the spectrum of the primary pulse would not be affected by transmission through layering and the thin layer effect would not be of consequence in the determination of absorption, as the transmission and reflection response of the vertically-incident, primary pulse would be independent of frequency.

Certain difficulties were found when attempting to determine the spectral effects of peg-leg multiples using an impulse as an input waveform to single- and multi-layer models (section 2.4). The values chosen for the layer thickness and the interval velocity must be such that their quotient is a multiple of the sampling interval of the input waveform, otherwise ripples occur when the frequency-domain calculations are inverse-transformed back to the time-domain, thereby causing unwanted amplitudes. In practical terms the phase delay ($j\omega$) of the transmission response through a layer (or layers) must be multiplied by an integer value of the sampling interval.

If reflection coefficients of up to 0.25 may be considered as realistic for unconsolidated materials (calculated using geotechnical data from Hamilton, 1972), as may layering of up to 1 m in near-surface sedimentary units and the seismic source delivers a pulse whose spectrum extends to a few kHz, a layered earth with physical characteristics similar to those outlined above is likely to filter the propagating pulse and modify its spectral characteristics with or without absorption taking place. For those techniques that rely on the recognition of spectral change between earlier and later events within a seismic section to determine absorption, such non-absorption filtering of the propagating pulse will lead to underestimation of Q, particularly in the multilayered case. The discrimination of the effects of peg-leg multiples presents a formidable problem when attempting to determine the absorption characteristics of a real layered earth.

7.3 Numerical Methods

This study examines the relationship between frequency and measured attenuation in the 100 Hz to 4 kHz band using surface seismic data from three case studies.

Prior to attempting to measure absorption from surface seismic data, current numerical methods were reviewed and assessed (Chapter 4). To assess the methods, synthetic traces were constructed using an impulse with a nominal frequency spectrum extending to 10 kHz (section 4.2). As well as applying a constant-Q absorption to this impulse, dispersion was incorporated using the dispersion relation of Futterman (Futterman, 1962). Using this relation, the phase velocity increases with increasing frequency albeit in a logarithmic manner. In practical terms, the higher frequencies shift to the front or earlier part of the pulse. However, using quality factors of $Q = 100$ and $Q = 50$, it has been shown that the change in the shape of the dispersed wavelet relative to the input wavelet will be slight when using the Futterman operator combined with realistic values for Q (from Hamilton, 1972). Synthetic traces were constructed using traveltimes of 10, 15, 20 and 25 ms with Q varying from 50 to 100. This range of values would be analogous to sandy / silty sediments (Hamilton, 1972) and sediment thicknesses of about 8 m to about 20 m between the seabed and the bottom of the seismic unit.

Windowing of data is an integral element of Fourier analysis. Although Pujol and Smithson (1991) suggested that the frequency dependence of Q may be biased by different methods of windowing data, Press *et al.*, (1986) found, for practical applications, no effective difference between the non-rectangular window types . In Chapter 4 the spectral ratio method was used to assess the Parzen, Hanning, Welch and rectangular window types for an arbitrary trace from the 49/10 case study. No effective variation in the value of the quality factor was found using the different window types. This was because the wavelets that were processed were emplaced within a much longer number array of zero-amplitude (zero-padding), which effectively masks the effects of applying any form of data-windowing. No windowing was, therefore, applied to the data within this study.

Correct determination of the traveltime (Δt) between two events on a seismic section eliminates a potential source of error in absorption estimation. The spectral ratio method (Båth, 1974) used in this study (section 4.3.1) underestimated Q by about 2%. This was because the method used the time difference between the onsets of energy of the two events. As the dispersion relation was built into the synthetic traces, the phase velocity of the higher frequencies caused onsets of energy earlier than the nominal Δt from which the traces were constructed, thus underestimating the true Δt. A correction factor using the value of $V(\omega)/V(0)$ from the Futterman operator brings the errors in measured Q to within $\pm 0.5\%$ of the true Q value (in a noise-free case). In the matching technique (Raikes and White, 1984) the spectral ratios are calculated by the determination of prediction operators which filter an earlier pulse into a later pulse and *vice versa* (section 4.3.5). With single channel data this technique produces essentially the same result as the spectral ratios technique as discussed in section 3.2.4 . With multichannel data the method could be used to provide statistical figures (the ordinary coherence function) to provide better signal spectrum estimates based upon signal-to-noise estimates.

The risetime method (Gladwin and Stacey, 1974) was assessed in the noise-free case in section 4.3.2 . An autocorrelation algorithm was used to estimate Δt. For short traveltimes, the absorbed, dispersed wavelets are still sharp, and therefore the autocorrelation algorithm estimates the true Δt to within 1.5%. For longer traveltimes the dispersion effect shortens the time to the peak amplitude. Accordingly, Δt will be underestimated, and so, therefore, will the quality factor. The synthetic wavelets were constructed using a finite-length discrete Fourier transform. Accordingly there will be small errors in the constructed wavelets as there are only a limited number of discrete frequency components. For very sharp pulses the dispersive effects and absorption effects may not be exactly expressed in a digital form. Spectral leakage in the frequency domain will cause amplitude errors in the time domain. This will have two effects, in that the peak amplitude will be in error and the maximum gradient of the initial rise will be in error. The risetime method, therefore, will only be successful when there are sufficient samples to be able to define a maximum gradient of the initial amplitude rise for both the earlier and later

wavelets and if a combination of high absorption and long travel time (high dispersion) do not cause large errors in the estimation of Δt in the noise-free case.

Wavelet modelling (Jannsen *et al.*, 1985) incorporates both absorption and dispersion in the numerical analysis of the data. An estimate of the traveltime between a reference wavelet and a deeper absorbed and dispersed wavelet is initially obtained via an autocorrelation of the seismic trace in section 4.3.3. The quality factor and the traveltime are then varied until an optimal theoretical wavelet is synthesised which best fits a later reflection event. This particular technique was error-free in the noise-free case as the same algorithm was used to create the synthetic traces in the first instance. Spectrum modelling (Jannsen *et al.*, 1985) provides a similar method to wavelet modelling but without using the phase information. The technique had two primary causes of error in the noise-free case (section 4.3.6). Firstly it provided an inferior Δt estimate compared to wavelet modelling (*cf.* spectral ratios technique), secondly the technique suffers from data windowing effects more than wavelet modelling. It has been shown in section 4.3.2 that when a short data window containing the target wavelet is placed within a much longer window of zero values prior to Fourier transformation, errors are introduced when a mathematical operation such as application of the absorption term (*e.g.* equation. 4(12)) is performed in the frequency-domain. These errors result in unwanted amplitudes when the data are transformed back to the time-domain . This is a result of the use of discrete rather than continuous Fourier transforms, where each discrete, complex value of the transform in the frequency domain is actually representing a band of frequencies rather than a single frequency.

Complex trace analysis (Taner *et al.*, 1979) when using the 'maximum method' (Engelhard *et al.*, 1986) yielded large errors in the estimations of Q when using the same set of synthetic traces as above (section 4.3.5). This was found to be caused by the effects of dispersion embodied within the synthetic traces. For a constant ratio of the quality factor to the traveltime, a suite of wavelets generated synthetically from a starting impulse would all have the same amplitude spectrum, but different phase spectra. This is because the complex exponential term for dispersion is a function of both Q and Δt. The errors

increased with lower Q (higher absorption) and longer traveltimes. The method was also applied to a set of synthetic traces formed from a single sinusoid rather than an impulsive input (section 4.3.5). Under these conditions, the maximum method estimated Q with errors of less than ± 0.5 %. If the Futterman operator describes dispersion reasonably well for noncohesive sediments, the complex trace technique (in the 'maximum method' form) incurrs very large errors and must be considered inappropriate for use with real sediments and real, non-sinusoidal seismic wavelets (section 4.3.5). A possible remedy for this problem would be to transform the seismic wavelets concerned to sine waves only (rather than both sines and cosines in the Fourier transform) via a sine transform (e.g. Press *et al.*, 1986) and to use these wavelets as part of the maximum method.

In a recent development, LeBlanc *et al.*, (1992) converted the data from other workers (such as Hamilton *et al.*, 1956; McCann and McCann, 1969; and Hamilton, 1972) into a parameter termed the relaxation time (τ, measured in μs) . This is the time taken for the density of a volume of sediment to change following application of sudden pressure. Using the measured attenuation of the peak amplitude of a correlated chirp pulse, along with the travel time, the relaxation time can be determined (up to 100 kHz) without any measurement of the acoustic velocity or the distance travelled. The method assumed negligible phase dispersion. An empirical equation was developed by LeBlanc *et al.*, (*op cit.*) that related relaxation time to grain size and showed the maximum relaxation time to occur at a grain size of about 3 ϕ, or fine sand (where the maximum absorption occurs (Hamilton, 1972)). The complex trace method that was developed by LeBlanc *et al.*, (*op cit.*) to determine the relaxation time is based upon absorption causing a shift in the mean instantaneous frequency of a propagating chirp pulse. The method relies on the fact that this central frequency will vary in a stochastic fashion as it passes through a sequence of scatterers within marine sediments, and that the mean central position will still represent the centre frequency of the spectrum of the reflected pulse. It is by using such a high-frequency source that many reflections from volume scatterers can be analysed for changes in the central frequency of the reflected pulse. The technique may be difficult to apply with seismic data displaying less backscattered energy. No figures were presented on the

reliability of the method within noisy data sets by LeBlanc *et al.*, (*op cit.*) , but the *a priori* knowledge of the spectral content of the initial pulse and its repeatability was suggested by LeBlanc *et al.*, (*op cit.*) to overcome the problem of spectral distortion from overlapping reflection events.

Random noise was added to the synthetic traces and the numerical methods were again assessed for reliability in the estimation of Q (Chapter 4). Levels of noise ranged from 5% to 30% (as a percentage of the variance of the noise-free synthetic trace). The results are plotted in Figure 4.8c. At a noise level of 5%, all of the methods could estimate the true quality factor to within ±10%. Above a noise level of 10%, the risetime method yielded large errors (>20%) compared to an upper noise ceiling of 5% reported for this method by Jannsen *et al.*, (1985). Given noise levels of over 20%, only the wavelet modelling method yielded errors in measured Q of less than 20% for Q = 75. By increasing the noise level to over 30%, none of the methods could yield a Q-estimate with an error of less than 20% for Q = 75 and Q = 100. The spectral ratio, spectrum modelling and matching methods could yield estimates with errors of less than 20% for Q = 100, providing noise levels were 20% or lower.

The reliability of the methods as a function of reflector spacing were not assessed in this study. Jannsen *et al.*, (1985) tested the reliability for several numerical methods in the case of two interfering reflectors. For noise levels of less than 15%, Q can be determined for layers separated by at least 1.5 wavelengths for wavelet modelling and 3 wavelengths by spectral methods for a quality factor of less than Q = 60 according to Jannsen *et al.*, (1985). For sediments with acoustic velocities of about 1700 ms^{-1} and a dominant wavelet frequency of 1.5 kHz, this represents a minimum of 1.7 m separation for wavelet modelling and 3.4 m for the spectral methods. Noise levels of over 15% precluded the use of spectral methods in the case of interfering reflections (Jannsen *et al.*, 1985) . The data windows used by Jannsen *et al.*(either in the frequency- or time-domains) were not specified over which Q was calculated.

For the current work, the determination of signal-to-noise ratios using single-channel data was estimated by identifying coherent signal spectra between traces and

discriminating 'noise' as tails at the upper end of the spectra (Chapter 3, Figure 3.1). Although this method is very approximate, it does indicate those parts of the frequency spectrum which have a reasonable signal-to-noise ratio for two reflection events in order that some spectral comparison can take place.

In general, an increase in Q (lower absorption rates) for a given noise level will lead to larger errors in the Q estimates for any of the numerical methods (section 4.4). Although computationally slow, the wavelet modelling technique appeared to be the most robust method in the presence of noise at all three Q values (50, 75, 100). The interpretation of the plotted data (Figure 4.8c) warrants a certain amount of caution; the plot should only be seen as being broadly comparative between the methods. This is because each of the methods is open to a certain degree of subjectivity in the derivation of the final estimate. Each of the methods is dependent upon a reasonably accurate estimate of Δt . The optimal source of this value is from wavelet modelling. The Δt values for the spectrum modelling and matching techniques were provided by wavelet modelling. Another method might be to use initial amplitude onsets, which will underestimate the true Q; this was the case with the spectral ratio method (section 4.3.1). Another would be to use the trace autocorrelation, which was used by the risetime method (section 4.3.2). The spectral methods are problematic in that Q may be calculated from only a very short section of the spectral ratios curve, that is, from only a few spectral components. The spectrum modelling and wavelet modelling techniques will yield different Q values depending upon the bandwidth (or for wavelet modelling the time interval) over which the modelling takes place. In terms of the significance of the plotted data to practical applications, the risetime method may be too sensitive to noise (and suffer from an inadequate sampling rate) for marine seismic work. Its use has been shown to be a practical method, however, for short propagation paths and low-Q terrestrial sediments (Jongmans, 1990).

The spectral ratios, and matching techniques did not yield significantly different results at the level of the analysis undertaken as shown in section 4.4. Spectrum modelling does appear to give smaller errors for a given noise level than these methods. For the practical applications of this project, the matching technique (in this variant form) will

initially be used to determine Q from the spectral ratios. The spectral coherence determined from signal to noise power ratios will indicate the optimal band over which to calculate absorption for the spectral ratios and for spectrum modelling. The preferred technique was, however, wavelet modelling (section 4.3.3) which encompasses both absorption and dispersive effects. Wavelet modelling (section 4.4) has been shown to be a robust estimator of the quality factor in the presence of noise for Q values that are not unrealistic for unconsolidated sediments ($Q < 100$), for traveltimes of up to 25 ms (about 20 m of sediment thickness), and for an initial seabed spectrum of up to 10 kHz.

7.4 Measurement of the Quality Factor, Q

The first case study, Chapter 5, from block 49/10 in the southern North Sea, was based upon data acquired using a "Uniboom" Boomer source. Two sedimentary units occur immediately beneath the seabed. Unit A is composed of fine sands (as determined from gravity cores) and occurs to the east of the area, whilst Unit B is composed of coarse sands (as determined from gravity cores) and occurs to the west of the survey area. Unfortunately, no further geotechnical information was available. Both seismic units have the Red Event as a basal reflection event. The peak frequency of the seabed reflection was found to be about 3 kHz for the top of Unit A and 2.1 kHz for Unit B. The Red Event forming the base of Unit A had a peak frequency of between 2.3 kHz and 2.5 kHz, whilst the base reflection of Unit B had a peak frequency of about 1.3 kHz and 1.8 kHz. For Unit A, the mean Q measurement was 56 ±3.6 from wavelet modelling and 63 ±6.9 from spectrum modelling, yielding an overall averaged Q of 60 for both methods from 8 different areas within the survey area. For Unit B, the mean Q measurement was 44 ±3.4 from wavelet modelling and 50 ±5.1 from spectrum modelling, yielding an overall averaged Q of 47 for both methods from 10 different areas within the survey area. Hamilton (1972), using frequencies of between 14 kHz and 100 kHz, found the quality factor to vary

between 29 and 35 for medium to coarse sands and between 29 and 44 for fine sands from *in-situ* sediments off San Diego. McCann and McCann (1969) gave attenuation coefficients at 30 kHz for four types of land and beach sediment of mean grain-size diameter of 2.5 ϕ (fine sands) to 5.32 ϕ (coarse silt). The values for their attenuation coefficients in dBm^{-1} at 30 kHz can be converted to Q-values as follows. If α, the attenuation coefficient, is expressed in dBm^{-1}, at a frequency f expressed in kHz, then $1/Q$ can be calculated as:

$$\frac{1}{Q} = \frac{aV}{\pi f} \quad \ldots\ldots\ldots 7(1)$$

where $a = \alpha/8.686$ and V is the velocity (Hamilton, 1972).

Thus for the fine and very fine sands of mean sediment diameter 2.5 ϕ, 3.05 ϕ and 3.8 ϕ, Q was calculated as 50 ±18, 33 ±11 and 30 ±1 respectively. For the coarse silt of mean diameter 5.32 ϕ, Q was calculated as 48 ±19.

The 49/10 case study found that the measured attenuation was greater for Unit B (coarse sands) than for unit A (fine sands). This is in conflict with the generally accepted decrease in attenuation with increasing grain size above that of fine sands (McCann and McCann, 1969; Hamilton, 1972). The conflict may have arise from inadequate geotechnical information for the whole of the seismic units under analysis. The value of about 47 for Q within the coarse sand unit is about 50% greater in the 49/10 study than the values obtained by Hamilton (1972) for similar grain-sized sediments off San Diego. It should be noted however, that the 49/10 results were obtained at frequencies of less than 3 kHz whilst the lower values of Hamilton were obtained at 14 and 100 kHz respectively. In a later paper McCann and McCann (1985) measured attenuation in a beach sand of mean grain-size 2.5 ϕ and an artificial sediment (glass beads) of mean grain-size 3.6 ϕ. The results were presented in the form of $\alpha = kf^n$. At a frequency of 367 kHz, the beach sand had a Q of about 50 (converted using eq. 7(1)). The standard deviations on this value were ±27 for variations in f and ±20 for variations in k. At a frequency of 535 kHz, the

glass-bead sediment had a Q of about 60 (converted using eq. 7(1)). The standard deviations on this value were ±22 for variations in f and ±16 for variations in k.

The Q estimates of McCann and McCann (*op cit.*) are comparable to those measured from the 49/10 case study for which the mean Q was 60 for fine sands from wavelet and spectrum modelling. The Q values are thus similar despite the difference of more than two decades of frequency between the investigations.

For the optimum-fit wavelet and spectrum, the wavelet and spectrum modelling techniques derive a single value for the quality factor, Q . A good similarity between the wavelets over the early part of the Red Event, and over the higher frequency end of the observed and synthesised frequency spectrum of the Red Event has been found (section 6.5).

An important conclusion of section 6.5 is that a constant-Q absorption mechanism appears to fit the observed data from the 49/10 case study for a limited band of frequencies between about 1 kHz and 3 kHz..

The matching and spectrum modelling methods yield essentially the same Q measurement for any given stacked trace, as there was a good predictability of the observed wavelet from the seabed event for the 49/10 case study. The matching technique was not used to obtain spectral ratios in the other two case studies, but the estimation of the signal and noise components (section 4.3.5) was continued to indicate over which part of the spectrum the spectrum modelling method could be used. The spectrum modelling technique measured Q by fitting an optimal spectrum to the observed spectrum in the L_2-norm. A statistical figure to represent the quality of the fit of the synthetic spectra to the observed spectra was not developed.

A measure of spectral coherence, based on the estimated signal-to-noise ratios of the seabed and target reflection events was used in each case study. For the 49/10 case study a spectral coherence of greater than 0.7 was used as a threshold to determine the portion of the frequency spectrum which had enough signal for the spectral methods. This threshold was also used for the Bruce and Atlantic Frontiers case studies.

The Atlantic Frontiers case study in Chapter 6 used both spectrum and wavelet modelling to determine Q from seismic data in the sub-300 Hz frequency range. The top 80 ms of the seismic data below the seabed were examined. This top seismic unit probably corresponds to the Morrison Formation (Stoker, 1990). BGS data (Stoker, *op cit.*) reported the unit to be made up of debris flows of glacigenic origin consisting of sandy diamicts with a derived shelf fauna, and are poorly sorted. Particle size analysis from cores taken from the top 3 to 4 m of the sequence indicate that the sediments consist of 70% to over 90% silt size fraction and above (Stoker, 1990).

Wavelet modelling for this case study discussed in Chapter 6 gave a Q of 54 ±9 whilst spectrum modelling gave a Q of 63 ±9 between the seabed and the Blue Event at about 70 m below the seabed. These results are similar to those for sands presented in McCann and McCann (1985), but geotechnically the media are very different. At best the attenuation results from this case study would suggest that the seismic unit under investigation is *prone* to be sandier rather than muddy in nature for the following reason. The quality factors which were determined are considerably lower than those obtained by Hamilton (1972) for clayey silt ($104 < Q < 437$).

As with the 49/10 case study, the similarity between the observed and synthesised data suggests that a constant-Q mechanism may apply within the frequency band of 100 Hz to 240 Hz. It should be noted that neither of the 49/10 or Atlantic Frontiers case studies cover the sub-100 Hz frequency band within which attenuation is predicted to become non-linear with frequency for sandy sediments (Kibblewhite, 1989).

For the 49/10 case study, using a stacked trace for single-channel data yields effectively the same results as processing a number of individual unstacked traces for Q measurement (section 5.5.4), providing the number of traces is well aligned (via an crosscorrelation algorithm) so as not to cause any smearing effects on either the seabed or the target events which would lead to spectral distortion. In general, spectrum modelling yielded quality factor estimates which were about 14% higher than those obtained by wavelet modelling for the same input data. In the wavelet modelling method, the whole of the wavelet was generally used to compare observed and synthesised events (analogous to

using the whole width of the available frequency spectrum). With spectrum modelling, only that part of the spectrum which was deemed to have adequate estimated signal-to-noise ratios was used. As wavelet modelling uses the whole of the available spectrum, the highest frequencies up to the Nyquist will be modelled by the software. This difference, however, would lead to wavelet modelling yielding higher Q-estimates. At the higher frequencies the signal-to-noise ratio is much lower in the observed data; the synthesised attenuated wavelets do not contain noise and therefore a higher Q value will be necessary to match the seabed to the observed wavelet. The discrepancy between the results from spectrum and wavelet modelling probably arises from the inclusion of dispersion in the latter. Within the 49/10 seabed reflection event, most of the energy is concentrated at the beginning of the waveform. With wavelet modelling, amplitudes at the front of the wavelet become preferentially larger owing to phase dispersion with increasing traveltime and absorption rate (lower Q). It is the larger amplitudes that are important when comparing the fit of observed and modelled waveforms in the time domain. Therefore Q must be a little lower (or absorption higher) to match the observed wavelets to the synthesised wavelets that have been dispersed compared to fitting an observed spectrum to one that has only had the effects of absorption applied.

7.5 Low-Frequency Spectral Characteristics

Between about 1 kHz and 3 kHz the modelled wavelets fitted the observed wavelets well in both the time- and frequency-domains in the 49/10 case study. This is manifested as similar waveforms in the former and similar shaped spectra in the latter. One of the most consistent results of spectrum modelling of the 49/10 data was an apparent lack of low-frequency amplitude in the observed reflection event relative to a modelled wavelet synthesised from the same traveltime and an optimum value for Q (Figure 6.22). This effect was observed for both Unit A (below 1300 Hz) and Unit B (below 1100 Hz - 1400 Hz). In the time-domain, this effect was observed as a low-frequency tail in the

synthesised wavelet which was not apparent in the observed reflection. From the spectral measurements, it was shown in section 6.5 that the observed spectrum of the Red event was lacking in low-frequency information relative to the (assumed) unattenuated seabed spectrum.

Within the Atlantic Frontiers case study (Chapter 6), the observed and synthesised spectra were similar in shape between the frequencies of 100 Hz and 240 Hz (*e.g.* Figure 6.14e) . Below 100 Hz the observed reflection spectrum had an apparent lack of low-frequency amplitude relative to the observed seabed spectrum. Again, this was manifested in the time-domain as a low-frequency tail in the synthesised wavelet which did not occur in the observed event.

The Bruce case study in Chapter 6 assessed the spectral characteristics of a first-order multiple reflection in comparison to a primary seabed reflection in the 70 Hz to 400 Hz frequency band. Spectrum and wavelet modelling was used to fit a synthesised wavelet, created from the seabed reflection, to the first-order multiple (Green Event). Between 130 and 300 Hz the observed and synthesised wavelets and spectra were very similar in both the time- and frequency-domains, suggesting that constant-Q mechanism for seawater at such frequencies. The mean quality factor of the seawater was found to be about 2000 , but minute variations in the traveltime or the modelled frequency band or wavelet length caused very large variations in Q at such low attenuation rates. These figures must be seen as a guide because it has been shown that even the wavelet modelling method becomes unreliable once Q became greater than about 150 with noise levels of below 5%. Below about 130 Hz the observed first-order multiple lacked the low-frequency information which was apparent in the synthesised event.

It is first necessary to discount potential causes of these observations at the lower-frequency ends of the observed spectra. In all three case studies, there was no filtering which was applied to the frequency band under consideration, either as a simple band-pass or as time-variant filtering. Spectral notching due to the source or receiver depth below the strong sea-surface reflector would not lead to this phenomenon. Any notches in the source spectrum would enter and leave the seabed to be recorded at the receiver. Any notching

due to the response characteristics of the hydrophone would be apparent in both earlier and later reflected events.

Invoking the peg-leg effect (O' Doherty and Anstey, 1980) arising from thin layers within the seismic unit between the reflection events, cannot be used to explain the lack of low frequencies, as the peg-leg paths occurring between the seabed and the modelled reflection events would add a low frequency tail to the propagating pulse in a similar way as absorption. This low frequency tail would be reflected back to the surface along with the primary pulse assuming that the reflector forming the lower boundary of the seismic unit under investigation has an all-pass spectral characteristic. Therefore a lack of low-frequencies would not be observed. The opposite effect is observed in the 49/10, Bruce and Atlantic Frontiers case studies; the low-frequency tail is absent in the observed wavelets. The reflection events may arise from thin layers whose reflection response is similar to that described by Ziolkowski and Fokkema (1986), in that depending on the thickness of the layer and the frequency content of the incoming wave, a layer will have a pass-band below which the layer will become increasingly acoustically transparent with lower frequency. In the Bruce case study the seabed has acted as a low-pass filter to the incident wave, which is due to near-surface layering. A thin layer at the seabed will have a strong effect as the thin-layer response increases with larger contrasts in acoustic impedance. In the 49/10 case study, the Red Event has acted as a low-pass filter, as has the Blue Event in the Atlantic Frontiers case study. The Red and Blue Events therefore probably arise as composite reflections from thin layering at the appropriate traveltime. The spectra of the observed wavelets display the reflection response of a thin layer or sequence of thin layers. The thin-layer reflection response occurs when the thickness of the thin layer (d) is less than one-quarter of the seismic wavelength (λ) (Widess, 1973; Ziolkowski and Fokkema (1986)). There will be a particular frequency within the spectrum of the incident pulse where $\lambda = 4d$ which corresponds to the "tuning thickness". Below this threshold, the reflection response decreases rapidly with decreasing frequency.

Within the Bruce case study, the lack of low-frequency information is centred at about 80 Hz in the Green Event frequency spectrum. At a sediment velocity of 1600 ms^{-1},

80 Hz represents a wavelength of about 20 m entering the seabed from above. Note that within the Bruce case study, the seabed reflection itself has a very rapid decay of amplitude below about 110 Hz (*e.g.* Figure 6.11b). A layer of only a few metres thickness at the seabed could allow the initial preferential transmission of low frequencies of the seabed spectrum and subsequently further low-pass filter the first-order multiple. In practical terms, as the distance between two reflecting interfaces at the seabed decreases beyond the $\lambda = 4d$ threshold, the events will become increasingly difficult to discern on the seismic section. Layers that would show the strongest low-pass transmission response or high-pass reflection response would be beyond the resolution of the propagating pulse and would appear as single reflection events.

In the Atlantic Frontiers case study, the Blue Event has a lack of low frequencies centered at about 60 Hz (*e.g.* Figure 6.14d). This represents seismic wavelength of the order of 27 m given a sediment velocity of about 1600 ms^{-1} . A layer with a thickness of only a few metres will preferentially transmit much of the energy at such low frequencies and will leave the reflected wave deficient in the lower part of the spectrum.

The lack of low frequencies in the 49/10 data occurs at about 700 Hz, which equates to a seismic wavelength of just over 2 m at a sediment velocity of 1600 ms^{-1}. A thin-layer of the order of tens of cm in thickness would be sufficient to ensure much of the low-frequency energy would be preferentially transmitted.

The findings of these case studies are in general agreement with a statement made by Ziolkowski and Fokkema (1986):

"There is probably a lack of low-frequency energy in the reflection seismogram, by comparison with the spectrum of the incident wave.".

Within the 49/10 and Atlantic Frontiers case studies, the seabed reflection is assumed to represent the spectral characteristics of the incident wave. This is a simplification as near-surface layering may alter the spectral characteristics of the

downgoing pulse prior to reflection back to surface, as was seen in the Bruce case study. For numerical methods (such as spectrum modelling) that rely on spectral shape to determine parameters such as the quality factor from seismic data, the non-white reflection and transmission response of thin layers (that are not recognised as such) will be problematical.

7.6 Summary of Results

The most important findings of this study are:

1. Wavelet modelling proved to be the most reliable method to measure Q In both the noise-free case and in the presence of varying amounts of random noise. It also provides the best method for measurement of the travel time between two reflection events.

2. Of the spectral methods, spectrum modelling appeared to be the most robust method for estimating Q in the presence of random noise.

3. Complex trace analysis was shown to be a very unreliable numerical technique for measurement of Q when tested with a synthetic data set, even in the noise-free case.

4. When used with single-channel data, the matching technique will yield essentially the same results as the spectral ratios method.

5. The risetime method will be of little practical use for measuring Q as it suffers badly in the presence of noise.

6. In the 49/10 case study, Q was found to be about 60 for fine sands and about 47 for coarse sands measured in the 1 kHz to 3 kHz frequency band.

7. In the Atlantic Frontiers case study, Q was found to be about 59 for sediments which are probably poorly sorted sandy diamicts in the 100 Hz to 240 Hz frequency band.

8. A constant-Q mechanism would account for the spectral behaviour between the seabed and the deeper target reflection events in the two case studies above, but only between the defined frequency limits.

9. A lack of low frequency amplitude occurs within the observed target reflection events in the 49/10 and Atlantic Frontiers case studies. This is likely to be due to low-pass transmission filtering by composite reflection events.

10. The seabed can also act as a low-pass transmission filter in the case of near-surface thin-layering. The Bruce case study showed that the seabed can have a low-pass transmission response.

7.7 Conclusions

As a parameter to characterise the seismic absorption between two reflection events, the quality factor, Q , must be viewed as an approximation within the 49/10 and Atlantic Frontiers case studies . Firstly, there is scant geotechnical information for the sediments within the seismic units under investigation. In the 49/10 case, the gravity cores had a maximum penetration of only 1.5 m, which represents about the top 13 % of the seismic unit. In the Atlantic Frontiers case (if the approximate location of 204/24 is correct) , the source of information was also based on cores with a maximum penetration of a few metres (Stoker, 1990) compared to a thickness of over 70 m for the top seismic unit. The internal structure (with the exception of Unit A in the 49/10 case) of the seismic units investigated was not transparent. Some internal reflection almost certainly occurred, although it has been shown that internal peg-leg activity within the top seismic units cannot account for the spectral shape of the Red and Blue reflections.

The precise mechanism for absorption (frictional sliding and / or viscous dissipation) is difficult to investigate using the kind of data contained within the case studies. The observed constant-Q behaviour was only seen in very restricted frequency intervals and clearly there are non-absorption factors affecting the lower parts of the frequency spectra. However, within the frequency limits of each investigation, the results suggest a constant-Q mechanism for the measured attenuation from the 49/10 and Atlantic Frontiers studies.

The doubt over the linear relationship between absorption and frequency for sandy sediments may be very difficult to investigate using surface seismic techniques. This is because at frequencies below 100 Hz, seismic wavelengths may be of the order of 15 m or more in unconsolidated sands. Within this 15 m there are likely to be thin layers as massive homogenous sands of 15m+ are geologically not common. Several cycles of propagation will therefore be required to determine any attenuation over a path within which the bulk

properties of the sediments may vary greatly. The longer wavelengths will entail thin-layer effects at the lower end of the frequency-spectrum.

With silty sediments, the frequency, at which the attenuation may become non-linear is much higher (above c. 1 kHz, Kibblewhite,(1989)), entailing shorter wavelengths and a greater likelihood of determining the frequency/absorption relationship over shorter vertical distances with better and more precise geotechnical control.

The 49/10 and Bruce case studies examined the spectral characteristics of the uppermost seismic units beneath the seabed. Clearly the likelihood of problems associated with inadequate signal-to-noise ratios and layering effects will increase with a greater number of reflection events bounding and within the seismic units under investigation.

7.8 Recommendations For Future Work

Despite the vast archive of shallow commercial seismic data, there is generally a lack of well-defined geotechnical information for the whole of the seismic unit under analysis. This is because much of the geotechnical information is derived from the first few metres of sediment from shallow cores. These sediment samples may well be disturbed by the coring procedure and recovery. Such information includes bulk sediment properties such as grain size, porosity and density, as well as the vertical distribution of acoustic impedance from which internal reflection events would arise. There is a dearth of soil borings extending 10's of metres which have electrical logging and *in-situ* sample analyses followed by detailed laboratory-based sample analyses. The lack of geotechnical data applies particularly to noncohesive sands and silts, where recovery of borehole and gravity cores has always been less successful than with cohesive clays and muds.

Whether or not the relaxation time, τ, as defined by LeBlanc *et al.*, (1989) will be found to be diagnostic of a sediment type, or it becomes a local parameter for a particular seismic unit will be seen with future investigations using Chirp seismic.

A programme of research using different seismic sources with digital recording over the same marine areas with well-documented geotechnical information of the sub-surface is required. There are many sources which would be suitable for the purpose. These include Boomers (selectable broad-band frequency spectrum c. 300 Hz to c. 10 kHz), Pingers (selectable narrow-band 2 kHz to 15 kHz), Sparkers (selectable broad-band 100 Hz to 5 kHz), Mini Airguns (selectable broad-band c. 50 Hz to c.750 Hz), Chirp Sonar (c. 2 kHz to 14 kHz) and Bubble Pulsers (narrow-band centred on about 400 Hz). Thus the problem of linearity over the practical range of frequency between 100 Hz and 15 kHz will be addressed. The experiments should be carried out over identical lines where possible, crossing boreholes penetrating a range of sediment types from which there is good quality geotechnical information including density, sonic and electric logs for a range of sediment types. Such well controlled experiments would not only contribute to investigations of the dependence of attenuation upon frequency as there are different

bandwidths for different sources, but would also help to refine the attenuation rates for different surface sediment types, whether they conform to a constant-Q model or not. With good borehole control, synthetic seismograms could also be generated to assess the likely effects of thin layering upon the propagating pulse in terms of frequency-dependent reflection and transmission responses as against the normal use of synthetic seismograms (for seismic and well data correlation). The separation of the absorption and non-absorption attenuation effects may then be possible.

Given that there is a very restricted literature concerning the evaluation of seismic attenuation from marine seismic data, this project has made a contribution to the field of attenuation measurement for noncohesive, mainly sandy sediments. The aim of identifying sediment type from quantifiable seismic characteristics requires much more investigation. The relationship between measured attenuation and sediment type or lithology remains an objective for both the Oil and the Geotechnical industries. This thesis shows that the words of Born (1941) may be an optimistic *over-simplification*:

*"The **problem** involved in determining the attenuation characteristics of earth materials is therefore **simply** that of evaluating the loss factor, α."*

APPENDIX A

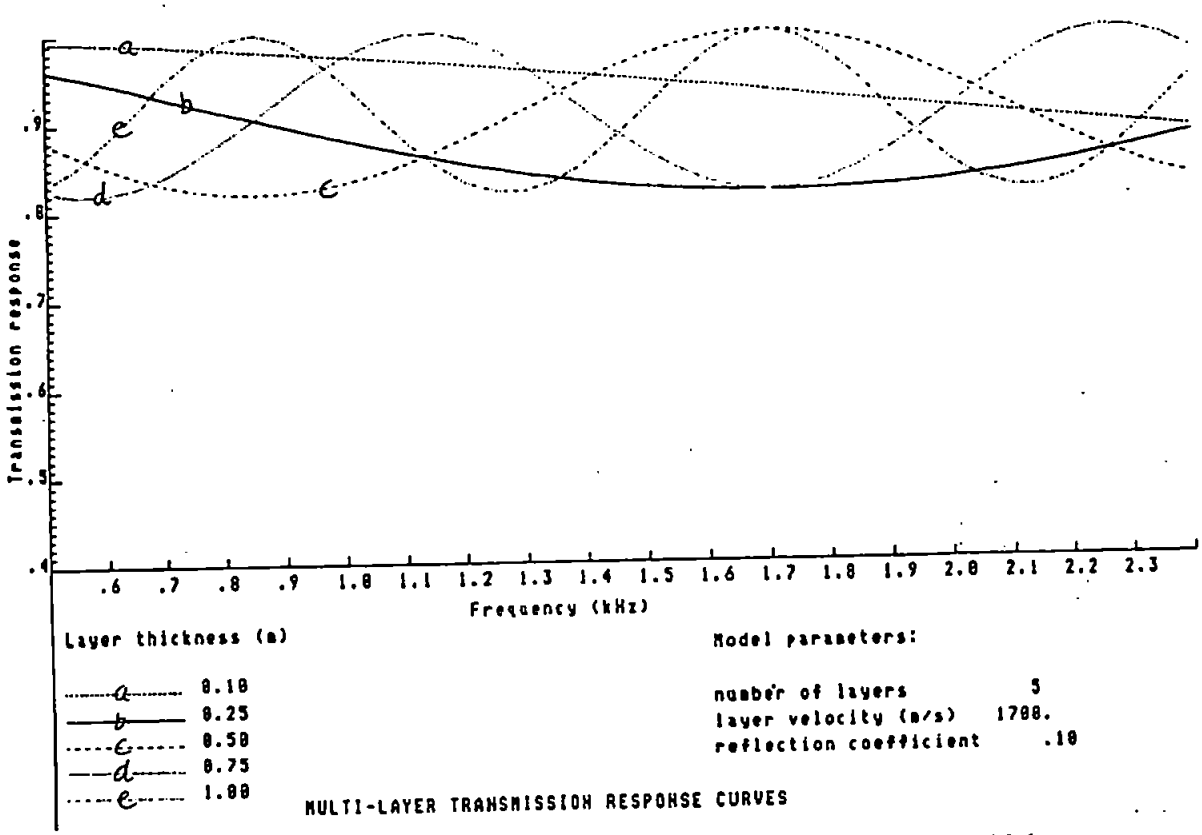

Figure 2.2e Transmission response for 5 layers as a function of Layer thickness
Reflection coefficient = 0.10

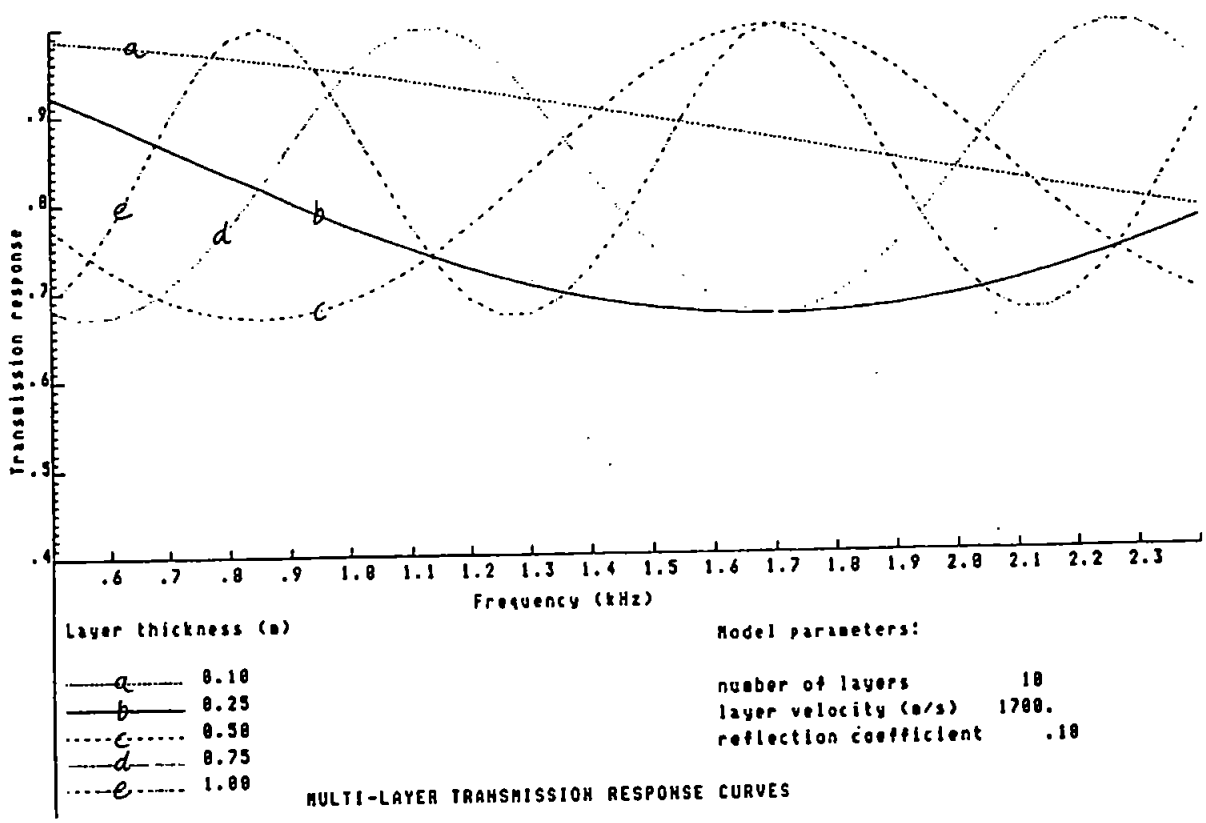

Figure 2.2f Transmission response for 10 layers as a function of Layer thickness
Reflection coefficient = 0.10

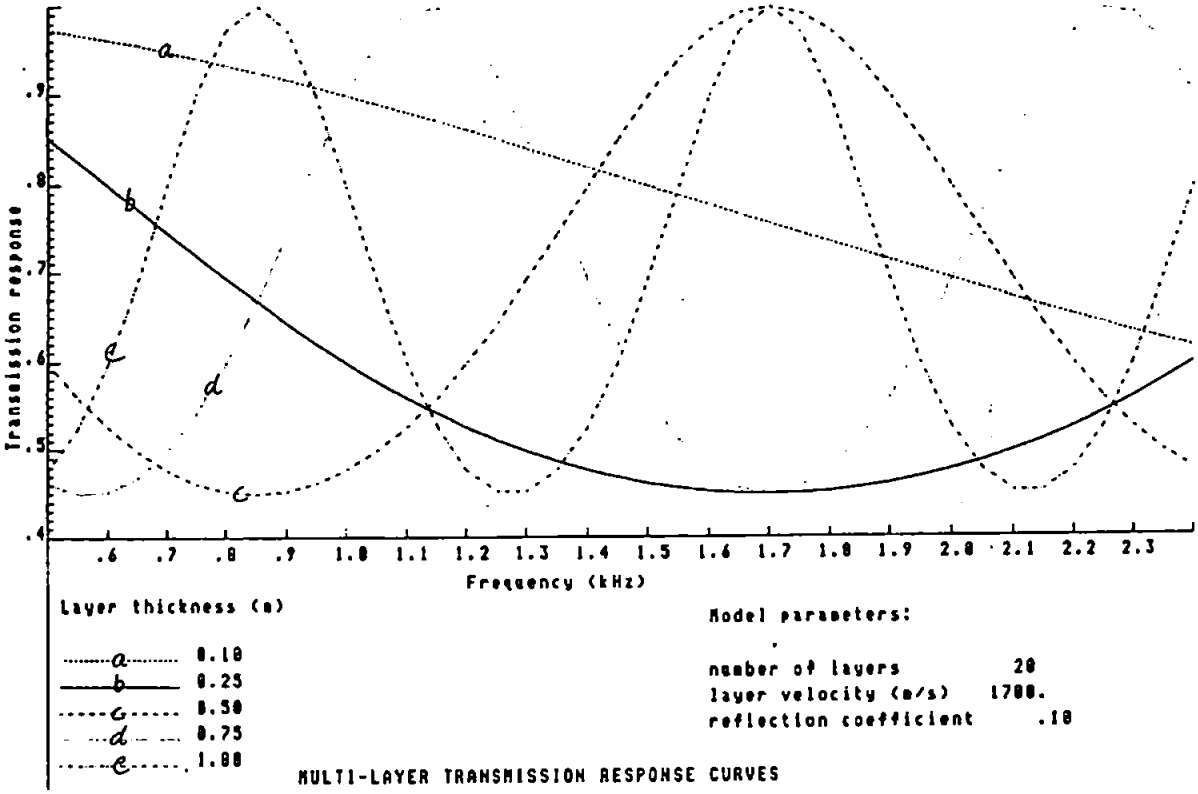

Figure 2.2g Transmission response for 20 layers as a function of Layer thickness
Reflection coefficient = 0.10

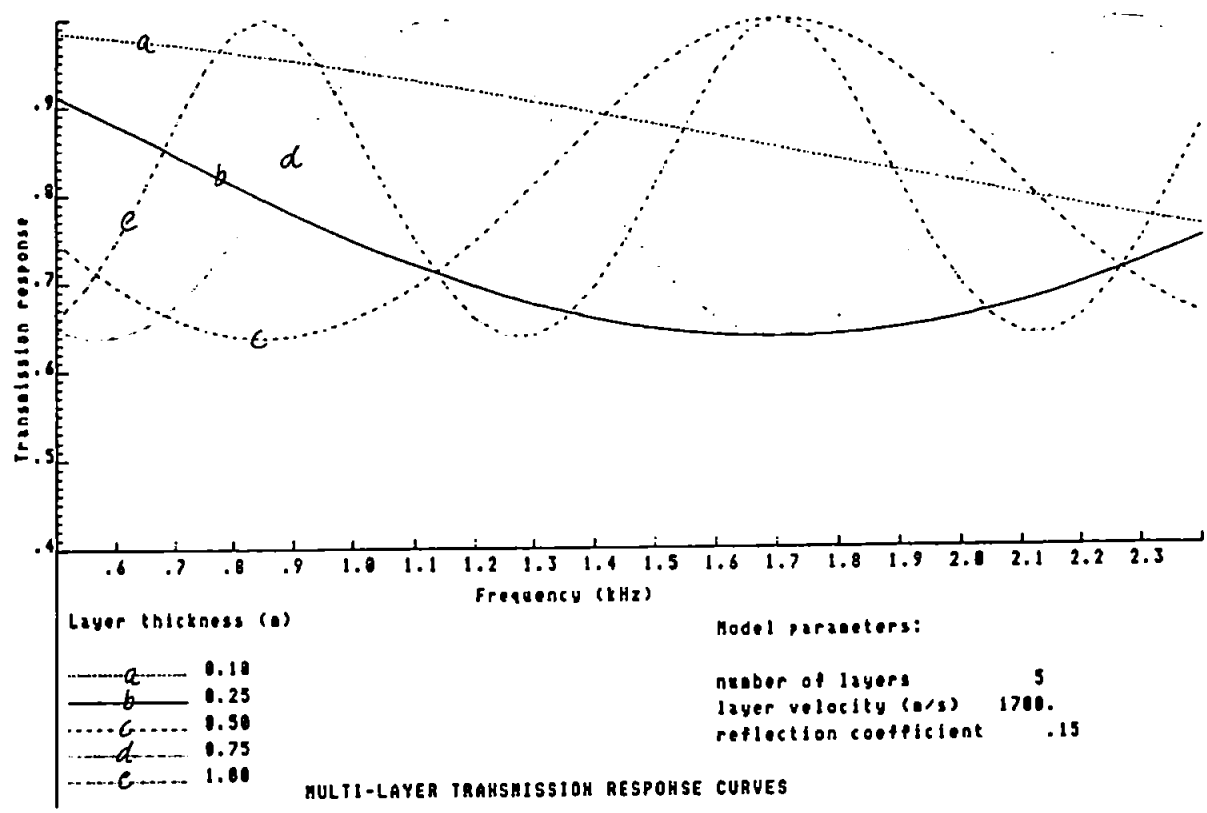

Figure 2.2h Transmission response for 5 layers as a function of Layer thickness
Reflection coefficient = 0.15

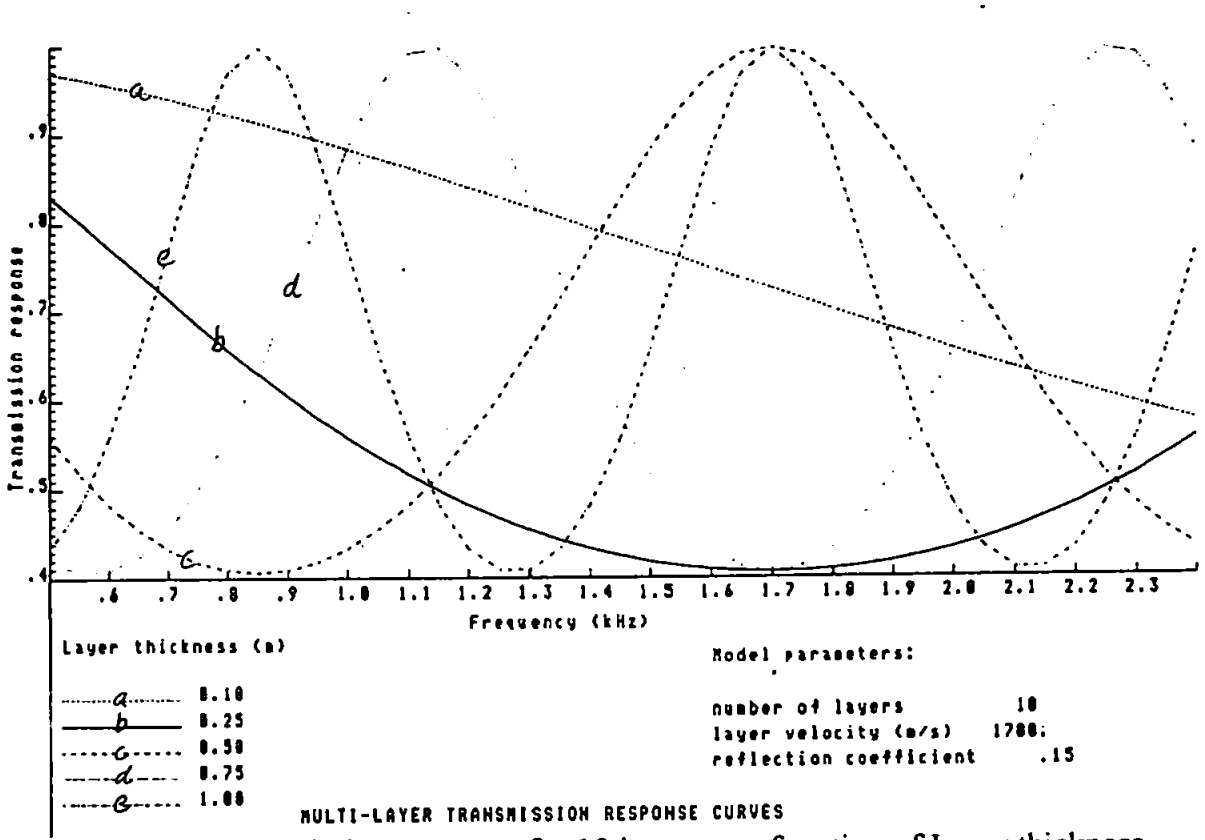

Figure 2.2i Transmission response for 10 layers as a function of Layer thickness
Reflection coefficient = 0.15

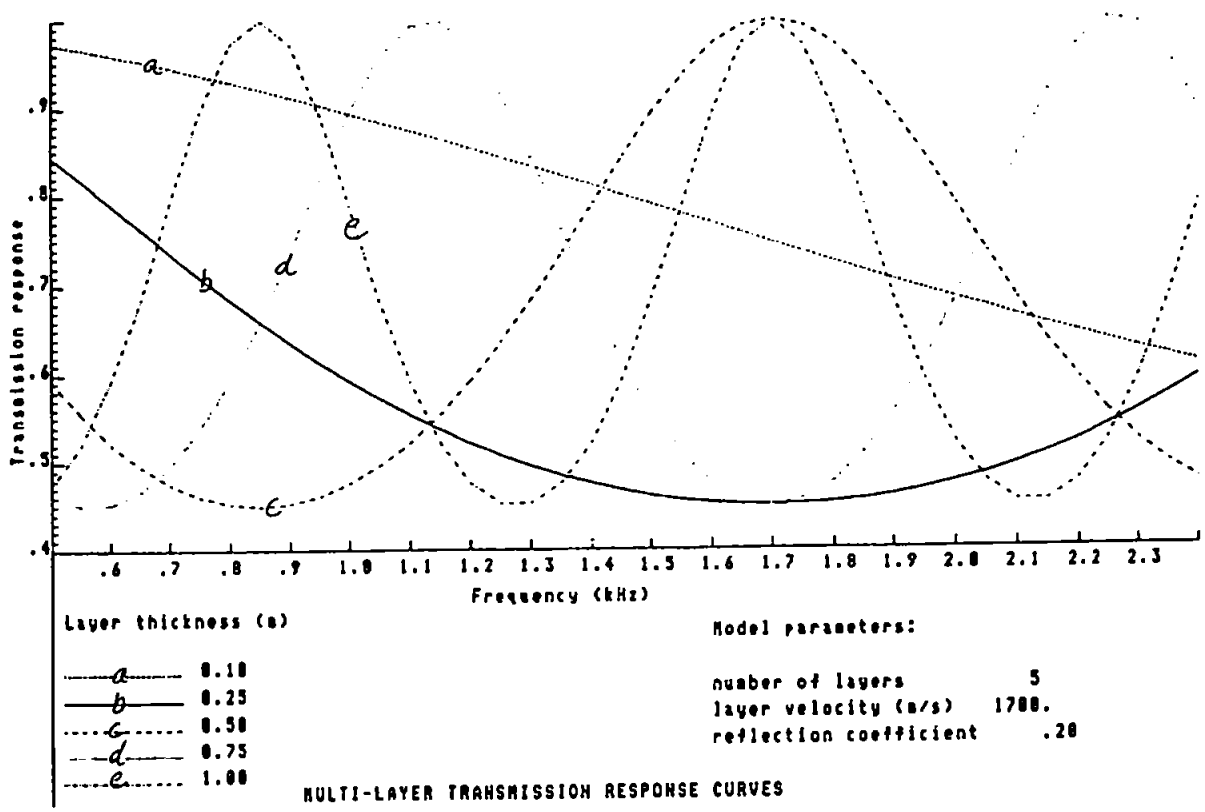

Figure 2.2j Transmission response for 5 layers as a function of Layer thickness
Reflection coefficient = 0.20

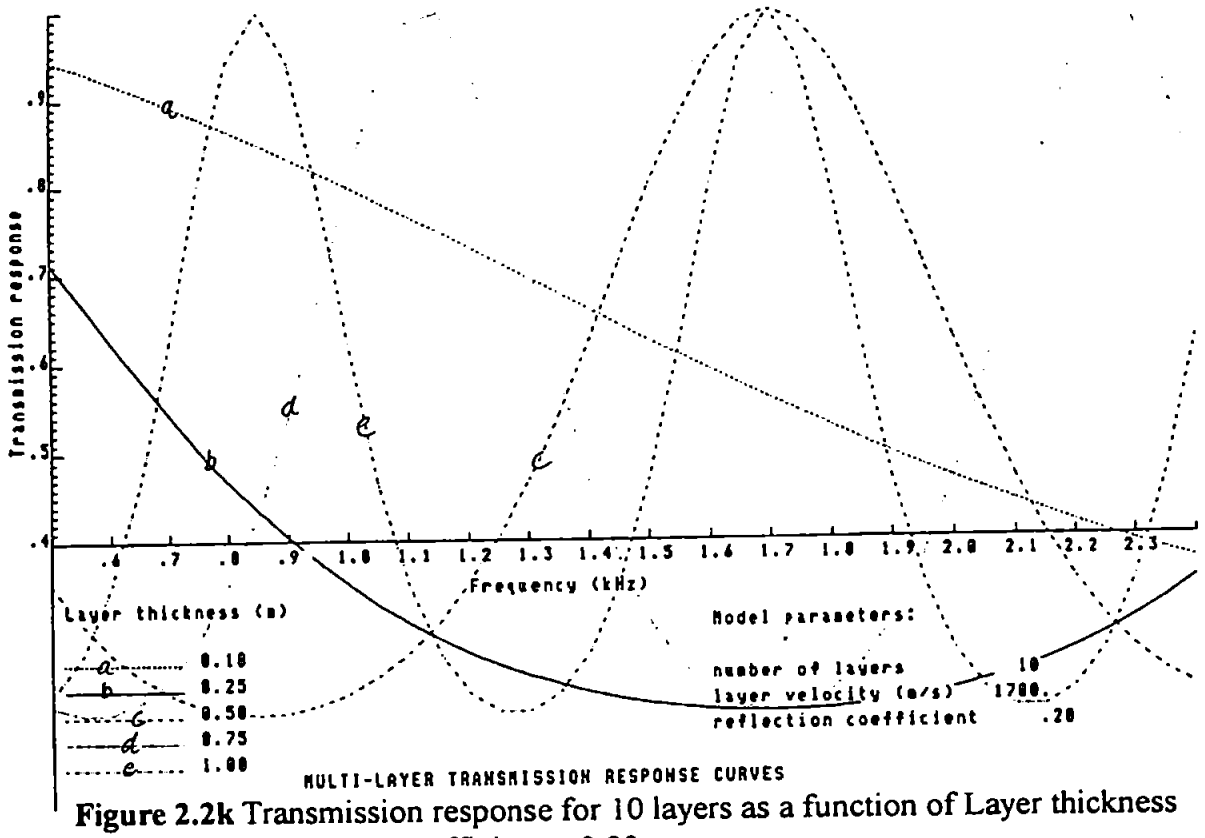

Figure 2.2k Transmission response for 10 layers as a function of Layer thickness
Reflection coefficient = 0.20

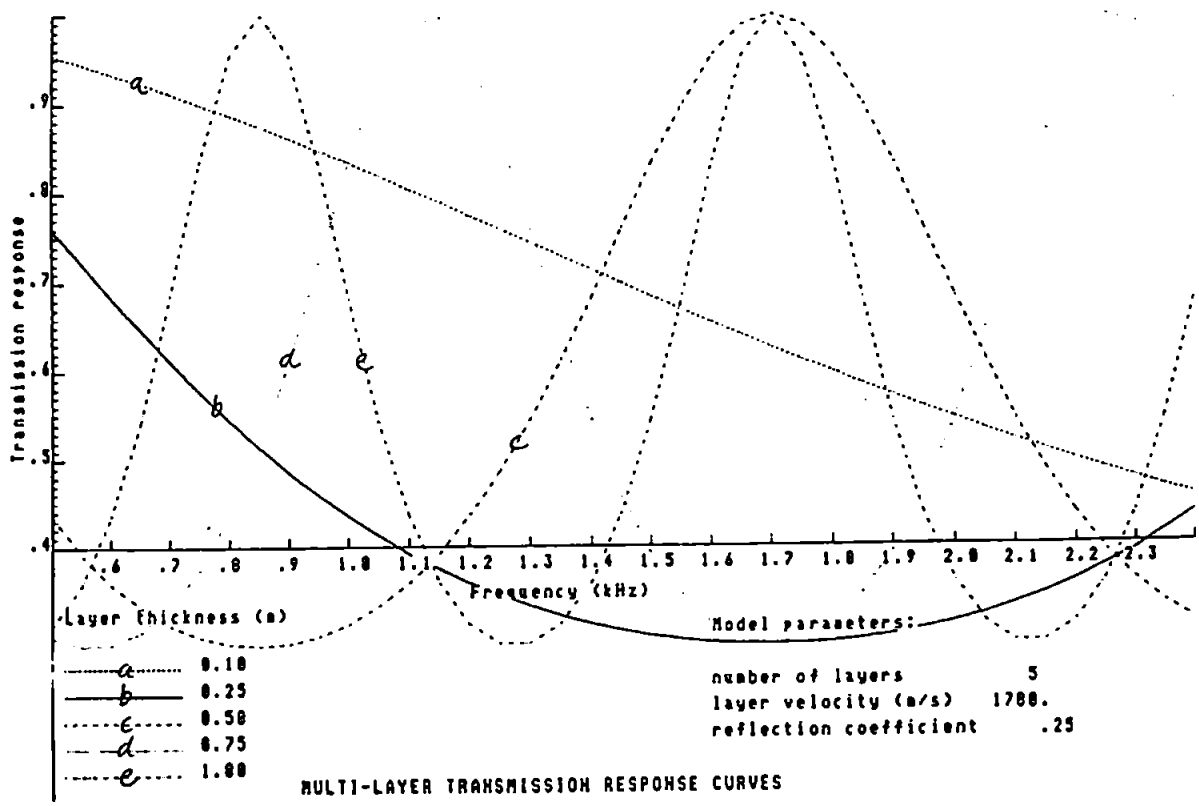

Figure 2.2l Transmission response for 5 layers as a function of Layer thickness
Reflection coefficient = 0.25

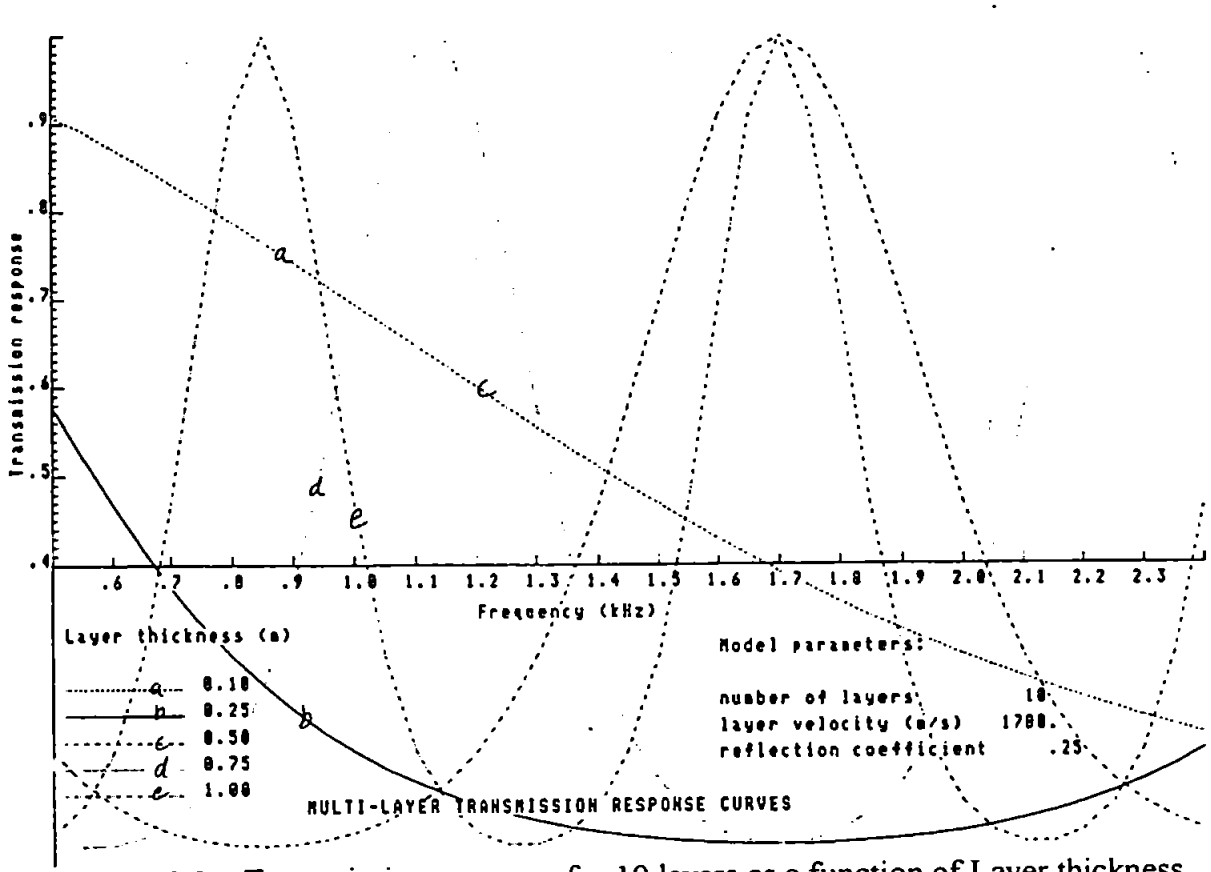

Figure 2.2m Transmission response for 10 layers as a function of Layer thickness
Reflection coefficient = 0.25

APPENDIX B

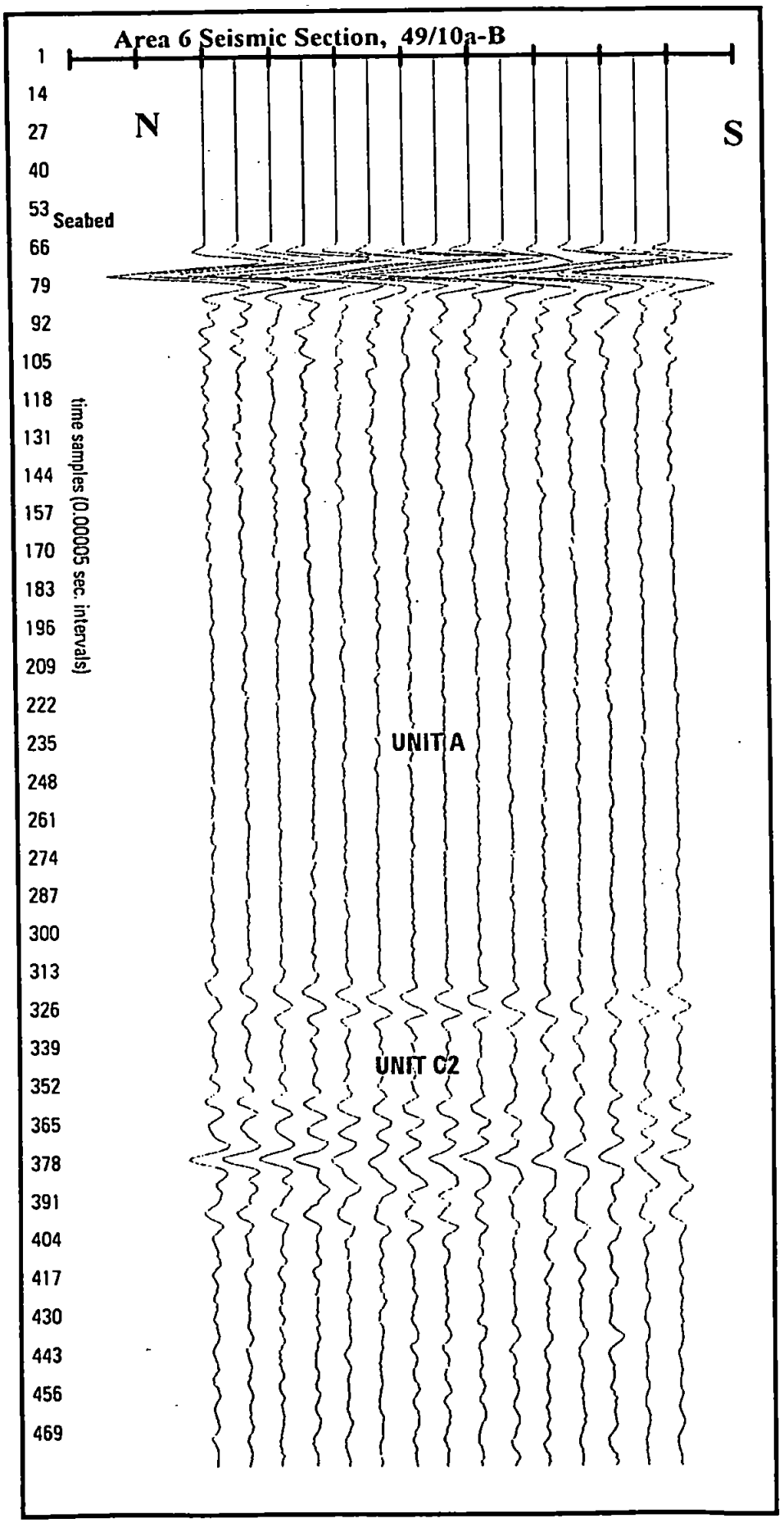

Figure 5.26a Area 6 seismic section, 49/10 survey area.

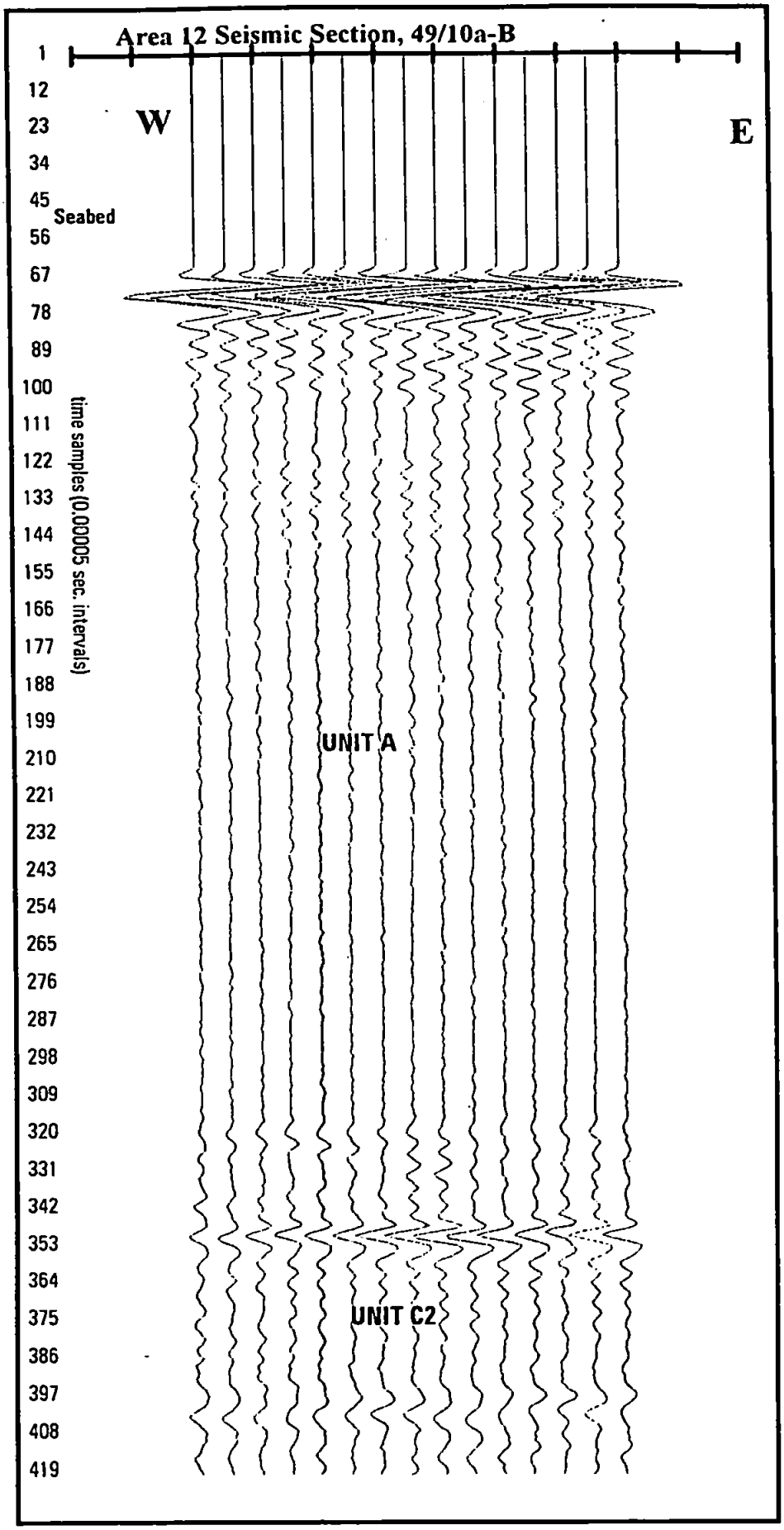

Figure 5.26b Area 12 seismic section, 49/10 survey area.

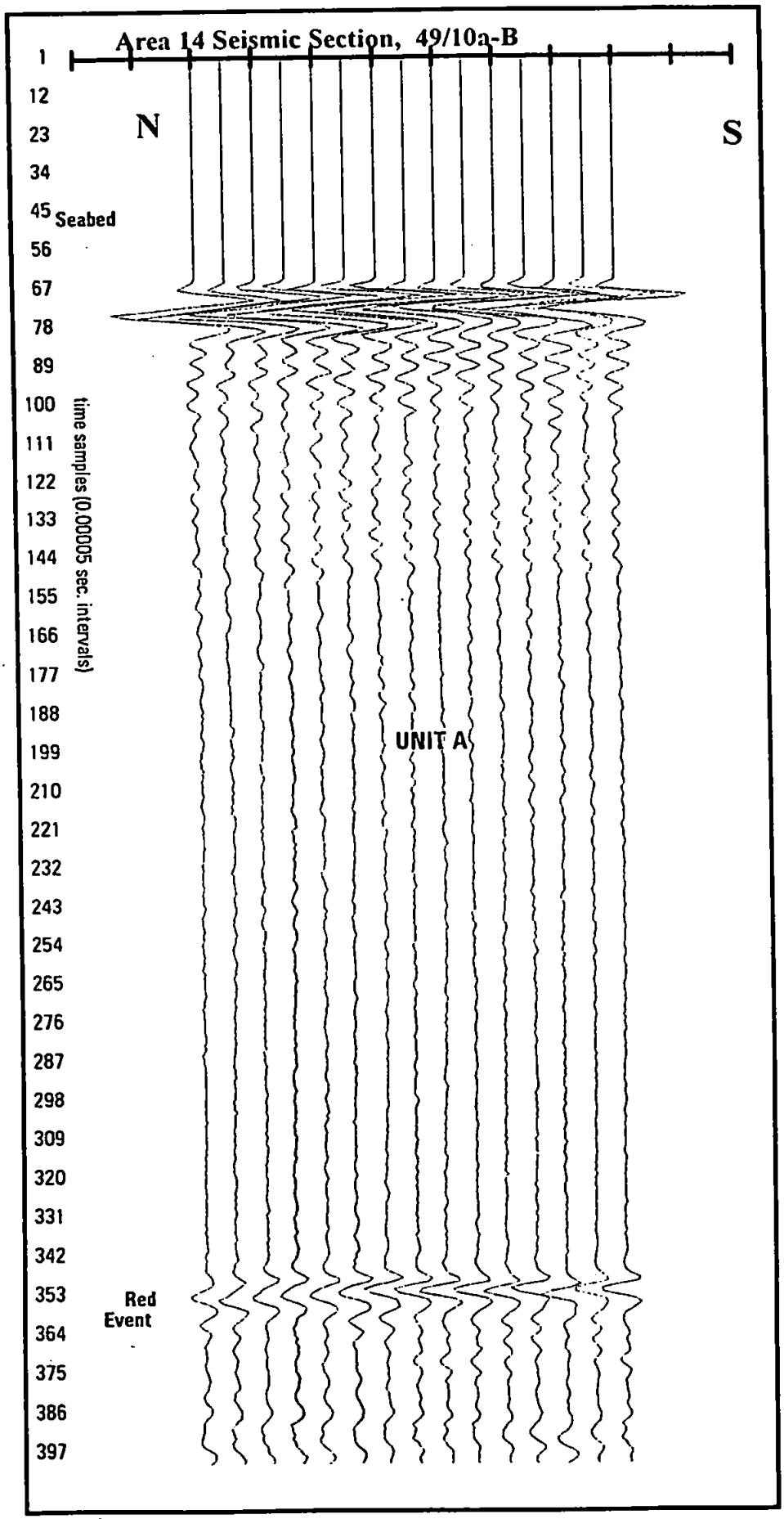

Figure 5.26c Area 14 seismic section, 49/10 survey area.

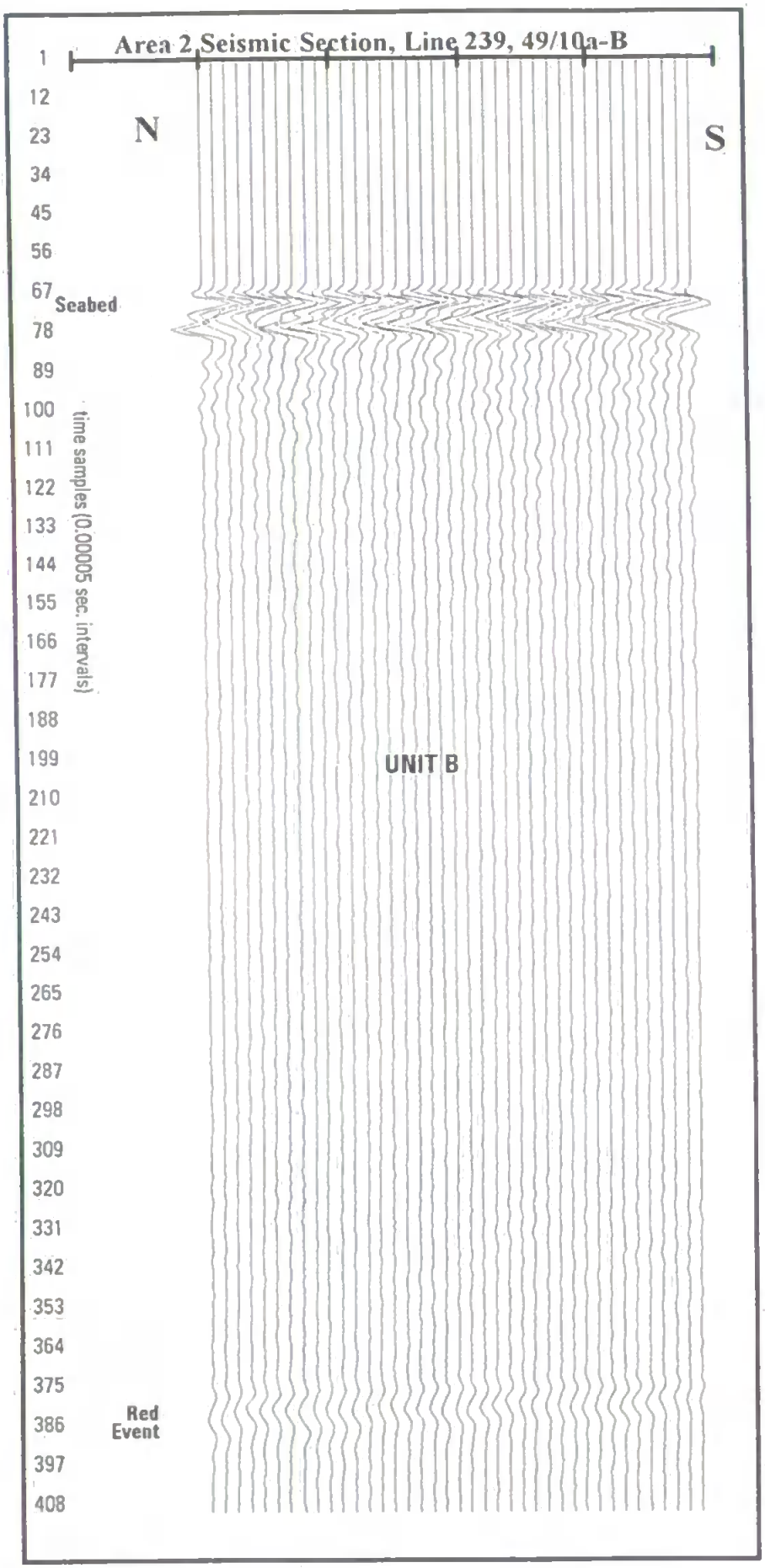

Figure 5.27a Area 2 seismic section, 49/10 survey area.

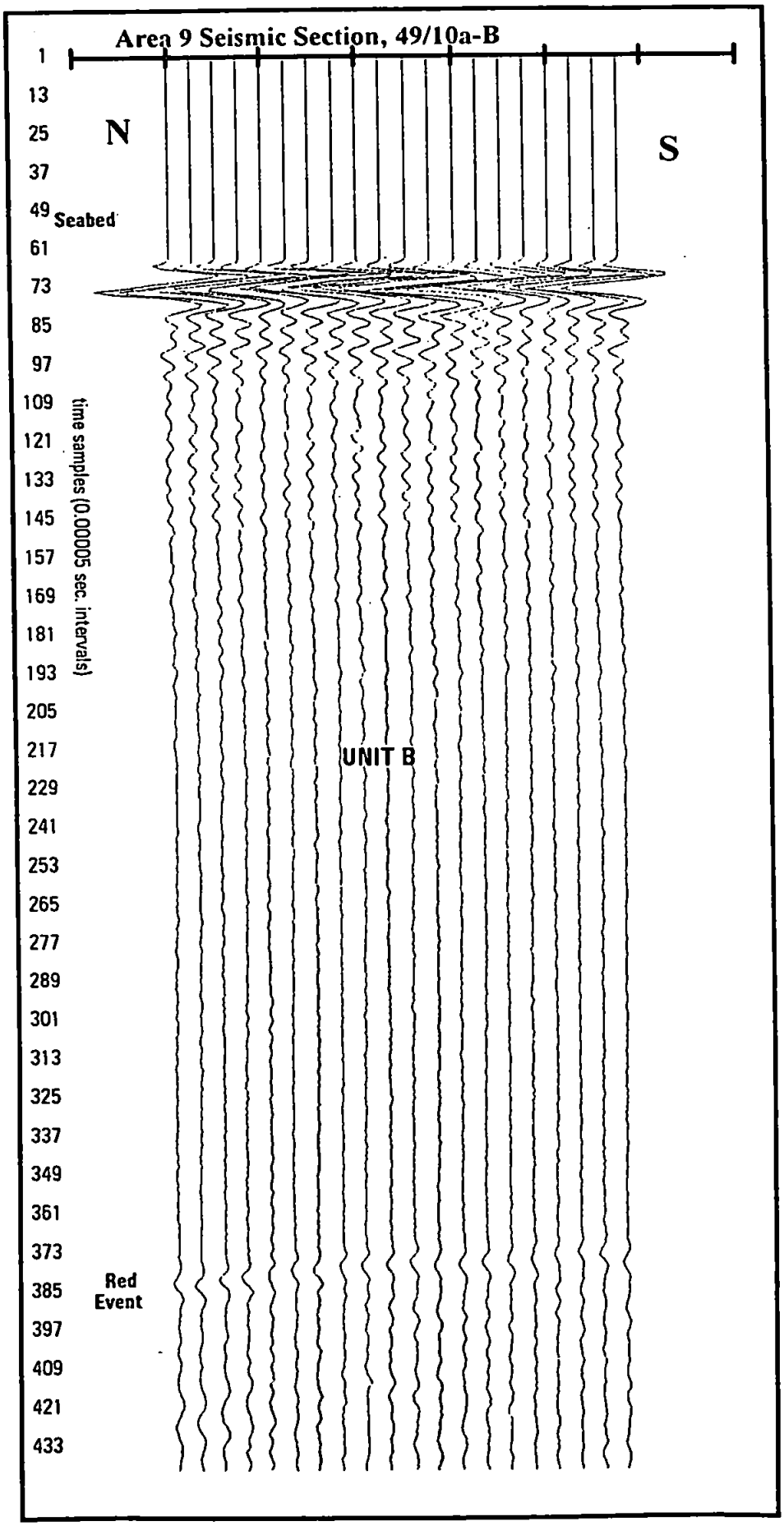

Figure 5.27b Area 9 seismic section, 49/10 survey area.

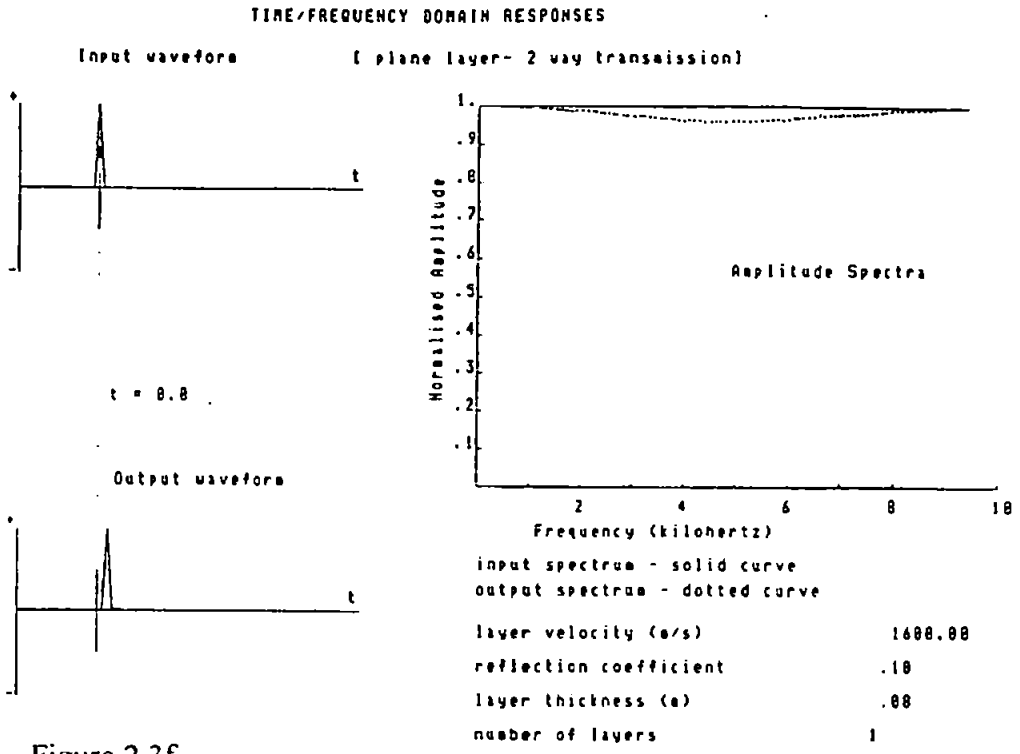

Figure 2.3f
Time and Frequency Domain Responses of a Single 0.08 m Layer using an Impulsive Input Waveform (Rc=.10)

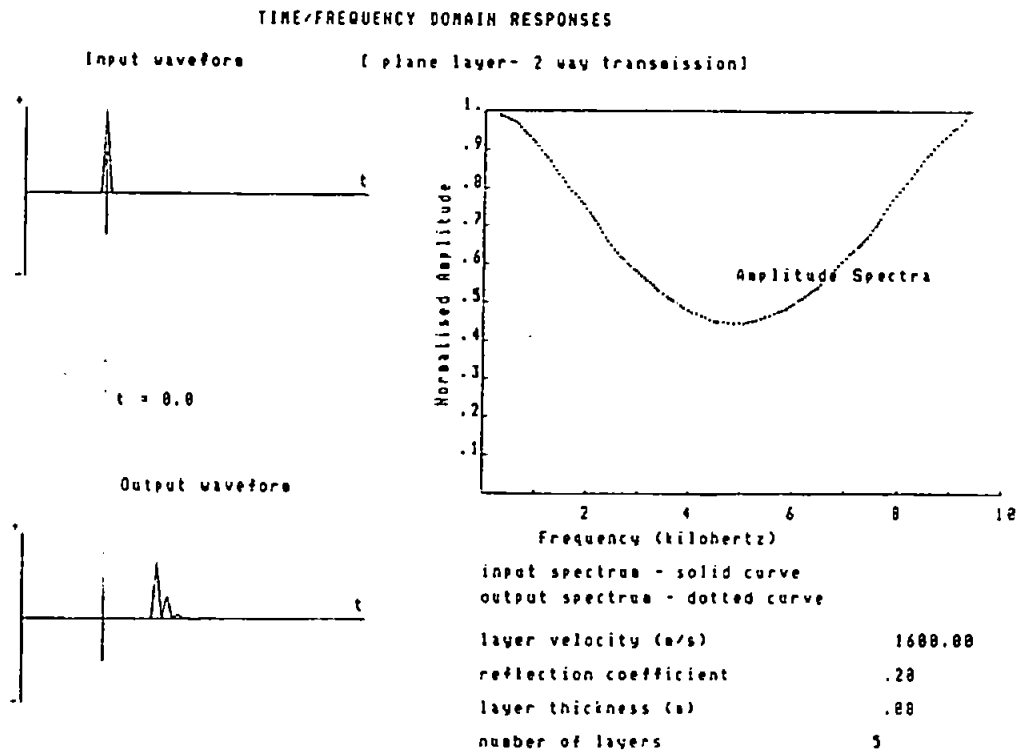

Figure 2.3g
Time and Frequency Domain Responses of 5 0.08m Layers using an Impulsive Input Waveform (Rc=.20)

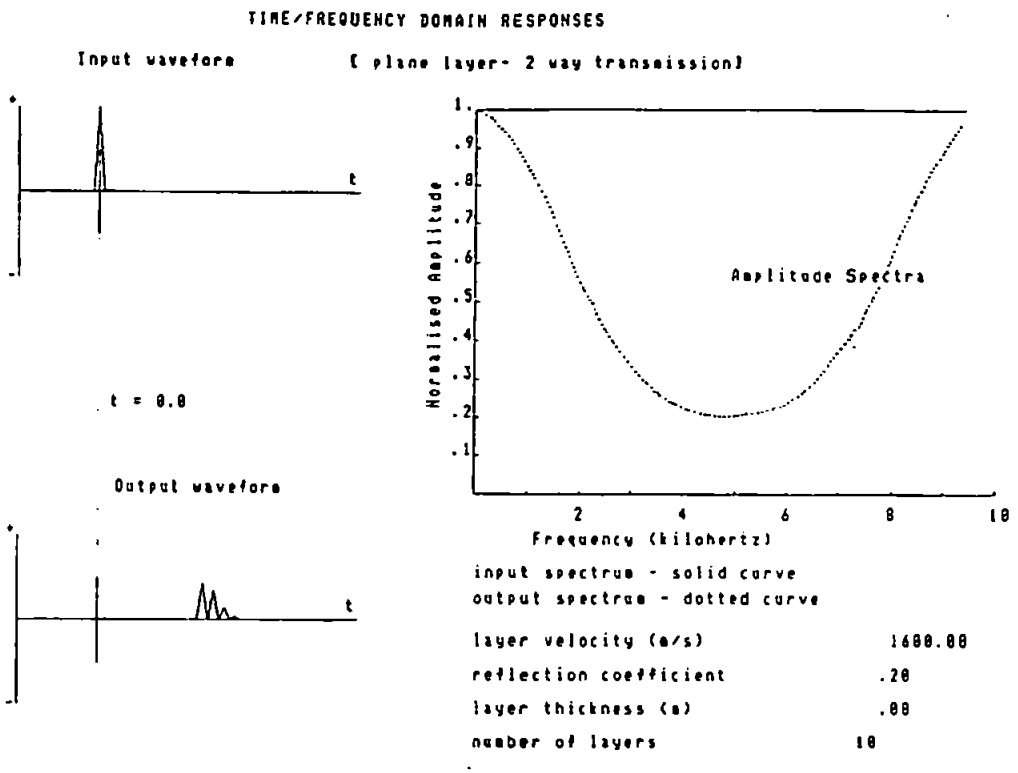

Figure 2.3h
Time and Frequency Domain Responses of 10 0.08 m Layers
using an Impulsive Input Waveform (Rc=.20)

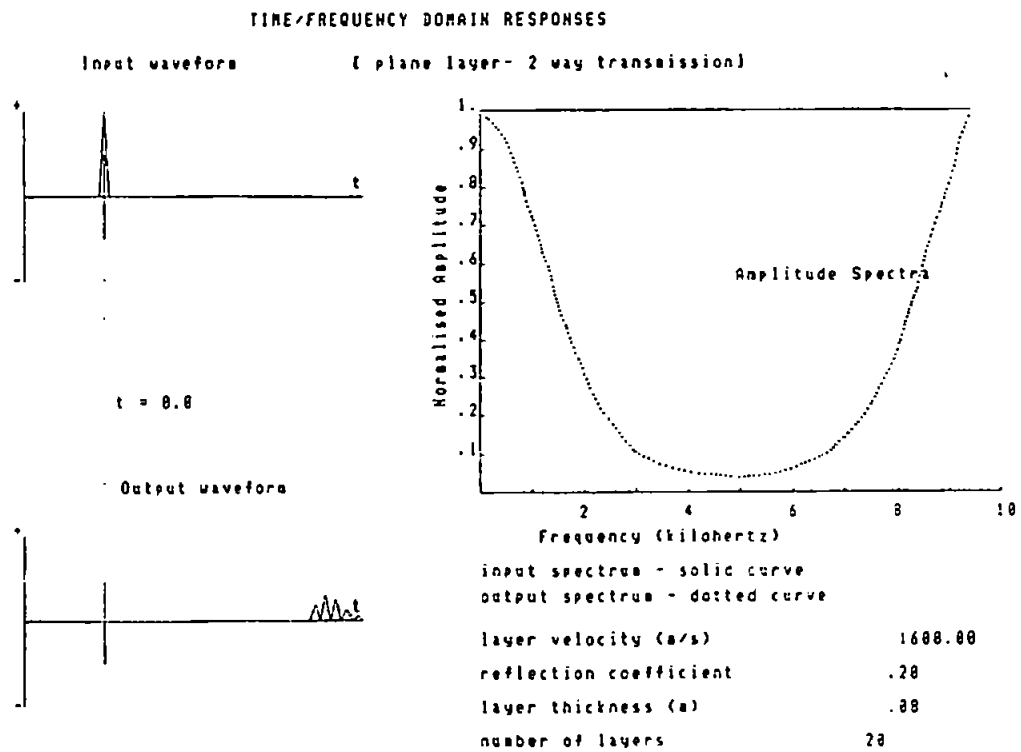

Figure 2.3i
Time and Frequency Domain Responses of 20 0.08 m Layers
using an Impulsive Input Waveform (Rc=.20)

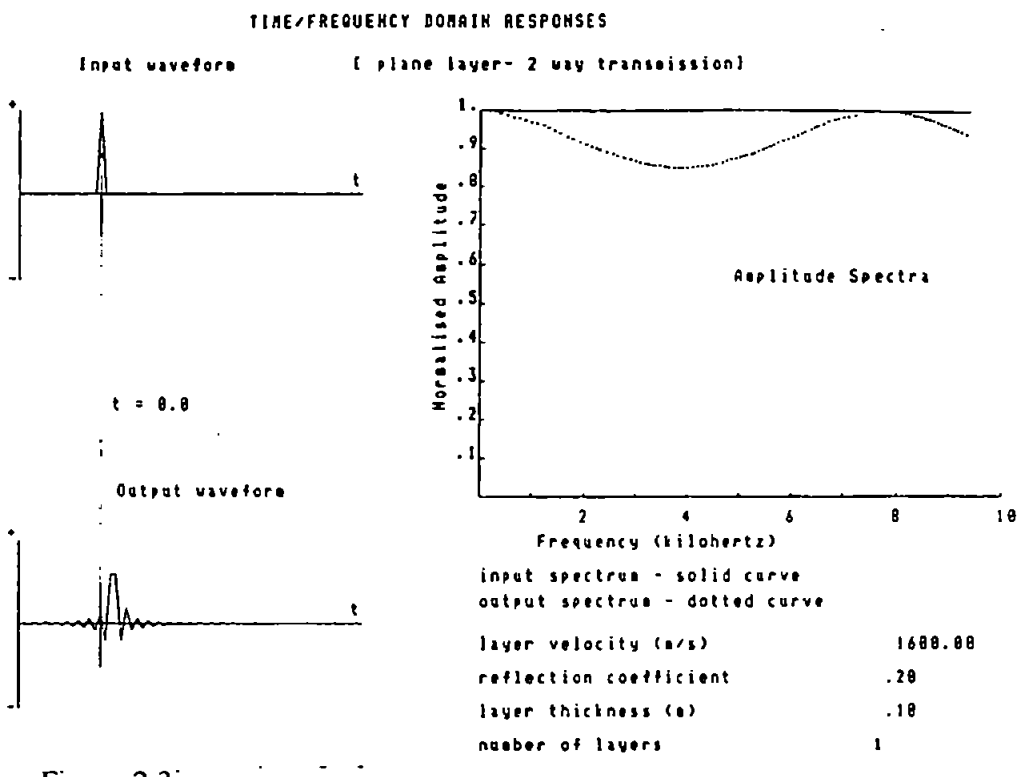

Figure 2.3j
Time and Frequency Domain Responses of a Single 0.10 m Layer using an Impulsive Input Waveform (Rc=.20)

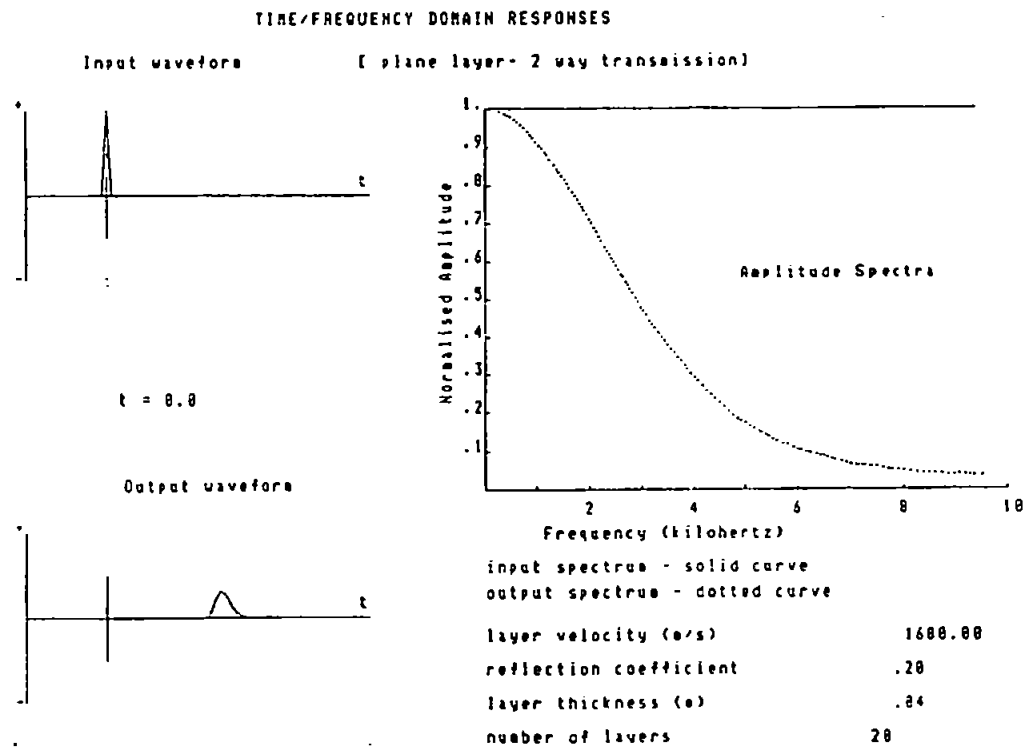

Figure 2.3k
Time and Frequency Doain Responses of 20 0.04m Layers using an Impulsive Input Waveform (Rc=.20)

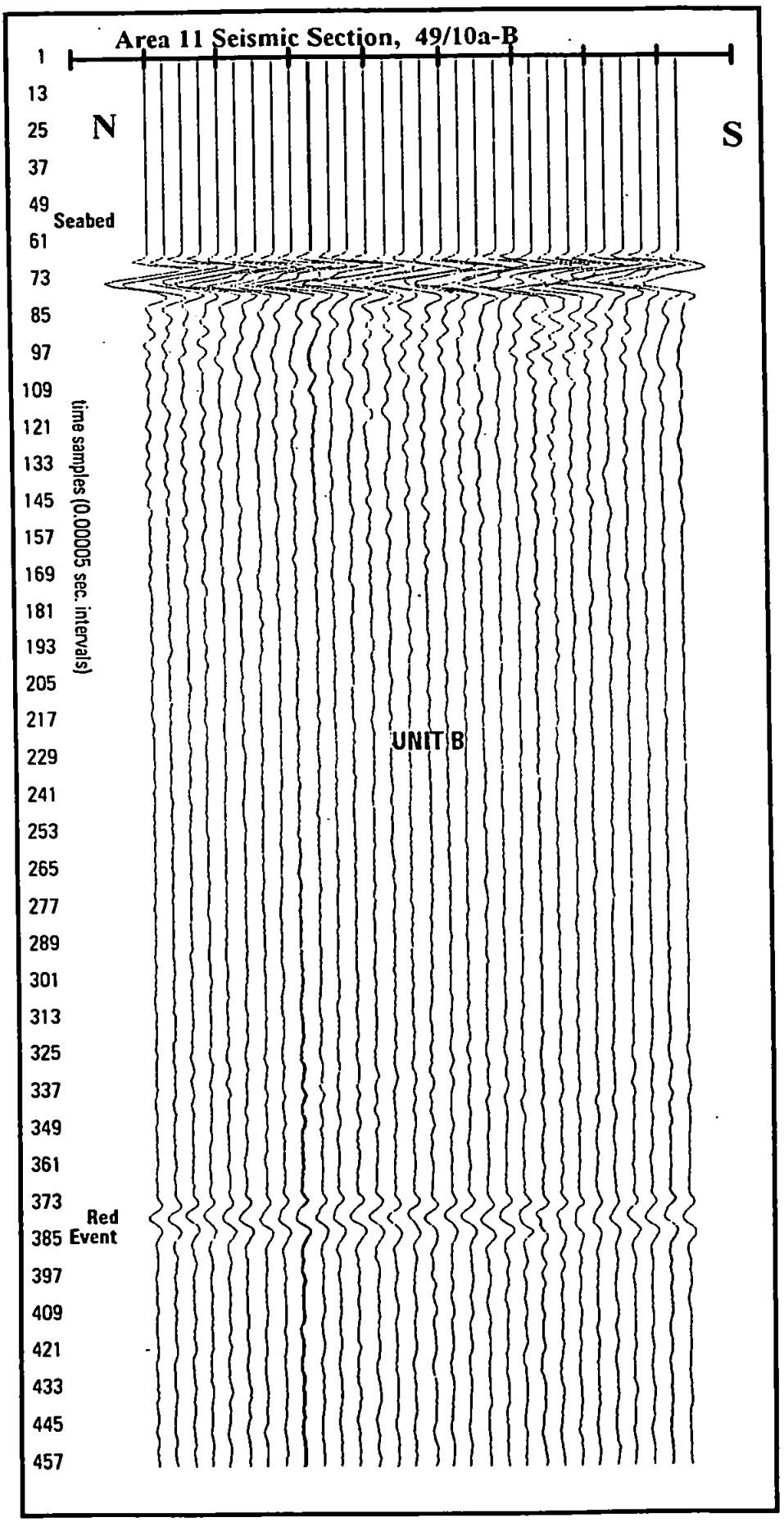

Figure 5.27c Area 11 seismic section, 49/10 survey area.

REFERENCES

Albers, V. M., 1960. *Underwater Acoustics Handbook.* The Pennsylvania University Press, Lancaster.

Attewell, P.B., and Ramana, Y.V., 1966. Wave attenuation and internal friction as functions of frequency in rocks. *Geophysics*, **31**: 1049-1056.

Angeleri, G.P. and Loinger, E., 1984. Phase distortions due to absorption in seismograms and VSP. *Geophys. Prosp.*, **32**: 406-424.

Anstey, N.A., 1960. Attacking the problems of the synthetic seismogram. *Geophys. Prosp.*, **8**: 242-259.

Badri, M. and Mooney, H.M., 1987. *Q* measurements from compressional seismic waves in unconsolidated sediments. *Geophysics*, **52:** 772-784.

Båth, M., 1974. *Spectral Analysis in geophysics.* Amsterdam, Elsevier.

Bennet, L. C., 1967. In-situ measurements of acoustic absorption in unconsolidated sediments (abstract). *Trans. Am. Geophys. Union*, **48**: 144.

Berzon, I. S., 1967. Analysis of the spectral characteristics of a thin-bedded sequence, in Seismic wave propagation in real media., Consultants Bureau, New York and London.

Biot, M.A., 1941. General theory of three-dimensional consolidation. *J. Appl. Phys.*, **12** : 155-164.

Biot, M.A., 1956a. Theory of propagation of elastic waves in a fluid-saturated porous solid. I. Low-frequency range. *J. Acoust. Soc. Am.*, **28**: 168-178.

Biot, M.A., 1956b. Theory of propagation of elastic waves in a fluid-saturated porous solid. II. Higher frequency range. *J. Acoust. Soc. Am.*, **28**: 179-191.

Biot, M.A., 1962. Mechanics of deformation and acoustic propagation in porous media. *J. Appl. Phys.*, **33**: 1482-1498.

Biot, M.A., 1962. Generalised theory of acoustic propagation in porous, dissipative media. *J. Acoust. Soc. Amer.*, **34**: 1254-1264.

Born, W.T., 1941. The attenuation constant of earth materials. *Geophysics*, **6:** 132-148.

Bradley, J. J. and Fort, A.N., Jnr.,1966. Internal friction in rocks, in Handbook of physical constants, S. P. Clark, Jnr., ed., *Geol. Soc. Am. Memoir*, **97**: 175-194.

Brillouin, L.,1960. *Wave propagation and group velocity,* New York, Academic Press.

Buchan, S., Dewes, F.C.D., McCann, D.M., and Taylor Smith, D., 1967. Measurements of the acoustical and geotechnical properties of marine sediment cores, in *Marine Geotechnique*, Richards, A.F. (Ed.), Univ. of Illinois Press.

Buchan, S., McCann, D.M., and Taylor Smith, D., 1972. Relations between the acoustic and geotechnical properties of marine sediments. *Q. Jl. Engng. Geol*, **5**: 265-284.

Busby, J. and Richardson, E.G., 1957. The absorption of sound in sediments. *Geophysics*, **12**: 821-828.

Cameron T.D.J., Laban, C., Mesdag, C.S. and Schüttenhelm, R.T.E.,1986. Indefatigable, Sheet 53°N-02°E , Quaternary Geology, 1:250 000 Map Series. British Geological Survey.

Cameron, T. D. J., Crosby, A., Balson, P. S., Jeffrey, D. H., Lott, G. K., Bulat, J., and Harrison, D. J., 1992. *United Kingdom offshore regional report: the geology of the southern North Sea*. London, HMSO (for the British Geological Survey).

Cameron, T. D. J., Schüttenhelm, R.T.E., and Laban, C., 1989. Middle and Upper Pleistocene and Holocene stratigraphy in the southern North Sea between 52° and 54°N, 2° to 4° E. 119-135 in *The Quaternary and Tertiary geology of the Southern Bight, North Sea.* Henriet, J.P., and De Moor, G., (Eds.).Brussels: Belgian Geological Survey.

Champeney, D.C.,1973. *Fourier Transforms and their Physical Applications*. New York, Academic Press.

Childers, D. G. (ed.), 1978. *Modern Spectral Analysis*. New York, IEEE Press.

Claerbout, J. F., 1976. *Fundementals of Geophysical Data Processing*. McGraw-Hill Book Co.

Clark, V. A., Tittmann, B.R. and Spencer, T.W., 1980. Effect of volatiles on attenuation (Q^{-1}) and velocity in sedimentary rocks. *J. Geophys. Res.*, **85**: 5190-5198.

Clark, G. M. and Cooke, D., 1992. *A basic course in statistics*. London, Edward Arnold.

Cole, B.F., 1965. Marine sediment attenuation and ocean-bottom reflected sound. *J. Acoust. Soc. Amer.*, **37**: 291-297.

Collins, F., and Lee, C.C., 1956. Seismic wave attenuation characteristics from pulse experiments. *Geophysics*, **21**: 16-40.

Edrington, T.S. and Calloway, T.M., 1984. Sound speed and attenuation measurements in gassy sediments in the Gulf of Mexico. *Geophysics*, **49**: 297-299.

Eliot, D.F. and Rao, K.R., 1982. *Fast Transforms: Algorithms, Analyses, Applications*. New York, Academic Press.

Engelhard, L., Doan, D., Dohr, G., Drews, P., Gross, T., Neupert, F., Sattlegger, J. and Schönfeld, U., 1986. Determination of the attenuation of seismic waves from actual field data, as well as considerations to fundemental questions from model and laboratory measurements. DGMK Report, **254**, 83-119.

Foster, M. R. and Guinzy, N. J., 1967. The coefficient of coherence: Its estimation and use in geophysical data processing.*Geophysics*, **32**: 602-616.

Futterman, W. I., 1962. Dispersive body waves. *J. Geophys. Res.*, **67**: 5279-5291.

Gardner, G.H.F., Wyllie, M.R.J., 1964. Effects of pressure and fluid saturation on the attenuation of elastic waves in sands. *J. Petrol. Tech.* 189-198.

Gladwin, M.T. and Stacey, F.D., 1974. Anelastic degradation of acoustic pulses in rock. *Phys. Earth Planet. Int.*, **8**: 332-336.

Grieves, I., 1993. Personal Communication.

Hauge, P.S., 1981. Measurements of attenuation from vertical seismic profiles. *Geophysics*, **46**: 1548-1558.

Hamilton, E. L., 1956. Low sound velocities in high-porosity sediments. *J. Acoust. Soc. Amer.*, **28:** 16-19.

Hamilton, E. L., 1963. Sediment sound-velocity measurements made in-situ from bathyscaph Trieste. *J. Geophys. Res.*, **68**: 5991-5998.

Hamilton, E. L., 1970. Sound velocity and related properties of marine sediments, North Pacific. *J. Geophys. Res.*, **75:** 4423-4446.

Hamilton, E. L., 1972. Compressional wave attenuation in marine sediments. *Geophysics*, **37**: 620-646.

Hamilton, E. L., 1980. Geoacoustic modelling of the sea floor. *J. Acoust. Soc. Amer.*, **68:** 1313-1340.

Hamilton, E. L., 1987. Acoustic properties of sediments, *in Acoustics and Ocean Bottom*. Lara-Saenz, A., Ranz Guerra, C., and Carbofine, C. [Consejo Superior de Investigaciones Cientificas (CSIC), Madrid.

Hampton, L. D., 1985. Acoustic properties of sediments: an update. *Rev. Geophysics*, **23**: 49-60.

Hampton, L. D., and Anderson, A. L., 1974. Acoustics and gas in sediments: applied research laboratories (ARL) experience, *in* Natural gases in marine sediments. I. R. Kaplan, ed., New York, Plenum Press.

Hovem, J.M. and Ingram, G.D., 1979.Viscous attenuation of sound in saturated sand. *J. Acoust. Soc. Amer.*, **66:** 1807-1812..

Hunter, A.N., Legg, R., and Matsukawa, E., 1961. Measurement of acoustic attenuation and velocity in sand. *Acustica,* **11**: 26-31.

Jannsen, D., Voss, J. and Theilen, F., 1985. Comparison of methods to determine Q in shallow marine sediments from vertical reflection seismograms. *Geophys. Prosp.*, 23: 479-497.

Johnston, D. H., and Toksöz, M. N., 1980. Ultrasonic P- and S-wave attenuation in dry and saturated rocks under pressure. *J. Geophys. Res.*, **85**: 925-936.

Jongmans, D., 1990a. In-situ attenuation measurements in soils. *Engineering Geology*, **29**: 99-118.

Jongmans, D., 1991. Near-source pulse propagation: application to Q-determination. *Geophys. Prosp.*, **39**: 943-952.

Keller, J. D., 1989. Acoustic wave propagation in composite fluid-saturated media. *Geophysics*, **54**: 1554-1563.

Khintchine, A., 1934. Korrelationstheorie der stationären stochastischen Prozesse. *Mathematische Analen*, **109**: 604-615.

Kibblewhite, A. C., 1989. Attenuation of sound in marine sediments: A review with emphasis on new low-frequency data. *J. Acoust. Soc. Amer.*, **86:** 716-738.

Kjartansson, E., 1979. Constant Q-wave propagation and attenuation. *J. Geophys. Res.*, **84**: 4737-4748.

Klimentos, T. and McCann, C., 1990. Relationships between compressional wave attenuation, clay content, porosity and permeability in sandstones.*Geophysics*, **55**: 998-1014.

Knopoff, L., 1964. Q. *Rev. Geophys. Space Phys.*, **2:** 625-660.

Knopoff, L. and MacDonald, G. J. F., 1958. Attenuation of small amplitude stress waves in solids. *Rev. Modern Phys.*, **30:** 1178-1192.

Koefoed, O. and De Voogd, N., 1980. The linear properties of thin layers, with an application to synthetic seismograms over coal seams. *Geophysics*, **45**: 1254-1268.

LeBlanc, L. R., Panda, S. and Schock, S. G., 1992. *J. Acoust. Soc. Amer.*, **91**: 116-126.

Long, D., 1990. Bressay Bank, Sheet 59°N-00°, Quaternary Geology. 1:250 000 Map Series. British Geological Survey.

McCann, C., 1969. Compressional wave attenuation in concentrated clay suspensions. *Acustica*, **22**: 352-356.

McCann, C., and McCann, D.M., 1969. The attenuation of compressional waves in marine sediments. *Geophysics*, **34**: 882-892.

McCann, C., and McCann, D.M., 1985. Theory of compressional wave attenuation in non-cohesive sediments. *Geophysics*, **50**: 1311-1317.

McCann, C., and McCann, D.M., 1990. The Acoustic Properties of Marine Sediments. *Underwater Technology*, **16** (4): 23-27.

McCann, D.M., 1968. *Acoustic Properties of North Atlantic Cores.* PhD Thesis. University of Wales. Unpublished.

McLeroy, E. C., and DeLoach, A., 1968. Sound speed and attenuation from 15 to 1500 kHz, measured in natural sea-floor sediments. *J. Acoust. Soc. Amer.*, **44**: 1148-1150.

McQuillin, R., Bacon, M. and Barclay, W., 1984.*An Introduction to Seismic Interpretation*. Oxford, England. Graham and Trotman.

Mindlin, R.D., 1949. Compliance of elastic bodies in contact. *J. Appl. Mech.*, 16: 259-268.

Mindlin, R.D., 1953. Mechanics of granular media, *Proc. 2nd Nat. Congr. Appl. Mech*, **13**.

Murphy, W. F., 1982. Effects of partial water saturation on attenuation in Massilion sandstone and Vycor porous glass. *J. Acoust. Soc. Amer.*, **71**: 1458-1468.

Newman, P., 1973. Divergence effects in a layered earth. *Geophysics*, **38**: 481-488.

Nur, A. and Winkler, K., 1980. The role of friction and fluid flow in wave attenuation in rocks (abstract). *Geophysics*, **45**: 591-592.

O'Doherty, R.F. and Anstey, N. A., 1971. Reflections on amplitudes. *Geophys. Prosp.*, **19** : 430-458.

Press, W. H., Flannery, B. P., Teukolsky, S.A., and Vetterling, W. T., 1986. *Numerical Recipes: The Art of Scientific Computing*. Cambridge, England, Cambridge University Press.

Pujol J. and Smithson S., 1991. Seismic wave attenuation in volcanic rocks from VSP experiments. *Geophysics*, **56**: 1441-1455.

Raikes, S.A. and White, R. E., 1984. Measurements of earth attenuation from downhole and surface seismic recordings. *Geophys. Prosp.*, **32**: 892-919.

Ricker, N., 1953. The form and laws of propagation of seismic wavelets. *Geophysics*, **18**: 10-40.

Sams, M. and Goldberg, D., 1990. The validity of Q estimates from borehole data using spectral ratios. *Geophysics*, **55**: 97-101.

Schirmer, F., 1970. Schallausbreitung im Schlick. *Deut. Hydrogr. Z.*, **23**(1): 24-30.

Schöenberger, M. and Levin, F. K., 1974. Apparent attenuation due to intrabed multiples. *Geophysics*, **39**: 278-291.

Schöenberger, M. and Levin, F. K., 1978. Apparent attenuation due to intrabed multiples II. *Geophysics*, **43**: 730-737.

Sengbush, R. L., 1983. *Seismic exploration methods*. Boston, IHRDC.

Sheriff, R. E., 1975. Factors affecting seismic amplitudes. *Geophys. Prosp.*, **23**: 125-138.

Sheriff, R. E. and Geldhart, L. P., 1982. *Exploration Seismology Vol. 1, History, theory and data acquisition*. Cambridge, England. Cambridge University Press.

Shumway, G., 1956. A resonant chamber method for sound velocity and attenuation measurements in sdeiments. *Geophysics*, **21**: 305-319.

Shumway, G., 1960. Sound speed and absorption studies of marine sediments by a resonance method, Part I. *Geophysics*, **25**: 451-467.

Shumway, G., 1960. Sound speed and absorption studies of marine sediments by a resonance method, Part II. *Geophysics*, **25**: 659-682..

Spencer, T. W., Edwards, C. M., and Sonnad, J. R., 1977. Seismic wave attenuation in nonresolvable cyclic stratification. *Geophysics*, **42**: 939-949.

Spencer, T. W., Sonnad, J. R., and Butler, T. M.,1982. Seismic Q- stratigraphy or dissipation. *Geophysics*, **42**: 939-949.

Stoker, M.S., 1990. Judd, Sheet 60°N-06°W, Quaternary Geology. 1:250 000 Map Series. British Geological Survey.

Stoll, R.D., 1974. Acoustic waves in saturated sediments, *in Physics of sound in marine sediments*: L. D. Hampton, ed. New York, Plenum Press.

Stoll, R.D., 1977. Acoustic waves in ocean sediments. *Geophysics*, **42**: 715-725.

Stoll, R.D., 1989. Sediment Acoustics. Lecture Notes in Earth Sciences 5.Berlin. Springer Verlag.

Stoll, R.D. and Kan, T. K., 1981. Reflection of acoustic waves at a water-sediment interface. *J. Acoust. Soc. Amer.*, **70**: 149-156.

Taner, M. T., Koehler, F. and Sheriff, R. E., 1979. Complex trace analysis. *Geophysics*, **44**: 1041-1063.

Taylor Smith, D., 1974. Discussion of geotechnical mapping of sea-floor sediments by use of geophysical techniques (McCann & Taylor Smith, 1973), *Trans/Sect B (Applied earth science) Inst. Min. Metall.*, **83**: 83, pp.B70-71.

Toksöz, M. N., and Johnston, D. H., 1981. Seismic wave attenuation. *Soc. Explor. Geophys.*

Tonn, R., 1989. Comparison of seven methods for the computation of Q. *Phys. Earth Planet. Int.*, **55**: 259-268.

Tonn, R., 1991. The determination of the seismic quality factor Q from VSP data: A comparison of different computational methods. *Geophys. Prosp.*, **39**: 1-27.

Treitel, S. and Robinson, E. A., 1966. Seismic wave propagation in terms of communication theory. *Geophysics*, **31**: 17-32.

Tullis, F. N. and Reid, C., 1969. Seismic attenuation of Gulf Coast sediments. *Geophysics*, **34**: 516-528.

Ulonska, A., 1968. Versuche zur Messung der Schallgeschwindigkeit und Schalldamfung im Sediment in situ: *Deut. Hydrogr. Z.*, **21**(2): 49-58.

Urick, R. J., 1947. A sound velocity method for determining compressibility of finely divided substances. *J. Appl. Phys.*, **18**: 983-987.

Urick, R. J., 1948. Absorption of sound in suspensions of irregular particles. *J. Acoust. Soc.Amer.*,**20**: 283-289.

Waters, K.H., 1978. *Reflection Seismology*: New York, Wiley.

Webb, S. C. and Cox, C. S., 1986. Observations and modelling of seafloor microseism. *J. Geophys. Res.*, **91**: 7343-7358.

White, J. E., 1965. Seismic waves: radiation, transmission and attenuation. New York. McGraw-Hill Book Co. Inc.

White, J. E., 1966. Static friction as a source of seismic attenuation. *Geophysics*, **31**: 333-339.

White, R. E., 1973. The estimation of signal spectra and related quantities by means of the multiple coherence function. *Geophys. Prosp.*, **21**: 660-703.

White, R. E., 1980. Partial coherence matching of synthetic seismograms with seismic traces. *Geophys. Prosp.*, **28**: 333-358.

White, R. E., 1992. The accuaracy of estimating Q from seismic data. *Geophysics*, **57**: 1508-1511.

Widess, M. B., 1973. How thin is a thin bed ?. *Geophysics*, **38**: 1176-1180.

Wiener, N., 1930.Generalised harmonic analsyis. *Acta Mathematica*, **55**: 117-258.

Wood, A. B., and Weston, D. E., 1964. The propagation of sound in mud. *Acoustica*, **14**: 156-162.

Wyllie, M. R. J., Gardner, G. H. F., and Gregory, A.R., 1962. Studies of elastic wave attenuation in porous media. *Geophysics*, **27**: 569-589.

Zhou, J., Zhang, X., Rogers, P. H., and Jarynski, J., 1987. Geoacoustic parameters in a stratified sea bottom from shallow water acoustic propagation. *J. Acoust. Soc. Amer.*, **82**: 2086-2074.

Ziolkowski, A. and Fokkema, J. T., 1986. The progressive attenuation of high-frequency energy in seismic reflection data. *Geophys. Prosp.*, **34**: 981-1001.

Zoeppritz, K., 1919. Über reflexion und durchgang seismischer wellen durch Ünstetigkerlsflaschen. Berlin, *Über Erdbebenwellen VII B, Nachrichten der Königlichen Gesellschaft der Wissenschaften zu Göttingen, math-phys.* K1: 57-84.